



Photochemical Modeling of the Formation of Conduction Electrons at a Heterojunction in an Organic Solar Cell

Ala Aldin M Hani Mahmood Darghouth

► To cite this version:

Ala Aldin M Hani Mahmood Darghouth. Photochemical Modeling of the Formation of Conduction Electrons at a Heterojunction in an Organic Solar Cell. Theoretical and/or physical chemistry. Université Grenoble Alpes, 2017. English. NNT : 2017GREAV091 . tel-01844536

HAL Id: tel-01844536

<https://theses.hal.science/tel-01844536>

Submitted on 19 Jul 2018

HAL is a multi-disciplinary open access archive for the deposit and dissemination of scientific research documents, whether they are published or not. The documents may come from teaching and research institutions in France or abroad, or from public or private research centers.

L'archive ouverte pluridisciplinaire **HAL**, est destinée au dépôt et à la diffusion de documents scientifiques de niveau recherche, publiés ou non, émanant des établissements d'enseignement et de recherche français ou étrangers, des laboratoires publics ou privés.



THÈSE

Pour obtenir le grade de

DOCTEUR DE LA COMMUNAUTÉ UNIVERSITÉ GRENOBLE ALPES

Spécialité : Chimie Physique Moléculaire et Structurale

Arrêté ministériel : 25 mai 2016

Présentée par

Ala Aldin M Hani Mahmood DARGHOUTH

Thèse dirigée par **Mark CASIDA (EDCSV)**, UGA

préparée au sein du **Laboratoire Département de Chimie
Moléculaire**
dans l'**École Doctorale Chimie et Sciences du Vivant**

Modélisation photochimique de la formation des électrons de conduction au sein de l'hétérojonction d'une cellule solaire organique

Photochemical Modeling of the Formation of Conduction Electrons at a Heterojunction in an Organic Solar Cell

Thèse soutenue publiquement le **22 décembre 2017**,
devant le jury composé de :

Monsieur MARIO BARBATTI

PROFESSEUR, UNIVERSITE AIX-MARSEILLE, Rapporteur

Madame TSONKA MINEVA

DIRECTRICE DE RECHERCHE, CNRS DELEGATION LANGUEDOC-
ROUSSILLON, Rapporteur

Madame ANNE MILET

PROFESSEUR, UNIVERSITE GRENOBLE ALPES, Président

Monsieur ROLAND MITRIC

PROFESSEUR, UNIVERSITE DE WURTZBOURG - ALLEMAGNE,
Examineur

Monsieur MATHIAS RAPACIOLI

CHARGE DE RECHERCHE, CNRS DELEGATION MIDI-PYRENEES,
Examineur

Monsieur HAIBIN SU

PROFESSEUR ASSOCIE, UNIV. TECHNOLOGIE DE NANYANG -
SINGAPOUR, Examineur

Monsieur MARK E. CASIDA

PROFESSEUR, UNIVERSITE GRENOBLE ALPES, Directeur de thèse

Acknowledgments

I wish to express my warmest thanks to Prof. Mark E. CASIDA. He has been an attentive thesis director who somehow always managed to make time for me despite his many responsibilities. His competence, scientific rigor, and clairvoyance have been and will remain an inspiration for my work as a researcher.

Thanks also to all the members of my jury: Prof. Anne MILET, Prof. Mario BARBATTI, Prof. Roland MITRIĆ, Prof. Haibin SU, Dr. Tsonka MINEVA, and Dr. Mathias RAPACIOLI. My gratitude also goes out to all my friends and, in general, to all the people who have helped in the realization of this work.

A special thanks must go to the theoretical chemistry group whose friendly and supportive climate made it all the easier and more enjoyable to work. The many discussions that I have had with the wonderful people of or otherwise associated with the *Département de Chimie Moléculaire (DCM)* greatly enriched my experience as a doctoral student. Thank you for your support and encouragement.

In most endeavors, there are people behind the scenes that help the show to go on. To them also goes a large thank you: To Dr. Pierre GIRARD for all his efforts to solve program porting and other computer issues and to the administrative staff of the *DCM*.

Dr. Hemanadhan MYNENI and Alexander HUMENIUK were most helpful to me in many ways, not the least of which were useful discussions.

Speaking from deep within my heart, I would like to address all my affection to my family and to dedicate this thesis to them. This includes my wife Asmaa and my children, Yaman and Yahya, who surrounded me with their love. It also includes my loving mother who made me understand that not all problems can be solved through mathematical formulae and algorithms. And, though he has passed away and so is no longer with us, my thanks and dedication go out as a special thought to the memory of my father.

To my extended family in Iraq (my brothers, my sister, and their families): Thank you for your support, your prayers, and your love.

Last but not least, I would like to thank the French and Iraqi governments for

support through *Campus France*. The ORGAVOLT (ORGAnic solar cell VOLTage by numerical computation) *Association National de Recherche (ANR)* group is also acknowledged for travel support and stimulating meetings whether away or at home via videoconference.

To France, I would like to add a special thanks. You are one of the most successful national models of peaceful coexistence that I know. Living in France has made me see life from a different perspective.

Résumé

L'intérêt au domaine de l'électronique organique croît, en partie, à cause des faits que les matériaux de type polymère conducteur sont légers, peu coûteux à mettre en forme et peuvent même être imprimés avec des technologies déjà disponibles. Les cellules photovoltaïques organiques sont parmi les plusieurs applications de l'organique électronique et sont le cible particulier de la recherche de la thèse actuelle.

Un composant critique des cellules photovoltaïques organiques modernes est l'interface entre un matériau accepteur d'électrons et un matériau donneur d'électrons. La structure électronique de la cellule photovoltaïque à cette interface est critique à étudier afin de mieux comprendre la fonction de la cellule et afin d'augmenter son efficacité. Les niveaux quantiques des donneurs et des accepteurs doivent être soigneusement alignés à l'interface afin d'optimiser la probabilité de dissociation de charge nécessaire pour une haute efficacité de conversion d'énergie des photons à l'énergie électronique. Quand il y a suffisamment de recouvrement des fonctions d'ondes des électrons et des trous, alors un exciton peut se trouver lié à l'interface pour former un exciplex avec un caractère significatif de type transfert de charge et une énergie plus basse que celle des électrons et trous totalement dissociés. L'évidence pour un tel exciplex est trouvée dans certains matériaux dans l'existence d'une luminescence importante — en particulier avec un temps de vie radiative d'ordre d'environ 100 ns et un déplacement spectroscopique vers le rouge. Il est anticipé que la dissociation de l'exciplex dépendra de la différence entre le potentiel d'ionisation du matériau donneur et de l'affinité électronique du matériau accepteur qui, ensemble, créera une force énergétique favorisant la séparation des charges. La thèse actuelle est justement une contribution vers une meilleure compréhension de la mécanisme de séparation de charge, principalement par la caractérisation de la capacité de la méthode de liaisons fortes basées sur la théorie de la fonctionnelle de la densité (c-à-d la *DFTB*, de l'anglais *density-functional tight binding*) pour la description des différents aspects de la séparation de charge aux interfaces organiques et puis par une application de la *DFTB* dépendant du temps (*TD-DFTB* pour l'anglais *time-dependent DFTB*) à l'étude de la photodynamique de ce processus. Le projet de

thèse présenté ici se divise en une étude à trois étapes :

Dans la première étape, nous avons évalué la capacité de la *DFTB* pour prédire les potentiels d'ionisation et les affinités électroniques des molécules d'une importance pour l'électronique organique. En particulier, les potentiels d'ionisation et les affinités électroniques des molécules de taille moyenne important pour des applications de type photovoltaïques organiques ont été calculés avec la *DFTB* avec des charges autocohérent jusqu'au troisième ordre (*DFTB3*) et comparés avec des valeurs expérimentales et des valeurs calculés à partir d'une méthode de type premier principe, appelé par le nom de la fonction de Green multiplié par le potentiel écranté (*GW*). Nous avons confirmé que la *DFTB* se comporte bien comme la théorie de la fonctionnelle de la densité (la *DFT* pour l'anglais *density-functional theory*) dans sa capacité à prédire les potentiels d'ionisation et les affinités électriques, pourtant avec une certaine perte de précision inévitable associés avec les approximations semi-empiriques. Selon cette étude la meilleure façon à calculer les potentiels d'ionisation et les affinités électroniques avec la *DFTB3* est la méthode Δ SCF.

Dans la deuxième étape, nous avons évalué la capacité de la *DFTB* dépendante du temps (*TD-DFTB* pour l'anglais *time-dependent DFTB*) la plus au point pour reproduire les résultats de la *DFT* dépendante du temps (*TD-DFT* pour l'anglais *time-dependant DFT*) pour la description des effets excitoniques dans les spectres des agrégats des excitons. En particulier, ces calculations comprend à la fois une correction pour l'effet de dispersion appliquée à l'état fondamental et l'utilisation d'une fonctionnelle de type de séparation selon la distance de la répulsion électronique (*RSH* pour l'anglais *range-separated hybrid*) dans l'application de la théorie de réponse dépendante du temps utilisée pour le calcul des spectres. Il est important, et non évident, de savoir séparer les effets de transfert d'énergie d'excitation et de transfert de charge entre molécules dans l'analyse des effets excitoniques. Nous avons fait ceci à travers une analyse soigneuse d'un modèle simple des molécules d'éthylène entassées parallèlement que nous avons pu appliquer essentiellement sans modification au cas des molécules de pentacène entassées parallèlement. Ceci nous a permis à confirmer le résultat anticipé que les effets d'utiliser un *RSH* sont plus important pour les excitations de type transferts de charge que pour les excitations de type transfert d'énergie. Néanmoins le *RSH* CAM-B3LYP utilisé pour paramétriser la méthode *TD-lc-DFTB* (de l'anglais *TD long-range corrected DFTB*) nous semble loin d'optimal pour ce type d'application vu que des calculs *TD-DFTB* basés sur le *DFTB* paramétrisé avec la fonctionnelle B3LYP se comportaient de manière similaire et beaucoup mieux comparées avec l'expérience et des calculs Bethe-Salpeter pour les effets excitoniques dans les spectres pour la structure "chevrons" ou "arêtes

d'hareng" des cristaux de pentacène que c'est le cas pour le *TD-lc-DFTB* ou que pour le *TD-CAM-B3LYP*. Nous considérons que les difficultés avec les calculs *TD-lc-DFTB* et *TD-CAM-B3LYP* viennent d'une mauvaise comportement à distance de la fonctionnelle CAM-B3LYP.

La troisième et dernière, étape dans cette thèse n'est pas une évaluation de la qualité du *DFTB* mais plutôt une application du *DFTB* afin de mieux comprendre la mécanisme de separation de charge à l'interface. L'idée est de profiter de l'avantage de la similarité du *DFTB* avec le *DFT* ensemble avec la plus grande simplicité de calcul du *DFTB* pour étendre notre étude bien plus loin que le calcul des potentiels d'ionisation, des affinités électroniques, et des effets excitoniques spectraux. En fait nous avons utilisé le *DFTB* dans une étude détaillée de la photodynamique de la séparation de charge pour le modèle le plus simple d'une hétérojonction organique comprenant une seule molécule de pentacène (le donneur d'électrons) en complexe van der Waals avec une seule molécule de buckminsterfullerine (un accepteur d'électrons). Nous avons utilisé la dynamique semiclassique de type Tully mélangeant le *TD-lc-DFTB* pour le traitement des électrons et la mécanique classique pour produire des trajectoires de noyaux avec des sauts de surfaces et ceci afin de modéliser en tant que processus photochimique le processus de comment une excitation locale se sépare pour former une paire électron/trou conducteur, à la différence de l'approche Born-Oppenheimer des noyaux figés favorisée, disons, par la plupart des physiciens de matière condensé. Comme dans la deuxième étape déjà discutée, il est critique de savoir faire distinguer la différence entre le transfert d'énergie et de charge si on veut correctement interpréter les résultats obtenus. En faisant cette distinction, nous avons pu démontrer que le premier transfert d'énergie intermoléculaire se passe en moins que 20 fs approximativement avec ensuite une tendance de continuer à transférer d'énergie entre les molécules assez rapidement jusqu'à l'apparence d'un vrai transfert de charge beaucoup plus tard vers 127 fs. Comme notre système est trop petit pour éviter des raccourcies, le transfert de charge n'est que temporaire. Néanmoins il nous semble que notre étude est la première étude théorique à donner une compréhension claire de la dynamique du transfert de charge et que nous pouvons espérer que des études similaires sur des systèmes encore plus grands comprenant plus de molécules montreraient la création des états de conduction avec un temps de vie significatif.

Abstract

Interest in organic electronics is rapidly increasing, in part, because conducting plastics are light weight, inexpensive to cast into various shapes, and can even be printed. Organic solar cells are one among many of several applications of organic electronics and constitute the particular area of application addressed in this thesis.

A critical element of modern organic solar cells is an interface between an electron acceptor material and an electron donor material. The electronic structure of the organic solar cell at this interface is a critical element in studies of function and of efficiency. Donor and acceptor energy levels at the interface must be carefully matched to get the optimal charge dissociation needed for high energy conversion efficiency. When the electron and hole wave functions overlap enough, then an exciton may be bound at the interface to make an exciplex having significant charge transfer character and lower energy than separated electrons and holes. Evidence for this exciplex is found in some materials through the presence of considerably luminescence — in particular a radiative lifetime of about 100 ns and a substantial red shift. Dissociation of the exciplex is expected to depend upon the difference between the ionization potential of the donor material and the electron affinity of the acceptor material which, together, provide a downhill energetic driving force for the charge separation. This thesis contributes to a better understanding of charge separation at the interface mainly by characterizing the ability of the density-functional tight-binding (DFTB) method for describing various aspects of charge separation at organic interfaces and then by applying time-dependent DFTB (TD-DFTB) to study the photochemical dynamics of this process. This thesis may be regarded as a three-step study.

In step one, we have assessed the ability of DFTB to be able to calculate the ionization potentials and electron affinities of molecules of importance for organic electronics. Specifically the ionization potentials and electron affinities obtained with DFTB with self-consistent charges included through third order (DFTB3) of medium-sized molecules important for organic solar cell applications were assessed against experiment and against first principles Green's function times screened po-

tential (*GW*) calculations. We found DFTB to act much like DFT in its ability to predict ionization potentials and electron affinities, albeit with some loss of precision. The best way to calculate ionization potentials and electron affinities using DFTB3 was found to be with the Δ SCF method.

In step two, we assessed how well state-of-the-art time-dependent DFTB (TD-DFTB) is able to reproduce state-of-the-art time-dependent density-functional theory (TD-DFT) for describing excitonic effects in the spectra of pentacene aggregates. In particular, these calculations include both a dispersion correction for the ground state and the use of a range-separated hybrid functional in the time-dependent response theory used to calculate spectra. It is important, and unobvious, to separate excitonic and charge-transfer effects between molecules in analyzing excitonic effects. We did this by a careful analysis of a simple model of parallel-stacked ethylene molecules which could be carried over directly to the case of parallel-stacked pentacene molecules. This allowed us to confirm the expected result that range-separation has a larger impact on charge-transfer excitations than upon energy-transfer excitations. However the CAM-B3LYP range-separated functional used to parameterize TD-lc-DFTB (TD long-range-corrected DFTB) calculations appears to be far from optimal for this type of application as TD-DFTB calculations based upon DFTB parameterized with the B3LYP functional did behave analogously and significantly better compared with both experiment and Bethe-Salpeter calculations for excitonic effects on the experimentally-known herringbone structure of crystalline pentacene, than does either TD-lc-DFTB and TD-CAM-B3LYP. We attribute this to an incorrect long-range behavior of the CAM-B3LYP range-separated functional.

The third, and last step as far as this thesis is concerned, is not an assessment of DFTB but rather an application of DFTB towards understanding the mechanism of charge-transfer at the interface. The idea is to take advantage of the similarity of DFTB with DFT together with the greater simplicity of DFTB to extend our study well beyond the calculation of mere ionization potentials, electron affinities, and excitonic effects on spectra. Instead we wish to use DFTB in a detailed photodynamics study of charge separation for the simplest possible model of an organic heterojunction, namely for a supermolecule consisting of a single pentacene molecule (an electron donor) in a van der Waals complex with a single buckminsterfullerene molecule (an electron acceptor). We used Tully-type mixed TD-lc-DFTB/classical trajectory surface hopping dynamics to model the process of how a local excitation separates to form a conducting electron/hole pair as a photochemical-type reaction, as opposed to the Born-Oppenheimer fixed-nuclei approach favored by, say, most solid-state physicists. As in the second step mentioned above, distinguishing

between exciton energy transfer and charge transfer turns out to be critical in interpreting the results. By separating these two effects, we were able to show that the time required for the first energy exciton transfer is within about 20 fs with continuing exciton energy transfer back and forth between the molecules until charge transfer is obtained much later, after approximately 127 fs. As our system is too small to avoid dynamical recurrances, the charge transfer is not permanent. Nevertheless this appears to be the first study of the kind to give a clear dynamical picture of the charge transfer process and we may hope that similar studies applied to larger aggregates consisting of more molecules may show the creation of long-lived conduction-like states.

Articles

- [**DCT+15**] Ala Aldin M.H.M. Darghouth, Mark E. Casida, Walid Taouali, Kamel Alimi, Mathias P. Ljungberg, Peter Koval, Daniel Sánchez-Portal, and Dietrich Foerster, “[Assessment of Density-Functional Tight-Binding Ionization Potentials and Electron Affinities of Molecules of Interest for Organic Solar Cells Against First-Principles GW Calculations](#)”, *Computation* **3**, 616 (2015). (Proceedings of the 16th International Conference on Density Functional Theory and its Applications, 31 August - 4 September 2015, Debrecen, Hungary)
- [**MADC17**] Tarek Mestiri, Kamel Alimi, Ala Aldin M.H.M. Darghouth, and Mark E. Casida, “[Density-Functional Theory Study of the Optoelectronic Properties of \$\pi\$ -Conjugated Copolymers for Organic Light-Emitting Diodes](#)”, Preprint: <https://arxiv.org/abs/1708.05247>.
- [**DCJ+17**] Ala Aldin M.H.M. Darghouth, Gabriela Calinao Correa, Sacha Juillard, Mark E. Casida, Alexander Humeniuk, and Roland Mitrič, “[Davidov-Type Excitonic Effects on the Absorption Spectra of Parallel-Stacked and Herringbone Aggregates of Pentacene: Time-Dependent Density-Functional Theory and Time-Dependent Density-Functional Tight Binding](#)”, Preprint: <https://arxiv.org/abs/1803.00056> .
- [**DCS+17**] Ala Aldin M.H.M. Darghouth, Mark E. Casida, Xi Zhu, Bhaarithi Natarajan, Haibin Su, Alexander Humeniuk and Roland Mitrič, “[How Long Do Energy and Charge Transfer Take? Tully-Type Mixed Time-Dependent Tight-Binding Density-Functional/Classical Trajectory Surface Hopping Study of a Model Buckminsterfullerine/Pentacene Heterojunction with and without Long-Range Correction](#)”, *manuscript in preparation*.

Contents

Remerciements	i
Résumé	iii
Abstract	vii
1 Introduction	3
Introduction	5
Bibliography	8
I General Background	9
2 Organic Solar Cells	11
2.1 Organic Electronic Materials	11
2.2 Types of Organic Solar Cell	14
2.3 The Fundamental Mechanism of Power Conversion	16
2.4 Experimentally Measured Quantities	17
2.5 The Mechanism of the Charge Separation	21
Bibliography	22
3 Photochemistry	25
3.1 Introduction	25
3.2 Light Absorption	26
3.2.1 Transition Dipole Moment and Selection Rules	27
3.2.2 Beer-Lambert Law and Molecular Spectra	28
3.3 The Photophysical and Photochemical Deactivation of Excited states	29
3.4 Jablonski Diagram	30
3.5 Potential Energy Surfaces	32
3.5.1 Intramolecular Radiative Processes of Excited States	32

3.5.1.1	Fluorescence	34
3.5.1.2	Phosphorescence	35
3.5.2	Intramolecular Radiationless Processes of Excited States . . .	35
3.5.2.1	Internal Conversion	35
3.5.2.2	Intersystem Crossing	36
3.5.3	Intermolecular Processes of Excited States	37
3.5.3.1	Electronic Energy Transfer Process	40
3.5.3.2	Electron Transfer Process	43
3.5.3.3	Vibrational Relaxation	44
3.5.4	Photochemical Reactions	44
3.5.4.1	The Pathway of Photochemical Reaction	45
	Bibliography	47
4	Theoretical Methods	51
4.1	Quantum Mechanical Preliminaries	51
4.1.1	Atomic Units	51
4.1.2	Schrödinger Equation	52
4.1.3	Some Properties of Wave Functions	53
4.1.4	Molecular Hamiltonian	54
4.1.5	Born-Oppenheimer Approximation	55
4.1.6	Molecular Orbitals	55
4.1.7	Variational Principle	56
4.2	Ground-State Theory	57
4.2.1	Hartree Product	57
4.2.2	Hartree-Fock Approximation	58
4.2.2.1	Roothaan Equations	60
4.2.3	Density-Functional Theory	62
4.2.3.1	The Thomas-Fermi Model	62
4.2.3.2	First Hohenberg-Kohn Theorem	63
4.2.3.3	Second Hohenberg-Kohn Theorem	64
4.2.3.4	Levy Constrained Search	64
4.2.3.5	Kohn-Sham Formulation	66
4.2.3.6	Some of the Different Types of Exchange-Correlation Approximations	67
4.2.4	Density-Functional Tight Binding	70
4.3	Excited State Calculation	75
4.3.1	Second Quantization	75
4.3.2	Configuration Interaction Singles (CIS)	76

4.3.3	Time-Dependent Density Functional Theory	77
4.3.4	Time-Dependent Density Functional Tight Binding	78
	Bibliography	79
II	Original Research	83
5	Assessment of Density-Functional Tight-Binding Ionization Potentials and Electron Affinities of Molecules of Interest for Organic Solar Cells Against First-Principles <i>GW</i> Calculations	85
5.1	Introduction	87
5.2	Theoretical Methods	90
5.3	Computational Details	99
5.4	Small Molecules	103
5.5	Medium-Sized Molecules	113
5.6	Conclusion	121
	Bibliography	127
6	Davydov-Type Excitonic Effects on the Absorption Spectra of Parallel-Stacked and Herringbone Aggregates of Pentacene: Time-Dependent Density-Functional Theory and Time-Dependent Density-Functional Tight Binding	137
6.1	Introduction	139
6.2	Exciton Analysis	143
6.2.1	Monomer	144
6.2.2	Dimer	147
6.2.3	Trimer	150
6.2.4	Higher Oligomers	153
6.3	(TD-)DFT AND (TD-)DFTB	158
6.3.1	DFT	159
6.3.2	TD-DFT	164
6.3.3	DFTB	167
6.3.4	TD-DFTB	172
6.4	Computational Details	172
6.5	Results	174
6.5.1	Monomer	175
6.5.2	Stacking	179
6.5.2.1	Intermolecular forces	179

6.5.2.2	Energy versus charge transfer	182
6.5.2.3	Spectra	191
6.5.3	Herringbone	194
6.5.4	Re-examination of Kasha's Model	198
6.6	Conclusion	203
6.7	acknowledgments	205
6.8	Author Contributions	205
6.9	Conflicts of Interest	206
6.10	Abbreviations	206
	Bibliography	209
7	How Long Do Energy and Charge Transfer Take? Tully-Type Mixed Time-Dependent Tight-Binding Density-Functional/Classical Trajectory Surface Hopping Study of a Model Buckminsterfullerene/Pentacene Heterojunction with and without Long-Range Correction	221
7.1	Introduction	223
7.2	Theoretical methods	228
7.2.1	FSSH	229
7.2.2	TD-DFT FSSH	231
7.2.3	TD-DFTB FSSH	235
7.3	Computational Details	240
7.4	Results	243
7.4.1	Assignment of Absorption Spectra	243
7.4.2	Initial Excited States	246
7.4.3	Exciton Energy Transfer Dynamics	247
7.4.4	Charge Transfer Dynamics	253
7.4.4.1	Traj 6: Example of a P-type initial state	253
7.4.4.2	Traj 27: Example of a DL-type initial state	259
7.4.4.3	Summary of all six CT times	259
7.4.5	Charge Transfer Dynamics without Long-Range Correction . .	262
7.5	Conclusion	265
7.6	Acknowledgements	266
	Bibliography	270
III	Summary and Outlook	295
8	Summary	297

Chapter 1

Introduction

Introduction

Our lives have been enriched and facilitated by an increasing number of electrical tools including kitchen appliances, air conditioning, computers, and smart phones, to name just a few of many modern conveniences. A consequence is that the world is now consuming more electricity than ever before. At the same time, we are increasingly conscious of the problems associated with this energy consumption including, but not limited to, limited fossil fuel resources, pollution concerns (including global warming), and distribution problems (including fragility due to political problems and the need to protect the distribution system from possible terrorist attacks). Alternative energy sources are part of the solutions to these problems. This thesis is concerned with one particular alternative energy source, namely solar energy—the direct conversion of sunlight into electrical energy.

Conventional solar energy uses inorganic electronics to construct useful, robust photovoltaic (i.e., solar) cells. Even so, solar cells were too expensive until recently to use except for very specialized purposes such as space satellites and lighthouses. Solar energy became affordable for many everyday applications as inexpensive highly pure silicon became available as a by-product of the production of ultra highly pure silicon for computer chips. But the use of these inorganic solar cells is still less general than might be possible with organic electronics because inorganic electronics are heavy and fragile. This thesis concerns organic solar cells.

Organic electronics is an area of rapidly growing importance. This is because conducting plastics are light and inexpensive to mold into different forms. Organic circuits may also be printed on paper, cloth, and plastic using existent or only slightly modified technology. Imagine, for example, the possibility of a printable portable phone powered by its own printed organic solar cell ! We may not be there yet, but we are moving towards this level of technology. So far, however, organic solar cell applications are limited by a relatively low photoconversion efficiency. Improving this efficiency depends upon understanding how organic solar cells work.

The main processes involved in the mechanism of power conversion, the essential steps in the photovoltaic conversion are: light absorption, excitation, exciton

diffusion charge dissociation, charge transport, and charge collection [1].

Modern organic solar cell: involve an electron-donating (donor, D) material and an electron-accepting (acceptor, A) material. These two materials join at a donor-acceptor (D/A) heterojunction. The capacity of the D to give up electrons and of the A to accept electrons is one critical aspect explored in this thesis. Absorbed light forms a particle-hole pair which is more or less delocalized. The extent of this delocalization is also explored in this thesis.

Perhaps the most interesting problem is how the D/A interface is able to separate the particle-hole pair into separate particle (i.e., electrons) and holes (i.e., positive charges due to missing electrons) at near 100% efficiency. This is especially mysterious because naïve electrostatics suggests that the particle/hole separation should require 0.1–0.5 eV of energy while only 0.025 eV of thermal energy is available [2]. How can this happen and on what time scale does it happen? Results of a direct photodynamics simulation are reported in this thesis, thereby adding new clues to the underlying photoprocesses.

The structure of the thesis consists of two parts. The first part consists of two chapters. The first chapter provides a brief review of organic electronics whereas the second chapter presents the quantum chemical theory behind the methods employed in the second part of this thesis.

The second part of the thesis, which consists of three chapters, presents the original research. The first chapter in the second part entitled “Assessment of Density-Functional Tight-Binding Ionization Potentials and Electron Affinities of Molecules of Interest for Organic Solar Cells Against First-Principles *GW* Calculations”. It mainly focuses on the calculation by using density functional tight binding (DFTB) with self-consistent charge and non-self-consistent charge to calculate the ionization potential and electron affinity for eight molecules which enter in the composition of organic solar cell.

In the second chapter, we assess how far TD-DFT and TD-DFTB have progressed towards a correct description of J-type Davydov exciton bands in Pentacene aggregates by including both a dispersion correction for the ground state and a range-separated hybrid functional for the excited state. That chapter is entitled: “How Well Does Time-Dependent Density-Functional Tight-Binding Represent Time-Dependent Density-Functional Theory for Describing J-Type Davydov Exciton Bands in Pentacene Aggregates?”.

In the third chapter, the nonadiabatic dynamics within the long-range corrected time-dependent density functional tight binding method (lc-TD-DFTB) of an intense excited state of pentacene- C_{60} model, has been monitored for 500 fs to see how

the electronic excited state changes its characteristic from a local to a charge transfer state. That chapter is entitled: “How Long Do Energy and Charge Transfer Take? Tully-Type Mixed Time-Dependent Tight-Binding Density-Functional/Classical Trajectory Surface Hopping Study of a Model Buckminsterfullerene/Pentacene Heterojunction with and without Long-Range Correction.”.

This second part of the thesis is followed by a third and final part which takes stock of what has been accomplished and of what more could be done to further our comprehension of the basic problem addressed in this thesis.

Bibliography

- [1] G. Li, R. Zhu, and Y. Yang, [Polymer solar cells.](#), Nat. Photonics **6**, 153 (2012).
pages 6
- [2] S. Few, J. Frost, and J. Nelson, [Models of charge pair generation in organic solar cells](#), Physical Chemistry Chemical Physics. **17**, 2311 (2015). pages 6, 224, 225

Part I

General Background

Chapter 2

Organic Solar Cells

Organic solar cells offer multiple advantages: They can be produced in high volume at low production cost. They are light weight, may be flexible, and may be printed. Also, unlike inorganic solar cell materials, organic solar cell materials are diverse enough that they are open to molecular engineering to optimize absorption spectra, conductivity, etc. [1, 2, 3, 4]. In spite of these advantages, organic solar cells still suffer from some problems. In particular organic solar cells have low power conversion efficiencies. The Fig. 2.1 illustrates the development of efficiency of several types of solar cells.

The first section of this chapter introduces organic electronic materials. The second section goes through some types of organic solar cells. The third section clarifies some experimentally-measured quantities. The fourth section describes the fundamental mechanism of power conversion. In the fifth section, the emphasis is on the mechanism of the charge separation.

2.1 Organic Electronic Materials

In this section, I try to shed light on the common features of organic electronic materials. Organic electronic materials are semiconductors. They can be classified according to their size into two categories: small molecules or oligomer, and polymer as shown in the Fig 2.2. The common feature of most organic electronic materials is that they have a conjugated systems of π bonds. Mostly, they have a carbon backbone. But you can also find oxygen, nitrogen, or sulphur in the backbone. The atoms are sp^2 -hybridized and the rest are p -atomic orbitals. Electrons p -orbital delocalize and form delocalized π bonding orbitals with a π^* antibonding orbitals [5]. The high absorption coefficients of organic electronic materials compared with the inorganic semiconductors, makes it possible to use them in the form of thin films

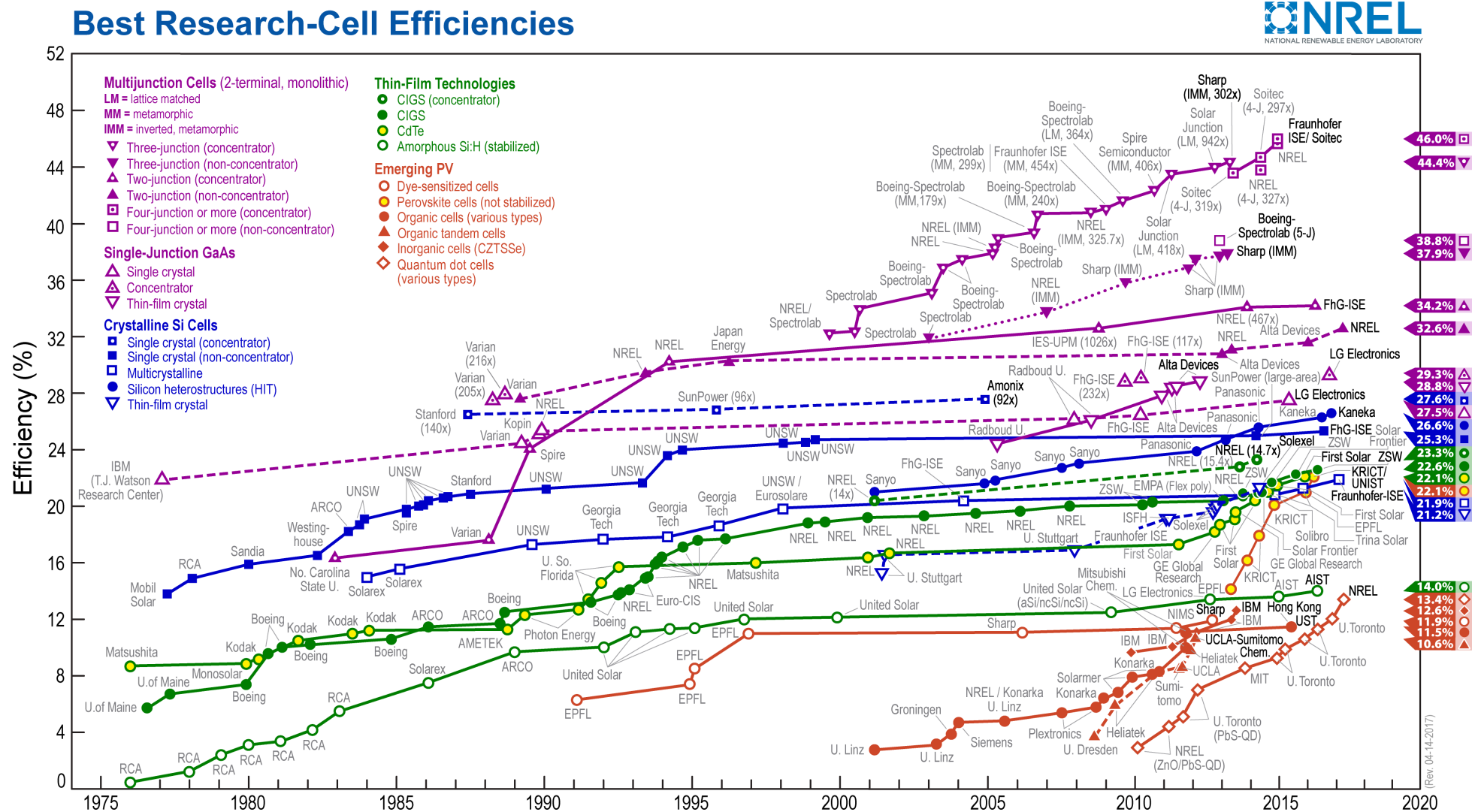


Figure 2.1 – Chart showing the evolution of the efficiency of different types of cells. From the American National Renewable Energy Laboratory 2017. Organic solar cells are represented by filled red circles (lower right hand side of the graphic.)

(50-200 nm). Furthermore organic electronic materials have lower density than inorganic semiconductors. The combination of these two factors leads to their low cost of use [6]. Organic electronic materials have low dielectric constants. The much lower dielectric constant can not prevent the electrostatic interaction between the hole and the electron across the donor and acceptor interface in the excitons. The wide range band gap of organic semiconductors, which is higher than 1.4 eV but below that of an insulator (around 3.0 eV), hinders the improvement of the power conversion energy because this band gap only absorbs light with a wavelength shorter than 900 nm which, in the best cases, is only 30% of sunlight. Keep in mind that narrowing band gap to decrease the efficiency by decreasing the open circuit voltage. The ideal band gap provides a compromise solution between harvesting the largest amount of light and providing the appropriate energy offset between the donor and acceptor. The ideal solar cell should have low charge carrier density at room temperature and dark. But, it can be improved by photochemical and electrochemical doping [5]. In electronics, the charge carrier mobility is one of the critical parameters. The overlap between the π orbital between adjacent atoms will lead to strengthening the charge carrier mobility in organic electronics materials.

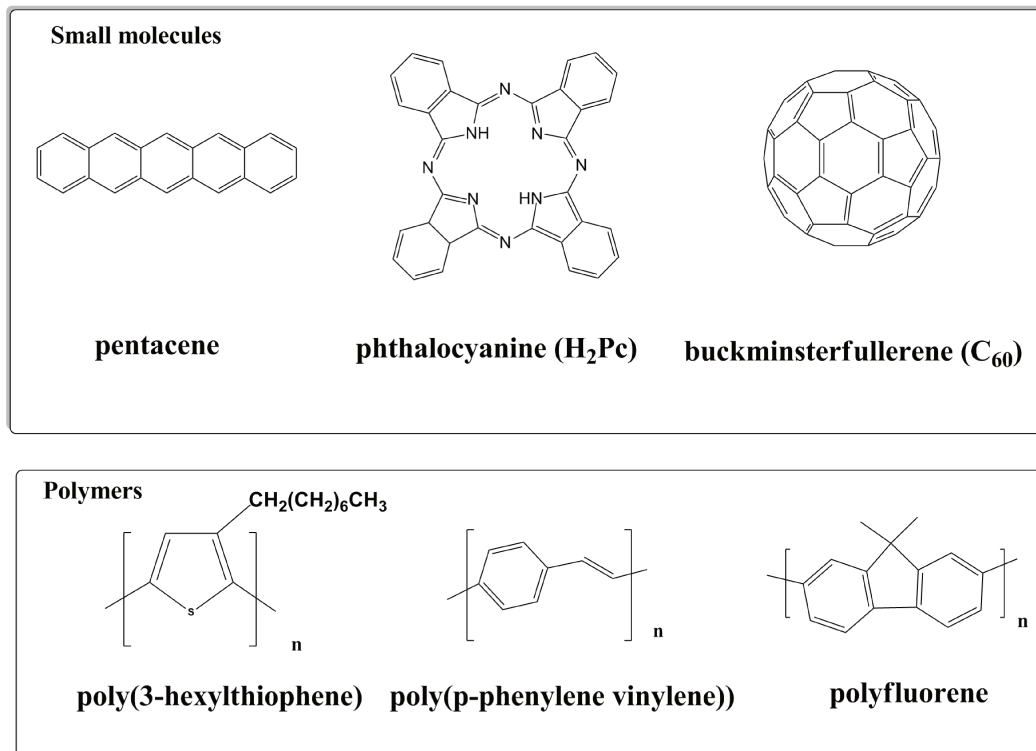


Figure 2.2 – Some organic electronics materials.

2.2 Types of Organic Solar Cell

Most organic solar cell have at least two active layers. One of them is the electron donor and the second one is the electron acceptor. The donor should have a strong absorption of the light in a broad spectral region overlapping with the solar spectrum (see Fig. 2.3) in order to harvest enough solar light. They also need high mobility to ensure fast hole transport. Furthermore they need suitable energy levels to fit well with the acceptor in order to get enough free electrons from excitons. These properties can give high power conversion efficiency (PCE) of the organic solar cell. There are several types of the organic solar cell according to the types of junctions: single layer organic solar cell, bilayer organic solar cells, and bulk heterojunction solar cells (see Fig. 2.5).[7].

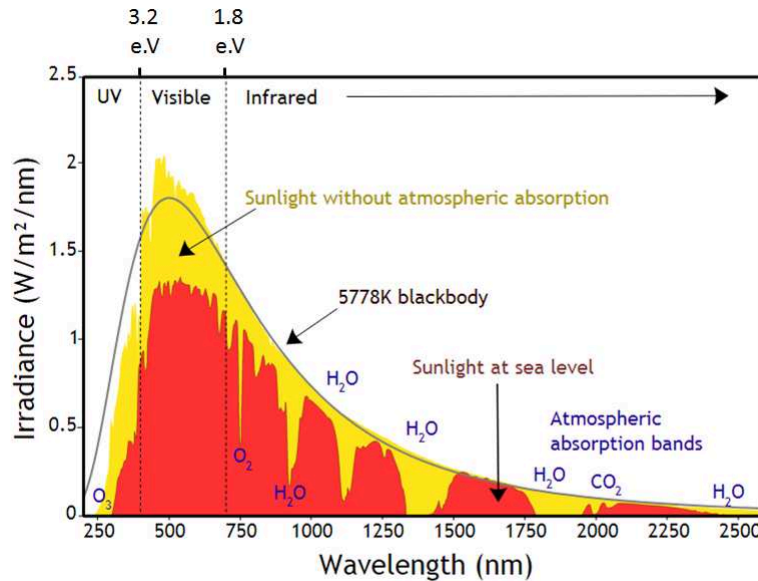


Figure 2.3 – Solar Spectrum reference taken from reference [8]

Kearns and Calvin discovered the photovoltaic effect in 1958 while studying a pristine organic material (magnesium phthalocyanine) between two electrodes [9]. This was a very inefficient single layer organic solar cell (OSC). This kind of OSC consists of one layer of organic electronic material in between two conducting electrodes. These electrodes differ in their work function. One of them [e.g., indium tin oxide (ITO)] has a high work function, and the other [e.g., aluminum (Al), magnesium (Mg), or calcium (Ca)] has a low work function. After light absorption by the organic layer, excitation occurs to generate excitons by transferring an electron from the highest occupied molecular orbital (HOMO) to the lowest unoccupied molecular

orbital (LUMO). Because of the difference in the work functions of the two electrodes, an electric field is set up in the organic layer. This electric field helps to split the exciton into independent electrons and holes. The hole collects at the electrode with the lower work function, and the electron, which collects at the electrode with the higher work function (see Fig. 2.4).

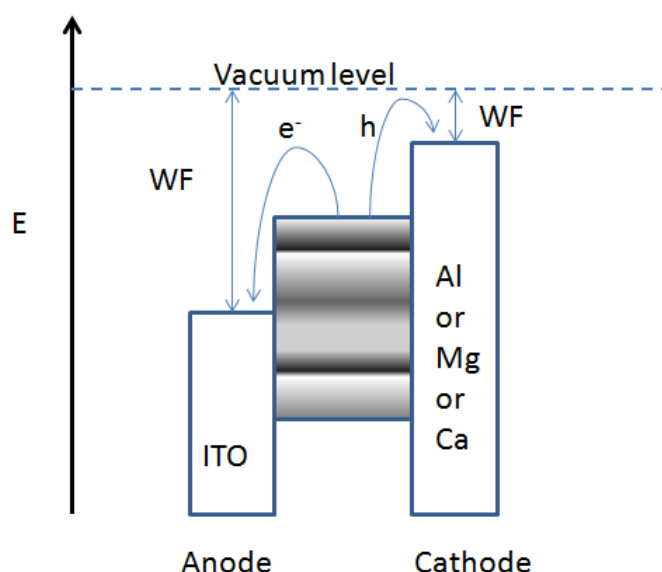


Figure 2.4 – Scheme illustrates how the difference in the work function of the electrodes leads to separate the hole and the particle.

Single layer OSCs suffer from low conversion efficiency less than 0.1% and low quantum efficiency less than 0.01% [10]. We can attribute this low efficiency to the inability of the electric field, created by the difference in the work function of two electrodes, to split the excitons into holes and electrons. Also, when created, the holes and the electrons recombine before reaching to the electrodes. As we showed, the efficiency in the single layer OSC depends mainly on the electrode properties. The efficiency stayed around 0.1% for about twenty years until a major innovation by Tang.

In 1986 [11], Tang invented the second generation of OSC called two (or bilayer) layers OSC. This type of OSC consists of two layers of organic electronic material between two conductive electrodes. The two layers differ in their electron affinities and ionization potentials. The difference in the electron affinities and ionization potentials between the two layers creates electrostatic forces in the interface between the two layers which are responsible for splitting the excitons. The acceptor is the layer which has a higher electron affinity and a higher ionization potential and the other layer is the donor. The bilayer OSC differs from single layer OSC in that the interface

between the two organic layers is crucial in determining its photovoltaic properties. The efficiency of two-layer OSCs increased compared with single layer OSCs but, the efficiency was still low. The problem with this type of OSCs is that only a small amount of the excitons can reach the interface because the organic layer needs a thickness around 100 nm to absorb sufficient light whereas the excitons diffusion length around 10 nm, so the excitons recombine before reaching the interface.

The third generation of OSCs is bulk heterojunction OSCs [12]. In this type of OSC, the organic layer which absorbed light has been made by blending the donor and acceptor at nanoscale distances. The blend has been made on the order of less than the exciton diffusion length to enable most of the excitons to reach the interface. The concept of bulk heterojunction has been critical in improving in the efficiency of OSCs.

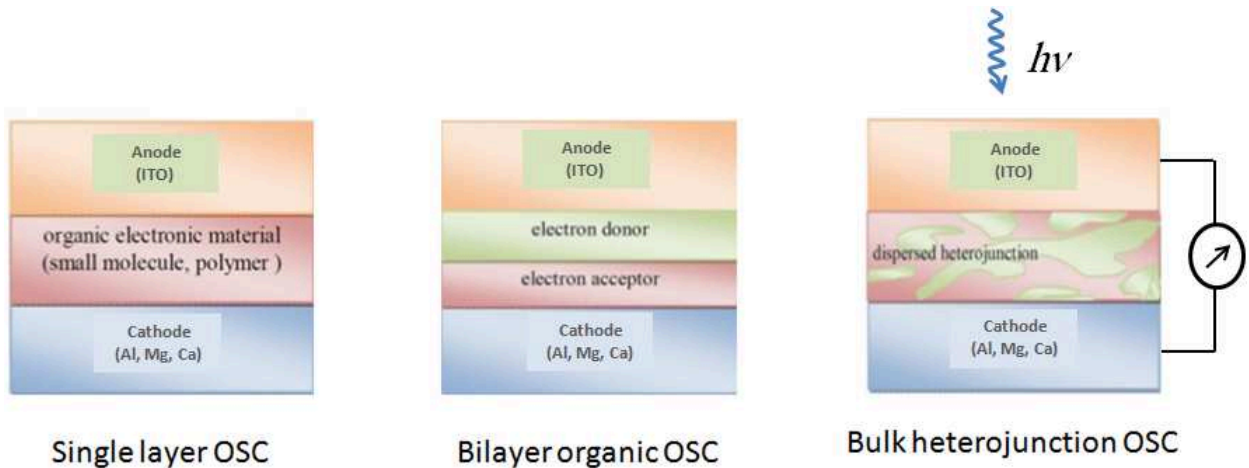


Figure 2.5 – Types of organic solar cell. Redrawn based on a figure from ref. [13]

2.3 The Fundamental Mechanism of Power Conversion

Organic solar cell efficiency recently has reached up to 10% [14, 15]. In order to further progress in the efficiency, significant effort must be focused on optimization and improvement to make it commercially successful. These efforts should be based on the basic mechanism of the process. The fundamental steps involved in the mechanism of power conversion are: first, light absorption which leads to generating of excitons; second, the exciton diffusion; third, the exciton dissociation which leads to generating of charge; and finally charge transport and charge collection [16]. The

essential steps of power conversion from light absorption to charge collection have been shown in the Fig. 2.6

The summation of the efficiencies of all steps is the external quantum efficiency (EQE) which can be defined as the percentage of incident photons converted to electrical current [17, 6],

$$EQE = \eta_A + \eta_{Edif} + \eta_{Edis} + \eta_{Tr} + \eta_{CC}, \quad (2.1)$$

where the η_A is the absorption efficiency which is determined by the absorption coefficient of the donor and its thickness. The absorption efficiency decreases by incomplete absorption of the solar spectrum either due to insufficient thickness of the donor or the donor has a narrow absorption band [18]. The η_{Edif} is the exciton diffusion efficiency which determined by the ability of the excitons to diffuse through the polymer without recombination. Keep in our mind that the exciton diffusion length in the organic electronic materials is around 10 nm [19]. The η_{Edis} is the efficiency of the exciton dissociation which is mostly determined by the outcome of the competition between several pathways of the charge transfer state to give separate charges. The η_{Tr} and η_{CC} are the charge carrier transport efficiency and the charge collection efficiency respectively [20].

Whereas the internal quantum efficiency (IQE) is the percentage of absorbed photons converted to electrical current. Usually, quantum efficiency (QE) refers to the internal quantum efficiency [17]. It is clear that the active layer donor-acceptor governs all the steps of the mechanism except the charge collection. Charge collection mainly depends on the electronic nature of the interface between the conductive electrodes and the active layer.

2.4 Experimentally Measured Quantities

In the previous section, the fundamental steps involved in the power conversion mechanism have been illustrated in addition to the efficiency of each step and the quantum efficiency of both types internal and external. In 1961, Shockley and Queisser managed to calculate the maximum possible theoretical efficiency for a single junction semiconductor as a function of bandgap energy. It called the Shockley-Queisser limit efficiency or the detailed balance limit of efficiency. Shockley and Queisser assumed that all avoidable losses are absent. Here, avoidable losses mean, the losses caused by reflection, series resistances, light transmission resulting from some surface properties. The limit of maximum efficiency for a single junction semi-

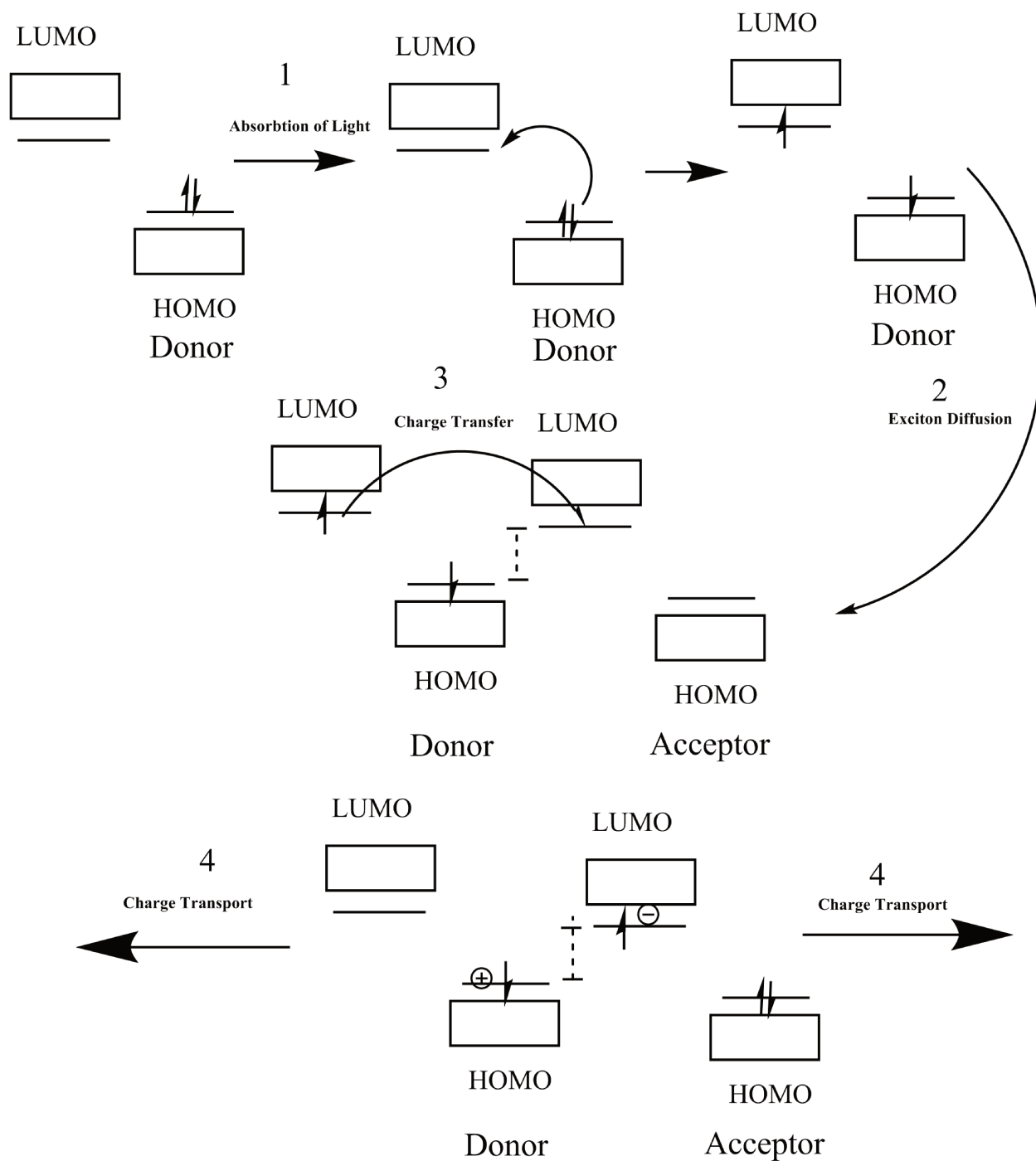


Figure 2.6 – The fundamental steps involved in the mechanism of power conversion at N/D interface in an organic solar cell.

conductor took several considerations into account for the losses which decrease the maximum theoretical efficiency under 34% for optimal bandgap energy 1.34 e.V (see Fig 2.7) . The unavoidable losses that Shockley and Queisser took them in their consideration are the radiative recombinations, the black-body radiation, thermal losses, and spectral losses.

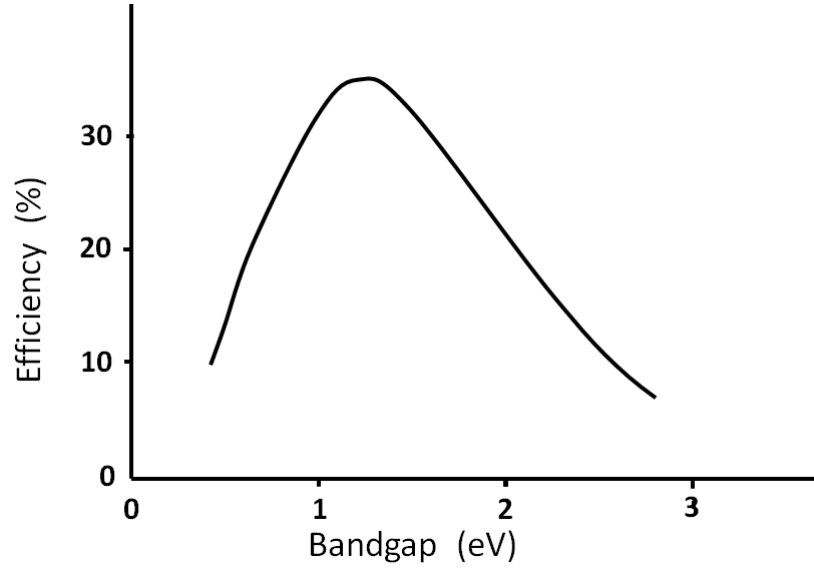


Figure 2.7 – The Shockley-Queisser limit for the efficiency of a solar cell. Redrawn based on a figure from ref. [17]

Short circuit current density (J_{sc}) and open circuit voltage (V_{oc}) are two of the important parameters for efficiency [21]. We can define the short-circuit current as the current at which the externally applied voltage is 0. Whereas the open circuit voltage can be defined as the voltage at which the current density output is 0. These parameters can give a high power conversion efficiency of the organic solar cell through high values of open-circuit voltage and short circuit current, and fill-factor (FF) [22, 23, 6]. The fill-factor can be define as the ratio between the maximum power (mpp) output point and the maximum attainable power output,

$$FF = \frac{J_{mpp} V_{mpp}}{J_{sc} V_{oc}}, \quad (2.2)$$

where J_{mpp} and V_{mpp} are the corresponding current density and voltage at the point of maximum output power respectively (see Fig. 2.8). So, the power conversion

efficiency (PCE) can be calculated from the FF , J_{sc} , and V_{oc} as

$$PCE = \frac{(FF)(J_{sc})(V_{oc})}{P_{in}}, \quad (2.3)$$

where P_{in} is the input power density [18]. The characterization method of efficiency of the OSC must be done under standard test conditions at specified temperature 25 °C, irradiance of 1000 W/m², an air mass 1.5 (AM1.5) spectrum, a clear day with sunlight incident upon a sun-facing 37° tilted surface, The sun at an angle of 48° above the horizon [6].

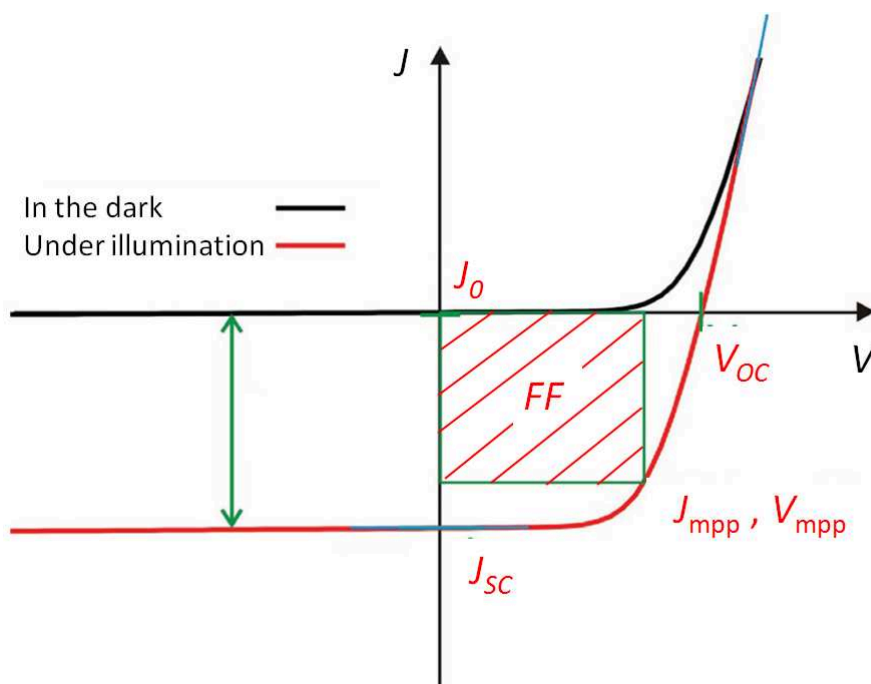


Figure 2.8 – Current-voltage curves for dark and light currents in solar cells with J_{sc} , V_{oc} , FF , J_{mpp} and V_{mpp} . Redrawn based on a figure from ref. [6].

Many experimental efforts have focused on understanding the apparent relationship between open circuit voltage and the difference between the highest occupied molecular orbital (HOMO) of the donor and lowest unoccupied molecular orbital (LUMO) of the acceptor [24, 25]. In other words, the apparent relationship between open circuit voltage and the difference between ionization potential of the donor and the electron affinity of the acceptor (hence the importance both of the ionization potential and of the electron affinity.)

One of the characterization methods of the organic solar cells is the current-voltage (J vs. V) characterization. The J vs. V characteristics can be considered as the simplest and essential characterization methods for the solar cell. The J vs.

V characteristics of the solar cell can be calculated by using the Shockley diode equation under illumination. Simply, it is an equation that gives the relationship between the current flow through an ideal p-n junction and the voltage in order to get more understanding of the recombination losses,

$$J(V) = J_0 \left(e^{\left(\frac{qV}{nkT}\right)} - 1 \right) - J_{gen}, \quad (2.4)$$

where $J(V)$ and J_0 are the total current and dark saturation current respectively, q is the elementary charge, V is the voltage across the p-n junction, n is the diode ideality factor, kT is the thermal energy (Boltzmann constant times temperature), and J_{gen} is the photogenerated current [26]. The Fig 2.8 represents the current-voltage (J vs. V) characterization in the dark and under illumination of a solar cell.

2.5 The Mechanism of the Charge Separation

The picture is not as simple as we showed. The function and efficiency of the organic solar cell are dependent mainly on the electronic structure of the interface between the donor and the acceptor because only at the interface can exciton dissociation into separate electron and hole happen [27]. At the interface the energy levels must be matched to get optimal charge dissociation and then maximal energy conversion efficiency.

Charge separation at organic donor/acceptor heterojunctions is a key factor in the successful design of organic solar cell [28, 29, 30, 27]. Understanding the mechanism of the charge separation in the organic solar cell still represents a significant challenge. There are several hypotheses talking about the mechanism of dissociation. Typically semiconducting organic materials have low dielectric constants. These low dielectric constants cannot prevent the electrostatic interactions between electron and hole across the donor and acceptor interface, which can lead to the formation of interfacial bound electron-hole pairs. Often called charge transfer (CT) states [31], then the particular mechanism of this dissociation probably involves a relatively high level of delocalization of hot CT states [32, 33, 34]. For some materials, sufficient overlap of electron and hole wavefunctions has been shown for charge exciton transfer evidenced by considerable luminescence (radiative lifetime strongly increased about 100 ns and substantially red shift). This “exciplex” has significant charge-transfer character and is lower in energy than the charge-separated state [35].

Regarding this change in the nature of the excited state from localized to delocalized: A photochemist might say that we are facing a problem of some kind of a conical intersection of two potential energy surface-the region where the two

potential energy surfaces are degenerate for the set of molecular geometry points and the non-adiabatic couplings between these two states are not disappearing. The Born-Oppenheimer approximation breaks down, allowing non-adiabatic processes to take place in this region. At any time the system is propagated in one potential surface, but allows the transition between different electronic states. The probability of switching to the surface of the non-adiabatic depends on the strength of non-adiabatic coupling. Small energy difference between the two surface generally result in high transition probabilities. surface hopping, tend to occur mainly in the region of the surface crossings [36].

We have decided to attack this problem using mixed time-dependent density-functional tight binding/classical surface hopping method. Particular interest will be placed upon electronic potential energy surface funnel regions as nuclear geometries change.

Bibliography

- [1] B. Maennig and et al., [Organic p-i-n solar cells](#), Applied Physics A: Materials Science and Processing **79**, 1 (2004). pages 11
- [2] A. Mishra and P. Bauerle, [Small molecule organic semiconductors on the move: Promises for future solar energy technology.](#), Angew. Chem. Int. Ed. **51**, 2020 (2012). pages 11
- [3] S. Braun, W. Salaneck, and M. Fahlman, [Energy-Level Alignment at Organic/Metal and Organic/Organic Interfaces.](#), Adv. Mater. **21**, 1450 (2009). pages 11
- [4] M. Fahlman et al., [Electronic structure of hybrid interfaces for polymer-based electronics.](#), J. Phys.: Condens. Matter **19**, 183202 (2007). pages 11
- [5] H. Huang and W. Deng, [Introduction to Organic Solar Cells.](#) , in *Organic and Hybrid Solar Cells.*, edited by H. Huang and J. Huang, Springer International Publishing, 2014. pages 11, 13
- [6] B. P. Rand and H. Richter, [Organic Solar Cells Fundamentals, Devices, and Upscaling.](#), Pan Stanford CRC Press, 2014. pages 13, 17, 19, 20, 309
- [7] J. Nelson, [Organic photovoltaic films.](#), Current Opinion in Solid State and Materials Science **6**, 87 (2002). pages 14
- [8] Sunlight, <https://en.wikipedia.org/wiki/Sunlight>. pages 14, 309
- [9] D. Kearns and M. Calvin, [Photovoltaic Effect and Photoconductivity in Organic Laminated Systems.](#), J. Chem. Phys. **29**, 950 (1958). pages 14

- [10] S. Karg, W. Riess, V. Dyakonov, and M. Schworer, [Electrical and optical characterization of poly\(phenylene-vinylene\) light emitting diodes.](#), *Synthetic Metals* **54**, 427 (1993). pages 15
- [11] C. W. Tang, [Two-layer organic photovoltaic cell.](#), *Appl. Phys. Lett.* **48**, 183 (1986). pages 15, 124, 224
- [12] G. Yu, J. Gao, J. C. Hummelen, F. Wudl, and A. J. Heeger, [Polymer Photovoltaic Cells: Enhanced Efficiencies via a Network of Internal Donor-Acceptor Heterojunctions.](#), *Science* **270**, 1789 (1995). pages 16, 87
- [13] Organic solar cell, https://en.wikipedia.org/wiki/Organic_solar_cell. pages 16, 309
- [14] S. Duhm et al., [Orientation-dependent ionization energies and interface dipoles in ordered molecular assemblies.](#), *Nat. Mater.* **7**, 326 (2008). pages 16
- [15] W. R. Salaneck, [Intermolecular Relaxation Energies in Anthracene.](#), *Phys. Rev. Lett.* **40**, 60 (1978). pages 16
- [16] C. J. Brabec, N. S. Sariciftci, and J. C. Hummelen, [Plastic solar cells.](#), *Advanced Functional Materials* **11**, 15 (2001). pages 16
- [17] W. Shockley and H. Queisser, [Detailed balance limit of efficiency of \$p-n\$ junction solar cells.](#), *J. Appl. Phys.* **32**, 510 (1961). pages 17, 19, 126, 309
- [18] D. D. S. Fung and W. C. H. Choy, [Introduction to Organic Solar Cells.](#), in [Organic Solar Cells Materials and Device Physics.](#), edited by W. C. Choy, Springer, London, 2013. pages 17, 20
- [19] P. E. Shaw, A. Ruseckas, and I. D. W. Samuel, [Exciton diffusion measurements in poly\(3-hexylthiophene\).](#), *Advanced Materials* **20**, 3516 (2008). pages 17
- [20] S. M. Mortuza and S. Banerjee, [Relating Synthesis Parameters to the Morphology of the Photoactive Layer in Organic Photovoltaic Solar Cells Using Molecular Dynamics Simulations.](#), in *Organic Solar Cells Materials, Devices, Interfaces, and Modeling.*, edited by Q. Qiao, CRC Press, 2015. pages 17
- [21] C. Tengstedt et al., [Fermi level pinning at conjugated polymer interfaces.](#), *Appl. Phys. Lett.* **88**, 053502 (2006). pages 19
- [22] S. H. Park et al., [Bulk heterojunction solar cells with internal quantum efficiency approaching 100%.](#), *Acc. Chem. Res.* **42**, 1709 (2009). pages 19
- [23] J. Hou et al., [Synthesis and Photovoltaic Properties of Two-Dimensional Conjugated Polythiophenes with Bi\(thienylenevinylene\) Side Chains.](#), *J. Am. Chem. Soc.* **128**, 4911 (2006). pages 19

- [24] M. Scharber et al., [Design rules for donors in bulk-heterojunction solar cells — Towards 10% energy-conversion efficiency](#), *Adv. Mater.* **18**, 789 (2006). pages 20
- [25] C. J. Brabec et al., [Origin of the Open Circuit Voltage of Plastic Solar Cells.](#), *Adv. Functional Mater.* **11**, 374 (2001). pages 20
- [26] B. Foertig, J. Rauh, V. Dyakonov, and C. Deibel, [Shockley Equation Parameters of Organic Solar Cells derived by Transient Techniques.](#), *Phys. Rev. B.* **86**, 115302 (2012). pages 21
- [27] H. Ma and A. Troisi, [Direct Optical Generation of Long-Range Charge-Transfer States in Organic Photovoltaics](#), *Adv. Mater.* **26**, 6163 (2014). pages 21
- [28] T. M. Clarke and J. R. Durrant, [Charge photogeneration in organic solar cells.](#), *Chem. Rev.* **110**, 6736 (2010). pages 21, 224
- [29] J. Bredas, J. E. Norton, J. Cornil, and V. Coropceanu, [Molecular understanding of organic solar cells: the challenges.](#), *Acc. Chem. Res.* **42**, 1691 (2009). pages 21, 224
- [30] X. Y. Zhu, Q. Yang, and M. Muntwiler, [Charge-transfer excitons at organic semiconductor surfaces and interfaces.](#), *Acc. Chem. Res.* **42**, 1779 (2009). pages 21, 224
- [31] C. Deibel, T. Strobel, and V. Dyakonov, [Role of the Charge Transfer State in Organic Donor-Acceptor Solar Cells.](#), *Adv. Mater.* **22**, 4097 (2010). pages 21
- [32] A. A. Bakulin et al., [The role of driving energy and delocalized States for charge separation in organic semiconductors.](#), *Science.* **335**, 1340 (2012). pages 21
- [33] H. Tamura and I. Burghardt, [Ultrafast Charge Separation in Organic Photovoltaics Enhanced by Charge Delocalization and Vibronically Hot Exciton Dissociation](#), *J. Am. Chem. Soc.* **135**, 16364 (2013). pages 21
- [34] D. Fazzi, M. Barbatti, and W. Thiel, [Hot and Cold Charge-Transfer Mechanisms in Organic Photovoltaics: Insights into the Excited States of Donor/Acceptor Interfaces](#), *J. Phys. Chem. Lett.* **8**, 4727 (2017). pages 21
- [35] A. Morteani et al., [Barrier-Free Electron-Hole Capture in Polymer Blend Heterojunction Light-Emitting Diodes.](#), *Adv. Mater.* **15**, 1708 (2003). pages 21
- [36] E. Fabiano, G. Groenhof, and W. Thiel, [Approximate switching algorithms for trajectory surface hopping.](#), *Chemical Physics* **351**, 111 (2008). pages 22

Chapter 3

Photochemistry

3.1 Introduction

Photochemistry [1, 2, 3, 4] is the branch of the chemistry which treats the chemical reactions of electronically excited molecules. These excited molecules may be produced by absorbing light in the nearby ultraviolet spectrum (wavelength from 100 to 400 nm), visible spectrum (400 - 750 nm) or infrared radiation (750 - 2500 nm). Photochemical reactions are fundamental to life. They take their importance from their roles in the photosynthesis, vision, health care, energy production, and the formation of vitamin D with sunlight. Also, for example, methane gas, ammonia and carbon dioxide as the simplest gases which react through photochemical reactions to form organic compounds such as proteins and nucleic acids. Other things related to photochemistry are also found in various applications in science and technology. Organic photochemical synthesis is a method for the manufacture of many chemicals whose reactions do not occur in the dark, because of photochemical paths access high energy intermediates that cannot be generated thermally. Light is also an initiator for polymerization and can be used in photoprinting (offset printing), and the industrial printing of circuits for the electronic industry. The effect of sunlight on the colour of cotton is a common experience, as may be attested to by old curtains. The light absorbed everyday by the cloth starts with oxidation and continuous interaction in the cellulose of cloth, which leads to easy breakage in organic compounds. Similarly the photodecomposition is observed in plastic. Here researchers seek the colors (i.e., optical stabilizers) whose addition can help to stabilize the plastic, making it take up higher excitation energy to make it less fragile. Such as orthohydroxybenzophenol compounds.

The photophysical phenomena of fluorescence and phosphorescence have applications in fluorescent light tubes, x-rays, visuals and displays for bright clocks,

colour paints in commodity advertisements, alarms for specific signals on the road or reagents used in precise analyses. Also, photochemistry is gaining importance through its role in the search for alternative green solutions for modern living.

3.2 Light Absorption

A photon of electromagnetic radiation in the visible or ultraviolet region has the ability to excite an electron from state I to state K when the photon has an energy equal to the energy difference between these two stationary states,

$$E_K - E_I = h\nu. \quad (3.1)$$

Here, $h\nu$ represents photon energy where h is Planck's constant (6.63×10^{-34} Js) and ν is the frequency of oscillation of the photon in units of s^{-1} or Hertz (Hz).

It is not sufficient to consider only the transition between electronic states to explain the light absorption by the molecular system, the full explanation of the electronic excitation in the molecular system should take into account the nuclear motion. The total energy of the molecular system consists of the electronic energy in addition to the energy resulting from nuclear motion which in turn consists of vibrational energy and rotational energy,

$$E_t = E_e + E_v + E_r, \quad (3.2)$$

where E_t is the total energy of the molecular system, E_e is the electronic energy, E_v is the vibrational energy, and E_r is the rotational energy. The energy difference between the electronic energy and the other types of the energy (i.e., vibrational and rotational) in the molecular system is very large. This leads to treating each one of them separately according to the Born-Oppenheimer approximation [5].

Because the energy gap between the electronic states is larger than the energy gap between the vibrational states which in turn is larger than the energy gap between the rotational state, we can describe the electronic transition effect adequately by considering only the electronic and vibrational states. The transitions caused by light absorption in the ultraviolet and visible region which leads to changes in the vibrational and electronic states of the molecular systems are called vibronic transitions.

According to Boltzmann's distribution law, at the room temperature, most of the molecules will be at the lowest vibrational level $v = 0$ of the ground electronic state level S_0 and the excitations by the light absorption in the molecular systems occur

from that level to the higher level. Boltzmann's distribution law gives the probability of a certain state I as a function of the energy of that state,

$$\frac{N_I}{N} = \frac{e^{-\varepsilon_I/kT}}{\sum_{J=1}^M e^{-\varepsilon_J/kT}} \quad (3.3)$$

where N is the total number of the molecules, N_I is the number of the molecules in the energy state I , k is the Boltzmann constant, T is the temperature of the system and M is the number of all states accessible to the system [6]. So absorption is usually from the ground electronic state.

3.2.1 Transition Dipole Moment and Selection Rules

The light absorption and simultaneous excitation from the stationary state I to state K , which are described by the wave functions Ψ_I and Ψ_K respectively, can occur only if the light can interact with the transition dipole moment of the given transition. The transition dipole moment is a complex vector corresponding either to electric dipole moment, to the magnetic dipole moment or to the electric quadrupole moment associated with the transition between the two states. The direction of the transition dipole moment represents the polarization of the transition which controls how the system interacts with an electromagnetic wave of specified polarization. The square of the scalar product between the electric field vector of the light and the transition moment vectors of a given molecular system gives the probability of an electric dipole transition. The intensity of the resulting absorption is proportional to the square of the transition dipole moment times the excitation energy. The square of the scalar product between the electric field vector of the light and the transition moment vector of given molecular system gives the probability of an electric dipole transition [7, pg.5].

Transitions between energy levels in organic molecules are subject to certain constraints known as selection rules. The selection rules have been derived from the theoretical expression of the transition moment which allows us to distinguish between the "allowed" and "forbidden" transitions. Simply, the transitions which lead to vanishing the transition moment are forbidden transitions and their intensity should be zero. Whereas the allowed transitions have non-vanishing transition moment. The selection rules related to the state multiplicity of the initial and the final states are known as a spin selection rules. According to the spin selection rules, the transitions which involve states with a different spin (singlet \leftrightarrow triplet transitions) are forbidden because these transitions will lead to vanishing transition moment. The

electric dipole and quadrupole moment operators do not operate on spin because of the integration over the spin variables will yield zero when the initial state and the final state are different in the spin. Whereas the allowed transitions occur when the initial and final state have the same multiplicity (singlet \leftrightarrow singlet or triplet \leftrightarrow triplet transitions).

In addition to the spin selection rules, there are orbital symmetry selection rules. According to the orbital symmetry selection rules, the transitions are forbidden if the integrand of the product of the wave functions of initial and final states and the dipole moment operator is antisymmetric with respect to at least one symmetry operation of the point group of the molecule so the integral will vanish [7, pg.30]. When the initial and final wave functions mostly resemble each other, the coupling between them will be strong and leads to most probable transition with high molar absorption coefficient. That explains why the transition from π to π^* has higher molar absorption coefficient than the transition from n to π^* [5].

3.2.2 Beer-Lambert Law and Molecular Spectra

Light absorption by molecular systems relies on the Beer-Lambert law [8], which relates the intensity I of light transmitted at a given wavelength through a sample to the intensity I_0 incident on the sample,

$$\frac{I}{I_0} = 10^{-\varepsilon cl} \quad (3.4)$$

where ε is the molar absorption coefficient, l is the sample thickness in cm, and c is the molar concentration in mol. l⁻¹. By taking logarithms of the Eq. (3.4), we get,

$$-\log\left(\frac{I}{I_0}\right) = \varepsilon cl \quad (3.5)$$

The left side of the equation represents the absorbance A . So we can rewrite the equation to get,

$$\begin{aligned} A_{molecule} &= A_{solution} - A_{blank} \\ A &= \varepsilon cl, \end{aligned} \quad (3.6)$$

where the blank absorbance is equal to solvent + container. The extent of light absorption varies from one system to another according to the probability of absorption being indicated by the molar absorption coefficient. A plot of molar absorption versus the wavelength is called the absorption spectrum of molecular system [5, 9] as

shown in the Fig 3.1 .

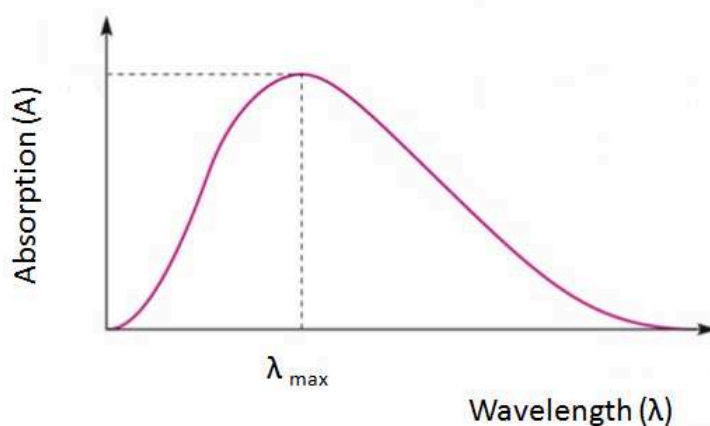


Figure 3.1 – The absorption spectrum of molecular system

In the visible and ultraviolet regions, the atomic absorption spectrum has more sharp lines than the molecular absorption spectrum which shows broad bands that can be attributed to some vibrational structure especially in the case of the rigid molecular system. The polyatomic molecular systems have a large number of closely-spaced normal vibrational modes of varying frequencies [7, pg.9].

3.3 The Photophysical and Photochemical Deactivation of Excited states

The electronically-excited state has excess energy. The excess energy of the electronically excited state can be lost within a short period of time through a number of deactivation processes. If the deactivation process leads to the formation of new chemical structures, then it is a photochemical process. There are several photochemical processes such as photosynthesis in plants, photodecomposition in the plastic, and suntan. When the deactivation process returns back to the ground state without any changes in the structure, then it is photophysical processes. The physical deactivation processes are either energy conversion to heat or light emission. The electronically-excited state may also take place through electron transfer or energy transfer with the ground state molecules

The photophysical deactivation processes can be classified into two categories: intramolecular processes, and intermolecular processes.

The intramolecular processes may take place via radiative or radiationless transitions. In the radiative case, the electronically-excited state relaxes to the ground state by the emission of electromagnetic radiation such as luminescence. Whereas in the radiationless case, there is no electromagnetic emission instead there is internal conversion or intersystem crossing.

The intermolecular processes are relaxation processes which happen between two different molecules. The intermolecular physical deactivation processes can be classified into three categories, vibrational relaxation, energy transfer and electron transfer.

Vibrational relaxation happens when the electronically excited state relaxes to the lowest vibrational level by collision between the electronically excited molecule and a solvent molecule or another molecule. The energy transfer process typically happens in donor-acceptor systems. The excess energy of the electronically excited donor transfers to a lower electronic state in the acceptor. And then lower electronic state in the acceptor uses the energy to promote itself to higher excited state. The third type of intermolecular physical deactivation processes is the electron or charge transfer process. It is a typical example of the photophysical process in the organic solar cell. Where the electronically excited donor interact with the ground state acceptor leading to electron transfer from the donor to the acceptor. The scheme Fig. 3.2 illustrates and summarises the photophysical deactivation processes of excited states.

3.4 Jablonski Diagram

A Jablonski diagram is a compact way to denote the electronically excited states and their transitions of molecules in the molecular spectroscopy . In a Jablonski diagram (Fig. 3.3), the energies of the electronically singlet and triplet excited states are arranged vertically. The energies of singlet excited states are indicated by S_0 , S_1 , and S_2 whereas, the energies of the triplet excited state are indicated by T_1 . The vibrational levels related with each singlet and triplet state are arranged vertically in order of increasing energy. We can easily distinguish between radiative and radiationless transitions from the arrow type: the straight arrows indicate radiative transitions whereas the wavy arrows indicate radiationless transitions.

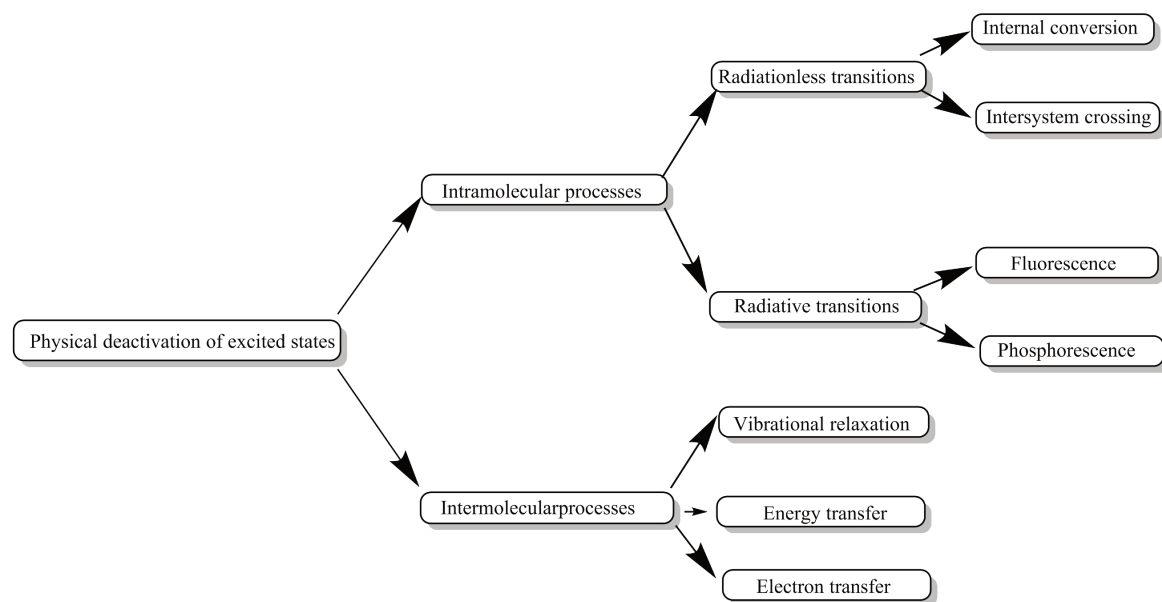


Figure 3.2 – The photophysical deactivation processes of electronically-excited states.

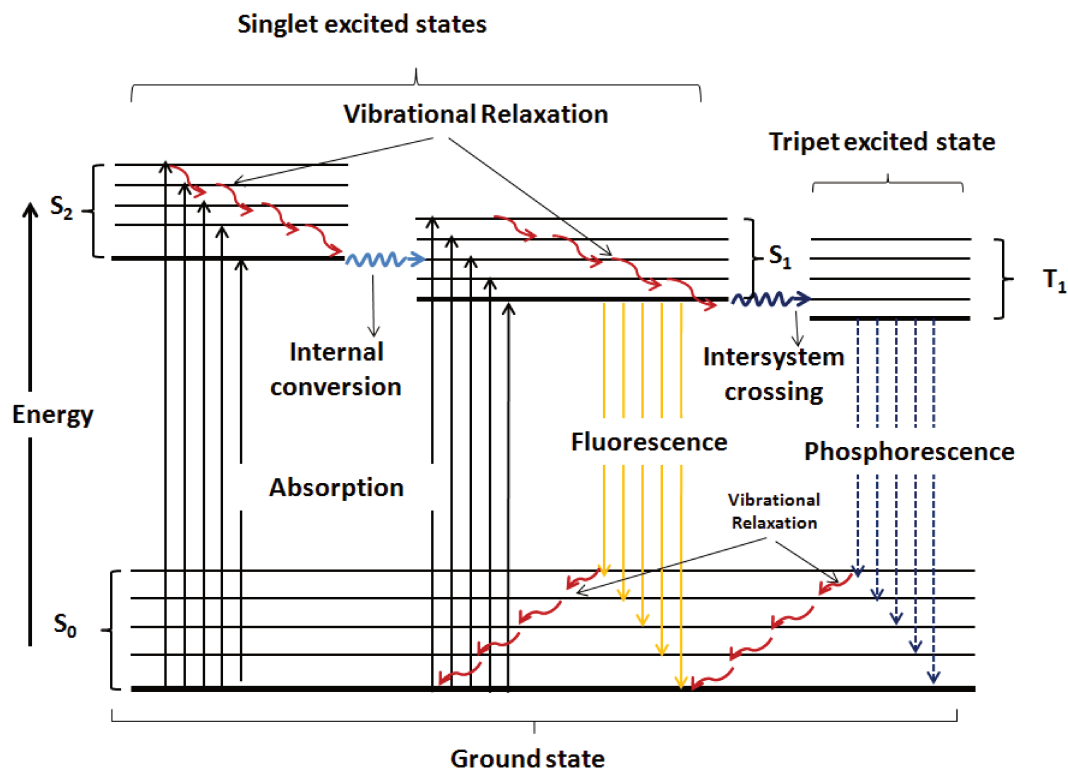


Figure 3.3 – Jablonski diagrams

3.5 Potential Energy Surfaces

Energy differences and transition probabilities are the most important factors which have to be calculated theoretically to predict the photochemical and photophysical properties of molecular system [10]. These two factors give the ability to describe the potential energy surface conveniently. Besides, they provide us with the nonadiabatic matrix elements which we need to get the probability of energy transfer [4]. According to the orbital symmetry selection rule, the electron transition is most probable when the coupling between the initial and final wave functions is strongest.

The computation of the potential energy surfaces is a complicated process. This is especially so in the case of excited states. The difficulty arises from the different classes of excited states (singlet and triplet states) each one of which has different amounts of electronic correlation. The complexity of calculating potential energy surfaces of the excited states also can be attributed to the large number of minima that they include in addition to the surface crossings, transition states, and state couplings compared with the ground state energy surface [11]. The energy range of the absorption and emission bands can be provided by the vertical absorption energies at the ground state minimum, adiabatic transitions between the state minima, and vertical energy differences at the optimized geometry of the excited state [11]. More complex treatment is required for calculations of potential energy surfaces when they are close to each other. Photochemical funnels can connect different potential energy surfaces regions where the probability is very high to jump among different potential energy surfaces, sometimes leading to chemical reactions. A high probability of transfer arises from the strong coupling between the vibrational and electronic states at these regions [3]. The Fig. 3.4 illustrate the potential energy surfaces of the ground state (S_0), the singlet excited state (S_1) and triplet excited state (T_1) and the main photophysical and photochemical processes.

3.5.1 Intramolecular Radiative Processes of Excited States

In the schematics shown in Fig. 3.2 and Fig. 3.4, we gave an overview of the intramolecular radiative processes of the excited states. These processes can be categorised as fluorescence or phosphorescence. The main feature that distinguishes these two categories is the spin multiplicity of the initial and final states involved in the radiative transition. Simply, the intramolecular radiative processes are vertical transitions. This can be rationalized using the Franck-Condon principle [12]. Transition probability is related to the overlap between the square of the wave

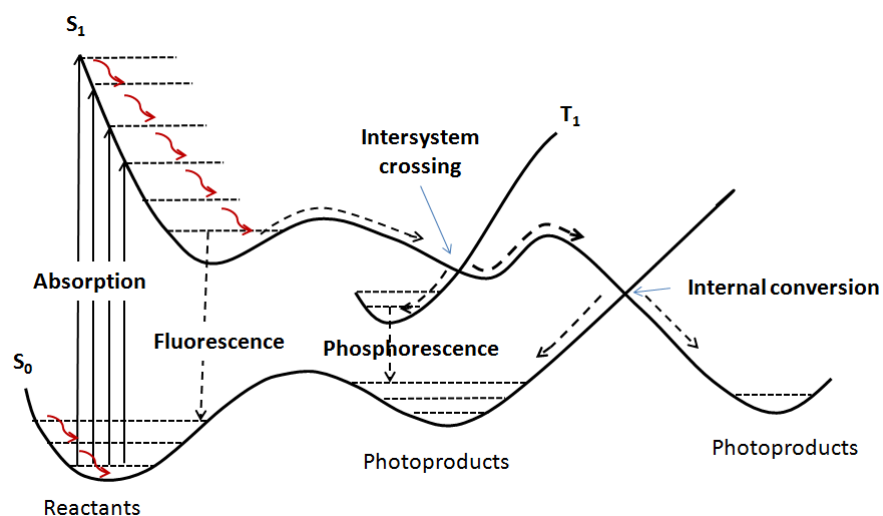


Figure 3.4 – The photophysical and photochemical processes. Taken from Ref. [11]

function of the vibronic level of the ground state and excited state. The larger is the overlap between the states, the larger is the probability of electronic transition to happen. Figure 3.5 illustrates the quantum picture of the probability of electronic transitions from the Franck-Condon principle.

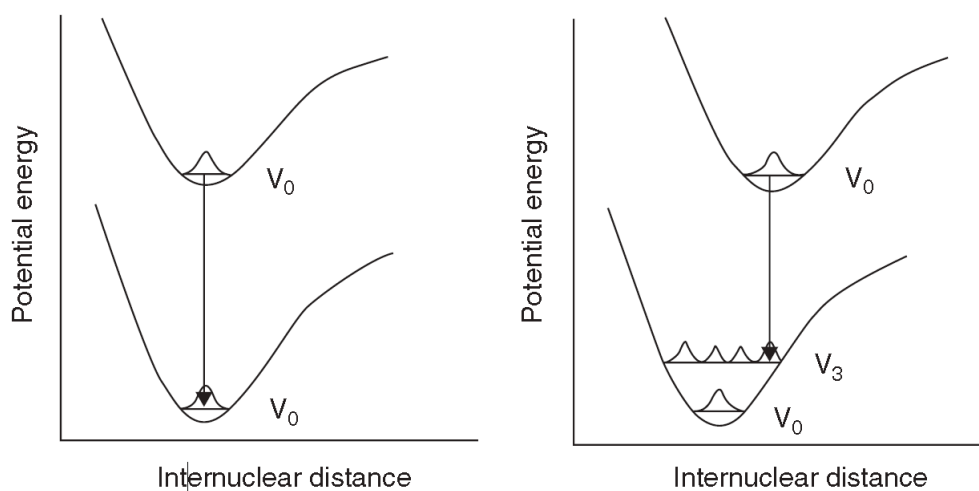


Figure 3.5 – The quantum picture of the probability of electronic transitions from Franck-Condon principle. Taken from Ref. [5]

3.5.1.1 Fluorescence

Fluorescence is a radiative process which involves a transition (photon emission) between two states with the same multiplicity. It is spin-allowed. The transition usually happens in appreciable yield from the lowest vibrational level of the lowest singlet excited state to the ground state because of the rapid nature of relaxation (Kasha's rule) [13]. Typically, fluorescence emission timescales are the order of $10^{-12} - 10^{-6}$ s. In general, the emitted radiation has lower energy than the absorbed radiation by the amount of non-radiatively dissipated energy as shown in Fig. 3.6. So the fluorescence emission light has a longer wavelength (lower energy) than the absorption light. The difference between the energy of the absorbed photon and that of the emitted photon is the Stokes shift. The 0-0 bands for absorptions and fluorescence happens at slightly different wavelength because of the different intermolecular interactions in the ground and excited states [7].

Frequently, mirror-image symmetry exists between the fluorescence spectrum and the absorption spectrum, due to the fact that the excited-state vibrational frequencies and the ground-state vibrational frequencies are similar when the geometries of the ground state S_0 and the first excited state S_1 are quite similar [7].

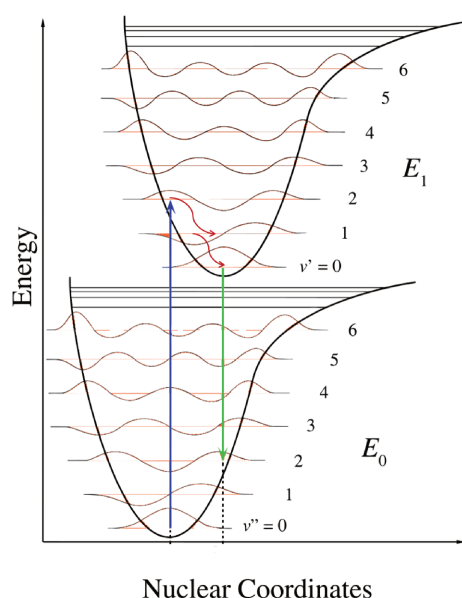


Figure 3.6 – The energy difference between the absorbed and emitted radiation. Redrawn based on a figure from ref. [14]

3.5.1.2 Phosphorescence

Phosphorescence is an intramolecular radiative processes of excited states. It is a spin forbidden transition because it happens between states with different spin multiplicity. Because of the very fast radiationless transitions, phosphorescence occurs from the thermally equilibrated lowest triplet state T_1 into the ground state S_0 [7]. Like the fluorescence spectrum, mirror-image symmetry of the $S_0 \rightarrow T_1$ absorption spectrum exists in the phosphorescence spectrum. Because phosphorescence is a spin forbidden transition, it is less intense than fluorescence [5]. It has time scales larger than fluorescence because of the transition moment of the spin forbidden $T_1 \rightarrow S_0$ is very low [7]. So, the timescales of phosphorescence emissions are in the order of $10^{-3} - 10^2$ s.

3.5.2 Intramolecular Radiationless Processes of Excited States

The intramolecular radiationless transitions can be described as a horizontal crossing between the energy levels. So, we can distinguish between the radiative and radiationless transitions as the radiative transitions are a vertical crossing between the energy levels whereas radiationless transitions are a horizontal crossing between the energy levels. The crossing between the energy levels occurs between a lowest vibrational energy of the upper electronic state and one of several closely vibrational level of the lower electronic energy surface as shown in the Fig. 3.7 [5].

Typically, the difference in the energy between electronic states is greater than between vibrational states. This fact allows treating electronics and vibrational states separately by using a Born-Oppenheimer approximation. In reality, that is not the case in the radiationless transition because of molecular vibrations do affect the electronic energy of the molecule. So, we need to take the electronic and vibrational energy into account when we treat the radiationless transitions. The breakdown of the Born-Oppenheimer approximation is resulting in the occurrence of radiationless transitions. Radiationless transitions occur between vibronic states with same energy whereas the radiative transitions occur between vibronic states with different energy as shown in the Fig 3.7.

3.5.2.1 Internal Conversion

Internal conversion refers to intramolecular radiationless transitions where the transition occurs between two isoenergetic vibronic states of the same multiplicity and the vibronic states involve mostly states having an entirely different energy at their equilibrium geometries. In other words, it is a relaxation from an upper vibronic

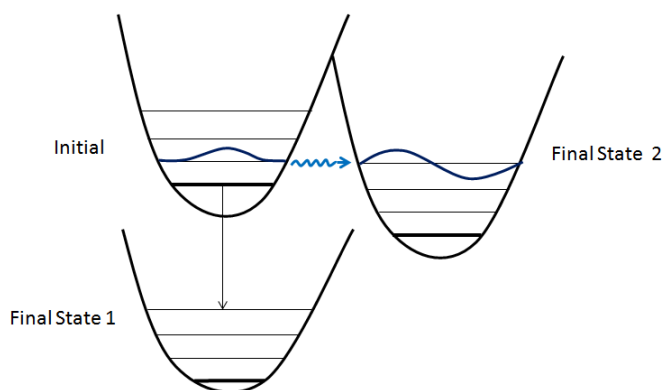


Figure 3.7 – The horizontal crossing between the energy levels in the intramolecular radiationless transitions.

state to a lower vibronic state (or vice versa) of the same multiplicity.

$$\begin{aligned} S_n^v &\rightarrow S_{n-1}^{v'} \\ T_n^v &\rightarrow T_{n-1}^{v'}, \end{aligned} \quad (3.7)$$

where n is the electronic energy level, v and v' are the vibrational energy levels.

Because of the energy difference between the upper excited states is very small and they are very close to each other in the energy, the transition probability is very high between the lower vibrational level of upper excited state (S_n) and the higher vibrational level of lower excited state (S_{n-1}). That explains the relatively fast rate of the radiationless transitions.

According to Kasha's rule, the fact that luminescence quantum yields from a higher excited state is minuscule can be attributed to the fast radiationless transition in competition with the luminescence from higher excited states having short life times. That also explains why the luminescence occurs from the lowest excited states [7].

Typically, the time scales of internal conversions between the excited state ($S_n \rightsquigarrow S_{n-1}$) are of the order of $10^{-14} - 10^{-11}$ s which are shorter than the timescales of internal conversion between the lowest excited states and the ground state ($S_1 \rightsquigarrow S_0$) [5].

3.5.2.2 Intersystem Crossing

Intersystem crossing is an intramolecular spin-forbidden radiationless process of excited states where the transition occurs between two isoenergetic vibronic states

of the different spin multiplicity. Through spin inversion, the transitions between different multiplicity states becomes possible. The intersystem crossing transition rate depends on the extent of spin-orbit coupling, the interaction between the spin of the electrons and the magnetic field resulting from the orbit of electrons around the nucleus, as well as the energy gap between the states involved in the transition [7, 5]. For example, the intersystem crossing transition $S_1 \rightsquigarrow T_1$ can take place either by direct spin-orbit coupling of S_n to the higher vibrational level of T_1 or by spin-orbit coupling to one of the upper states than T_1 and then followed by internal conversion to the T_1 [7]. The intersystem crossing transitions between states of different spin multiplicity are not all allowed. It controlled by El Sayed's rules [15] that is the intersystem crossing rate for radiationless transition involving a change of orbital type is larger than that of the radiationless transition involving a same orbital type,

$$\begin{aligned}
 {}^1(n, \pi^*) &\leftrightarrow {}^3(\pi, \pi^*) \quad \text{allowed transition} \\
 {}^3(n, \pi^*) &\leftrightarrow {}^1(\pi, \pi^*) \quad \text{allowed transition} \\
 {}^1(n, \pi^*) &\leftrightarrow {}^3(n, \pi^*) \quad \text{forbidden transition} \\
 {}^1(\pi, \pi^*) &\leftrightarrow {}^3(\pi, \pi^*) \quad \text{forbidden transition.}
 \end{aligned} \tag{3.8}$$

The timescale of intersystem crossing has the order of $10^{-11} - 10^{-8}$ s [7, 5].

3.5.3 Intermolecular Processes of Excited States

The intramolecular processes are known as unimolecular processes and may be radiative or radiationless. In either case they are responsible for deactivation of the electronically excited states.

The other type of deactivation processes is called intermolecular processes. In this case, deactivation involves the transfer of the excitation energy from one molecule to the other. This type is also known as a bimolecular deactivation or quenching process. Some quenching processes involve the same kind of molecules, and the others occur between different types of molecules. The substance which responsible for increasing the rate of the deactivation process is known as a quencher. One of the very active substances for quenching is molecular oxygen.

A quenching process that does not result in chemical changes is called a photo-physical quenching process. It may be represented as,

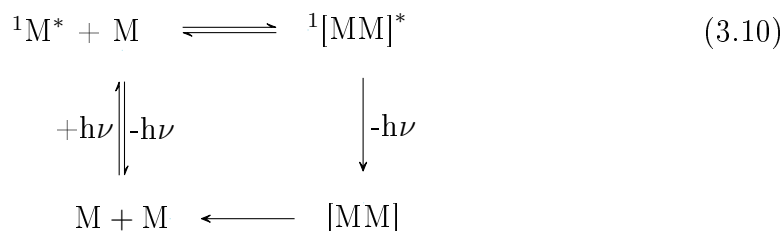


where Q is a quencher, M^* is the initial excited state, and M is a ground state or

another excited state which differs from the initial excited state.

According to whether Q is the same kind of molecule M or is different, we can distinguish two types of photophysical quenching process-namely, self-quenching or concentration quenching processes which involve the same types of molecules and impurity quenching processes which involve quencher differing from the molecule M .

The mechanism of the bimolecular deactivation processes occurs either through excimers, or via encounter exciplexes, or an exciplex involving some long-distance electron-transfer and energy-transfer mechanisms [7]. In a solution of pyrene irradiated with ultraviolet radiation, there are some effects which have been observed by increasing the concentration of pyrene. First, there is a decrease in the intensity of pyrene emission at a lower wavelength [7], Second, there is a new emission at a longer wavelength which increases in intensity by increasing the concentration of pyrene. That behaviour can be attributed to the formation of an excited state dimer of pyrene, excimer $[MM]^*$ [16], at high concentrations. At the long wavelength, the emission comes from the excimer whereas the emission at the low wavelength comes from the monomer as shown in the scheme 3.10 and Fig 3.8. This excimer has been formed by the interaction between the ground state of pyrene (M) and the excited state of pyrene (M^*),



The excimer wave function can be described by,

$$\Psi_{\text{excimer}} = c_1(\Psi_{MM^*} \pm \Psi_{M^*M}) + c_2(\Psi_{M^+M^-} \pm \Psi_{M^-M^+}), \quad (3.11)$$

where Ψ_{MM^*} and Ψ_{M^*M} are the exciton states resulting from the interaction between locally excited states, $\Psi_{M^+M^-}$ and $\Psi_{M^-M^+}$ are the Interaction with ion-pair or charge transfer states. The plus or minus combination give the stabilization which depends on the orientation of the ground and excited state to each other [7].

There is another type of complex which can be formed by the interaction between the excited state of one molecule (M^*) and the ground-state of another molecule which behaves as a quencher (Q). This type of complex is called as an excited complex or exciplex,

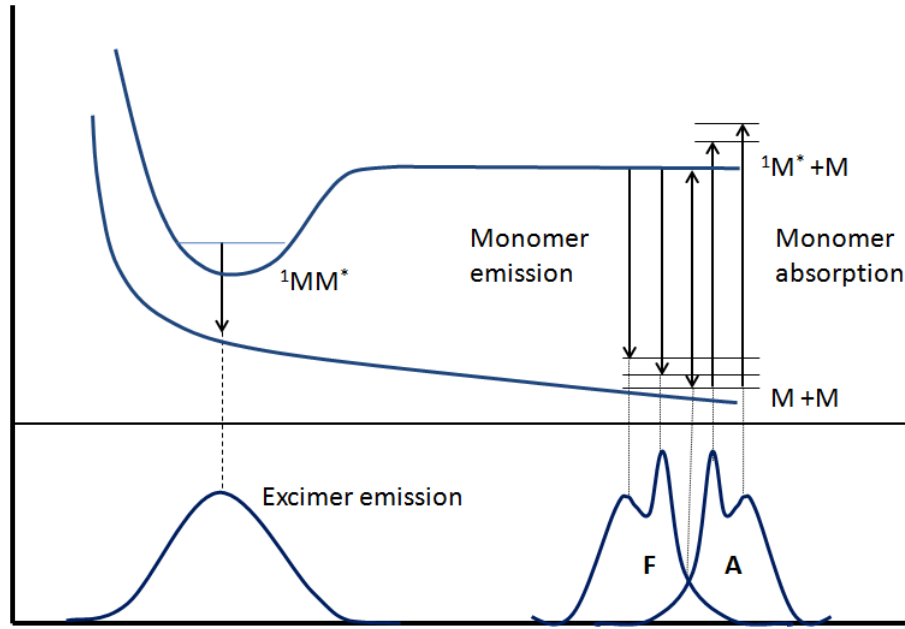
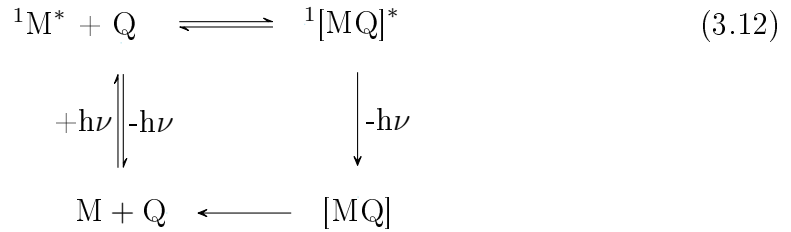


Figure 3.8 – The potential energy surfaces of the excimer formation in addition to the monomer emission and the excimer emission. Redrawn based on a figure from ref.[7]



The exciplex is observed in the solution of anthracene-dimethylaniline by a new emission at low energy due to the formation of an exciplex. One of the components of the exciplex behaves as a donor (D) and the other component behaves as an acceptor (A). So, the exciplex wave function can be described by,

$$\Psi_{\text{excplex}} = c_1 \Psi_{DA^*} + c_2 \Psi_{D^*A} + c_3 \Psi_{D^+A^-} + c_4 \Psi_{D^-A^+}, \quad (3.13)$$

where $c_1 \neq c_2$, $c_3 \neq c_4$, and the term $c_3 \Psi_{D^+A^-}$ corresponds to a charge-transfer excited state [7].

We can distinguish between excimers and exciplexes in that the excimers are nonpolar species, whereas the exciplexes are polar species.

An encounter complex can be describes as an intermolecular ensemble of an

excited-state and ground-state molecule. The ground and excited state molecules in the encounter complex usually separated by a small distance (~ 7 Å). They are usually surrounded by several shells of solvent molecules. The size, shape, and charge of the components involved in the encounter complex, in addition to their interactions with the solvent cage, are affected the structure of the encounter complex [17].

After forming encounter complexes, exciplexes, or excimers, the excitation energy can be lost either through fluorescence or phosphorescence, by energy transfer to decay into $M + Q^*$, by electron transfer to give $M^+ + Q^-$ or $M^- + Q^+$, by the internal conversion process, and by intersystem crossing process [18, 7].

3.5.3.1 Electronic Energy Transfer Process

The electronic energy transfer is a quenching process of the electronically excited entity (the donor, D^*) by transfer of its excitation energy to the other component (the acceptor, A). According to the molecular orbital picture, the energy transfer can be described as electron motion between occupied and unoccupied orbitals of the two components (D^* and A). By energy transfer, we get a ground state donor and excited state acceptor (D and A^*). So, the photochemical reaction and the luminescences will be associated with the acceptor instead of the donor. Fundamentally, energy transfer can take place by three different mechanisms.

The first mechanism is called an electron exchange mechanism. Two single independent electron transfers, one in each direction, lead to a ground state donor and an excited state acceptor [17] as shown in the Fig. 3.9.

The energy transfer by the electron exchange mechanism needs very short range separation between the donor and the acceptor with distances less than 10 Å [17, 7]. Dexter theory [19] illustrates the distance dependence of energy transfer by the exchange mechanism as,

$$k_{ET(exchange)} \propto e^{2R_{DA}}, \quad (3.14)$$

where R_{DA} is the donor-Acceptor distance [5]. This short range separation leads to orbital overlap between the donor and acceptor. So, the energy transfer by electron exchange mechanism usually occurs through the intervention of an encounter complex.

In the energy transfer by electron exchange mechanism, the spin of the donor excited state matches the spin of the excited acceptor excited state. So, the singlet-

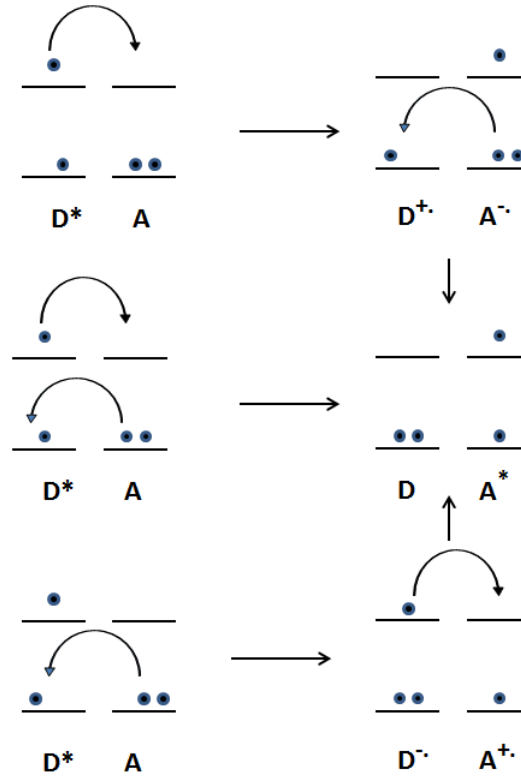
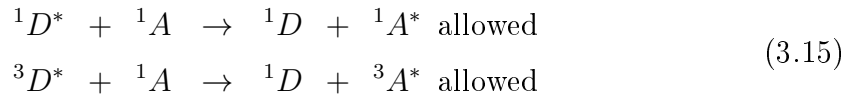


Figure 3.9 – The electron exchange mechanism of the electronic energy transfer.

singlet and triplet-triplet energy transfer are allowed [17],



The second type of energy transfer mechanism is the coulombic mechanism. This type of mechanism is also known as the Förster mechanism. The coulombic mechanism occurs as the result of the mutual electrostatic repulsion between the electrons of the donor and acceptor molecules. The excited state relaxation of the donor from D^* to D and the simultaneous electronic excitation of the acceptor from A to A^* interact in which the oscillating electrons in the donor relaxation are coupled with those in acceptor excitation by an induced dipole interaction [17] as shown in the Fig. 3.10.

The energy transfer by coulombic mechanism does not require effective orbital overlap between the donor and acceptor. The mechanism can occur with separation between the donor and the acceptor from the collision distance of less than 10 Å to the separation distance up to 100 Å [20].

In the energy transfer by coulombic mechanism, the spin multiplicity conservation

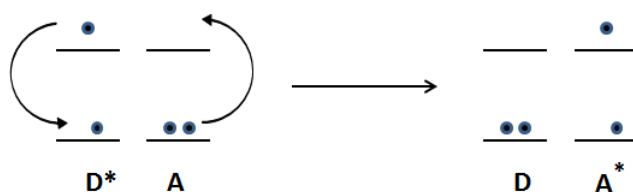
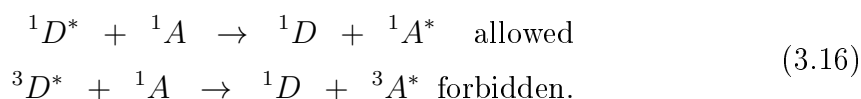


Figure 3.10 – The coulombic mechanism of the electronic energy transfer.

in the energy transfer is observed. The coulombic mechanism only happens when a large transition dipole moment is created. Depending on that the singlet-singlet energy transfer by coulombic mechanism is allowed where there is no change in the multiplicity. Whereas the triplet-triplet energy transfer in the coulombic mechanism is forbidden [17, 5],



Because of the excited state relaxation energy in the donor and the simultaneous electronic excitation energy in the acceptor are identical or in resonance as shown in the Fig. 3.11 in addition to this mechanism was developed by Förster, this type of energy transfer known as Förster resonance energy transfer (FRET) [20, 5].

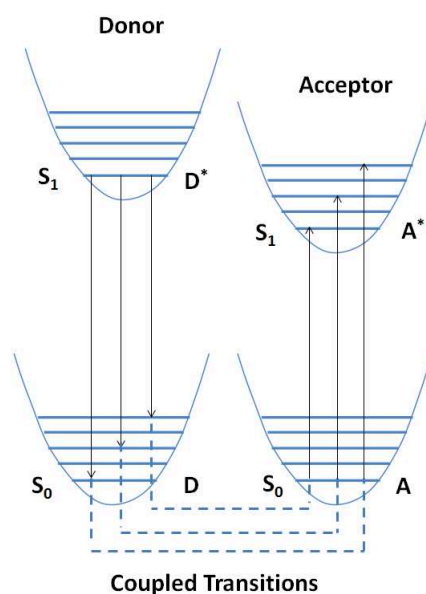


Figure 3.11 – Illustration of Förster resonance energy transfer (FRET). Redrawn based on a figure from ref. [5]

The energy transfer by both electron exchange and coulombic mechanisms considered as non-radiative transfer.

The third type of the energy transfer mechanism is a radiative energy transfer mechanism. This type of the mechanism occurs by the absorption of the photon by the ground state acceptor which is emitted by the electronically excited state donor,



Radiative energy transfer requires a sufficient overlap between the acceptor absorption spectrum and the donor emission spectrum. It can happen at a large separation distance between the donor and acceptor because the photon can travel a long distance before being absorbed by the acceptor. It is controlled by the same rules of intensity absorption because the radiative energy transfer occurs by emission and absorption. So, the singlet-triplet energy transfer is forbidden [5, 7].

3.5.3.2 Electron Transfer Process

Electron transfer is an important problem in organic photovoltaics. In the first instance this may be understood as transferring (ionizing) an electron from the donor and adding the electron (electron attachment) to an acceptor. The energy levels of the highest-occupied molecular orbital (HOMO) and the lowest-unoccupied molecular orbital (LUMO) of the two components involved in the photoinduced process determine which of the two components is the donor or acceptor as shown in the Fig 3.12.

According to the molecular orbital picture, electron transfer can be described as electron motion from an occupied molecular orbital in the donor to the unoccupied molecular orbital in the acceptor. The mechanism goes through many steps. Two of the important steps of the mechanism are exciton formation and exciton dissociation. The exciton formation step is related to the HOMO-LUMO gap which leads directly to estimate the initial excitation energy. The other thing concerning exciton dissociation is that exciton dissociation depends deeply on the difference between the ionization potential and the electron affinity between the donor and the acceptor which are responsible for creating a downhill energetic driving force at the interface between the donor and the acceptor, leading to exciton separation. The range of separation distance between the donor and acceptor is less than 10 Å because electron transfer requires close effective orbital overlap. Spin conservation is observed in the

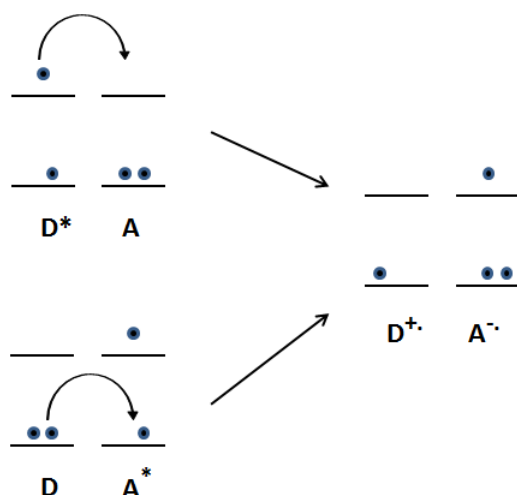


Figure 3.12 – The electron transfer mechanism.

electron transfer mechanism.

3.5.3.3 Vibrational Relaxation

Vibrational relaxation is an intermolecular radiationless process of an electronically excited state which has an excess of vibrational energy. As such it excludes transitions occurring between the zero-point vibrational levels. The vibrational relaxation occurs when the electronically hot excited state collides with one other molecule or with the solvent molecule to relax to the lowest vibrational level of a particular electronic energy level. The time scales of vibrational radiationless relaxation processes are of the order of $10^{-13} - 10^{-9}$ s in condensed phase [5].

3.5.4 Photochemical Reactions

Ground state reactions can be modelled by one potential energy surface. The reactants are represented by points on the potential energy surface. Then, the ground state reaction can be described by the pathway of this point from one minimum to another, where the minimums respectively represent the reactants and the product, and the saddle between them represents the transition state or the activated complexes. Since all the photochemical reactions being by absorbing a photon which puts the reactant in high energy state, photochemical reaction modelling requires at least two potential energy surfaces, the ground state energy surface with reactant and product minima in addition to the excited state energy surface on which the photoreaction is started. The mechanism of the photochemical reaction can be realized from the knowledge of the shapes of the ground state energy surface (S_0), the

first singlet excited state energy surface (S_1) and the first triplet excited state energy surface (T_1). By the shape, we can distinguish where are the minima and the funnel regions, the set of molecular geometry points where the potential energy surfaces are degenerate and the crossing occur between them, in the S_1 and T_1 potential surfaces. Also from the shapes of the ground state energy surface, we can determine the return products we get from the funnel regions of the S_1 and T_1 potential surfaces.

3.5.4.1 The Pathway of Photochemical Reaction

After light absorption, the electronically excited state is formed by vertical excitation according to the Franck Condon rules. Several scenarios can happen with the electronically excited state. In general, the trend of electronically excited states is to react in two ways:

First, a concerted process, the process which includes one single step to give the product such as the series of pericyclic reactions, the reactions which initiated from the lowest singlet excited state $S_1(\pi, \pi^*)$ with a cyclic transition state. In this type of photochemical reaction, a concerted rearrangement of electrons occur leading to break and form σ and π bonds simultaneously [5],



Second, the photochemical reactions occur through the formation of a reactive intermediate or intermediates proceeding through radical intermediates and then followed by radical reactions, usually dark processes. The ketone reactions which are initiated from the lowest single excited state $S_1(n, \pi^*)$ or $T_1(n, \pi^*)$ are a good example of this type of reactions [5],



One of the ways of visualizing the potential energy of the molecular system is from the point of view of the potential energy changes that happen during the chemical reaction. That is simply represented as the reaction profile where the potential energy values of the reactants, products, intermediates, and transition states can be plotted against the reaction coordinates

For the photochemical reactions, we need to model at least two potential energy surfaces, namely the ground state surface which represents the thermal reaction and the excited state energy surface from which the excitation where started.

Figure 3.13 gives a schematic explains the reactions pathway of the excited state

after excitation with and without intermediates which includes the potential energy surfaces of the ground state and the excited state.

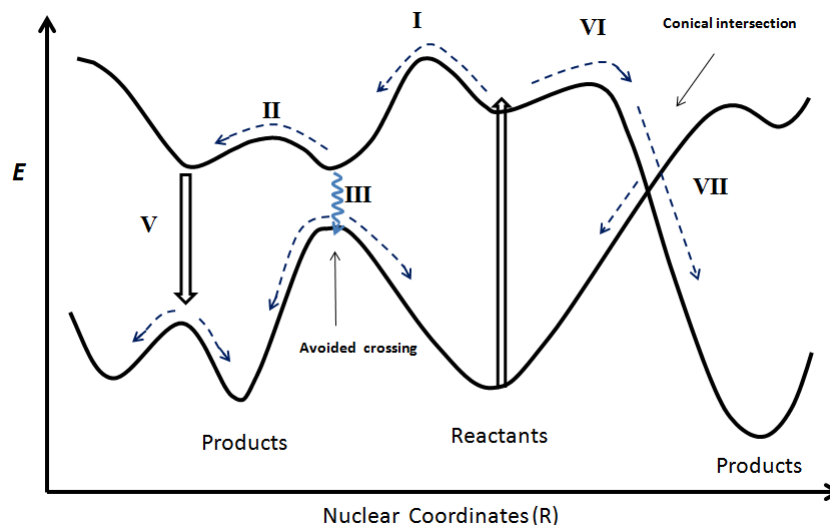


Figure 3.13 – The schematic explains the reactions pathway of the excited state after excitation which includes the potential energy surfaces of the ground state and the excited state.

After excitation, the electronically excited state has the same geometry as the ground state. Subsequently, the nuclear motion finds itself governed by new potential energy surface which leads to a new geometry with time.

The electronically excited state, in a short time on the order of a few picoseconds, may reach the local minimum in the potential energy surface of the excited state as shown in the path *I* of the Fig 3.13. Energy is released to the surrounding molecules.

These minima in the lowest S_1 or T_1 excited state potential energy surface may include molecules or intermolecular complexes (excimer or exciplex) where the geometries are near the ground state equilibrium geometries. The return to the ground state from these two types of minima usually does not produce any chemical changes (see the right side of the path *III* in the Fig 3.13) unless there is noteworthy geometrical changes go with the minima exist on the ground state surface as shown in the left side of the path *III* Fig 3.13.

If the excited state molecule reached these minima by crossing some barriers, due to the kinetic energy of the nuclei, where these minima are in the given potential energy surface but far away from the geometry of the starting species, then this process is known as a hot excited-state reaction (Fig 3.13 path *II*). This types of reaction can be detected by the product emission as shown in the path *V* in the Fig 3.13.

Finding the local minima in the lowest excited state is of great importance. By locating these minima on the potential energy surface, we get an idea of where the excited state and the ground state may come close to each other. The importance of these regions arises from the potential energy surfaces can a cross or avoid each other at these regions.

In general, the Born-Oppenheimer approximation is invalid at and near regions where the surfaces are crossing. Conical intersections or funnels are the region where the two potential energy surfaces cross or more have degenerate energy values, and the nonadiabatic coupling between them is high. According to the non-crossing rule, the touchings or crossing between two potential energy of two states are invalid for the diatomic systems which have a single degree of freedom unless the states have different symmetry. Whereas the intersection or touching between the potential energy surfaces of two states is allowed for the polyatomic systems even, if they have the same symmetry [21].

The photochemical reactions which begin and end in the ground state potential energy surface are called nonadiabatic processes. These types of reactions contain a crossing between the potential energy surface of the excited state and the ground state potential energy as shown in the Fig 3.13 path *VII*.

If the initial excited state was in the upper excited state of given spin multiplicity, Then upper excited state undergoes a fast process of internal conversion to reach the lowest excited state of the same spin multiplicity. In some cases, the lowest excited state S_1 crosses the ground state potential energy surface S_0 at the funnel region via internal conversion so fast that the first thermal equilibration of the vibrational motion of these molecules is achieved in a minimum in the S_0 state. These types of photoreaction are known as a direct reactions (Fig 3.13 path *VII*) [7].

Bibliography

- [1] J. D. Coyle, *Introduction To Organic Photochemistry.*, Wiley, Great Britain, 1991. pages 25
- [2] M. Montalti, A. Credit, L. Prodi, and M. T. Gandolfi, *Handbook of Photochemistry, Third Edition*, Taylor and Francis, United Kingdom, 2006. pages 25, 115
- [3] M. Robb, M. Olivucci, and F. Bernardi, [Photochemistry](#), in *Encyclopedia of Computational Chemistry*, edited by P. V. R. Schleyer, Wiley, 2004. pages 25, 32

- [4] M. Merchán and L. Serrano-Andrés, [Ab initio methods for excited states](#), in *Computational Photochemistry*, edited by M. Olivucci, Elsevier, 2005. pages 25, 32
- [5] B. Wardle, [Principles and Applications of Photochemistry](#), A John Wiley & Sons Ltd., Chichester, United Kingdom, 2009. pages 26, 28, 33, 35, 36, 37, 40, 42, 43, 44, 45, 309, 310
- [6] P. W. Atkins, [Quanta](#), W. H. Freeman and Company, New York, 2010. pages 27
- [7] M. Klessinger and J. Michl, [Excited States and Photochemistry of Organic Molecules](#), VCH Publishers, Inc., New York, 1995. pages 27, 28, 29, 34, 35, 36, 37, 38, 39, 40, 43, 47, 310
- [8] J. Lambert, *Photometria sive de mensura et gradibus luminis, colorum et umbrae*, Germany, 1760, [Photometry, or, On the measure and gradations of light, colors, and shade](#). pages 28
- [9] M. Montalti, A. Credi, L. Prodi, and M. T. Gandolfi, [Handbook of Photochemistry](#), 3rd ed., CRC Press & Taylor & Francis Group, 6000 Broken Sound Parkway NW, Suite 300 Boca Raton, FL 33487-2742, 2006. pages 28
- [10] L. Serrano-Andrés and M. Merchán, [Spectroscopy: applications](#), in *Encyclopedia of Computational Chemistry*, edited by P. V. R. Schleyer, Wiley, 2004. pages 32
- [11] L. Serrano-Andrés and M. Merchán, [Quantum chemistry of the excited state: 2005 overviews](#), Journal of Molecular Structure: THEOCHEM **729**, 99 (2005). pages 32, 33, 309
- [12] J. Franck and E. G. Dymond, [Elementary processes of photochemical reactions](#), Transactions of the Faraday Society **21**, 536 (1926). pages 32
- [13] M. Kasha, New developments in molecular orbital theory, Discussions of the Faraday Society. **9**, 14 (1950), [Characterization of Electronic Transitions in Complex Molecules](#). pages 34
- [14] Franck-condon principle, <https://en.wikipedia.org/wiki/Franck> pages 34, 309
- [15] M. A. El-Sayed, [Spin-Orbit Coupling and the Radiationless Processes in Nitrogen Heterocyclics](#), J. Chem. Phys. **38**, 2934 (1963). pages 37
- [16] T. Forster and K. Kasper, [concentration reversal of the fluorescence of pyrene](#). pages 38
- [17] G. J. Kavarnos and N. J. Turro, [Photosensitization by reversible electron transfer: theories, experimental evidence, and examples](#), Chem. Rev. **86**, 401 (1986). pages 40, 41, 42

-
- [18] K. Schulten, H. Staerk, A. Weller, H.-J. Werner, and B. Nickel, [Magnetic Field Dependence of the Geminate Recombination of Radical Ion Pairs in Polar Solvents](#), Z. Phys. Chem. **101**, 371 (1976). pages 40
- [19] D. L. Dexter, [A Theory of Sensitized Luminescence in Solids](#), J. Chem. Phys. **21**, 836 (1953). pages 40
- [20] T. Forster, [10TH SPIERS MEMORIAL LECTURE TRANSFER MECHANISMS OF ELECTRONIC EXCITATION](#) , Faraday Discuss. Chem. Soc. **27**, 7 (1959). pages 41, 42
- [21] M. Klessinger, [Conical Intersections and the Mechanism of Singlet Photoreactions.](#), Angew. Chem. Int. Ed. Engl. **34**, 549 (1995). pages 47

Chapter 4

Theoretical Methods

4.1 Quantum Mechanical Preliminaries

4.1.1 Atomic Units

Since the dominant forces at the atomic scale are electromagnetic and since there are more than one system of electromagnetic units, a choice must be made. Nowadays the preferred system is the *Système Internationale* (SI). In SI units the potential energy V for two charges q_1 and q_2 separated by a distance r is

$$V = \frac{q_1 q_2}{(4\pi\epsilon_0)r}, \quad (4.1)$$

where ϵ_0 is the permittivity of free space. However the same potential energy has a simpler form in Gaussian units, namely

$$V = \frac{q'_1 q'_2}{r} \quad (4.2)$$

where

$$\begin{aligned} q'_1 &= \frac{q_1}{\sqrt{4\pi\epsilon_0}} \\ q'_2 &= \frac{q_2}{\sqrt{4\pi\epsilon_0}} \end{aligned} \quad (4.3)$$

are expressed in electrostatic units (esu) rather than in the SI unit coulomb. Note that esu and coulomb have different dimensions because ϵ_0 has units.

Unless otherwise indicated, equations in this thesis will be written in atomic units. These arise naturally when equations in the Gaussian system are written in dimensionless form in terms of the three intrinsic constants e (the absolute value

of the charge of the electron), m_e (the mass of the electron), and \hbar (Planck's constants h divided by 2π). One atomic unit (a.u.) of anything may be converted to Gaussian units by multiplying times the unique product of powers of e , m_e , and \hbar with the right physical dimension (e.g., energy, length, momentum, time, ...) Examples and conversion factors are given in Table 4.1.

Table 4.1 – Some atomic units and their SI Values. This table is taken from Ref. [1].

Quantity	Symbol	Name	SI value
Mass	m_e	Mass of electron	9.1094×10^{-31} kg
Charge	e	Elementary charge	1.6022×10^{-19} C
Angular momentum	\hbar	Planck's constant/ 2π	1.0546×10^{-34} J.s
Length	$a_o = \hbar^2/(m_e e^2)$	Bohr	5.2918×10^{-11} m
Energy	$E_h = m_e e^4/\hbar^2$	Hartree	4.3597×10^{-18} J
Time	$\hbar^3/(m_e e^4)$	Jiffy	2.41888×10^{-17} s

4.1.2 Schrödinger Equation

The time-independent Schrödinger equation is a partial differential equation which is used to describe stationary states. In 1926 [2], Schrödinger published the time-dependent Schrödinger wave equation,

$$\hat{H}\Psi(t) = i\frac{\partial}{\partial t}\Psi(t), \quad (4.4)$$

where \hat{H} is the Hamiltonian operator, and $\Psi(t)$ is the wave function. Wave functions with a well-defined energy, E_I , are called stationary states and have the form [3],

$$\Psi(t) = \Psi_I e^{-iE_I t}. \quad (4.5)$$

Inserting this equation in Eq. (4.4) easily leads to the time-independent Schrödinger equation,

$$\hat{H}\Psi_I = E\Psi_I \quad (4.6)$$

This equation is the cornerstone of Quantum Chemistry¹ because finding the solution for the energy and wave function provides us with optimized geometries and properties such as electric and magnetic moments, *etc.* [3].

1. Quantum chemistry is a branch of theoretical chemistry that applies quantum mechanics, quantum field theory and Born-Oppenheimer approximation to solve issues and questions in chemistry. An application of quantum chemistry is the study of the behaviour of atoms and molecules concerning their reactivity. Quantum chemistry is located on the boundary between chemistry and physics and is shared by specialists from both branches.

4.1.3 Some Properties of Wave Functions

The quantum mechanical quantity describing the state of a chemical system is the wave function Ψ (also called the state function). An acceptable wave function must be finite, continuous, single-valued, respect the indistinguishability of the identical particle, and the normalized integral of $|\Psi|^2$ over all space must be unity (i.e., Ψ must be square integrable) [4]. (Exceptions are made for continuum wave functions which, however, do not concern us in this thesis.) Classical observables—such as energy, position, momentum—are replaced by operators \hat{A} . Only the eigenvalues a of the operators are observables

$$\hat{A}\Psi_{ai} = a\Psi_{ai}, \quad (4.7)$$

where the index i is needed because more than one Ψ_{ai} may correspond to the same value of a . The eigenfunctions Ψ_{ai} allow us to expand the state function as

$$\Psi = \sum_{ai} \Psi_{ai} C_{ai}, \quad (4.8)$$

where

$$C_{ai} = \langle \Psi_{ai} | \Psi \rangle, \quad (4.9)$$

as long as Ψ is normalized and the Ψ_{ai} are orthonormalized. The probability $p(a)$ of measuring a is then given by

$$p(a) = |C_{ai}|^2. \quad (4.10)$$

Inserting Eq. (4.8) into

$$\hat{H}\Psi = E\Psi \quad (4.11)$$

gives

$$\sum_{bj} \hat{H}\Psi_{bj} C_{bj} = E \sum_{bj} \Psi_{bj} C_{bj} \quad (4.12)$$

Left multiplying by Ψ_{ai}^* and integrating then gives

$$\sum \langle \Psi_{ai} | \hat{H} | \Psi_{bj} \rangle C_{bj} = E C_{ai} \quad (4.13)$$

or

$$\mathbf{H}\vec{C} = E\vec{C} \quad (4.14)$$

where

$$H_{ai,bj} = \langle \Psi_{ai} | \hat{H} | \Psi_{bj} \rangle = \int \Psi_{ai}^*(\vec{x}_1, \vec{x}_2, \dots, \vec{x}_N) \hat{H} \Psi_{bj}(\vec{x}_1, \vec{x}_2, \dots, \vec{x}_N) d\vec{x}_1 d\vec{x}_2 \dots d\vec{x}_N \quad (4.15)$$

Note how Ψ has become an infinite dimensional column vector \vec{C} while \hat{H} has become an infinite dimensional matrix \mathbf{H} . This correspondence between operators and matrices and between wave functions and vectors is a re-occurring theme in quantum mechanics. In fact the original form of quantum mechanics was the matrix form of Heisenberg which later was replaced by Schrödinger's wave equation. Finally Dirac showed the equivalence of Heisenberg's matrix mechanics and Schrödinger's wave mechanics, though Schrödinger already mentioned the correspondance (4.15) in Ref. [2].

4.1.4 Molecular Hamiltonian

The molecular Hamiltonian operator is the total energy operator and, as such, is the sum:

$$\hat{H} = \hat{T}_n + \hat{T}_e + V_{en} + V_{ee} + V_{nn}, \quad (4.16)$$

where,

$$\hat{T}_n = - \sum_{I=1,M} \frac{1}{2M_I} \nabla_I^2, \quad (4.17)$$

is the kinetic energy operator for the nuclei,

$$\hat{T}_e = - \sum_{i=1,N} \frac{1}{2} \nabla_i^2, \quad (4.18)$$

is the kinetic energy operator for the electrons,

$$V_{en} = - \sum_{A=1,M} \sum_{i=1,N} \frac{Z_I}{r_{iI}}, \quad (4.19)$$

is the electron-nuclear attraction energy,

$$V_{ee} = + \sum_{i=1,N} \sum_{j=1,N}^{j>i} \frac{1}{r_{ij}}, \quad (4.20)$$

is the electron-electron repulsion energy, and

$$V_{nn} = + \sum_{I=1,M} \sum_{J=1,M}^{J>I} \frac{Z_I Z_J}{R_{IJ}}, \quad (4.21)$$

is the nuclear-nuclear repulsion energy. Here M_I is the mass of the nucleus I .

Equations (4.4) and (4.6) with the Hamiltonian in Eq. (4.16) are partial differential equations. To be able to solve these equations, it is useful to approximate both the Hamiltonian and the wave function.

4.1.5 Born-Oppenheimer Approximation

The Born-Oppenheimer approximation is based on the fact that the mass of any nucleus is much larger than the mass of the electron. So (classically speaking) electrons move much faster than the nuclei. Thus, to a first approximation, electrons move in the field of stationary nuclei. The corresponding electronic Hamiltonian is [5],

$$\hat{H}_{el} = \hat{T}_e + V_{en} + V_{ee}, \quad (4.22)$$

so we can write the electronic Schrödinger equation,

$$\hat{H}_{el}\Psi_I^{el} = E_I^{el}\Psi_I^{el}. \quad (4.23)$$

In the Born-Oppenheimer approximation, the nuclear Schrödinger equation is

$$\left(-\frac{1}{2} \sum_{I=1,M} \frac{1}{M_I} \nabla_I^2 + V_{pot}^I(\mathbf{R}) \right) \Psi_{nucl}(\mathbf{R}, t) = i \frac{\partial}{\partial t} \Psi_{nucl}(\mathbf{R}, t) \quad (4.24)$$

with

$$V_{pot}^K(\mathbf{R}) = E_K^{el}(\mathbf{R}) + \sum_{I,J}^{J>I} \frac{Z_I Z_J}{R_{IJ}}, \quad (4.25)$$

where $\mathbf{R} = (\vec{R}_1, \vec{R}_2, \dots, \vec{R}_M)$. The quantity V_{pot}^I is the potential energy hypersurface for the I th electronic state.

4.1.6 Molecular Orbitals

A wave function for a single electron is called a molecular orbital (MO). The wave function of the position vector \vec{r} which describes the spatial distribution of an electron is called a spatial orbital $\psi(\vec{r})$. The probability of finding an electron in the small volume element $d\vec{r}$ surrounding \vec{r} is given $|\psi(\vec{r})|^2 d\vec{r}$. Spatial molecular orbitals form an orthonormal set [6],

$$\int \psi_i^*(\vec{r}) \psi_j(\vec{r}) d\vec{r} = \delta_{ij}. \quad (4.26)$$

or may be orthonormalized if necessary (which sometimes occurs for energetically degenerate MOs).

The complete wave function for an electron must contain both the spatial and spin components. The spin components of an electron can be described by one of two orthonormal functions $\alpha(\omega)$ and $\beta(\omega)$. $\alpha(\omega)$ represents the spin up (\uparrow) and $\beta(\omega)$ represents the spin down (\downarrow). ω is a fictitious spin variable, integration over which corresponds to summation over α and β :

$$\int \sigma(\omega) d\omega = \alpha + \beta. \quad (4.27)$$

The wave function of an electron consisting of both the spatial and spin components is called a spin orbital, $\chi(\vec{x})$, where \vec{x} refers to both space and spin coordinates as shown below [6] ,

$$\chi(\vec{x}) = \begin{cases} \psi(\vec{r}) & \alpha(\omega) \\ & \text{or} \\ \psi(\vec{r}) & \beta(\omega) \end{cases}. \quad (4.28)$$

4.1.7 Variational Principle

Exact solutions of the Schrödinger equation are only known for very simple systems. One important way to find approximate solutions of the Schrödinger equation is the variational principle. The variational principle says that any trial wave function Ψ satisfying the boundary conditions of the exact wave function Φ has an expectation value of the Hamiltonian which is an upper bound to the ground state energy²,

$$E_o \leq E[\Psi] = \frac{\langle \Psi | \hat{H} | \Psi \rangle}{\langle \Psi | \Psi \rangle}. \quad (4.29)$$

The variational principle tells us to search for the wave functions which have the lowest expectation value for the energy:

$$E_0 = \min_{\Psi} E[\Psi]. \quad (4.30)$$

This means that we may choose an *Ansatz* for Ψ with parameters α_i and then determine the parameters by using the variational principle. At a critical point (e.g., a minimum) the variation dE will be zero for any arbitrary variation of the parameters

2. The square bracket notation $E[\Psi]$ means that E is a functional of Ψ . That is, E is a function of the function Ψ .

α_i :

$$dE[\Psi](\alpha_1, \alpha_2, \dots) = \frac{\partial E[\Psi]}{\partial \alpha_1} d\alpha_1 + \frac{\partial E[\Psi]}{\partial \alpha_2} d\alpha_2 + \dots = 0 \quad (4.31)$$

So, we have,

$$\frac{\partial E[\Psi]}{\partial \alpha_i} = 0 \quad \text{for all } i, \quad (4.32)$$

because the variations $d\alpha_i$ are independent.

4.2 Ground-State Theory

4.2.1 Hartree Product

A spin orbital describes a single electron. Hartree considered the hamiltonian of N noninteracting electrons,

$$\hat{H} = \sum_{i=1}^N \hat{h}(i), \quad (4.33)$$

where $\hat{h}(i)$ is the operator which describes the potential energy and kinetic energy of the electron i [6].

The Hamiltonian $\hat{h}(i)$ has a set of spin orbitals χ_j ,

$$\hat{h}(i)\chi_j(\vec{x}_i) = \varepsilon_j \chi_j(\vec{x}_i). \quad (4.34)$$

The corresponding eigenfunctions of \hat{H} are simple products of the spin-orbital wave functions for each electron,

$$\Psi^{\text{HP}}(\vec{x}_1, \vec{x}_2, \dots, \vec{x}_N) = \chi_1(\vec{x}_1)\chi_2(\vec{x}_2)\dots\chi_N(\vec{x}_N) \quad (4.35)$$

(or linear combinations of energetically-degenerate functions of this form). This Hartree product(4.35) satisfies the Schrödinger equation is,

$$\hat{H}\Psi^{\text{HP}} = E\Psi^{\text{HP}}, \quad (4.36)$$

with hamiltonian (4.33). The corresponding eigenvalue E is the sum of the spin-orbital energies of each spin orbital in Ψ^{HP} ,

$$E = \varepsilon_1 + \varepsilon_2 + \dots + \varepsilon_N. \quad (4.37)$$

The probability [6] of finding an electron i in the volume dx_i , centred at x_i is

$$|\Psi^{\text{HP}}(\vec{x}_1, \vec{x}_2, \dots, \vec{x}_N)|^2 d\vec{x}_1 \dots d\vec{x}_N = (|\chi_i(\vec{x}_1)|^2 d\vec{x}_1) (|\chi_j(\vec{x}_2)|^2 d\vec{x}_2) \dots (|\chi_k(\vec{x}_N)|^2 d\vec{x}_N). \quad (4.38)$$

That is, the probability of finding N electrons at $\mathbf{x} = (\vec{x}_1, \vec{x}_2, \dots, \vec{x}_N)$ is simply the product of the probabilities of finding each electron i in spin orbital $\chi(\vec{x}_i)$ at x_i . The Hartree product is an independent-electron approximation (IPA) [6].

4.2.2 Hartree-Fock Approximation

The Hartree product suffers from several deficiencies. One main deficiency in the Hartree product is that it does not take account of the indistinguishability of electrons. Also, the Hartree product violates the Pauli principle. In 1930 [7], Fock modified Hartree's method by approximating the N -electron wave function as an antisymmetrized product of N one-electron wave functions $\chi_i(\vec{x}_i)$ called a Slater determinant,

$$\Phi(x) = \frac{1}{\sqrt{N!}} \begin{vmatrix} \chi_1(\vec{x}_1) & \chi_2(\vec{x}_1) & \dots & \chi_N(\vec{x}_1) \\ \chi_1(\vec{x}_2) & \chi_2(\vec{x}_2) & \dots & \chi_N(\vec{x}_2) \\ \vdots & \vdots & \ddots & \vdots \\ \chi_1(\vec{x}_N) & \chi_2(\vec{x}_N) & \dots & \chi_N(\vec{x}_N) \end{vmatrix}, \quad (4.39)$$

where the χ_i are orthonormal spin orbitals.

The ideal Hartree-Fock (HF) energy and the wave function are acquired by using the variational principle to minimise the energy,

$$E_{\text{HF}} = \min_{\Phi \rightarrow N} E_{\text{HF}}[\Phi]. \quad (4.40)$$

The HF energy, E_{HF} , is given by,

$$E_{\text{HF}}[\Phi] = \langle \Phi | \hat{H}_{\text{el}} | \Phi \rangle = \sum_{i=1}^N \langle \chi_i | \hat{h} | \chi_i \rangle + \frac{1}{2} \sum_{i,j=1}^N [(ii||jj) - (ij||ji)], \quad (4.41)$$

where,

$$\langle \chi_i | \hat{h} | \chi_i \rangle = \int \chi_i^*(\vec{x}) [\hat{h} \chi_i(\vec{x})] d\vec{x} \quad (4.42)$$

and

$$(pq||rs) = \int \int \chi_p^*(\vec{x}_1) \chi_q(\vec{x}_1) \frac{1}{r_{12}} \chi_r^*(\vec{x}_2) \chi_s(\vec{x}_2) d\vec{x}_1 d\vec{x}_2, \quad (4.43)$$

is an electron repulsion integral in Mulliken (charge cloud) notation. (The quantity

$1/r_{12}$ is the Hartree kernel.)

Optimal spin orbitals minimise the energy expression in the Eq. (4.41) subject to the orbital orthonormality constraint. The minimisation is done by using the method of the Lagrange multipliers:

$$\mathcal{L} = \langle \Psi | H_{el} | \Psi \rangle - \sum_{i,j} \varepsilon_{i,j} (\langle \psi_i | \psi_j \rangle - \delta_{i,j}), \quad (4.44)$$

where $\varepsilon_{i,j}$ are the Lagrange multipliers. The minimization of Eq. (4.44) yields the Hartree-Fock orbital equation,

$$\hat{f}\psi_i(\vec{x}) = \sum_{j=1}^N \varepsilon_{i,j} \psi_j(\vec{x}), \quad (4.45)$$

where the Fock operator

$$\hat{f}(1) = -\frac{1}{2}\nabla_1^2 - \sum_{A=1}^M \frac{Z_A}{r_{1A}} + v_{HF}(\vec{x}_1). \quad (4.46)$$

is an effective one-electron operator. The Hartree-Fock potential is the average repulsive “potential” felt by the i th electron as a result of the remaining $N - 1$ electrons,

$$v_{HF}(\vec{x}_1) = \sum_j^N (\hat{j}_j(\vec{x}_1) - \hat{k}_j(\vec{x}_1)), \quad (4.47)$$

where \hat{j} is the Coulomb operator,

$$\hat{j}_j(\vec{x}_1) = \int |\chi_j(\vec{x}_2)|^2 \frac{1}{r_{12}} d\vec{x}_2, \quad (4.48)$$

which acts by multiplication. The second term $\hat{k}_j(\vec{x}_1)$ is the exchange part of the HF “potential”. The exchange operator has no classical form but its effect when acting on a spin orbital is giving by,

$$\hat{k}_j(\vec{x}_1)\chi(\vec{x}_1) = \left(\int \chi_j^*(\vec{x}_2) \frac{1}{r_{12}} \chi(\vec{x}_2) d\vec{x}_2 \right) \chi_j(\vec{x}_1). \quad (4.49)$$

(Strictly speaking it is not a potential because it is not multiplicative.) Because the Fock operator is invariant to a unitary transformation of the occupied orbitals, it is possible to further reduce Eq. (4.45) to N canonical Hartree-Fock molecular

spin-orbital equations of the form,

$$\hat{f}\chi_j = \varepsilon_j\chi_j, \quad j = 1, 2, \dots, N. \quad (4.50)$$

The ε_i are orbital energies whose physical meaning is given by Koopmans' theorem.

4.2.2.1 Roothaan Equations

In 1951 Roothaan [8] described matrix algebraic equations that permitted HF calculations to be carried out using a basis set representation for the MOs. He introduced a linear combination of atomic orbitals (LCAO) approximation to the MOs in the framework of the Hartree-Fock method. This development made the Hartree-Fock approximation practical for molecules. The approach employs a set of three-dimensional one-electron functions χ_μ , called atomic orbitals (AOs),

$$\phi_{i\sigma}(\vec{r}) = \sum_{\mu=1, K} \chi_\mu(\vec{r})c_{\mu i}^\sigma, \quad (4.51)$$

where $K \geq N$ is the size of the AO basis set. The $\phi_{i\sigma}(\vec{r})$ are the spatial part of the occupied spin orbitals $\phi_{i\sigma}(\vec{r})\sigma(\omega)$ which are used to form the Slater determinant. The $c_{\mu i}^\sigma$ are elements of the matrix of molecular orbital (MO) coefficients. The $\phi_{i\sigma}(\vec{r})$ are then minimized with respect to the matrix of $c_{\mu i}^\sigma$. A rigorous derivation using the variational principle and the basis set in the Eq. (4.51) yields,

$$\hat{f}^\sigma \sum_{\mu=1}^K \chi_\mu(\vec{r})c_{\mu q}^\sigma = \varepsilon_\alpha^\sigma \sum_{\mu=1}^K \chi_\mu(\vec{r})c_{\mu q}^\sigma. \quad (4.52)$$

Multiplication and integration with χ_ν results in the K equations,

$$\sum_{\mu=1}^K \langle \chi_\nu | \hat{f}^\sigma | \chi_\mu \rangle c_{\mu p}^\sigma = \varepsilon_p^\sigma \sum_{\mu=1}^K \langle \chi_\nu | \chi_\mu \rangle c_{\mu p}^\sigma. \quad (4.53)$$

These equations can be written in the matrix form as the Roothaan equation,

$$\mathbf{F}^\sigma \mathbf{C}^\sigma = \mathbf{S} \mathbf{C}^\sigma \mathbf{E}^\sigma, \quad (4.54)$$

where $F_{\mu,\nu}^\sigma$ is the Fock matrix,

$$F_{\mu,\nu}^\sigma = \langle \chi_\mu^\sigma | \hat{f}^\sigma | \chi_\nu^\sigma \rangle, \quad (4.55)$$

and $S_{\mu\nu}$ is the overlap matrix,

$$S_{\mu\nu} = \langle \chi_\mu | \chi_\nu \rangle, \quad (4.56)$$

and E_{pq} is a diagonal matrix of the orbital energies ε_p ,

$$E_{pq}^\sigma = \varepsilon_p^\sigma \delta_{p,q} \quad (4.57)$$

Since \mathbf{F}^σ is constructed from the MO coefficients [i.e. $\mathbf{F}^\sigma = \mathbf{F}^\sigma(\mathbf{c}^\alpha, \mathbf{c}^\beta)$], Eq. (4.54) must be solved iteratively. A Hartree-Fock calculation begins with an initial guess for the orbital coefficients $C_{p,\mu}^\sigma = c_{p,\mu}^\sigma$. \mathbf{F}^σ is constructed from these coefficients and Eq. (4.54) is solved to get a new set of orbital coefficients. The new set of orbitals is then used in the next iteration. This procedure continues until the energies and orbital coefficients remain constant from one iteration to the next. This technique is called the self-consistent field (SCF) procedure. It is represented schematically in Fig. 4.1

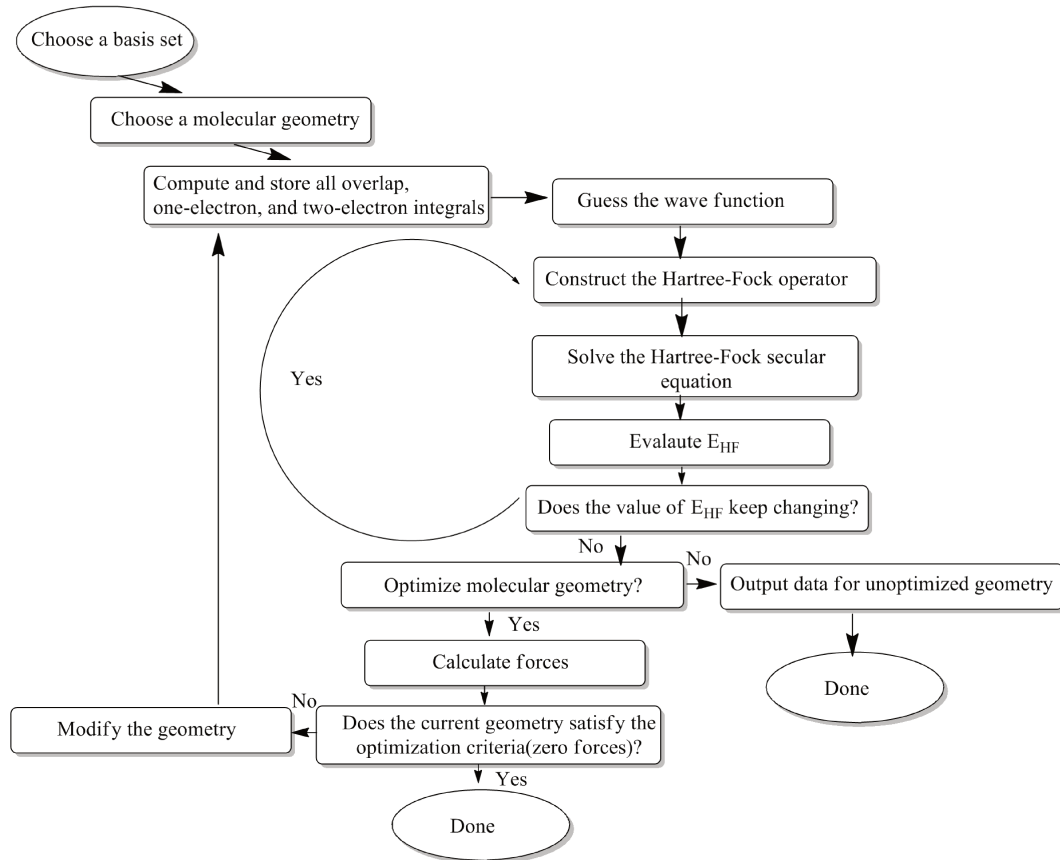


Figure 4.1 – Flow diagram for solving the HF equations.

4.2.3 Density-Functional Theory

4.2.3.1 The Thomas-Fermi Model

The Thomas-Fermi model is the earliest example of a density-functional theory. The total electronic energy is

$$E[n] = E_T[n] + E_V[n] + E_J[n] + E_{xc}[n] \quad (4.58)$$

The most difficult term in the electronic energy is the kinetic energy functional. The kinetic energy functional is based upon the uniform electron gas (UEG). The uniform electron gas is defined as N electrons in a cube of volume V with a uniform positive background charge adequate to make the system neutral. The uniform gas is then defined as the limit $V \rightarrow \infty$, $N \rightarrow \infty$, with the density $n = N/V$ remaining finite. Thus, it is completely defined by one variable, the electron density n [9, 10]. The Thomas-Fermi kinetic energy functional $E_T[n]$ for a molecule assumes that the kinetic energy density t at point \vec{r} in a molecule is the same as that in the UEG of density $n(\vec{r})$. This is an example of local density approximation. It can be shown [11, 12] that

$$\begin{aligned} E_T[n] &= \int t(n(r))n(r)d\vec{r} \\ &= \frac{3}{10}\left(\frac{3\pi^2}{2}\right)^{2/3} \int n^{5/3}(\vec{r})d\vec{r}. \end{aligned} \quad (4.59)$$

For a spin-polarized electron gas,

$$E_T[n_\alpha, n_\beta] = \frac{3}{10}(3\pi^2)^{2/3} \sum_\sigma \int n_\sigma^{5/3}(\vec{r})d\vec{r}. \quad (4.60)$$

For the system consisting of M nuclei fixed at $\{R_I\}$ with corresponding nuclear charges $\{Z_I\}$, the attraction energy of the electrons due to the nuclei can be expressed as,

$$E_V[n] = - \sum_{I=1,M} Z_I \int \frac{n(\vec{r})}{|\vec{r} - \vec{R}_I|} d\vec{r}. \quad (4.61)$$

The third term in the Thomas-Fermi approach deals with the coulomb energy of the electrons in their own field which is also really difficult to calculate. Here we assume that the electrons move independently (which they do not) and that each electron repels itself (which it does not). We can express the electron-repulsion energy functional as,

$$E_J[n] = \frac{1}{2} \int \int \frac{n(\vec{r}_1)n(\vec{r}_2)}{|\vec{r}_1 - \vec{r}_2|} d\vec{r}_1 d\vec{r}_2. \quad (4.62)$$

An additional term $E_{xc}[n]$ called the exchange-correlation energy corrects $E_J[n]$ to finally give us the exact coulomb energy.

4.2.3.2 First Hohenberg-Kohn Theorem

Hohenberg and Kohn were inspired by Thomas-Fermi theory which they sought to put on a more rigorous foundation. In 1964 [13], Hohenberg and Kohn formulated two famous theorems which define modern density functional theory. The first theorem, called the existence theorem, says that, “*The external potential $V_{ext}(\vec{r})$ is a unique functional of $n(\vec{r})$ up to a trivial additive constant*”. In other words, there is a one-to-one mapping between $V_{ext}(\vec{r})$ and the ground-state particle density $n(\vec{r})$. Given that $V_{ext}(\vec{r})$ thus determines \hat{H} up to an additive constant (i.e., up to a choice of energy zero), then it is seen that the full many particle ground state is a unique functional of $n(\vec{r})$ [1]. To prove this theorem, I follow the original paper [13]. Let us consider that we have two different external potentials $V_{ext}^{(1)}$ and $V_{ext}^{(2)}$ corresponding to the same *nondegenerate* ground state density $n(\vec{r})$, and seek a contradiction. The two different external potentials fix two different Hamiltonian operators $\hat{H}^{(1)}$ and $\hat{H}^{(2)}$. Each Hamiltonian operator is associated with specific ground-state wave functions $\Psi_0^{(1)}$ and $\Psi_0^{(2)}$ and their associated eigenvalues will be $E_0^{(1)}$ and $E_0^{(2)}$ respectively. Since $\Psi_0^{(1)}$ and $\Psi_0^{(2)}$ must differ by more than a simple phase factor, the variational principles tells us that,

$$E_0^{(1)} < \langle \Psi_0^{(2)} | \hat{H}^{(1)} | \Psi_0^{(2)} \rangle. \quad (4.63)$$

We can rewrite this expression as,

$$\begin{aligned} E_0^{(1)} &< \langle \Psi_0^{(2)} | \hat{H}^{(1)} - \hat{H}^{(2)} + \hat{H}^{(2)} | \Psi_0^{(2)} \rangle \\ &< \langle \Psi_0^{(2)} | \hat{H}^{(1)} - \hat{H}^{(2)} | \Psi_0^{(2)} \rangle + \langle \Psi_0^{(2)} | \hat{H}^{(2)} | \Psi_0^{(2)} \rangle \\ &< \langle \Psi_0^{(2)} | V_{ext}^{(1)} - V_{ext}^{(2)} | \Psi_0^{(2)} \rangle + E_0^{(2)} \end{aligned} \quad (4.64)$$

Because of the potentials $V_{ext}^{(1)}$ and $V_{ext}^{(2)}$ are one-electron multiplicative operators, we can rewrite the integral in the previous equation by using the ground-state density,

$$E_0^{(1)} < \int \left[V_{ext}^{(1)}(\vec{r}) - V_{ext}^{(2)}(\vec{r}) \right] n_0(\vec{r}) d\vec{r} + E_0^{(2)}. \quad (4.65)$$

We can use the same procedures to obtain,

$$E_0^{(2)} < \int \left[V_{ext}^{(2)}(\vec{r}) - V_{ext}^{(1)}(\vec{r}) \right] n_0(\vec{r}) d\vec{r} + E_0^{(1)}. \quad (4.66)$$

By adding the above two inequalities, we will get that

$$\begin{aligned} E_0^{(1)} + E_0^{(2)} &< \int \left[V_{ext}^{(2)}(\vec{r}) - V_{ext}^{(1)}(\vec{r}) \right] n_0(\vec{r}) d\vec{r} + \int \left[V_{ext}^{(1)}(\vec{r}) - V_{ext}^{(2)}(\vec{r}) \right] n_0(\vec{r}) d\vec{r} + E_0^{(2)} + E_0^{(1)} \\ &< \int \left[V_{ext}^{(2)}(\vec{r}) - V_{ext}^{(1)}(\vec{r}) + V_{ext}^{(1)}(\vec{r}) - V_{ext}^{(2)}(\vec{r}) \right] n_0(\vec{r}) d\vec{r} + E_0^{(2)} + E_0^{(1)} \\ &< E_0^{(2)} + E_0^{(1)}, \end{aligned} \quad (4.67)$$

which is obviously impossible (proof by contradiction). Therefore, different external potentials will always produce different densities.

4.2.3.3 Second Hohenberg-Kohn Theorem

The second theorem of Hohenberg and Kohn is a variational principle. It states that there is a universal functional

$$F_{HK}[n] = \min_{\Psi[n] \rightarrow n} \langle \Psi[n] | \hat{T} + \hat{V}_{ee} | \Psi[n] \rangle. \quad (4.68)$$

Here $n(\vec{r})$ is the trial density which is v -representable (i.e., comes from the ground-state wave function associated with some external potential) and fulfils the important boundary conditions, for example,

$$n(\vec{r}) \geq 0, \quad \int n(\vec{r}) d\vec{r} = N.$$

This functional may be used to obtain the lowest energy is by using the variational principle to get the exact ground-state density by minimization of $E_{V0}[n]$,

$$E_0 = \min_n E_{V0}[n], \quad (4.69)$$

where $E_{V0}[n]$ is,

$$E_{V0}[n] = F_{HK}[n] + \int V_{ext}(\vec{r}) n(\vec{r}) d\vec{r}. \quad (4.70)$$

4.2.3.4 Levy Constrained Search

The original proof of the second theorem of Hohenberg and Kohn is based on the assumption that all trial densities n are v -representable, meaning that the density

n comes from some external potential V . But not all the densities satisfying the conditions

$$n(\vec{r}) \geq 0, \int n(\vec{r}) d\vec{r} = N$$

have a corresponding potential [14, 15]. Without boundary condition, the variational principle,

$$E_0 \leq E_{V_0}[n], \quad (4.71)$$

is no longer valid. The proof can be corrected by using the Levy constrained search formulation [16, 15, 14]. Which gives a way around the issue of v -representability. Only N -representable densities are required—that is, densities which come from an anti-symmetric N -electron wave function. It can be shown that any n satisfying

$$n(\vec{r}) \geq 0, \quad (4.72)$$

$$\int n(\vec{r}) d\vec{r} = N, \quad (4.73)$$

$$\int |\nabla n^{1/2}|^2 d\vec{r} < \infty, \quad (4.74)$$

is N -representable [9]. The Levy constrained search formulation is an explicit construction of $E_{V_0}[n]$ in two steps: First, we search the subset of all the infinitely many antisymmetric wave functions Ψ that give a specific density n to find the wave function Ψ_{min} which generates the lowest energy for a given density. By using the universal Hohenberg and Kohn functional, the minimization of energy by the first step will look like,

$$F[n] = \min_{\Psi \rightarrow n} \langle \Psi | \hat{T} + \hat{V}_{ee} | \Psi \rangle \quad (4.75)$$

In the second step, we extend the search over all N -representable densities by lifting the constraint of a specific density in the first step. So the minimization of the energy will be,

$$E_0 = \min_{n \rightarrow N} \left(F[n] + \int n(\vec{r}) v_{ext}(\vec{r}) d\vec{r} \right) \quad (4.76)$$

The minimization to get the ground state density n_0 and the ground state energy E_0 by the two steps can be written as,

$$E_0 = \min_{n \rightarrow N} \left(\underbrace{\min_{\Psi \rightarrow n} \langle \Psi | \hat{T} + \hat{V}_{ee} | \Psi \rangle + \int n(\vec{r}) v_{Ne}(\vec{r}) d\vec{r}}_{E_{V_0}[n]} \right) \quad (4.77)$$

4.2.3.5 Kohn-Sham Formulation

In 1965 [17], Kohn and Sham realised that it is possible to find a system of N non-interacting electrons with the same ground-state density as that of N interacting electrons.

Kohn and Sham also showed that the total energy can be expressed as a functional of the exact ground state density

$$n(\vec{r}) = \sum_{i=1,N} |\psi_i(\vec{r})|^2 \quad (4.78)$$

where the ψ_i are the Kohn-Sham orbitals which are obtained variationally by minimising the energy,

$$E[n(\vec{r})] = E[\psi_1, \psi_2, \dots, \psi_N] = T_s[n] + E_{Ne}[n] + J[n] + E_{xc}[n], \quad (4.79)$$

subject to the orbital orthonormality constraint. Here $T_s[n]$ is the non-interacting kinetic energy,

$$T_s = -\frac{1}{2} \sum_{i=1,N} \langle \psi_i | \nabla^2 | \psi_i \rangle, \quad (4.80)$$

and $E_{Ne}[n]$ is the electron-nuclear attraction energy,

$$E_{Ne}[n] = - \sum_I \int \frac{Z_I n(\vec{r}_1)}{r_{1I}} d\vec{r}_1. \quad (4.81)$$

The E_{xc} is the exchange-correlation energy which has the terms that we must approximate,

$$E_{xc}[n] = T[n] - T_s[n] + V_{ee}[n] - J[n], \quad (4.82)$$

where $T[n]$ is the exact kinetic energy for the interacting system. Minimization of the total energy with respect to the orthonormal Kohn-Sham orbitals using the method of Lagrange multipliers,

$$\mathcal{L} = -\frac{1}{2} \sum_{i=1}^N \langle \psi_i | \nabla^2 | \psi_i \rangle + \int V_{ext}(\vec{r}) n(\vec{r}) d\vec{r} + V_{ee}[n] + E_{xc}[n] - \sum_{i=1}^N (\langle \psi_i | \psi_i \rangle - 1), \quad (4.83)$$

$$0 = \frac{\delta \mathcal{L}}{\delta \psi_i(\vec{r})}, \quad (4.84)$$

leads to the Kohn-Sham molecular orbital equation,

$$\hat{F}_{KS} \psi_i(\vec{r}) = \epsilon_i \psi_i(\vec{r}). \quad (4.85)$$

According to Kohn and Sham, this is the orbital Schrödinger equation for a system of noninteracting electrons. This means that the occupied orbitals must be successively filled from lowest to highest energy with no vacant orbitals intervening. This condition is sometimes called “non interacting v -representability.”

Evidently the Kohn-Sham density functional theory as a generalization of Hartree-Fock theory where the Hamiltonian was

$$\hat{F}_{HF} = -\frac{1}{2}\nabla^2 + v_{ext}(\vec{r}) + \int \frac{n(\vec{r}')}{|\vec{r} - \vec{r}'|} d\vec{r}' - \hat{k}. \quad (4.86)$$

In Kohn-Sham density functional theory,

$$\hat{F}_{KS} = -\frac{1}{2}\nabla^2 + v_{ext}(\vec{r}) + \int \frac{n(\vec{r}')}{|\vec{r} - \vec{r}'|} d\vec{r}' + v_{xc}(\vec{r}). \quad (4.87)$$

That is, the nonlocal integral operator $-\hat{k}$ has been replaced by the multiplicative operator $v_{xc}(\vec{r})$.

According to the Hohenberg-Kohn-Sham description, the exchange-correlation potential is the functional derivative of the exchange-correlation energy with respect to the density $n(\vec{r})$,

$$v_{xc}[n](\vec{r}) = \frac{\delta E_{xc}[n]}{\delta n(\vec{r})}. \quad (4.88)$$

Note that Kohn-Sham theory is exact for the exact functional E_{xc} , while Hartree-Fock theory is always approximate.

4.2.3.6 Some of the Different Types of Exchange-Correlation Approximations

Local Density Approximation As no practical exact form of the exchange-correlation energy is known, it must be approximated. The most commonly used approximation for the exchange-correlation functional is the local-density approximation (LDA),

$$E_{xc}^{LDA}[n] = \int \epsilon_{xc}(n(\vec{r}))n(\vec{r})d^3\vec{r}, \quad (4.89)$$

where $\epsilon_{xc}(n)$ is the exchange-correlation energy per particle of a homogeneous electron gas of charge density n . The general form of local-density approximation to include electron spin is the local spin-density approximation (LSDA),

$$E_{xc}^{LSDA}[n_{\uparrow}, n_{\downarrow}] = \int \epsilon_{xc}(n_{\uparrow}(\vec{r}), n_{\downarrow}(\vec{r}))n(\vec{r})d^3\vec{r}. \quad (4.90)$$

Global Hybrid Functionals Global hybrid functionals are advantageous for molecular density functional theory (DFT) applications, since they often give results near the experimental methods [1]. They incorporate ordinarily around 20% of Hartree-Fock (HF) exchange in addition to the traditional density functional exchange [18]. The achievement of global hybrid functionals can be ascribed to a halfway diminishment of the self-interaction error, without significantly diminishing the balance between exchange and correlation. The typical global hybrid functional is the B3LYP functional which has the the following form:

$$E_{xc}^{B3LYP} = E_x^{LSDA} + 0.2(E_x^{HF} - E_x^{LSDA}) + 0.72E_x^{B88} + 0.81E_c^{LYP} + 0.19E_c^{VWN}, \quad (4.91)$$

where E_x^{LSDA} is the exchange energy from the LSDA method, E_x^{HF} is the Hartree-Fock exchange energy, E^{B88} is the Becke's 1988 exchange potential generalized gradient approximation (GGA) [19], E_c^{LYP} is the Lee-Yang-Parr GGA correlation potential [20], and E_c^{VWN} is the the Vosko-Wilk-Nusair parametrization of the LDA correlation functional [21].

Sadly, introducing 20% Hartree-Fock exchange is inadequate to right such problems of approximate DFT functionals as the lack of a derivative discontinuity or the wrong asymptotic behaviour of the exchange potential. Rather than the right $1/r$ asymptotic behaviour of the hybrid exchange potential, one acquires a/r , where a is the amount of Hartree-Fock exchange in the hybrid. Asymptotically-corrected exchange potentials may enhance orbital energies and the state of orbitals, however they do not improve total energies [22].

Range-Separated Functionals An alternate methodology consists of treating the long-range part of the exchange-correlation energy and potential with a wave function method, by utilizing a suitable function to divide the Coulomb operator into short and long-range parts. This method, called range-separated or long-range corrected xc functionals was utilized by Savin and his collaborators [23, 24] to allay the aforementioned troubles. In particular, the idea is to divide the electron-electron interaction into short-range (sr) and long-range (lr) contributions

$$\frac{1}{r_{12}} = \underbrace{\frac{1 - \text{erf}(\omega r_{12})}{r_{12}}}_{sr} + \underbrace{\frac{\text{erf}(\omega r_{12})}{r_{12}}}_{lr}, \quad (4.92)$$

where the long range part is dealt with precisely, while the short-range part is dealt with using an altered pure density functional. In Eq. (4.92), the expression “erf”

gives the error function and ω is an empirical parameter, so

$$\text{erf}(\omega r_{12}) = \frac{2}{\sqrt{\pi}} \int_0^{\omega r_{12}} e^{-t^2} dt. \quad (4.93)$$

This approach may be seen as a special type of hybrid functional with settled weighting coefficients of density functional and HF exchange. Also, the error cancellation of density functionals for exchange and correlation is kept in the short range, while the self-interaction error is removed asymptotically through the long-range contribution.

In this work, a hybrid exchange-correlation named CAM-B3LYP is utilized. It consolidates the hybrid characteristics of B3LYP and long-range correction displayed by Tawada *et al.* [25]. The CAM-B3LYP functional involves 0.19 Hartree-Fock in addition to 0.81 Becke 1988 (B88) exchange interaction at short-range, and 0.65 HF in addition to 0.35 B88 exchange at long-range. The range separation uses the error function with parameter $\omega = 0.33$ [26].

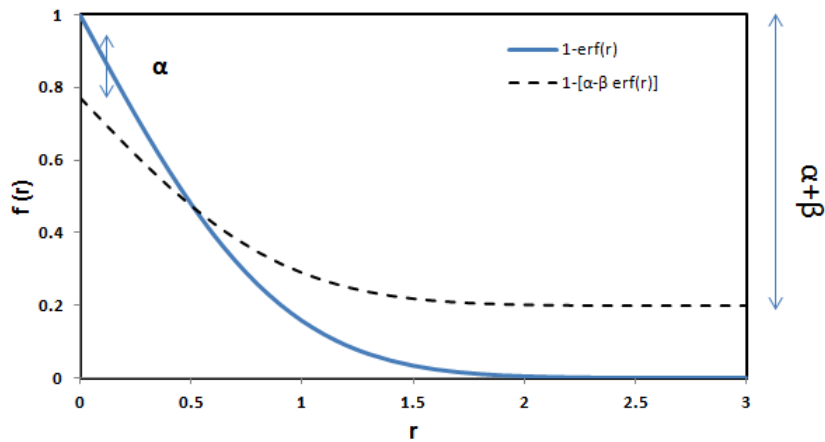


Figure 4.2 – Plots for $f(r) = 1 - \text{erf}(\omega r)$ and $f(r) = 1 - [\alpha + \beta \text{erf}(\omega r)]$. Redrawn based on a figure from ref. [26] values of $\alpha=0.19$ and $\beta=0.46$.

CAM-B3LYP generalizes the form of Eq. (4.92) using two extra parameters α and β as,

$$\frac{1}{r_{12}} = \underbrace{\frac{1 - [\alpha + \beta \cdot \text{erf}(\omega r_{12})]}{r_{12}}}_{sr} + \underbrace{\frac{\alpha + \beta \cdot \text{erf}(\omega r_{12})}{r_{12}}}_{lr}, \quad (4.94)$$

the parameter α enables us to merge the HF exchange contribution over the entire

range by a component of α , and the parameter β enables us to merge the DFT counterpart over the entire range by a component of $1-(\alpha+\beta)$. Fig. 4.2 plots the two functions, Eqs. (4.92) and (4.94). Yanai and *et al.* noticed that the generally-utilized hybrid functional B3LYP [27] is CAM-B3LYP exchange [Eq. (4.92)] but with $\alpha = 0.2$ and $\beta=0$ for the blending of Slater exchange E_X^{Slater} and the HF exchange E_X^{HF} . i.e.,

$$E_x^{B3} = (1 - \alpha)E_x^{LDA} + \alpha E_x^{HF} + E_x^{B88}. \quad (4.95)$$

4.2.4 Density-Functional Tight Binding

In chemistry, *ab initio* methods refer to (usually) Hartree-Fock-based electronic structure methods such as CI, MBPT, ect. —including CCSD(T), the famous “gold standard” of quantum chemistry. There are only 3 empirical parameters namely \hbar , m_e , and e . *Ab initio* calculations are accurate but computational resource intensive. DFT is a largely successful attempt to extend *ab initio* accuracy to treat larger or other wise more complex systems than would be possible with *ab initio* methods. Density functionals often contain additional fitted parameters (typically 3-12) which are supposed to be valid for the entire periodic table. Semiempirical methods provide a quantum mechanical approach which aims at being able to treat still larger and more complicated systems, albeit at the cost of losing some accuracy. Typical semiempirical methods gain efficiency by (i) treating only valence electrons, (ii) neglecting all but two-center integrals. Accuracy is maintained by using several fitting parameters per atom. Still larger systems may be treated by even more approximate methods such as molecular mechanics, but then quantum mechanics is lost and replaced by classical mechanics. A recent Nobel prize in chemistry was awarded for work on multiscale modeling which seeks appropriate combinations of these various methods to treat very large systems while maintaining accuracy for critical parts of system.

This thesis makes heavy use of the density-functional tight binding (DFTB) semiempirical method. DFTB is parameterized to behave as nearly as possible like DFT.

We can consider it to be a non-orthogonal tight-binding method parameterized from DFT. Its parameters for 2-center electron repulsion integrals are calculated from DFT [28]. A large number of applications have been reported showing its usefulness:

1. DFTB is mainly used to calculate large systems [29, 30].

2. It is possible to use DFTB to study systems which are too large to be treated by DFT [31].
3. While DFT is limited to only a few systems, DFTB can be used to gather statistics and trends from structural families. It can be used also for pre-screening of systems for subsequent DFT calculations [32].
4. Also DFTB may be useful for learning and teaching by running it on a laptop computer for discovering chemical bonding or realistic molecular wavefunctions [33].

The DFTB energy expression may be written as

$$E = E_{BS} + E_{coul} + E_{rep}, \quad (4.96)$$

where E_{BS} is the band-structure energy, E_{coul} is the coulomb interaction, and E_{rep} is the repulsive energy. Each of these terms is a semi-empirical expression which is fit to a well-defined part of the DFT energy expression. Over time DFTB has developed its own Jacob's Ladder of approximations (see Fig. 4.3). I will discuss each rung of the ladder in ascending order. There are now also variations in how different groups choose to handle the details of each rung which are beyond the scope of the present section. In the original form of DFTB (DFTB 0), $E_{coul} = 0$ and the calculation is noniterative. The calculation closely resembles what a solid-state physicist would call a tight-binding calculation and a chemist would call an extended Hückel calculation. As the band-structure energy is just the sum of the energies of the occupied orbitals,

$$E_{BS} = \sum_i n_i \epsilon_i. \quad (4.97)$$

(n_i is the occupation number of the i th orbital), then we must set up and solve an orbital Schrödinger equation

$$\mathbf{H}^0 \vec{C}_i = \epsilon_i \mathbf{S} \vec{C}_i, \quad (4.98)$$

where the valence wave functions have been expanded in a minimum basis of atomic orbitals

$$\psi_i(\vec{r}) = \sum_{\mu} \chi_{\mu}(\vec{r}) c_{\mu i}. \quad (4.99)$$

Unlike DFT, these atomic orbitals must be the solution of the Kohn-Sham equation for atom. The DFT expression for the Hamiltonian matrix element is

$$H_{\mu\nu} = \langle \chi_{\mu} | \hat{h}_c + V_H[n] + V_{xc}[n] | \chi_{\nu} \rangle. \quad (4.100)$$

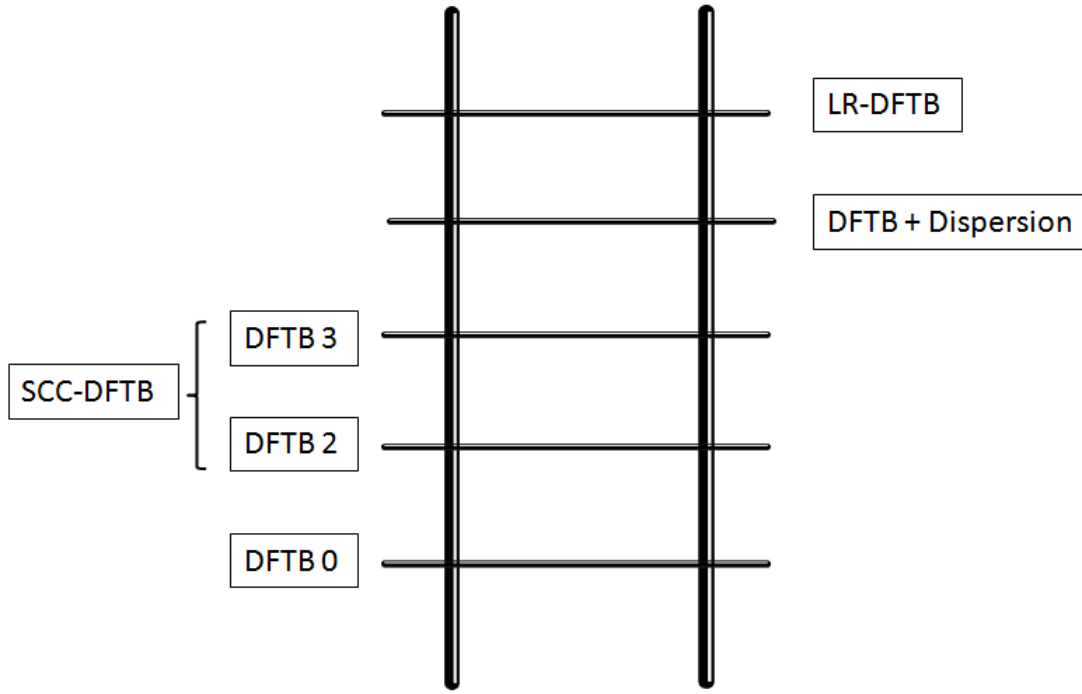


Figure 4.3 – Jacob's ladder of DFTB. DFTB 0 is the original noniterative version without self-consistent charges (SCC). DFTB 2 treats SCC to second order while DFTB 3 treats third order .

where

$$\hat{h}_c = -\frac{1}{2}\nabla^2 + V_{ext} \quad (4.101)$$

is the core hamiltonian and the external potential includes attraction to the ionic cores (assumed frozen). The density n is the density of only the valence electrons. In DFTB 0, n is taken as the sum over the undeformed atomic densities

$$n_0 = \sum_I^{atoms} n_0^I. \quad (4.102)$$

This gives

$$H_{\mu\nu}^0 = \langle \chi_\mu | \hat{h}_c + V_H[n_0] + V_{xc}[n_0] | \chi_\nu \rangle. \quad (4.103)$$

Since we wish to restrict our selves to the calculation of only two-center terms, we will need to make approximations. In extended Hückel,

$$H_{\mu\nu}^0 = K S_{\mu\nu} \left(\frac{H_{\mu\mu}^0 + H_{\nu\nu}^0}{2} \right). \quad (4.104)$$

where $K=1.7$ is a fitting factor. DFTB 0 is more sophisticated. In one formulation,

it is assumed that

$$V_{xc}[n_0] = \sum_I^{atoms} V_{xc}[n_0^I]. \quad (4.105)$$

(In another formulation, the assumption is $V_{xc}[n_0] = \sum_I^{atoms} V_{xc}^I[n_0]$.) Then

$$H_{\mu\nu}^0 = \sum_I^{atoms} \langle \chi_\mu | \hat{h}_c + V_H[n_0^I] + V_{xc}[n_0^I] | \chi_\nu \rangle. \quad (4.106)$$

and three-center terms are avoided by dropping all terms $\langle \chi_\mu | V_H[n_0^I] + V_{xc}[n_0^I] | \chi_\nu \rangle$ unless at least one of the atomic orbitals χ_μ or χ_ν is on atom I .

The total energy in DFTB 0 is the sum of E_{BS} and E_{rep} . The DFT quantity approximated by the DFTB 0 repulsive energy is

$$E_{rep} = E_{II} - \frac{1}{2} \int V_H[n_0](\vec{r}) n_0(\vec{r}) d\vec{r} + E_{xc}[n_0] - \int V_{xc}[n_0](\vec{r}) n_0(\vec{r}) d\vec{r}, \quad (4.107)$$

where E_{II} is the repulsion energy between the atomic cores. The first two terms $E_{II} - \frac{1}{2} \int V_H[n_0](\vec{r}) n_0(\vec{r}) d\vec{r}$ only involve two-centers at a time. The next two terms may be approximated as $\sum_{I,J}^{atoms} \int (E_{xc}[n_0^I](\vec{r}) - V_{xc}[n_0^I](\vec{r})) n_0^J(\vec{r}) d\vec{r}$. However, practical calculations simply assume that

$$E_{rep} = \sum_{I,J}^{atoms} V_{rep}^{I,J}(R_{I,J}) \quad (4.108)$$

and tabulated the functions $V_{rep}^{I,J}(R_{I,J})$ as a function of interatomic distances for different pairs of atoms. In reality $V_{rep}^{I,J}(R_{I,J})$ will differ a bit between different molecular environments, so the tabulated parameters represent a practical compromise.

The higher rungs of the DFTB Jacob's ladder add in self-consistent charge (SCC) correction E_{coul} . The density is written as

$$n(\vec{r}) = n_0(\vec{r}) + \delta n(\vec{r}) \quad (4.109)$$

and the energy is expanded to second (DFTB 2) or third (DFTB 3) order to obtain a non-zero E_{coul} . Only DFTB 2 is described here. The DFTB 2 term to be approximated is

$$E_{coul} = \frac{1}{2} \int \int \left(f_{xc}[n_0](\vec{r}, \vec{r}') + \frac{1}{|\vec{r} - \vec{r}'|} \right) \delta n(\vec{r}) \times \delta n(\vec{r}') d\vec{r} d\vec{r}'. \quad (4.110)$$

where

$$f_{xc}[n_0](\vec{r}, \vec{r}') = \frac{\delta^2 E_{xc}[n]}{\delta n(\vec{r}) \delta n(\vec{r}')} \Big|_{n=n_0} \quad (4.111)$$

known as the xc-kernel. If we make the approximation

$$f_{xc}[n_0](\vec{r}, \vec{r}') = \sum_I^{atoms} f_{xc}[n_0^I](\vec{r}, \vec{r}') \quad (4.112)$$

and neglect three-center terms then

$$\begin{aligned} E_{coul} &= \sum_{I,J}^{atoms} \frac{1}{2} \int \int \left[f_{xc}[n_0^K](\vec{r}, \vec{r}') (\delta_{K,I} + \delta_{K,J} - \delta_{I,J}) + \frac{1}{|\vec{r} - \vec{r}'|} \right] \delta n^I(\vec{r}) \times \delta n^J(\vec{r}') d\vec{r} d\vec{r}'. \\ &= \sum_{I,J}^{atoms} E_{coul}^{IJ} \end{aligned} \quad (4.113)$$

In practice, in DFTB, δn^I is replaced by the induced Mulliken charges

$$\Delta q_I = \sum_{\mu \in I} \sum_{\nu} S_{\mu\nu} \left(\sum_i c_{\nu i} n_i c_{\mu i}^* \right) \quad (4.114)$$

and

$$E_{coul}^{I,J} = \begin{cases} \frac{1}{2} U_H^I (\Delta q_I)^2; & I = J \\ \frac{1}{2} \Delta q_I \Delta q_J \gamma_{I,J}(R_{I,J}); & I \neq J \end{cases} \quad (4.115)$$

The Hubbard parameter U_H^I may be identified as the chemical hardness of atom I . The γ_{IJ} is a distance-dependant charge-charge interaction function.

The DFTB 2 method is a self-consistent problem with energy expression

$$E = \sum_{\mu\nu} H_{\mu\nu}^0 \left(\sum_i c_{\nu i} n_i c_{\mu i}^* \right) + \frac{1}{2} \sum_{I,J} \Delta q_I \Delta q_J \gamma_{I,J}(R_{I,J}) + \sum_{I < J} V_{rep}^{I,J}(R_{I,J}). \quad (4.116)$$

Minimization subject to the orbital normality constraint

$$L = E - \sum_i \epsilon_i \sum_{\mu,\nu} c_{\mu i}^* S_{\mu\nu} c_{\nu i} \quad (4.117)$$

$$0 = \frac{\partial L}{\partial c_{\mu i}^*} \quad (4.118)$$

gives

$$\sum_{\nu} \left(H_{\mu\nu}^0 + \sum_{I,J} \Delta q_I \gamma_{I,J} \sum_{\kappa \in J} S_{\kappa\mu} \right) c_{\nu i} = \epsilon_i \sum_{\nu} s_{\mu\nu} c_{\nu i}. \quad (4.119)$$

Thus the DFTB 2 orbital hamiltonian is

$$H_{\mu\nu}^{DFTB2} = H_{\mu\nu}^0 + \sum_{I,J} \Delta q_I \gamma_{I,J} \sum_{\kappa \in J} S_{\kappa\mu}. \quad (4.120)$$

Solving the orbital equation self-consistently and inserting into the energy expression provides us with a complete electronic structure method. The third-order method DFTB 3 is similar but the basic formulae are more complicated.

4.3 Excited State Calculation

4.3.1 Second Quantization

First quantization of quantum mechanics is when observables are represented by operators and states by functions. In the second quantization formulation, operators are expressed in terms of products of creation and annihilation operators. Operators (e.g., the Hamiltonian) and wavefunctions are described by a single set of elementary creation and annihilation operators. The creation operator is defined by

$$\hat{a}_i^\dagger |ijkl\dots\rangle = |ijkl\dots i\rangle, \quad (4.121)$$

in terms of determinants of spin orbitals. We thus have that

$$\hat{a}_i^\dagger : H_N \rightarrow H_{N+1} \quad (4.122)$$

The adjoint, \hat{a}_i , of the creation operator, \hat{a}_i^\dagger , is the corresponding annihilation operator,

$$\hat{a}_i : H_N \rightarrow H_{N-1} \quad (4.123)$$

where H_N is the Hilbert space of N -electron wavefunctions. The following index convention is used:

$$\underbrace{abc\dots gh}_{\text{virtual}} \quad | \quad \underbrace{ijklmn}_{\text{occupied}} \quad | \quad \underbrace{opq\dots xyz}_{\text{unspecified occupancy}} \quad (4.124)$$

In second quantization, one electron operators are written as,

$$\hat{H} = \sum \langle p | \hat{h} | q \rangle p^\dagger q \quad (4.125)$$

$$\hat{H} = \sum h_{pq} p^\dagger q. \quad (4.126)$$

If we want to include the electron repulsions, then the electron hamiltonian operator then will be,

$$\hat{H} = \sum \langle p | \hat{h} | q \rangle p^\dagger q + \frac{1}{4} \sum \langle pq || rs \rangle p^\dagger q^\dagger sr \quad (4.127)$$

$$\hat{H} = \sum \langle p | \hat{h} | q \rangle p^\dagger q + \frac{1}{2} \sum (pr || qs) p^\dagger q^\dagger sr \quad (4.128)$$

where

$$\begin{aligned} \langle pq || rs \rangle &= \int \psi_p^*(1) \psi_q^*(2) \frac{1}{r_{12}} \psi_r(1) \psi_s(2) d1 d2 \\ &- \int \psi_p^*(1) \psi_q^*(2) \frac{1}{r_{12}} \psi_s(1) \psi_r(2) d1 d2 \\ &= (pr || qs) - (ps || qr) \end{aligned} \quad (4.129)$$

4.3.2 Configuration Interaction Singles (CIS)

The ground state wave function can be represented by single determinant of the occupied orbitals (physical vacuum),

$$|\Psi_0\rangle = |\Phi\rangle. \quad (4.130)$$

The excited state wave function and the energy of the excited state are represented as,

$$|\Psi_I\rangle = \sum |\Phi_i^a\rangle C_{ia}^I = \sum a^\dagger_i |\Phi\rangle C_{ia}^I, \quad (4.131)$$

$$\hat{H}|\Phi_i\rangle = E_I|\Phi\rangle. \quad (4.132)$$

The coefficients and excitation energies are obtained in the Tamm-Dancoff approximation by solving an eigenvalue problem,

$$\mathbf{A} \vec{C}_I = \underbrace{(E_I - E_0)}_{\hbar\omega_I = \omega_I} \vec{C}_I \quad (4.133)$$

$$\sum_{jb} \langle \Phi_i^a | \hat{A} | \Phi_j^b \rangle C_{jb}^I = \omega_I \underbrace{\sum \langle \Phi_i^a | \Phi_j^b \rangle C_{jb}^I}_{C_{ia}^I}. \quad (4.134)$$

Where,

$$\omega_I = E_I - E_0, \quad (4.135)$$

and

$$\mathbf{A} = \mathbf{H} - E_0 \mathbf{1}. \quad (4.136)$$

Since

$$\langle \Phi_i^a | \hat{H} | \Phi_j^b \rangle = \mathbf{A}_{ia,jb} + \underbrace{\langle \Phi | \hat{H} | \Phi \rangle}_{E_0} \delta_{ij} \delta_{ab}, \quad (4.137)$$

in the absence of electron repulsions,

$$\mathbf{A}_{ia,jb} = h_{ab} \delta_{ij} - h_{ji} \delta_{ab}. \quad (4.138)$$

So its eigenvalues are the excitation energies which, at this level, are just differences between occupied and unoccupied energy levels. When electron repulsions are included, then

$$\mathbf{A}_{ia,jb} = \delta_{ij} \delta_{ab} (\epsilon_a - \epsilon_i) + (jb||ai) - (ab||ji). \quad (4.139)$$

4.3.3 Time-Dependent Density Functional Theory

In linear response time-dependent density functional LR-TD-DFT, Casida's equations [34] are used to calculate the excitation energies

$$\begin{bmatrix} \mathcal{A}(\omega) & \mathcal{B}(\omega) \\ \mathcal{B}^*(\omega) & \mathcal{A}^*(\omega) \end{bmatrix} \begin{bmatrix} \vec{X}(\omega) \\ \vec{Y}(\omega) \end{bmatrix} = \omega \begin{bmatrix} \mathbf{1} & \mathbf{0} \\ \mathbf{0} & -\mathbf{1} \end{bmatrix} \begin{bmatrix} \vec{X}(\omega) \\ \vec{Y}(\omega) \end{bmatrix} \quad (4.140)$$

Here

$$\mathcal{A}_{ia\sigma,jb\tau}(\omega) = \delta_{\sigma,\tau} \delta_{i,j} \delta_{a,b} (\epsilon_{a\sigma} - \epsilon_{i\tau}) + \mathbf{K}_{ia\sigma,bj\tau}(\omega), \quad (4.141)$$

$$\mathcal{B}_{ia\sigma,jb\tau}(\omega) = \mathbf{K}_{ia\sigma,jb\tau}(\omega), \quad (4.142)$$

where $\epsilon_{i\sigma}$ corresponds to the Kohn-Sham orbital energy, and the coupling matrix

$$\mathbf{K}_{ia\sigma,bj\tau}(\omega) = (ia | \delta_{\sigma,\tau} f_H + f_{xc}^{\sigma,\tau}(\omega) | bj), \quad (4.143)$$

where

$$f_{xc}^{\sigma,\tau}(\vec{r}_1, \vec{r}_2; \omega) = \int_{-\infty}^{+\infty} e^{i\omega(t_1-t_2)} \frac{\delta^2 A_{xc}[n \uparrow, n \downarrow]}{\delta n_{\sigma}(\vec{r}_1 t_1) \delta n_{\tau}(\vec{r}_2 t_2)} d(t_1 - t_2). \quad (4.144)$$

where A_{xc} is the exchange-correlation action functional which plays a role analogous to the exchange-correlation energy functional in the time-independent theory [34]. In the case of LR-TD-DFT the two-orbital two-electron model (TOTEM) will be,

$$\begin{bmatrix} \epsilon_a - \epsilon_i + (ia|f_H|ai) + (ia|f_{xc}^{\uparrow,\uparrow}|ai) & (ia|f_H + f_{xc}^{\uparrow,\downarrow}|ai) \\ (ia|f_H + f_{xc}^{\uparrow,\downarrow}|ai) & \epsilon_a - \epsilon_i + (ia|f_H|ai) + (ia|f_{xc}^{\downarrow,\downarrow}|ai) \end{bmatrix} \times \begin{bmatrix} C_i^a \\ C_i^{\bar{a}} \end{bmatrix} = \omega \begin{bmatrix} C_i^a \\ C_i^{\bar{a}} \end{bmatrix} \quad (4.145)$$

where $i \rightarrow a$ is $i \uparrow \rightarrow a \uparrow$ and $\bar{i} \rightarrow \bar{a}$ is $i \downarrow \rightarrow a \downarrow$. There are two solutions. The triplet solution is,

$$\begin{aligned} \omega_T &= \epsilon_a - \epsilon_i + (ia|f_{xc}^{\uparrow,\uparrow} - f_{xc}^{\uparrow,\downarrow}|ai) \\ C_i^{\bar{a}} &= -C_i^a = \frac{1}{\sqrt{2}}. \end{aligned} \quad (4.146)$$

the singlet solution is,

$$\begin{aligned} \omega_S &= \epsilon_a - \epsilon_i + 2(ia|f_H|ai) + (ia|f_{xc}^{\uparrow,\uparrow} + f_{xc}^{\uparrow,\downarrow}|ai) \\ C_i^{\bar{a}} &= +C_i^a = \frac{1}{\sqrt{2}}. \end{aligned} \quad (4.147)$$

4.3.4 Time-Dependent Density Functional Tight Binding

In the tight-binding approximation, Niehaus [35] calculated the excited states in the framework of linear-response time-dependent DFT by replacing transition densities $\phi_i(\mathbf{r})\phi_a(\mathbf{r})$ by transition charge q_A^{ia} to get the simplified coupling matrix,

$$\mathbf{K}_{ia,jb} \approx \sum_{A=1}^{N_{at}} \sum_{B=1}^{N_{at}} q_A^{ia} \gamma_{AB} q_B^{jb}, \quad (4.148)$$

where q_A^{ia} is the transition charges,

$$q_A^{ia} = \frac{1}{2} \sum_{\mu \in A} \sum_{\nu} (c_{\mu i} c_{\nu a} + c_{\nu i} c_{\mu a}) S_{\mu\nu}, \quad (4.149)$$

where $S_{\mu\nu}$ is the overlap matrix between the atomic orbitals μ and ν and $c_{\mu i}$ is the coefficient of the atomic orbital μ in the molecular orbital i . In the same manner, the transition dipoles between Kohn-Sham (KS) orbitals are reduced to sums over transition charges on different atoms,

$$\langle i|\vec{r}|a\rangle \approx \sum_A \vec{R}_A q_A^{ia}. \quad (4.150)$$

In the TDDFTB, the matrix elements of \mathcal{A} and \mathcal{B} are,

$$\mathcal{A}_{ia,jb}(\omega) = \delta_{i,j}\delta_{a,b}(\varepsilon_a - \varepsilon_i) + 2\mathbf{K}_{ia,bj}(\omega), \quad (4.151)$$

$$\mathcal{B}_{ia,jb}(\omega) = 2\mathbf{K}_{ia,jb}(\omega), \quad (4.152)$$

Bibliography

- [1] W. Koch and M. C. Holthausen, *A Chemist's Guide to Density Functional theory.*, WILEY-VCH, New York, 2001. pages 52, 63, 68, 305
- [2] E. Schrödinger, *An Undulatory Theory of the Mechanics of Atoms And Molecules.*, Physical Review **28**, 1049 (1926). pages 52, 54
- [3] F. C. LOZANO, *Photochemistry from Density-Functional Theory.*, PhD thesis, UNIVERSITY JOSEPH FOURIER - GRENOBLE 1, 2007. pages 52
- [4] C. J. Cramer, *Essentials of Computational Chemistry Theories and Models*, John Wiley & Sons Inc., 2004. pages 53
- [5] M. Born and J. R. Oppenheimer, *Zur Quantentheorie der Molekeln.*, Ann. Phys. **84**, 457 (1927). pages 55
- [6] A. Szabo and N. Ostlund, *Modern Quantum Chemistry: Introduction to Advanced Electronic Structure Theory.*, McGraw-Hill Inc., New York, 1989. pages 55, 56, 57, 58
- [7] V. Fock, *Näherungsmethode zur Lösung des quanten-mechanischen Mehrkörper-probleme.*, Physik **61**, 126 (1930). pages 58
- [8] C. C. J. Roothaan, *New Developments in Molecular Orbital Theory.*, Phys. Rev. **23**, 69 (1951). pages 60
- [9] R. G. Parr and W. Yang, *Density-Functional Theory of Atoms and Molecules.*, Oxford University Press, Oxford, 1989. pages 62, 65, 90, 159, 231
- [10] R. I. G. Hughes, *Theoretical Practice: the Bohm-Pines Quartet.*, Perspectives on Science **14**, 457 (2006). pages 62
- [11] L. H. Thomas, *The calculation of atomic fields.*, Proc. Camb. Phil. Soc. **23**, 542 (1927). pages 62
- [12] E. Fermi, *Un Metodo Statistico per la Determinazione di alcune Prioprieta dell Atomo.*, Rend. Accad. Naz. Lincei **6**, 602 (1927). pages 62

- [13] P. Hohenberg and W. Kohn, [Inhomogeneous electron gas.](#), Phys. Rev. **136**, B864 (1964). pages 63, 94, 231
- [14] E. H. Lieb., [Density Functionals for Coulomb systems.](#), MIT Press, Cambridge, 1982. pages 65
- [15] M. Levy., [Electron densities in search of hamiltonians.](#), Phys. Rev. A. **26**, 1200 (1982). pages 65
- [16] M. Levy., [Universal variational functionals of electron densities, first-order density matrices, and natural spin-orbitals and solution of the v-representability problem.](#), Proc. Natl. Acad. Sci. USA **76**, 6062 (1979). pages 65
- [17] W. Kohn and L. J. Sham, [Self-consistent equations including exchange and correlation effects.](#), Phys. Rev. **140**, A1133 (1965). pages 66, 94, 159, 164, 231
- [18] A. D. Becke, [A new mixing of Hartree-Fock and local density-functional theories.](#), J. Chem. Phys. **98**, 1372 (1993). pages 68
- [19] A. D. Becke, [Density-functional exchange-energy approximation with correct asymptotic behavior.](#), Phys. Rev. A **38**, 3098 (1988). pages 68
- [20] C. Lee, W. Yang, and R. G. Parr, [Development of the Colle-Salvetti correlation-energy formula into a functional of the electron density.](#), Phys. Rev. B **37**, 785 (1988). pages 68, 161, 240
- [21] S. H. Vosko, L. Wilk, and M. Nusair, [Accurate spin-dependent electron liquid correlation energies for local spin density calculations: a critical analysis.](#), Can. J. Phys. **58**, 1200 (1980). pages 68, 100, 161
- [22] I. Gerber and J. Ángyán, [Hybrid functional with separated range.](#), Chemical Physics Letters **415**, 100 (2005). pages 68
- [23] T. Leininger, H. Stoll, H.-J. Werner, and A. Savin, [Combining long-range configuration interaction with short-range density functionals .](#), Chem. Phys. Lett. **275**, 151 (1997). pages 68
- [24] A. Savin, [On degeneracy, near-degeneracy and density functional theory.](#) , in *In Recent Developments and Applications of Modern Density Functional Theory. On degeneracy, near-degeneracy and density functional theory.*, edited by J. Seminario, volume 4 of 4, chapter 9, page 327, Elsevier, Amsterdam, 1 edition, 1996, Theoretical and Computational Chemistry. pages 68
- [25] Y. Tawada, T. Tsuneda, S. Yanagisawa, T. Yanai, and K. Hirao, [A long-range-corrected time-dependent density functional theory.](#), J Chem Phys. **120**, 8425 (2004). pages 69

- [26] T. Yanai, D. P. Tew, and N. C. Handy, [A new hybrid exchange-correlation functional using the Coulomb-attenuating method \(CAM-B3LYP\)](#)., Chem. Phys. Lett. **393**, 51 (2004). pages 69, 310
- [27] A. D. Becke, [Density-functional thermochemistry. III. The role of exact exchange.](#), J. Chem. Phys. **98**, 5648 (1993). pages 70
- [28] A. F. Oliveira, G. Seifert, T. Heine, and H. A. Duarte, [Density-functional based tight-binding: an approximate DFT method.](#), J. Braz. Chem. Soc. **20**, 1193 (2009). pages 70
- [29] M. Elstner, T. Frauenheim, E. Kaxiras, G. Seifert, and S. Suhai, [A Self-Consistent Charge Density-Functional Based Tight-Binding Scheme for Large Biomolecules.](#), Physica Status Solidi (b) **217**, 357 (2000). pages 70
- [30] T. Frauenheim et al., [A Self-Consistent Charge Density-Functional Based Tight-Binding Method for Predictive Materials Simulations in Physics, Chemistry and Biology.](#), Physica Status Solidi (b) **217**, 41 (2000). pages 70
- [31] P. Koskinen, H. Häkkinen, B. Huber, B. von Issendorff, and M. Moseler, [Liquid-liquid Phase Coexistence in Gold Clusters: 2D or Not 2D?](#), Phys. Rev. Lett. **98**, 15701 (2007). pages 71
- [32] P. Koskinen, S. Malola, and H. Häkkinen, [Self-Passivating Edge Reconstructions of Graphen.](#), Phys. Rev. Lett. **101**, 115502 (2008). pages 71
- [33] P. Koskinen and V. Mäkinen, [Density-functional tight-binding for beginners.](#), Computational Materials Science **47**, 237 (2009). pages 71
- [34] M. Casida, [Time-dependent density-functional response theory for molecules](#), in *in Recent Advances in Density Functional Methods, Part I*, edited by D. Chong, page 155, World Scientific, Singapore, 1995. pages 77, 78
- [35] T. Niehaus et al., [Tight-binding approach to time-dependent density-functional response theory.](#), Phys. Rev. B. **63**, 085108 (2001). pages 78

Part II

Original Research

Chapter 5

Assessment of Density-Functional Tight-Binding Ionization Potentials and Electron Affinities of Molecules of Interest for Organic Solar Cells Against First-Principles *GW* Calculations

**Assessment of Density-Functional Tight-Binding Ionization Potentials
and Electron Affinities of Molecules of Interest for Organic Solar Cells
Against First-Principles *GW* Calculations**

**Ala Aldin M. H. M. Darghouth^{1,7}, Mark E. Casida^{1,*}, Walid Taouali²,
Kamel Alimi², Mathias P. Ljungberg^{3,4}, Peter Koval^{4,5}, Daniel
Sánchez-Portal^{4,5}, and Dietrich Foerster⁶**

¹ Département de Chimie Moléculaire (DCM, UMR CNRS/UJF 5250), Institut de
Chimie Moléculaire de Grenoble (ICMG, FR2607), Université Joseph Fourier
(Grenoble I), 301 rue de la Chimie, BP 53, F-38041 Grenoble Cedex 9, France;
E-mail: ala.darghouth@univ-grenoble-alpes.fr

² Unité de Recherche: Matériaux nouveaux et Dispositifs Électroniques Organiques
(UR 11ES55), Faculté des Sciences de Monastir, Université de Monastir, 5000
Monastir, Tunisia; E-mails: tawali_walid@yahoo.fr (W.T.); kamealimi@yahoo.fr
(K.A.)

³ Department of Physics, Phillips-University Marburg, Renthof 5, 35032 Marburg,
Germany; E-mail: mathias.ljungberg@gmail.com

⁴ Donostia International Physics Center (DIPC), Paseo Manuel de Lardizabal 4,
E-20018 San Sebastián, Spain; E-mails: koval.peter@gmail.com (P.K.);
sqbsapod@ehu.eus (D.S.-P.)

⁵ Centro de Física de Materiales CFM-MPC, Centro Mixto CSIC-UPV/EHU,
Paseo Manuel de Dadizabal 5, E-20018 San Sebastián, Spain

⁶ CPMOH/LOMA, Université de Bordeaux 1, 351 Cours de la Liberation, 33405
Talence, France; E-mail: dietrich.foerster@u-bordeaux.fr

⁷ Department of Chemistry , College of Science, University of Mosul, Mosul 41002,
Iraq

* Author to whom correspondence should be addressed; E-mail:
mark.casida@univ-grenoble-alpes.fr; Tel.: +33-04-76-63-56-28.

Academic Editors: Karlheinz and Agnes Nagy

*Received: 14 August 2015 / Accepted: 19 november 2015 / Published: 4 December
2015*

Abstract

Ionization potentials (IPs) and electron affinities (EAs) are important quantities
input into most models for calculating the open-circuit voltage (V_{oc}) of organic solar

cells. We assess the semi-empirical density-functional tight-binding (DFTB) with the third-order self-consistent charge (SCC) correction and the 3ob parameter set against experiment (for smaller molecules) and against first-principles *GW* calculations (for larger molecules of interest in organic electronics) for the calculation of IPs and EAs. Since *GW* calculations are relatively new for molecules of this size, we have also taken care to validate these calculations against experiment. As expected, DFTB is found to behave very much like density-functional theory (DFT) but with some loss of accuracy in predicting IPs and EAs. For small molecules best results were found with Δ SCF SCC-DFTB calculations for first IPs (good to ± 0.649 eV). When considering several IPs of the same molecule, it is convenient to use the negative of the orbital energies [which we refer to as Koopmans' theorem (KT) IPs] as an indication of trends. Linear regression analysis shows that KT SCC-DFTB IPs are nearly as accurate as Δ SCF SCC-DFTB eigenvalues (± 0.852 eV for first IPs but ± 0.706 eV for all the IPs considered here) for small molecules. For larger molecules, SCC-DFTB was also the ideal choice with IP/EA errors of $\pm 0.489/0.740$ eV from Δ SCF calculations and of $\pm 0.326/0.458$ eV from (KT) orbital energies. Interestingly the linear least squares fit for the KT IPs of the larger molecules also proves to have good predictive value for the lower energy KT IPs of smaller molecules, with significant deviations appearing only for IPs of 15-20 eV or larger. We believe that this quantitative analysis of errors in SCC-DFTB IPs and EAs may be of interest to other researchers interested in DFTB investigation of large and complex problems such as those encountered in organic electronics.

5.1 Introduction

Organic electronics is a rapidly-growing alternative to silicon-based electronics. In contrast to the latter which is well-enough understood [1] that fabless manufacturing may be used to for circuit design using modeling software such as SPICE [2] and then be outsourced to a semiconductor foundry for actual fabrication, organic electronics is a rapidly growing but much less well understood [3, 4, 5, 6, 7, 8] technology. One example is organic solar cells [9, 10, 11, 12] which offer the advantage of being relatively inexpensive to manufacture, flexible, and printable. The problem then is to be able to understand such devices well enough to be able to optimize and ultimately to engineer devices with them. This implies modeling and modeling of organic solar cells almost always requires ionization potentials (IPs) and electron affinities (EAs) as input. However the size of the molecules (or clusters of molecules) used in modeling organic solar cells rapidly makes first-principles cal-

culations prohibitive if not impossible. The semi-empirical density-functional tight binding (DFTB) method is highly attractive for overcoming size and complexity modeling constraints but it needs to be carefully assessed to determine the expected accuracy. In this paper, we complement previous efforts [13, 14] (Ref. [14] concerns implementing range-separated hybrids in DFTB[15, 16]) by assessing DFTB against accurate first-principles *GW* calculations [17, 18, 19] for the calculation of the IPs and EAs of medium-sized molecules.

Our particular interest is in modeling organic solar cells for which phenomenological models are reviewed in the Appendix. Ideally we would like to be able to extract parameters for these models from atomistic modeling. Given the size and complexity of minimum sized cluster models or unit cells of periodic models for a reasonable description of organic solar cells, it is clear that we need a highly efficient method. This is especially clear for such things as charge diffusion lengths and the size of depletion zones. But it is also true for the seemingly relatively straightforward calculation of IPs and EAs. Figure 5.1 gives minimum size examples of some typical molecules which are used in organic electronics. While some are “medium-sized” molecules which come within the range of *ab initio* calculations, many of the examples shown are just oligomers intended to represent the much longer polymers used in real organic solar cells. To make matters worse, charge transfer excitons are often present which are delocalized over several “medium-sized” molecules so that it is necessary to use clusters of molecules to have a physically-reasonable model. All of these reasons encourage us to look for an efficient and hopefully reasonably accurate semi-empirical approach. An appealing approach which may meet our needs is the density-functional tight-binding (DFTB) approach which will be briefly reviewed in the next section. To our knowledge, there is only one previous application of DFTB to organic solar cells [13]. That study focused on the problem of calculating charge transfer energies and made a comparison against experimental values.

We have chosen a different approach to assessing the accuracy of DFTB here by choosing to compare DFTB IPs and EAs against first-principles *GW* values. The advantage of this approach is that experimental IPs and EAs for large molecules are often extracted from condensed phase (bulk, thin film, or solution) measurements, introducing uncertainties when it comes to trying to extract molecular values. We will show that our *GW* calculations do indeed give good IPs when compared with experimental IPs for medium-sized molecules and we will then assume that this is also true for the other medium-sized molecules where molecular IPs are not available, and also for EAs. Taking the *GW* values as the “true values”, we then calculate error bars on the DFTB estimate of the *GW* values.

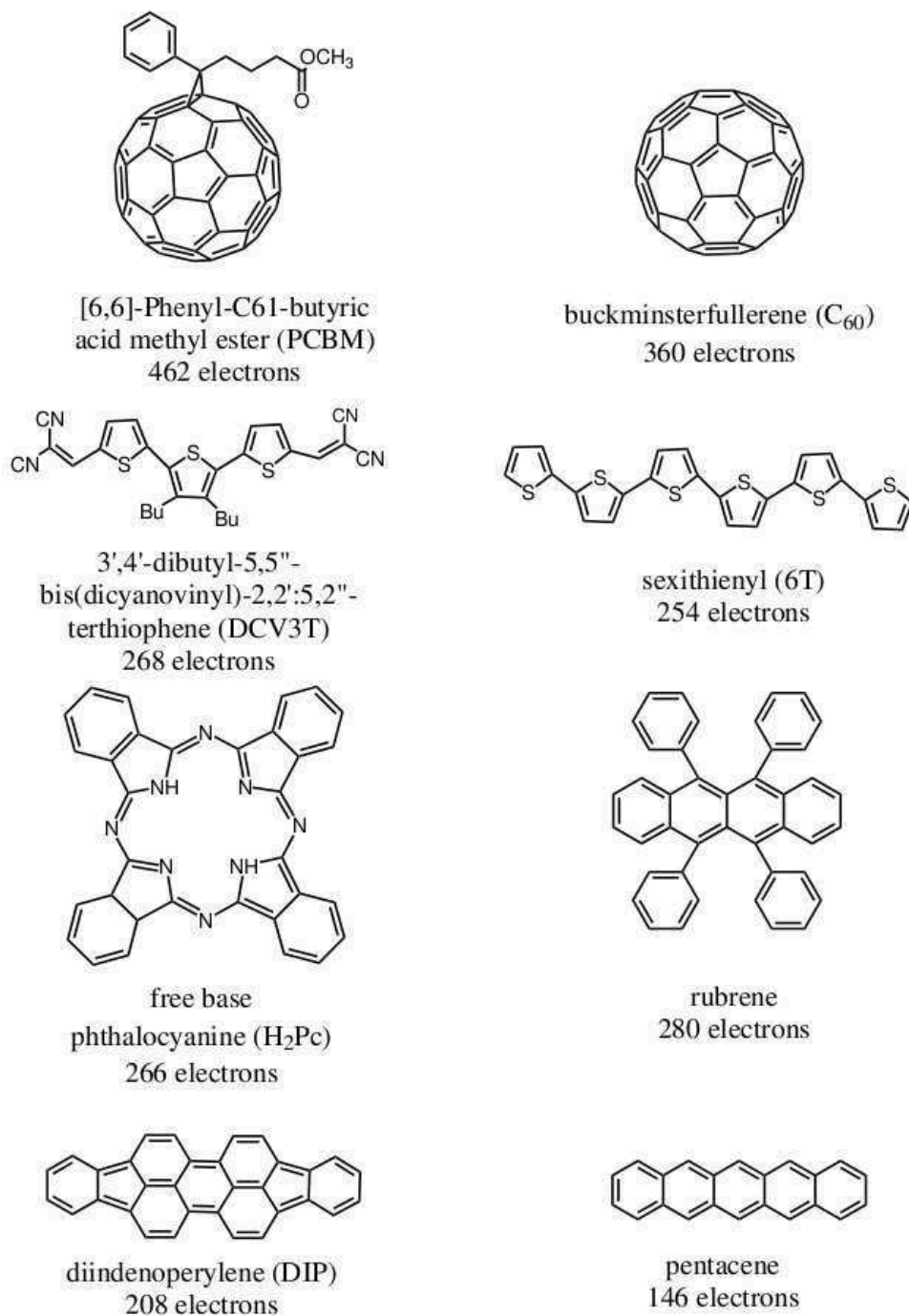


Figure 5.1 – Eight typical molecules that are often used as acceptors or donors in organic electronics.

The rest of this paper is organized as follows: The next section gives a brief review of the basic electronic structure methods used in this paper. Section 5.3 provides computational details. Section 5.4 goes on to describe and apply our analytical procedure for assessing the quality of DFTB IPs and EAs for the case of small molecules where good and theoretically well-understood experimental data is available. This gives us a useful first indication of how DFTB might work for the case which really interests us, namely for larger molecules of interest in organic electronics. Section 5.5 then extends our analysis to a set of medium-sized molecules typical of organic electronics. The assessment is complicated by the dearth of theoretically well-understood experimental data. We show that this dearth of experimental data may be compensated by high-quality *GW* calculations which agree well with available experimental data, and best when for gas phase data where the comparison is cleanest. We therefore use the *GW* results as our benchmark for evaluating DFTB IPs and EAs for medium-sized molecules. Section 5.6 provides a concluding discussion.

5.2 Theoretical Methods

While the Hartree-Fock (HF) approximation and density-functional theory (DFT) are now so familiar that they hardly seem worth discussing, this is less the case for *GW* Green's function calculations and for the DFTB semiempirical approximation to DFT. (HF is treated in most text books on quantum chemistry, such as Ref. [20] while DFT is treated in many of the recent text books. Nevertheless more detailed information regarding DFT may be found in Refs. [21, 22, 23, 24, 25].) These latter approaches will be briefly described in this section, with emphasis on calculating IPs and EAs. Unless otherwise specified, we will use Hartree atomic units ($\hbar = m_e = e = 1$). We will also use a reduced notation where $q = (\mathbf{r}_q, \sigma_q)$ represents the space and spin coordinates of particle q while $\mathbf{q} = (q, t_q)$ (bold face) is enriched to include time.

All approaches involve a molecular orbital (MO) equation,

$$\hat{f}(1; \epsilon_s) \psi_s(1) = \epsilon_s \psi_s(1). \quad (5.1)$$

The MO hamiltonian has the form,

$$\hat{f}(1; \omega) = \hat{h}_H(1) + \hat{\Sigma}_{xc}(1, \omega), \quad (5.2)$$

where \hat{h}_H is the Hartree hamiltonian. The frequency-dependence of the self-energy belongs to the *GW* method and does not apply for the HF approximation or for

Kohn-Sham DFT. The exchange-correlation (xc) “self-energy”, $\hat{\Sigma}_{xc}(1; \omega)$, is just the exchange integral operator $[-\hat{K}(1)]$ in HF and the functional derivative $v_{xc}(1) = \delta E_{xc}/\delta \rho(1)$ in pure DFT (we use ρ for the density). The MO equation is obtained in both cases from the variational minimization of the corresponding energy expressions. It is now also common practice to mix HF and pure DFT to make hybrid functionals such as the popular B3LYP functional.

One way to calculate the (first) IP, I , and (first) EA, A , in DFT, is to carry out self-consistent field calculations of the total energies for the N -electron system, the $(N - 1)$ -electron system, and the $(N + 1)$ -electron system. The Δ SCF IPs and EAs are then given respectively by,

$$\begin{aligned} I_S &= E_S^{(N-1)} - E_0^{(N)} \\ A_S &= E_0^{(N)} - E_S^{(N+1)}, \end{aligned} \quad (5.3)$$

where $E_0^{(N)}$ is the energy of the ground state of the N -electron molecule, $E_S^{(N-1)}$ is the energy of the same system with one electron removed in its S th electronic state, and $E_S^{(N+1)}$ is the energy of the same system but with one more electron in its S th excited state. Note that the concepts of IP and EA have thus been generalized beyond the usual definition where $S = 0$ (ground state). Together the IPs and EAs form a (generalized) band spectrum. Note also that S is a state label, as opposed to an MO label which would have been a small s . In the quasiparticle part of the band spectrum, each principle IP or EA corresponds to removing or adding an electron to an orbital s . In this case, S may be identified with s . The Δ SCF IPs and EAs may be estimated using Slater’s transition orbital method whereby the Δ SCF IP or EA is given by minus the orbital energy recalculated with half an electron removed from or added to the orbital. The Δ SCF method works for small molecules, but must inevitably fail for pure DFT [where the density functional depends only upon the density as in the local density approximation (LDA) or generalized gradient approximations (GGAs)] in the limit of a large system with delocalized hole and electron states because the change in the charge density is then insignificant [26]. Also the Δ SCF method is known to fail to give good IPs and EAs in the HF approximation because it includes only relaxation effects and not correlation effects which are known to partially cancel each other for outer valence ionization. In this case, it is better to use the Koopmans’ theorem IPs and EAs which are just the negative of the orbital energies. Such IPs and EAs are still approximate.

Green’s Function Methods Green’s function methods may be thought of as adding terms to the xc self-energy so that Koopmans’ theorem IPs and EAs become exact. That is, minus the energies of the occupied orbitals are the vertical IPs and minus the unoccupied orbital energies are the vertical EAs. More exactly, the MO equation has two types of solutions, namely the IP solutions and the EA solutions. For the IP solutions,

$$\begin{aligned}
 \epsilon_S &= E_0^{(N)} - E_S^{(N-1)} \\
 \psi_S(1) &= \langle \Psi_S^{(N-1)} | \hat{\psi}(1) | \Psi_0^{(N)} \rangle \\
 &= \sqrt{N} \int \left(\Psi_S^{(N-1)}(2, 3, \dots, N) \right)^* \\
 &\times \Psi_0^{(N)}(1, 2, 3, \dots, N) d2d3 \dots dN,
 \end{aligned} \tag{5.4}$$

while for the EA solutions,

$$\begin{aligned}
 \epsilon_S &= E_S^{(N+1)} - E_0^{(N)} \\
 \psi_S(1) &= \langle \Psi_0^{(N)} | \hat{\psi}(1) | \Psi_S^{(N+1)} \rangle \\
 &= \sqrt{N+1} \int \left(\Psi_0^{(N)}(2, 3, \dots, N+1) \right)^* \\
 &\times \Psi_S^{(N+1)}(1, 2, 3, \dots, N+1) d2d3 \dots d(N+1),
 \end{aligned} \tag{5.5}$$

where $\hat{\psi}(1)$ is an annihilation field operator in second-quantized notation, $\Psi_0^{(N)}$ is the ground-state N -electron wave function, $\Psi_S^{(N-1)}$ is the S th excited state of the $(N-1)$ -electron system, and $\Psi_S^{(N+1)}$ is the S th excited state of the $(N+1)$ -electron system. Note the use of capital indices referring to states rather than orbitals since there can be several different IP (or EA) states corresponding to the same orbital due to many-body effects. The MOs are then more properly described as Dyson amplitudes or as ion-molecule overlaps (both names are used). However for outer-valence ionization and the first few electron attachment states (i.e., in the so-called “quasiparticle regime”), a single state usually dominates and we may use lower case (i.e., orbital) notation. The definition of the Dyson amplitudes implies that they are not normalized to unity ($\langle \Psi_S | \Psi_S \rangle = P_S \neq 1$). The correct normalization (“pole strength”) of the MOs is obtained by

$$\langle \psi_S | \psi_S \rangle = \left[1 - \frac{\partial}{\partial \omega} \Re \frac{\langle \psi_S | \hat{\Sigma}_{xc}(\omega) | \psi_S \rangle}{\langle \psi_S | \psi_S \rangle} \Big|_{\omega=\epsilon_S} \right]^{-1}. \tag{5.6}$$

Note that any choice of normalization factor for MO may be used on the right-hand-side of the equation as the normalization factor cancels out on that side.

So far the Green’s function is exact, but also computationally useless until self-energy approximations are introduced. This is usually done in quantum chemistry by taking the HF approximation as the zero-order picture and expanding the self-energy in a perturbation series in the fluctuation potential (i.e., in the difference between the bare interelectronic coulomb repulsion and the HF self-consistent field). The lowest order corrections are second (GF2) and third (GF3) order because the first-order correction is zero by Brillouin’s theorem. However order-by-order expansion of IPs and EAs typically leads at best to slow oscillatory convergence. In the outer-valence Green’s function (OVGF) method, the GF2 and GF3 results are renormalized to obtain an infinite order estimate (Ref. [27] and appendix C of Ref. [28]). This is the conventional approach for most molecular Green’s function calculations. However there is another approach, due to Hedin [17], which is based upon an expansion in the dynamically screened interaction, $W(\mathbf{1}, \mathbf{2})$. The self-energy is essentially given by the Green’s function times the dynamically screened interaction,

$$\Sigma_{xc}(\mathbf{1}, \mathbf{2}) = iG(\mathbf{1}, \mathbf{2})W(\mathbf{1}^+, \mathbf{2}). \quad (5.7)$$

As both G and W are constructed from the solutions of the MO equation, the GW method should, in principle, be solved self-consistently. In practice, it is usually just applied in a one-step process (G_0W_0 approximation) after a DFT calculation and is hence dependent on the functional used in the original DFT calculation. After some early struggles [29, 30, 31, 32, 33, 34, 35], the GW approximation is also proving to be useful for molecules [36, 19]. The main advantage over the older OVGF molecular approach may be computational efficiency. This is particularly important as Green’s function calculations require larger basis sets than either HF or DFT. In the case of HF this is because of the neglect of electron correlation. In the case of DFT this is because it is easier to describe the charge density than the correlated wave function. In our work we take advantage of the efficiency of the dominant product algorithm for GW calculations [19].

It is interesting to note that the xc potential of pure DFT may be regarded as the best local approximation to the nonlocal xc self-energy of Green’s function theory [37] which is the basis of the popular target Kohn-Sham approximation in electron momentum spectroscopy [38, 39, 40]. In fact, experience has shown that Kohn-Sham orbitals are a reasonably good (apparently often better than HF) estimate of Dyson orbitals. Also, while Kohn-Sham “Koopmans’ theorem” IPs underestimate experimental IPs, they are in fact a better estimate than HF Koopmans’ theorem IPs, just

systematically down-shifted because of the particle-number derivative discontinuity effect on the long-range behavior of the xc-potential [41]. This is the molecular analogue of the solid-state scissor's operator correction to band energies [42, 43, 44]. We will return to this point again in the next section.

Density-Functional Tight Binding Having given a brief but hopefully adequately detailed discussion of the Green's function method so as to keep this paper relatively self-contained, let us now turn our attention to a brief review of the semi-empirical DFTB approximation to DFT. Although tight-binding theory has its roots in work by Erich Hückel [45, 46, 47], Slater and Koster [48], and Roald Hoffmann [49, 50, 51, 52], density-functional tight-binding (DFTB) [53, 54, 55, 56] also includes elements of modern semi-empirical theory [57, 58] and density-functional theory [59, 60]. As we will continue to use the same notation, our notation will be somewhat different than that typically used in the DFTB literature.

DFTB began as a way to extract an extended Hückel or tight-binding like approximation from DFT [53]. At the heart of DFTB is an assumption of separability which is actually exact for both the LDA and for GGAs of the xc energy. In DFTB we first separate the charge density into nonoverlapping atomic parts,

$$\rho(1) = \sum_I \rho_I(1). \quad (5.8)$$

The sum is over atoms I . It follows that the Hartree (H) potential is separable as,

$$v_H[\rho](1) = \sum_I v_H[\rho_I](1) = \sum_I v_H^I(1). \quad (5.9)$$

In the LDA and GGAs,

$$\begin{aligned} E_{xc}[\rho] &= \sum_I E_{xc}[\rho_I] = \sum_I E_{xc}^I \\ v_{xc}[\rho](1) &= \sum_I v_{xc}[\rho_I](1) = \sum_I v_{xc}^I(1). \end{aligned} \quad (5.10)$$

Hence the potential part of the Kohn-Sham operator is separable,

$$v_s(1) = \sum_I v_I(1) + \sum_I v_H^I(1) + \sum_I v_{xc}^I(1). \quad (5.11)$$

We may now make typical approximations familiar in semi-empirical theory in order

to avoid having to calculate more than two center integrals. Thus if atomic orbitals (AOs) μ and ν are both on atom I , then the matrix elements of the DFTB orbital hamiltonian

$$f_{\mu \in I, \nu \in I} = \delta_{\mu, \nu} \epsilon_{\mu}^I, \quad (5.12)$$

where ϵ_{μ}^I is the μ th AO of the free atom I . For off-diagonal elements where μ is on atom I and ν is on a different atom J then,

$$f_{\mu \in I, \nu \in J} = \langle \chi_{\mu \in I} | (\hat{t}_s + v_s^I + v_s^J) | \chi_{\nu \in J} \rangle, \quad (5.13)$$

where $\hat{t} = -(1/2)\nabla^2$. It is noteworthy that the “potential superposition approximation” of Eq. (5.13) is replaced by the “density superposition approximation,”

$$f_{\mu \in I, \nu \in J} = \langle \chi_{\mu \in I} | (\hat{t}_s + v_s^{I,J}) | \chi_{\nu \in J} \rangle, \quad (5.14)$$

with

$$v_s^{I,J} = v_I + v_J + v_H[\rho_I + \rho_J] + v_{xc}[\rho_I + \rho_J], \quad (5.15)$$

as significant differences in DFTB orbital energies may be expected between the two approaches and as the latter approach is that actually used in the DFTB program and parameters whose results are reported in this paper [14]. Whichever choice is used, the AOs χ_{μ} are typically calculated for a slightly confined atom to emulate the effect of an atom in a molecule. The overlap matrix,

$$s_{\mu \in I, \nu \in J} = \langle \chi_{\mu \in I} | \chi_{\nu \in J} \rangle, \quad (5.16)$$

is calculated exactly, as it only involves two-center integrals. No self-consistent procedure is then needed to set up and solve the matrix form of the Kohn-Sham equation in the AO basis set,

$$\mathbf{f} \vec{c}_r = \epsilon_i \mathbf{s} \vec{c}_r. \quad (5.17)$$

A very similar approximation is used to evaluate the so-called “repulsive energy”,

$$E_{rep} = \sum_{I < J} G_{I,J}. \quad (5.18)$$

The pair energies $G_{I,J}(R_{I,J})$ are obtained by fitting to a variation of E_{rep} as a function of the distance $R_{I,J}$ between atoms of the same types as I and J for a variety of molecules. This allows geometries to be optimized.

Notice that original form of DFTB *begins* with the orbital hamiltonian and *derives* the total energy from the orbital energies. However it is important to know how

to proceed the other way around—namely to know how to begin with the energy expression and derive the orbital hamiltonian. We can do this by *assuming* the repulsive energy to be independent of the density matrix,

$$\mathbf{P} = \sum_r \vec{c}_r n_r \vec{c}_r^\dagger, \quad (5.19)$$

and writing the so-called “band structure term” as,

$$E_{BS} = \text{tr}(\mathbf{P}\mathbf{f}). \quad (5.20)$$

Then,

$$f_{\nu,\mu} = \frac{\partial E}{\partial P_{\mu,\nu}} = \frac{\partial E_{BS}}{\partial P_{\mu,\nu}}, \quad (5.21)$$

is obtained in the usual way from the method of Lagrange multipliers.

A few years after the introduction of the original DFTB scheme, a self-consistent charge (SCC) term was added to the DFTB energy expression in order to describe charge rearrangement of atoms within molecules [61, 62]. In the original DFTB (DFTB2), the charge fluctuation term is only expanded up to second order in the variation of the atomic charge densities upon molecule formation. In recent years, the charge fluctuation term has been extended to third order to make DFTB3 [62]. We briefly describe the DFTB3 method here. The electronic energy expression thus gains what is known in DFTB as a charge fluctuation term (E_{coul}), so that

$$E = E_{BS} + E_{rep} + E_{coul}. \quad (5.22)$$

In the original DFTB (DFTB2), the charge fluctuation term is only expanded up to second order in the variation of the atomic charge densities upon molecule formation. In recent years, the charge fluctuation term has been extended to third order to make DFTB3 [62]. We briefly describe the DFTB3 method here. Thus,

$$\begin{aligned} E_{coul} &= E_{coul}^{(2)} + E_{coul}^{(3)} \\ E_{coul}^{(2)} &= \frac{1}{2} \int \int f_{Hxc}(1, 2) \delta\rho(1) \delta\rho(2) d1d2 \\ E_{coul}^{(3)} &= \frac{1}{6} \int \int \int g_{xc}(1, 2, 3) \delta\rho(1) \delta\rho(2) \delta\rho(3) d1d2d3, \end{aligned} \quad (5.23)$$

where the combined H and xc kernels are,

$$\begin{aligned} f_{Hxc}(1, 2) &= \frac{1}{r_{12}} + \frac{\delta E_{xc}}{\delta \rho(1) \delta \rho(2)} \\ g_{xc}(1, 2, 3) &= \frac{\delta^2 E_{xc}}{\delta \rho(1) \delta \rho(2) \delta \rho(3)}. \end{aligned} \quad (5.24)$$

By making use of the same separability assumptions as in the original DFTB, we arrive at,

$$\begin{aligned} E_{coul}^{(2)} &= \frac{1}{2} \sum_{I,J} \int \int f_{Hxc}^{I,J}(1, 2) \delta \rho^I(1) \delta \rho^J(2) d1 d2 \\ E_{coul}^{(3)} &= \frac{1}{3} \sum_{I,J} \int \int \int g_{xc}^{I,J,J}(1, 2, 3) \delta \rho^I(1) \delta \rho^J(2) \delta \rho^J(3) d1 d2 d3, \end{aligned} \quad (5.25)$$

where three-center integrals have been neglected in $E_{coul}^{(3)}$. Semiempirical approximations are applied to this final expression to obtain,

$$\begin{aligned} E_{coul}^{(2)}(\mathbf{R}) &= \frac{1}{2} \sum_{I,J} \gamma_{I,J}(R_{I,J}) \Delta q_I \Delta q_J \\ E_{coul}^{(3)}(\mathbf{R}) &= \frac{1}{3} \sum_{I,J} \Gamma_{I,J}(R_{I,J}) \Delta q_I \Delta q_J^2. \end{aligned} \quad (5.26)$$

Here Δq_I is the change in the Mulliken charge of atom I upon formation of the molecule,

$$\begin{aligned} q_I &= \sum_{\mu \in I} \sum_{\nu} P_{\mu,\nu} s_{\mu,\nu} \\ \Delta q_I &= q_I - q_I^0, \end{aligned} \quad (5.27)$$

$\gamma_{I,J}$ is an approximate electron repulsion integral (ERI), and $\Gamma_{I,J}$ is the derivative of $\gamma_{I,J}$ with respect to Δq_I (Δq_J). Minimizing the energy expression [Eq. (5.22)] while maintaining orthonormality of the MOs can be done in the usual way, using the method of Lagrangian parameters. The final orbital hamiltonian matrix is then,

$$f_{\mu \in I, \nu \in J} = f_{\mu \in I, \nu \in J}^{\text{DFTB}} + f_{\mu \in I, \nu \in J}^{\text{SCC}}, \quad (5.28)$$

where the first term on the right-hand side is just the one obtained from the original

DFTB method without self-consistent charges. The SCC contribution is given by,

$$\begin{aligned}
 f_{\mu \in I, \nu \in J}^{\text{SCC}} &= f_{\mu \in I, \nu \in J}^{\text{SCC}(2)} + f_{\mu \in I, \nu \in J}^{\text{SCC}(3)} \\
 f_{\mu \in I, \nu \in J}^{\text{SCC}(2)} &= \frac{s_{\mu \in I, \nu \in J}}{2} \sum_K (\gamma_{J,K} + \gamma_{K,I}) \Delta q_K \\
 f_{\mu \in I, \nu \in J}^{\text{SCC}(3)} &= s_{\mu \in I, \nu \in J} \sum_{\tau \in K} \left[\frac{1}{3} (\Delta q_I \Gamma_{I,K} + \Delta q_J \Gamma_{J,K}) + \frac{\Delta q_K}{6} (\Gamma_{K,I} + \Gamma_{K,J}) \right] \quad (5.29)
 \end{aligned}$$

As Δq_K depends upon the MO coefficients $c_{\mu,i}$, then Eq. (5.17) must now be solved self-consistently.

It remains to say a word about how the ERI are approximated. In early work, diagonal elements of $\gamma_{I,J}$ are calculated using Pariser's observation [63] that,

$$\gamma_{I,I} = \text{IP}_I - \text{EA}_I, \quad (5.30)$$

where IP_I and EA_I are respectively the ionization potential and electron affinity of atom I . In DFTB3, the $\gamma_{I,I}$ is estimated using Janak's theorem by taking a numerical derivative of the HOMO energy with respect to its occupation number in the neutral atom [62]. The off-diagonal elements are calculated using the zero differential overlap (ZDO) approximation for electron repulsion integrals,

$$(\mu\nu||\kappa\lambda) \approx \delta_{\mu,\nu} \delta_{\kappa,\lambda} (\mu\mu||\kappa\kappa), \quad (5.31)$$

and spherically-symmetric s functions on each of the two atoms,

$$\gamma_{I,J} = \gamma_{s \in I, s \in J}, \quad (5.32)$$

in order to avoid well-known invariance problems in semiempirical integral evaluation. The exact type of s function used to evaluate the $\gamma_{I,J}$ may vary depending upon the implementation of DFTB [53, 56]. The parameterization of the DFTB3 Γ parameters is explained in Ref. [62] along with other details not explained in this brief overview.

We do not expect DFTB to behave like exact DFT. We do not even expect it to be as accurate as density-functional approximations (DFAs). We regard DFTB as a more approximate form of a DFA which can be applied to answer properly-posed questions for larger or more complex systems than can normally be treated with DFAs. As such this paper focuses on how well DFTB can capture trends.

5.3 Computational Details

Three different programs were used in the present work — namely the DFTB+ program [64] for DFTB calculations, GAUSSIAN09 [65] for Hartree-Fock (HF), DFT, and OVGF calculations, and the post-SIESTA [66] program MBPT_LCAO [19, 67] for *GW* calculations. The DFTB calculations are entirely internally consistent in the sense that DFTB calculations were carried out at geometries optimized at the same level of DFTB methodology. Vibrational frequencies were calculated to verify true minima by the absence of imaginary vibrational frequencies.

Many of the other calculations are also completely internally consistent in the sense that the same basic method (and basis set) was used for geometry optimizations as for subsequent property calculations. However some of our calculations are property calculations using one method at a geometry optimized with another basis set. It is convenient to describe these calculations using a common notation for a “theoretical model chemistry”: method used/basis set [68]. If different models are used to optimize the geometry than for property calculations at that geometry then we will use the notation: property model//geometry used. For example, OVGF/6-31G//B3LYP/6-31G** means that the OVGF calculations with the 6-31G basis set were carried out at the geometry optimized using DFT with the B3LYP functional and the 6-31G** basis set.

DFTB+ All of the DFTB calculations reported in this paper were performed by using the version 4 release 1.2 of the DFTB+ program [64] and the parameter set in the 3ob Slater-Koster file downloaded from the DFTB site [69]. The self-consistent charge (SCC) were full third-order calculations activated by using the keyword `ThirdOrderFull = Yes` and specifying `HubbardDerivs` for all atoms (C, H, N, and S). The 3ob set has been optimized at the DFTB3 level for bio and organic molecules containing carbon, hydrogen, nitrogen, and oxygen [70]. It also contains additional parameters for sulfur and phosphorus [71] which, however, were not needed in this study. Clearly any conclusions of our assessment of DFTB are specific to this parameter set.

We noticed that some molecules with degenerate orbitals would not converge without the use of fractional occupation numbers. For these molecules convergence was obtained by using a Fermi orbital occupancy distribution with temperatures in the range 10-40 K.

GAUSSIAN09 Several types of calculations were carried out using the GAUSSIAN09 program [65]—namely, DFT (LDA and B3LYP), HF, and OVGF calculations. Two

different sets of HF calculations were carried out. The first set (HF/6-31G*//HF/6-31G*) was carried out using the 6-31G(d) (also known as the 6-31G*) basis set [72, 73]. Geometries were reoptimized using the HF method and this basis set and minima were verified by checking that all vibrational frequencies were real. The second set (HF/6-31G//B3LYP//6-31G**) was carried out as a step in our OVGf calculations. For PCBM even this was too computationally demanding for OVGf calculations and we report only results (HF/STO-3G//B3LYP//6-31G**) with the minimal STO-3G basis set [74].

DFT calculations with GAUSSIAN09 used either the LDA or the B3LYP functional. LDA calculations used the SVWN option which corresponds to the usual Vosko, Wilk, and Nusair parameterization of the random phase approximation (RPA) results for the homogeneous electron gas [75]. The B3LYP [76] functional is a variation on the B3P functional [77]. Both the LDA and B3LYP calculations used the 6-31G(d) (also known as the 6-31G*) basis set [72, 73]. Also in both cases, the minima from geometry optimizations were verified and no imaginary frequencies were found. Thus reported results are at the LDA/6-31G*//LDA/6-31G* and B3LYP/6-31G*//B3LYP/6-31G* levels of theoretical model chemistry. In addition B3LYP geometry optimizations were carried out with the larger 6-31G(d,p) (also known as 6-31G**) basis set [72, 73] and these B3LYP/6-31G** optimized geometries were used for all of our Green's function calculations.

Our outer-valence Green's function (OVGF) calculations were carried out using the 6-31G [72] basis set at the B3LYP/6-31G** optimized geometries. The OVGf calculations proved to be computationally demanding and we were not able to use more complete basis sets for these molecules. For the PCBM molecule, we were obliged to use the even smaller STO-3G basis set [74] (OVGF/STO-3G//B3LYP/6-31G**). Convergence with respect to basis set completeness was checked in the case of pentacene by also carrying out calculations using the larger 6-311++G** basis set [78, 79]. In going from the 6-31G to the 6-311++G** basis set at the B3LYP/6-31G** optimized geometry, the OVGf HOMO energy of pentacene changed by 0.49 eV while the corresponding HF HOMO energy changed by only about 0.18 eV. This is consistent with the usual observation that MBPT calculations require larger basis sets than HF in order to properly describe in-out and angular correlation effects. For this reason, our OVGf calculations should be considered as indicative, but certainly not conclusive, as we do not believe they are well converged with respect to the orbital basis set used.

MBPT_LCAO Our GW calculations were carried out with the recently developed post SIESTA [66] MBPT_LCAO code [19, 67] at the B3LYP/6-31G** optimized geometries previously optimized with GAUSSIAN09. The SIESTA part of the calculation used the norm-conserving Trouillier-Martins type pseudopotential together with a double-zeta polarized numerical atomic orbital basis set. Computational parameters were chosen in a uniform manner to be the same for all molecules, in such a way that calculations for the most computationally-demanding molecule (PCBM) still fit into the random-access memory (RAM). Even so, our PCBM calculation required 9 days and 8 hours on an Intel 12 core /190 GB RAM machine (model name: Intel(R) Xeon(R) 2.40 GHz E5645 CPU). The spatial extension of the orbitals was determined by the parameter **EnergyShift** for which we could afford the value **EnergyShift** = 50 meV with a frequency resolution of 0.12 eV. The calculations are G_0W_0 calculations constructed in the following way: LDA SIESTA orbitals were used as an initial guess to carry out a self-consistent HF calculation, producing HF orbitals and orbital energies. These are then used in a one-shot GW calculation that might best be termed a $G_0W_0(\text{HF})$ calculation. The IPs and EAs were estimated in two ways.

In the first, the density-of-states (DOS) was calculated using the expression,

$$\text{DOS}(\omega) = (\theta(\omega - \mu) - \theta(\mu - \omega)) \frac{1}{\pi} \Im \sum_s \langle \psi_s | \hat{G}(\omega) | \psi_s \rangle, \quad (5.33)$$

on an energy grid, the extent of which is governed by the maximal difference of the DFT orbital energies multiplied with a factor 1.15. The quantity μ is the “Fermi energy” separating IP solutions from EA solutions. Let us see the relation to the IPs and EAs. Since,

$$G(1, 2; \omega) = \sum_I \frac{\psi_I(1)\psi_I^*(2)}{\omega - \epsilon_I - i\eta} + \sum_A \frac{\psi_A(1)\psi_A^*(2)}{\omega - \epsilon_A + i\eta}, \quad (5.34)$$

in terms of ionization (I) and electron attachment (A) Dyson orbitals ψ_S and energies ϵ_S . Here η is infinitesimal in principle but is a small real number in practical calculations. Then, using the completeness of the MO basis set (ψ_s), Eq. (5.33) reduces to,

$$\text{DOS}(\omega) = \sum_I S_I L(\omega; \epsilon_I, \eta) + \sum_A S_A L(\omega; \epsilon_A, \eta), \quad (5.35)$$

where,

$$L(\omega; \epsilon_S, \eta) = \frac{1}{\pi} \frac{\eta}{(\omega - \epsilon_S)^2 + \eta^2}, \quad (5.36)$$

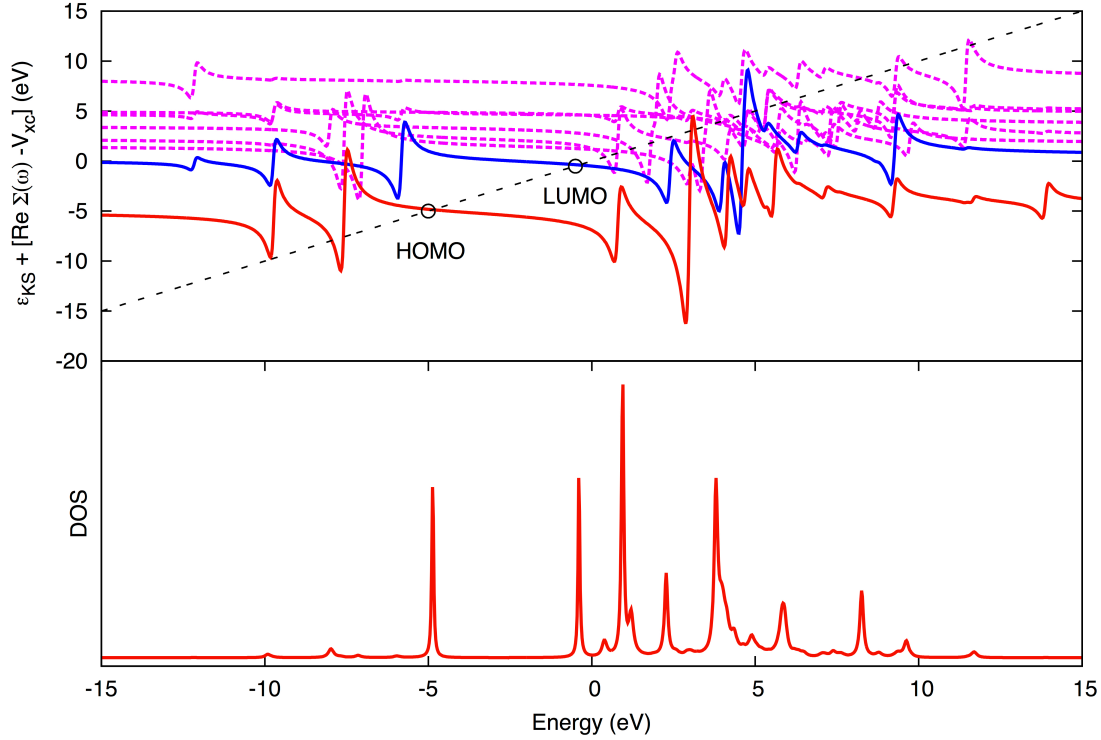


Figure 5.2 – Graphical solution in the QP method. Upper: the diagonal line corresponds to ω while the horizontal curves correspond to $\langle \psi_s | \hat{h}_H | \psi_s \rangle + \Re \langle \psi_s | \Sigma_{xc}^{G_0 W_0}(\omega) | \psi_s \rangle$ for different states, HOMO being red, LUMO blue, and higher states are jagged magenta. The QP solutions for HOMO and LUMO are marked with circles. Lower: the corresponding DOS. Pole strengths (the magnitude of the peaks in the DOS) are obtained from the slope where the diagonal line crosses the horizontal curves.

is the usual Lorentzian function and S_S is the pole strength of the transition. We thus expect the DOS to have maxima at the IPs and EAs. The scale parameter η is the half-width-at-half-maximum of the Lorentzian. This scale parameter was chosen to be 0.24 eV in our calculations as justified elsewhere [80]. Thus our DOS IP is obtained by fitting the highest peak below the gap in the DOS to a third-order polynomial, and calculating the maximum of the polynomial. The EA is determined in a similar way, by fitting the lowest peak above the gap.

The second way of estimating IPs and EAs is referred to in this paper as the quasiparticle (QP) method. It assumes that the starting MOs, ψ_s , are a good approximation to the final Dyson amplitudes, which is usually the case for solutions with significant pole strength (i.e., when the self-energy varies sufficiently slowly as

is typically the case close to the HOMO-LUMO gap). Then,

$$\omega_s^{(\text{QP})} = \langle \psi_s | \hat{h}_H | \psi_s \rangle + \Re \langle \psi_s | \Sigma_{xc}^{G_0W_0}(\omega^{(\text{QP})}) | \psi_s \rangle, \quad (5.37)$$

is solved graphically (Fig. 5.2). The advantage of using the QP method over using the DOS method is that the peaks may be more fully resolved and assigned to a corresponding MO, even for higher poles.

5.4 Small Molecules

In this section and in the next section we will explain our protocol for assessing DFTB for calculating IPs and EAs and give the results of our assessment. A division has been made between small molecules (this section) and medium-sized molecules (next section). This is because much more information is available for benchmarking small molecules while reliable information for benchmarking medium-sized molecules of interest for organic solar cell applications is much more scarce. In this section, we first review our protocol and illustrate how it works for known results from the literature. We then go on to apply our protocol to the assessment of DFTB calculations.

Benchmark Data Sets The identification and tabulation of reliable comparison data is a key part of the test cycle part of the development and successful implementation of a theoretical model for practical applications. The very important and, indeed essential, work involved in establishing such “benchmark data sets” (BDSs) can be substantial and relatively thankless as it may be regarded primarily as “literature work,” rather than as “new science.” An especially well-known example of such a test set is Charlette E. Moore’s tables of atomic spectra, now freely available from the American National Institute of Standards and Technology (NIST, www.nist.gov), which has proven essential in testing different approaches to quantum chemistry.

For small molecules, experimental and quantum chemistry ionization potentials (IPs) are readily available from the NIST Computational Chemistry Comparison and Benchmark Database (CCCBDB, <http://cccbdb.nist.gov/>). As we have chosen to use the same BDS as in previous work by Hamel *et al.* [40] for the molecules shown in Fig. 5.3, we have simply taken their values for our small-molecule BDS. This gives a total of 56 IPs (Tables 5.3 and 5.4). Note that these small molecules cannot be used to benchmark electron affinities (EAs) in the sense that most do not bind an extra electron. Hence we will not assess the quality of DFTB EAs for these small molecules.

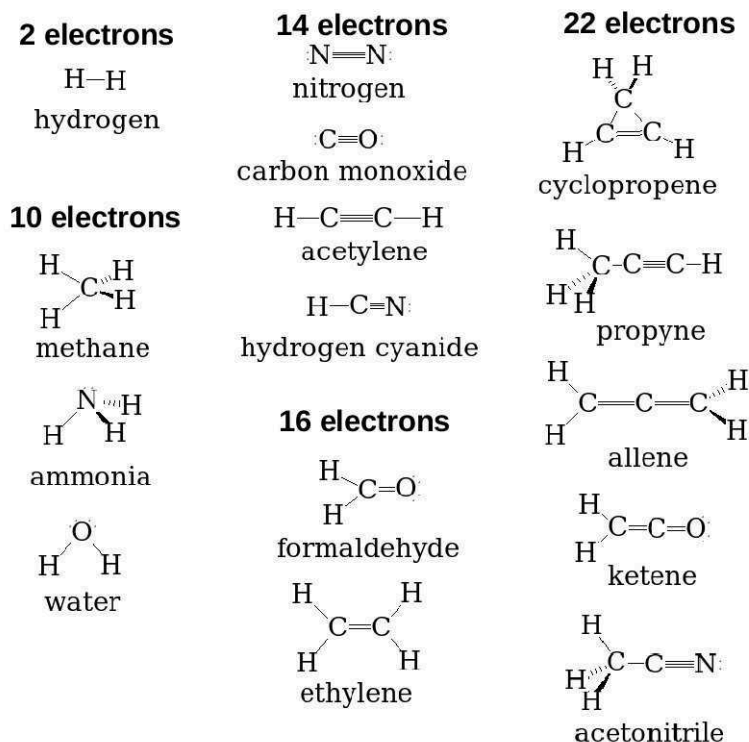


Figure 5.3 – The 15 small molecules treated here.

Analytical Protocol Figure 5.4 simply takes the data from Hamel *et al.* [40] to make a correlation plot of minus LDA orbital energies (LDA “Koopmans’ theorem IPs”) versus experimental IPs. It is clear that the LDA Koopmans’ theorem IPs underestimate the experimental IPs but that also there is an excellent linear correlation between the LDA Koopmans’ theorem IPs and the experimental IPs for these small molecules. We are thus faced with a dilemma regarding how good LDA Koopmans’ IPs are as a model for experimental IPs and the same dilemma may arise when trying to assess other methods. At this point, we may adapt one of two different quantum chemical philosophies which Coulson has famously called “group I” and “group II” [81]. (See also Refs. [82] and [83].) Roughly speaking group I focuses on getting good numbers for individual molecules, so that the best theory would have a slope m near unity and an intercept b near zero, while group II focuses on the ability to predict trends, so that the best theory is one where there is a systematic, and hence predictive, correlation between theory and experiment, even if the two give quantitatively different results.

In the spirit of group I, we should keep in mind that even the best computed molecular vertical IPs have an average error of about 0.2 eV compared to experimental vertical IPs determined by peak maxima in photoelectron spectra because

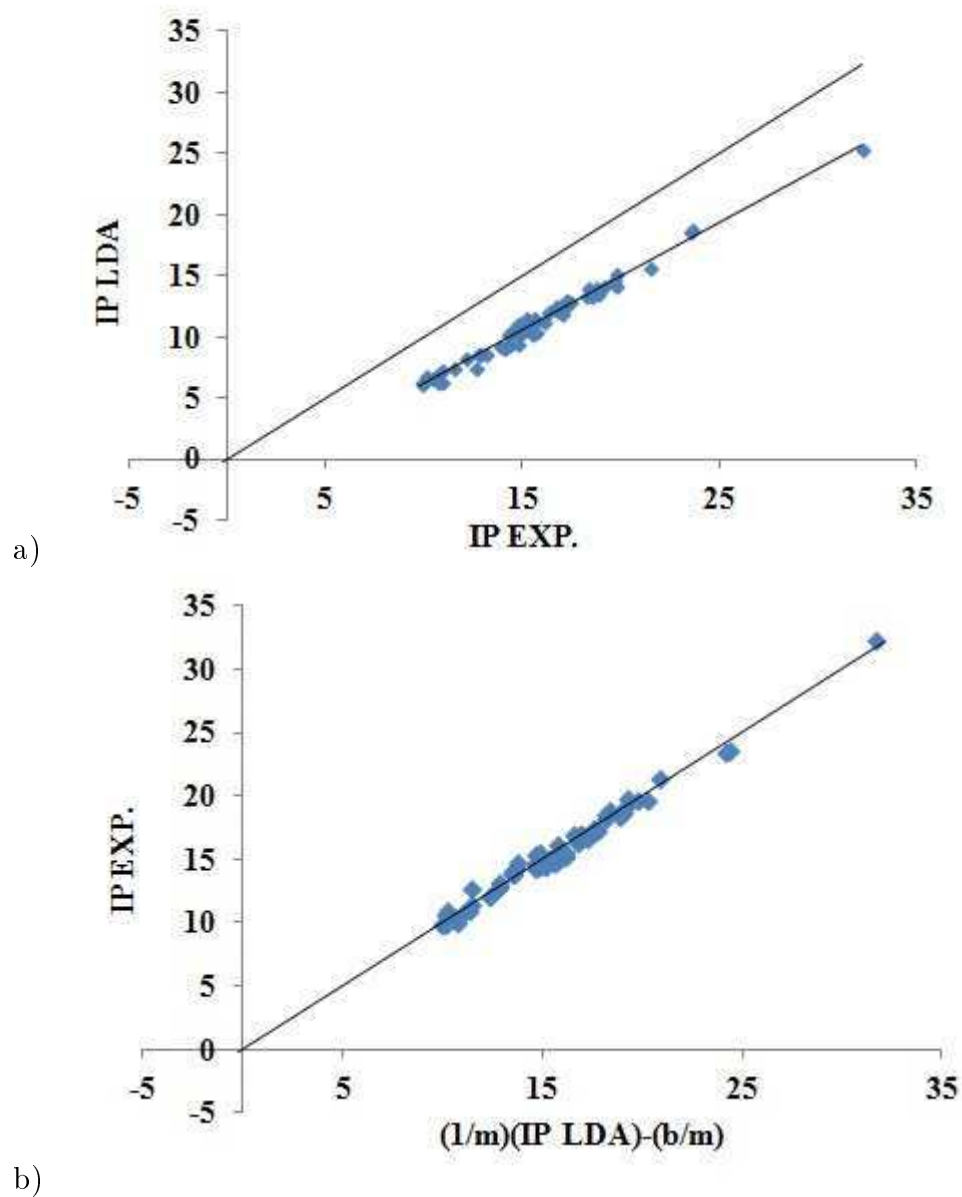


Figure 5.4 – a) Correlation plot for LDA “Koopmans’ theorem IPs” versus experimental IPs [40]. b) Inversion plot for the same data constructed using Eq. (5.40) to show the “predictive ability” of the LDA least squares fit. The units for both axes in these plots are in eV.

of neglect of vibrational (i.e., Franck-Condon) effects. In the spirit of group II, we have taken the standard error,

$$\Delta y = \sqrt{\frac{\mathcal{E}_y}{N-2}}, \quad (5.38)$$

where,

$$\mathcal{E}_y = \sum_{i=1,N} (y_i - mx_i - b)^2 \quad (5.39)$$

as the most transferable estimate of the goodness of the fit. However, if we now take the fit values of m and b found above for a particular method and then use them in the formula,

$$x = \frac{1}{m}y - \frac{b}{m}, \quad (5.40)$$

to try to estimate the error in the predicted value of BDS values corresponding to the results of the model, then the relevant standard error is

$$\Delta x = \sqrt{\frac{\mathcal{E}_x}{N-2}} = \frac{\Delta y}{|m|}, \quad (5.41)$$

where

$$\mathcal{E}_x = \sum_{i=1,N} \left(x_i - \frac{1}{m}y_i + \frac{b}{m} \right)^2 = \frac{\mathcal{E}_y}{m^2}. \quad (5.42)$$

Thus Δx is the relevant measure of the predictability of a given model.

The results of a statistical analysis of results in Ref. [40] for least square fits of various theoretical methods to experiment are shown in Tables 5.1 and 5.2. Consistent with Fig. 5.4, Table 5.1 shows that the DFT LDA Koopmans' theorem (KT) underestimates by 4 to 6 eV (i.e., $y - x = (m-1)x + b$ is -3.87 eV at $x = 10$. eV and -6.23 eV at $x = 30$. eV) and so is a dismal failure from the point of view of Coulson group I. This has been explained in terms of the particle number discontinuity in the DFT exchange-correlation (xc) potential [85]. The Hartree-Fock (HF) KT IPs are better from the point of view of Coulson group I, but tend to slightly overestimate the experimental IPs. This is consistent with early literature which proposed as a rule of thumb that agreement between HF KT and photoelectron spectroscopy (PES) IPs could be improved by multiplying the HF KT values by a factor less than one (e.g., 0.92 or the "8% rule" [86, 87]). Surprisingly localizing the HF exchange operator by the optimized effective potential method (OEP) so as to obtain an exact exchange-only xc-potential which includes a derivative discontinuity leads to much improved absolute agreement between KT and experimental IPs with a slightly reduced standard error (Δy). Part of the reason for the smaller value of Δy is that the

Table 5.1 – Fitting data for outer valence IPs: $y = mx + b$, where x is the experimental IP and y is the calculated IP, both in eV. HF, Hartree-Fock; OEP, optimized effective potential; LDA, local density approximation; DFTB, density-functional tight binding (without self-consistent charge); SCC-DFTB, self-consistent charge DFTB.

Method	m (unitless)	b (eV)	Δy (eV)	Δx (eV)
Koopmans' Theorem				
OEP ^a	0.958	0.748	0.659	0.688
HF ^a	1.236	-2.192	0.686	0.555
LDA ^a	0.882	-2.691	0.474	0.537
DFTB ^b	0.754	-1.071	0.651	0.863
SCC-DFTB ^b	0.758	-1.442	0.535	0.706
Δ SCF				
LDA ^c	1.65	2.54	1.65	1.85

^a Calculated from data in Ref. [40].

^b Present work.

^c Approximate Δ SCF values calculated using Slater's transition orbital method. "rTS" values from Ref. [84].

Table 5.2 – Fitting data for first IPs [40]: $y = mx + b$, where x is the experimental IP and y is the theoretical IP, both in eV. HF, Hartree-Fock; OEP, optimized effective potential; LDA, local density approximation; DFTB, density-functional tight binding (without self-consistent charge); SCC-DFTB, self-consistent charge DFTB.

Method	m (unitless)	b (eV)	Δy (eV)	Δx (eV)
Koopmans' Theorem				
HF ^a	1.143	-1.270	0.617	0.540
OEP ^a	1.145	-1.294	0.613	0.535
LDA ^a	0.727	-1.064	0.374	0.514
DFTB ^b	0.497	2.223	0.498	1.002
SCC-DFTB ^b	0.560	1.064	0.477	0.852
Δ SCF				
LDA ^c	1.00	0.49	0.43	0.43
DFTB ^b	0.497	2.223	0.498	1.002
SCC-DFTB ^b	0.838	2.239	0.534	0.649

^a Calculated from data in Ref. [40].

^b Present work.

^c Approximate Δ SCF values calculated using Slater's transition orbital method. "rTS" values from Ref. [84].

OEP corrects misorderings in the KT IPs which are present when KT is used with the nonlocal HF exchange operator. Note that the OEP procedure makes use of the constraint that the highest occupied molecular orbital (HOMO) energy be identical for HF and OEP *when both are evaluated with the OEP orbitals* [41]. Thus the OEP HOMO energy is almost, but not exactly, the same as the HF HOMO energy.

The outlook changes dramatically from the point of view of Coulson group II. Looking at Δx in Tables 5.1 and 5.2, we see that the LDA KT provides as much predictability (indeed somewhat more) as either the HF or OEP KT, indicating that, although shifted, the LDA KT IPs provide an excellent reflection of the trend in the experimental IPs. Closer analysis of why the LDA results are a bit better than the HF or OEP (smaller Δx) shows that the LDA KT IPs have fewer order reversals compared to experimental IPs than do the HF KT IPs. This also occurs when the HF exchange potential is localized in the OEP procedure, though Δx is larger for the OEP calculations than for the HF calculations indicating decreasing predictability upon localization. The above trends do not seem to be well-known to most users of quantum chemistry programs, but this does not seem to be the place to spend time and space giving further details. (See Ref. [41] for additional discussion.) Suffice it to say that the above information is “well-known to those who know about such things” and that further information is contained in the cited papers. It should also be evident that global hybrid functionals containing a nonzero amount of HF exchange will have a behavior inbetween the LDA and HF as can be easily checked using information from the NIST CCCBDB, but we shall not pursue this topic further here.

Assessment of DFTB The results of our DFTB+ calculations of IPs are shown in Tables 5.3 and 5.4. The results of a statistical analysis of our DFTB results relative to experiment are also shown in Tables 5.1 and 5.2.

Since DFTB has been designed as an approximation on DFT, we expect DFTB to behave in much the same, albeit not exactly, like DFT. We also expect the SCC option to give results closer to DFT than results without the SCC. Let us verify that this is true by first looking at calculations without the SCC option. A trivial consequence of the basic theory (previous section) is that the Δ SCF and Koopmans’ theorem IPs are identical for the original DFTB method and our results confirm this. Figure 5.5 shows how DFTB Koopmans’ theorem IPs correlate with experiment. As we would hope, this figure is remarkably similar to the corresponding LDA figure (Fig. 5.4). The DFTB Koopmans’ theorem IPs are underestimates of the experimental IPs in much the same way the the LDA underestimate Koopmans’

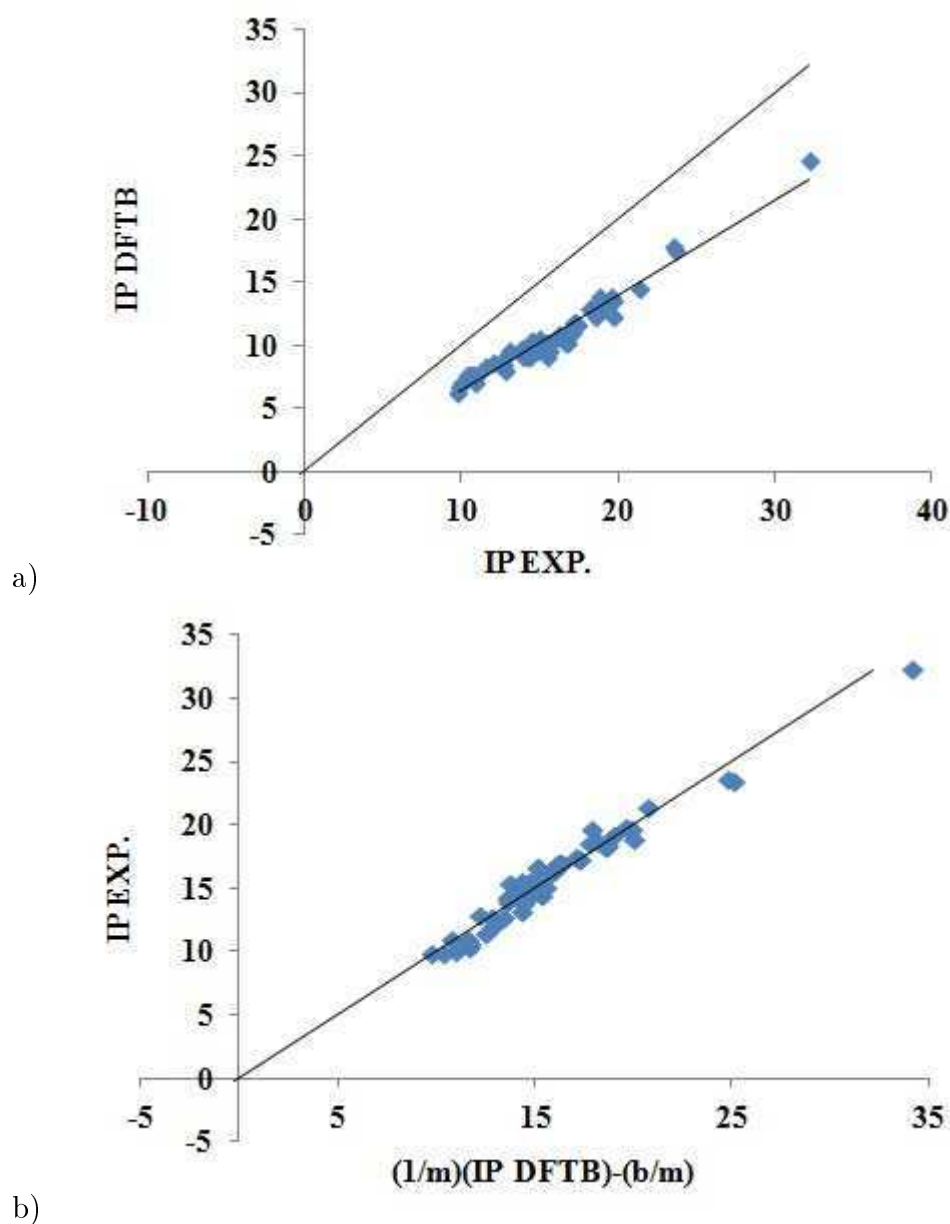


Figure 5.5 – Correlation plot for DFTB “Koopmans’ theorem IPs” versus experimental IPs. a) Correlation plot for DFTB “Koopmans’ theorem IPs” versus experimental IPs. b) Inversion plot for the same data constructed using Eq. (5.40) to show the “predictive ability” of the DFTB least squares fit. The units for both axes in these plots are in eV.

Table 5.3 – DFTB+ IPs (eV) for small molecules.

Molecule	Orbital	Expt. ^a	Without $-\epsilon_i$	SCC Δ SCF	With $-\epsilon_i$	SCC Δ SCF
2 electrons						
hydrogen (H ₂)	1a _g	15.43	9.26	9.26	9.26	14.67
10 electrons						
methane (CH ₄)	1t ₂	14.3	9.17	9.17	9.00	13.41
ammonia (NH ₃)	3a ₁	10.7	7.73	7.73	6.95	12.18
water (H ₂ O)	1b ₁	12.62	9.04	9.04	7.64	13.31
	3a ₁	14.74	10.28	-	9.03	-
	1b ₂	18.51	12.31	-	11.54	-
	2a ₁	32.2	24.65	-	23.48	-
14 electrons						
nitrogen (N ₂)	3σ _g	15.6	9.70	9.70	9.70	15.33
	1π	16.98	11.16	-	11.16	-
	2σ _u	18.78	13.98	-	13.98	-
carbon monoxide (CO)	5σ	14.01	9.16	9.16	9.16	14.47
	1π	16.91	11.21	-	11.18	-
	4σ	19.72	13.67	-	13.64	-
acetylene (C ₂ H ₂)	1π _u	11.49	8.33	8.33	7.86	12.23
	3σ _g	16.7	10.29	-	10.11	-
	2σ _u	18.7	12.66	-	12.45	-
	2σ _g	23.5	17.87	-	17.44	-
hydrogen cyanide (HCN)	1π	13.8	9.79	9.79	9.30	14.12
	5σ	14.15	9.84	-	9.31	-
	4σ	19.68	12.42	-	13.11	-
16 electrons						
formaldehyde (CH ₂ O)	2b ₂	10.9	7.06	7.06	6.43	10.98
	1b ₁	14.5	10.47	-	9.92	-
	5a ₁	16.1	10.78	-	10.37	-
	1b ₂	17.	11.08	-	10.96	-
	4a ₁	21.4	14.56	-	14.43	-
ethylene (C ₂ H ₄)	1b _{2u}	10.68	7.75	7.75	7.36	10.94
	1b _{2g}	12.79	8.10	-	7.88	-
	3a _g	14.8	9.65	-	9.35	-
	1b _{3u}	15.18	10.37	-	10.09	-
	2b _{1u}	19.1	13.20	-	12.91	-
	2a _g	23.59	17.60	-	17.24	-

^a Taken from Ref. [40].

Table 5.4 – DFTB+ IPs (eV) for small molecules (continued).

Molecule	Orbital	Expt. ^a	Without SCC		With SCC	
			$-\epsilon_i$	Δ SCF	$-\epsilon_i$	Δ SCF
22 electrons						
cyclopropene (C ₃ H ₄)	2 <i>b</i> ₂	9.86	6.75	6.75	6.28	10.00
	2 <i>b</i> ₁	10.89	7.64	-	7.20	-
	6 <i>a</i> ₂	12.7	8.59	-	8.11	-
	1 <i>b</i> ₂	15.09	10.01	-	9.52	-
	5 <i>a</i> ₁	16.68	10.36	-	10.04	-
	2 <i>b</i> ₁	18.3	13.01	-	12.69	-
	4 <i>a</i> ₁	19.6	13.95	-	13.48	-
propyne (CH ₃ CCH)	2 <i>e</i>	10.37	7.71	7.71	7.18	10.87
	1 <i>e</i>	14.4	9.71	-	9.65	-
	7 <i>a</i> ₁	15.5	10.00	-	9.69	-
	6 <i>a</i> ₁	17.2	11.91	-	11.56	-
allene (C ₃ H ₄)	2 <i>e</i>	10.02	7.21	7.21	6.85	10.43
	1 <i>e</i>	14.75	9.95	-	9.67	-
	3 <i>b</i> ₂	14.75	9.98	-	9.68	-
	4 <i>a</i> ₁	17.3	11.93	-	11.66	-
ketene (CH ₂ CO)	2 <i>b</i> ₁	9.8	6.27	6.27	6.20	10.21
	2 <i>b</i> ₂	14.2	9.24	-	9.23	-
	1 <i>b</i> ₁	15.	10.62	-	10.71	-
	1 <i>b</i> ₂	16.3	10.93	-	10.97	-
	7 <i>a</i> ₁	16.8	11.07	-	11.14	-
	6 <i>a</i> ₁	18.2	12.94	-	12.86	-
	acetonitrile (CH ₃ CN)	2 <i>e</i>	12.08	8.66	8.66	8.45
7 <i>a</i> ₁		13.11	9.69	-	8.96	-
1 <i>e</i>		15.5	10.25	-	10.36	-
6 <i>a</i> ₁		17.4	11.81	-	11.77	-

^a Taken from Ref. [40].

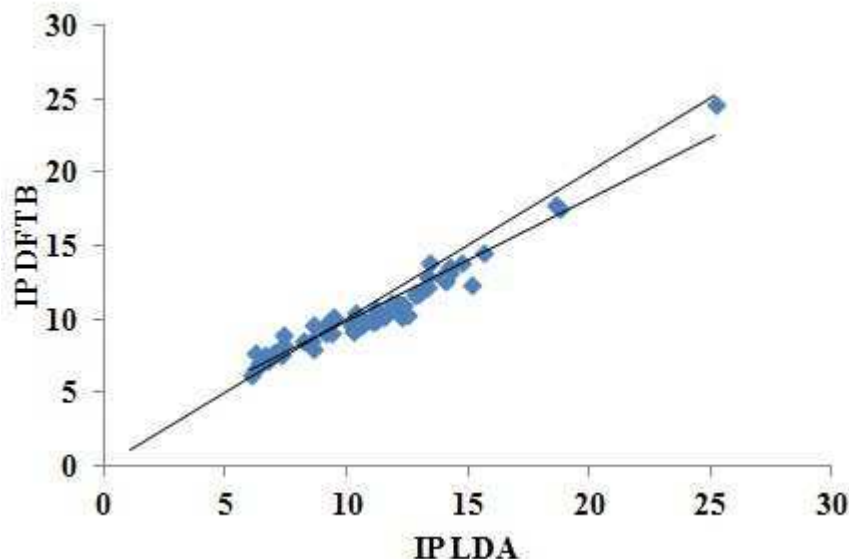


Figure 5.6 – Correlation plot for DFTB versus LDA “Koopmans’ theorem IPs.” The units for both axes are eV.

theorem. This is consistent with DFTB having been constructed to behave like DFT — a conclusion which is confirmed by Fig. 5.6 showing the excellent correlation between DFTB and LDA Koopmans’ theorem IPs. In spite of the similarity of the graphics, the LDA and DFTB values of Δx in Table 5.1 are a reminder that DFTB is significantly less predictive (error bar of ± 0.863 eV) than is the LDA (error bar of ± 0.537 eV).

According to Tables 5.1 and 5.2, including SCC in DFTB leads to a significant partial improvement. While SCC-DFTB still behaves much like the LDA, SCC-DFTB Koopmans’ theorem IPs are more predictive (error bar of ± 0.706 eV) than DFTB Koopmans’ theorem IPs, though still less than LDA Koopmans’ theorem IPs. If we restrict attention to the HOMO, than we can also compare Koopmans’ theorem with Δ SCF SCC-DFTB (which we recall are the same in the case without the SCC). Here we see that the Δ SCF method provides more predictive ability than does the Koopmans’ theorem approach. In fact, the SCC-DFTB Δ SCF error bar (± 0.649 eV) is becoming encouragingly close to the LDA Koopmans’ theorem error bar (± 0.514 eV), although it is still not as small as that of the “rTS” estimate of the LDA Δ SCF IPs (± 0.43 eV) whose calculation were reported in Ref. [84].

5.5 Medium-Sized Molecules

The small molecules in the previous section provide a good idea of how various methods work for calculating IPs for such systems. In particular we confirmed that DFTB behaves much like DFT and placed error bars on the predictive power of the method. Thus, for small molecules, DFT (or some other first-principles method) is preferable to DFTB. However, our interest is in organic electronics where interesting molecules, and their assembly into realistic systems, rapidly leads to calculations which are difficult to attack any other way except using a semi-empirical method such as DFTB. It is important to see to what extent what we have learned for small molecules also applies to larger molecules of more interest for organic electronics. This is especially true since methods tested and found to work well for small molecules do not always perform equally well for large molecules [26]. In this section, we focus on assessing DFTB for the calculation of IPs and EAs for a BDS of “medium-sized” molecules often used in organic electronics (Fig. 5.1).

Choice of Comparison Data Of course, the notion of “small,” “medium,” and “large” is not well-defined. In the present context molecules are “medium sized” in the sense that they are the smallest molecules of interest for organic electronics and yet they are already too large for the NIST CCBDB which is limited to species with no more than 26 atoms total. Our medium-sized molecules are also large enough that it is experimentally more natural to treat them either in the bulk phase, as either a thin film or in solution electrochemistry, than in the gas phase, though gas phase molecular data is available for a number of the molecules. IPs and EAs for these molecules are frequently determined by thin-film photoelectron or photoemission spectroscopy or by cyclic voltametry and involve a certain number of assumptions whose accuracy is not always easy to assess. In particular, in thin film photoelectron and photoemission spectroscopy, the difference between the ionization energy of the molecule and the bulk is sometimes referred to as “the polarization energy due to the molecular ion left in the solid after a photoelectron is removed” [88], which is a quantity which is not evident to calculate. Furthermore the relationship between the bulk ultraviolet photoemission spectroscopy ionization energy and the oxidation potential of cyclic voltametry requires a model in which it is assumed that the molecules form a thin film on the electrodes similar to that found in the bulk [89], which is also not easy to model theoretically. Because of these complications, we place our trust more firmly in gas phase results, where available, than in bulk phase results. Furthermore, as we shall see, reliable theoretical calculations are possible for the gas phase. Thus, once validated by comparison against gas phase data, we may

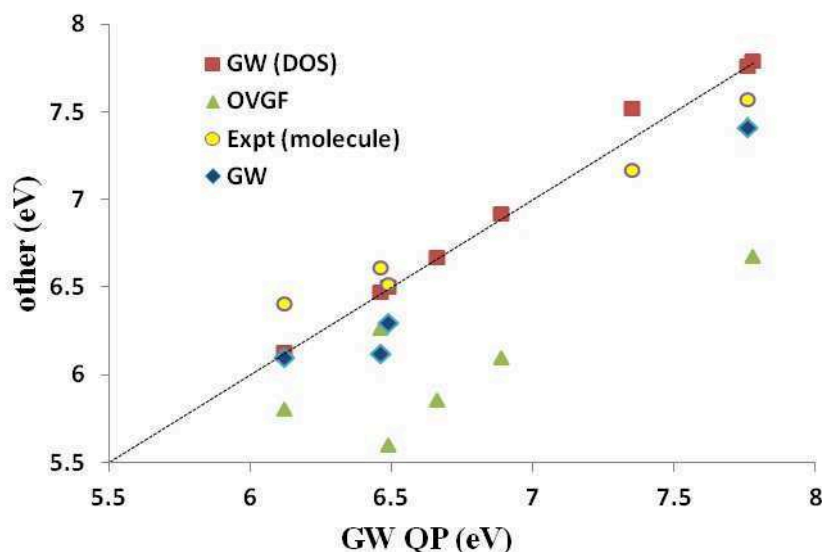


Figure 5.7 – Correlation graph of data from Table 5.5 showing how experimental and Green's function IPs compare. The label “*GW*” [as opposed to *GW* DOS and *GW* QP] are calculated values taken from the literature. (See Table 5.5.) Units are in eV. The *x*-axis corresponds to our *GW* QP calculations.

use appropriate theoretical methodology to obtain a BDS of IPs and EAs.

Assessment of our *GW* calculations Table 5.5 and Fig. 5.7 show how various Green's function calculations compare with experimental data for predicting IPs. It is immediately obvious that the experimental molecular (gas phase) IPs are in much better agreement with the Green's function IPs than are experimental bulk (solution or thin film) IPs. This is, of course, to be expected on the basis of the above discussion. Of the different sets of Green's function IPs, our OVGF values are in the worst agreement with the experimental molecular IPs. As stated earlier (Sec. 5.3), we believe that this is simply because we were unable to carry out OVGF calculations with extensive basis sets. Both our *GW* DOS and *GW* QP IPs agree as well, or better, with the available experimental molecular IPs than do the *GW* IPs taken from the literature. In the one case (PCBM) where a significant difference was observed between our *GW* DOS and *GW* QP IPs, it is the *GW* QP IPs which are closer to the available experimental molecular value. This is because the DOS approach failed due to the HOMO level being smeared by the three nearly degenerate levels HOMO-1, HOMO-2, and HOMO-3.

Reliable experimental EA comparison data for molecules of interest in organic

Table 5.5 – Comparison values of the first ionization potential for the medium-sized molecules from experiment and from quantum chemistry calculations.

Molecule	Expt.		OVGF	Green's function		Lit.
	bulk	molecule		<i>GW</i>		
				PW	QP ^{<i>q</i>}	
				DOS ^{<i>p</i>}		
pentacene		6.61 ^{<i>e</i>}	5.78 ^{<i>b</i>} 6.27 ^{<i>c</i>}	6.47	6.46	6.12 ^{<i>d</i>}
DIP	5.35 ^{<i>m</i>}		6.10 ^{<i>b</i>}	6.91	6.89	
H ₂ Pc		6.41 ^{<i>f</i>}	5.81 ^{<i>b</i>}	6.13	6.12	6.10 ^{<i>d</i>}
PCBM	5.87 ^{<i>h</i>}	7.17 ^{<i>n</i>}		7.52	7.35	
6T	4.7 ^{<i>m</i>}		5.86 ^{<i>b</i>}	6.67	6.66	
DCV3T	6.09 ^{<i>a</i>}		6.68 ^{<i>b</i>}	7.79	7.78	
C ₆₀	6.45 ^{<i>m</i>}	7.57 ^{<i>g</i>}	7.43 ^{<i>b</i>}	7.76	7.76	7.41 ^{<i>d</i>}
rubrene	5.92 ^{<i>i</i>}	6.52 ^{<i>i</i>}	5.60 ^{<i>b</i>}	6.50	6.49	6.30 ^{<i>l</i>}
Molecule	Koopmans' Theorem			Δ SCF		
	HF	B3LYP ^{<i>o</i>}	DFTB	SCC-DFTB	B3LYP ^{<i>o</i>}	SCC-DFTB
pentacene	5.91 ^{<i>j</i>} 6.09 ^{<i>k</i>}	4.59	5.38	4.97	5.93	6.81
DIP	6.54 ^{<i>j</i>}	5.12	5.73	5.35	6.32	6.99
H ₂ Pc	5.47 ^{<i>j</i>}	4.93	5.14	4.96	6.05	6.49
PCBM		5.65	5.48	5.38	6.81	7.01
6T	6.46 ^{<i>j</i>}	4.82	5.17	4.79	5.88	6.22
DCV3T	7.62 ^{<i>j</i>}	6.01	5.40	5.64	7.10	7.21
C ₆₀	7.95 ^{<i>j</i>}	5.98	5.67	5.67	7.22	7.41
rubrene	6.08 ^{<i>j</i>}	4.67	5.36	4.90	5.85	6.59

^a Estimated from cyclic voltammetry in CH₂Cl₂ [90]. ^b Present work: OVGF/6-31G//B3LYP/6-31G**. ^c Present work: OVGF/6-311++G**//B3LYP/6-31G**. ^d *GW* from Table II of Ref. [36]. ^e Gas-phase charge-stripping mass spectroscopy [91]. ^f Gas-phase photoelectron spectroscopy (PES) [92]. ^g From Ref. [93]. ^h Thin-film ultraviolet photoemission spectroscopy (UPS) [94]. ⁱ Gas and thin-film photoelectron spectroscopy (PES) [88]. ^j Present work: HF/6-31G//B3LYP/6-31G**. ^k Present work: HF/6-311++G**//B3LYP/6-31G**. ^l From Ref. [95]. ^m Ultraviolet photoemission spectroscopy (UPS) [96]. ⁿ Ref. [97]. ^o Present work: B3LYP/6-31G*//B3LYP/6-31G*. ^p Present work: inspection of the density of states. ^q Present work: solution of the quasiparticle equation.

Table 5.6 – Comparison values of the first electron affinity for the medium-sized molecules from experiment and from quantum chemistry calculations.

Molecule	Expt.		OVGF	Green's function		Lit.
	bulk	molecule		GW		
				PW	QP ^b	
				DOS ^a		
pentacene		1.35 ^f	0.001 ^c	0.985	0.981	
			0.755 ⁴	0.941	0.953	
DIP	2. ^g		0.421 ^c	1.31	1.30	
H ₂ Pc			1.063 ^c	1.64	1.68	
PCBM	5.96 ^j	2.63 ⁿ		1.94	2.01	
6T		1.25 ^m	-0.045 ^c	0.413	0.422	
DCV3T	3.90 ⁱ		1.201	1.85	1.86	
C ₆₀		2.68 ⁿ	1.486 ^c	2.14	2.14	
rubrene			-0.195 ^c	0.839	0.822	1.88 ^o

Molecule	Koopmans' Theorem			ΔSCF		
	HF	B3LYP ^e	DFTB	SCC-DFTB	B3LYP ^e	SCC-DFTB
pentacene	0.553 ^k -0.274 ^l	2.38	4.05	3.63	1.05	1.80
DIP	-0.251 ^k	2.59	4.14	3.75	1.39	2.10
H ₂ Pc	0.478 ^k	2.83	3.94	3.65	1.71	2.08
PCBM		3.09	3.89	3.75	1.92	2.07
6T	-0.519 ^k	2.14	3.52	3.22	1.09	1.85
DCV3T	0.792 ^k	3.46	3.93	4.12	2.37	2.61
C ₆₀	0.679 ^k	3.22	3.88	3.89	2.61	2.15
rubrene	-0.957 ^k	2.07	3.71	3.27	0.89	1.58

^a Present work: inspection of the density of states. ^b Present work: solution of the quasiparticle equation. ^c Present work: OVGF/6-31G//B3LYP/6-31G**. ^d Present work: OVGF/6-311++G**//B3LYP/6-31G**. ^e Present work: B3LYP/6-31G*//B3LYP/6-31G*. ^f Gas phase measurement using electron-transfer equilibria [98]. ^g Thin film UPS and IPES [96]. ^h Ref. [99]. ⁱ Cyclic voltametry in CH₂Cl₂ [90]. ^j Solid-phase threshold electron affinity [100]. ^k Present work: HF/6-31G. ^l Present work: HF/6-311++G**. ^m Gas-phase adiabatic electron affinity from photodetachment photoelectron spectroscopy [101]. ⁿ Gas-phase adiabatic electron affinity from low-temperature photoelectron spectroscopy [102]. ^o GW calculation from Ref. [95].

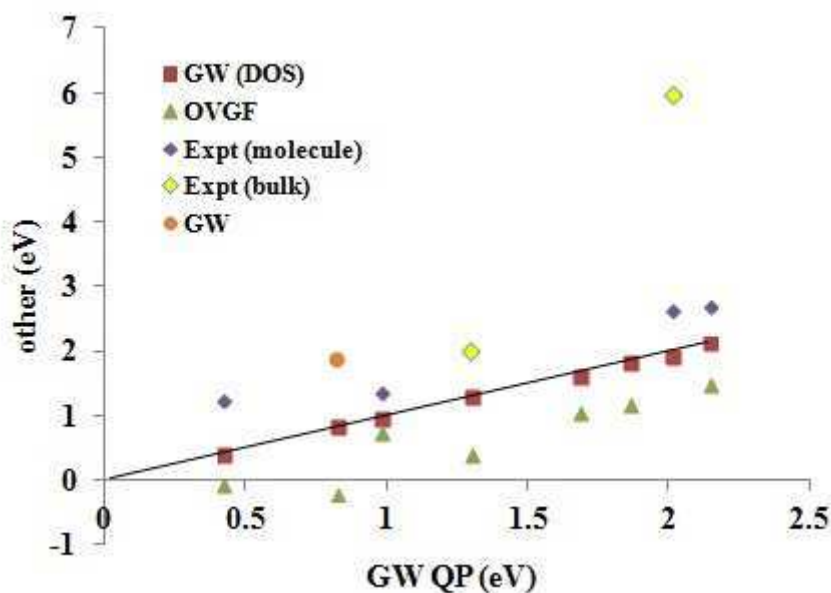


Figure 5.8 – Correlation graph of data from Table 5.6 showing how experimental and Green's function EAs compare. The label "GW" [as opposed to *GW* DOS and *GW* QP] are calculated values taken from the literature. (See Table 5.6.)

electronics is even harder to come across than for IPs. There are several reasons for this. Some are similar to those encountered with IPs, such as the difficulty of obtaining gas phase data. Some are particular to the experimental problem of obtaining electron addition rather than electron removal energies. Thus our calculated EAs are vertical while the experimental EAs are often best considered to be adiabatic because of the experiments used to measure them. Also it must be remembered that that EAs tend to be smaller than IPs, except in the case of good electron acceptors such as C_{60} and PCBM whose EAs are expected to be so similar that they may be difficult to distinguish by theoretical calculations. Nevertheless Table 5.6 and Fig. 5.8 show that our *GW* EAs also agree well with available experimental molecular (gas phase) data.

In conclusion, we feel justified in using our *GW* QP values of IPs and EAs as a BDS for medium-sized molecules. We will use these to judge the quality of DFTB IPs and EAs.

Assessment of our DFTB calculations Figure 5.9 shows how DFTB and other approximate theoretical methods compare with our *GW* QP IP BDS. Fitting data, including Δy and Δx values, are shown in Table 5.7. In general the HF KT and the Δ SCF methods give the best absolute agreement with the *GW* QP results.

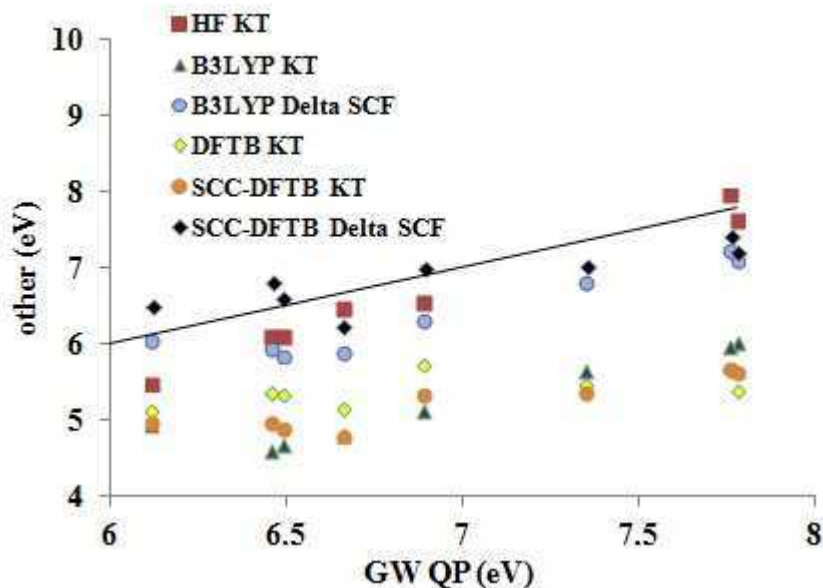


Figure 5.9 – Correlation graph of data from Table 5.5 showing how the DFTB, SCC-DFTB, and other methods compare with GW QP IPs.

Somewhat surprisingly the HF KT IPs underestimate the GW QP IPs, though HF KT IPs typically overestimate experimental IPs for small molecules. The B3LYP Δ SCF values underestimate the GW QP IPs somewhat more than do the HF KT IPs. The SCC-DFTB Δ SCF are perhaps closer in absolute values to the GW QP IPs, but the trend (slope m in Table 5.7) is better for the B3LYP Δ SCF ($m = 0.856$) than for the SCC-DFTB Δ SCF ($m = 0.520$) method. As expected the B3LYP KT, DFTB KT (same as DFTB Δ SCF), and SCC-DFTB KT values are shifted down. The trends are best represented by the B3LYP KT ($m = 0.867$) method, less so by the SCC-DFTB KT ($m = 0.504$) method, and very badly by the DFTB KT ($m = 0.199$) method. Focusing on Δx as a measure of the predictive value, we see that the B3LYP method is most predictive (Δ SCF $\Delta x = 0.256$ eV, KT $\Delta x = 0.270$ eV) but that the SCC-DFTB method is still fairly good (Δ SCF $\Delta x = 0.489$ eV, KT $\Delta x = 0.326$ eV). Surprisingly the SCC-DFTB KT approach seems to have somewhat more predictive power than does the SCC-DFTB Δ SCF method, but we would not count on this always being the case. Of course, the original DFTB is not nearly as good ($\Delta x = 0.982$ eV).

Figure 5.10 puts our results for medium-sized molecules in better perspective. In particular it shows that the inversion procedure [Eq. (5.40)] gives good results for the first IPs of both medium-sized and small molecules, but that a more sophisticated model than the present linear model would be required to maintain quantitative

Table 5.7 – Fitting data for first IPs of the medium-sized BDS molecules: $y = mx + b$, where x is the GW IP and y is another theoretical IP, both in eV. HF, Hartree-Fock; OVGf, outer valence Green’s function; LDA, local density approximation; DFTB, density-functional tight binding (without self-consistent charge); SCC-DFTB, self-consistent charge DFTB.

Method	m (unitless)	b (eV)	Δy (eV)	Δx (eV)
Koopmans’ Theorem				
HF ^a	1.484	-3.450	0.420	0.283
HF ^b	1.021	-0.674	0.856	0.838
HF ^c	1.344	-2.645	0.159	0.118
OVGF ^d	0.482	2.672	0.956	1.985
OVGF ^e	0.822	0.594	0.388	0.472
LDA	0.782	-0.024	0.361	0.461
B3LYP	0.867	-0.792	0.234	0.270
DFTB	0.200	4.030	0.197	0.982
SCC-DFTB	0.504	1.707	0.165	0.326
Δ SCF				
HF ^a	0.931	-1.074	1.069	1.149
LDA	0.644	2.472	0.318	0.493
B3LYP	0.856	0.457	0.219	0.256
DFTB	0.200	4.030	0.197	0.982
SCC-DFTB	0.520	3.235	0.254	0.489

^a HF/6-31G*//HF/6-31G* ^b HF/6-31G//B3LYP/6-31G**, except for PCBM which was calculated at the HF/STO-3G//B3LYP/6-31G** level. ^c HF/6-31G//B3LYP/6-31G**, excluding PCBM. ^d OVGF/6-31G//B3LYP/6-31G**, except for PCBM which was calculated at the OVGF/STO-3G//B3LYP/6-31G** level. ^e OVGF/6-31G//B3LYP/6-31G**, excluding PCBM.

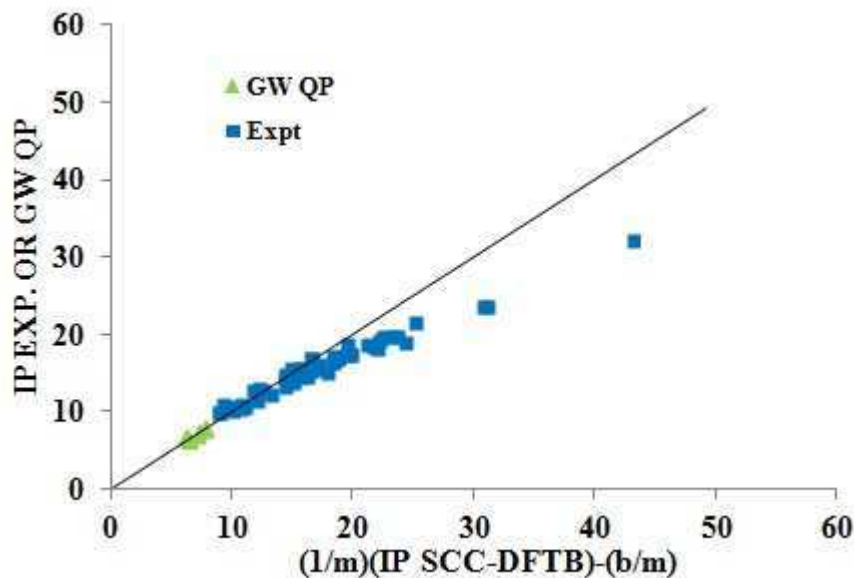


Figure 5.10 – Inversion plot showing how fitting parameters obtained for the SCC-DFTB KT IPs and medium-sized molecules predict the GW QP IPs of medium-sized molecules and the experimental IPs of small molecules.

fitting for the binding energies of more tightly-bound electrons. Thus our simple linear model seems to work well for band structure with 15 eV or less binding energy, while a more elaborate analysis is in order for binding energies above 20 eV.

Figure 5.11 shows how the DFTB and other approximate methods compare with our GW QP EA BDS. To get an idea of predictability, see Table 5.8. The HF KT EAs are expected to be an underestimate of the experimental values. Indeed, both relaxing the $(N+1)$ -electron state and taking into account the greater correlation energy of the $(N+1)$ -electron system compared to that of the N -electron system, indicates that the HF KT EAs may be expected to be smaller than the true EAs. In this case, many of the HF KT EAs are negative and hence are unreliable unbound values. DFT KT EAs are expected to behave very differently as the unoccupied DFT orbital energies may best be regarded as a first approximation on electronic excitation energies which typically smaller than EAs. This is seen in the overestimation of EAs by the DFTB KT and SCC-DFTB KT methods. As the B3LYP functional contains some admixture of HF exchange, it is normal that the B3LYP KT EAs lie somewhere inbetween the (SCC-)DFTB KT and HF KT methods. The Δ SCF method results in a dramatic improvement for EAs in both the SCC-DFTB and B3LYP cases, with particularly good absolute EAs being produced by the B3LYP Δ SCF method. Table 5.8 suggests that the main difference between the LDA, B3LYP, and SCC-DFTB

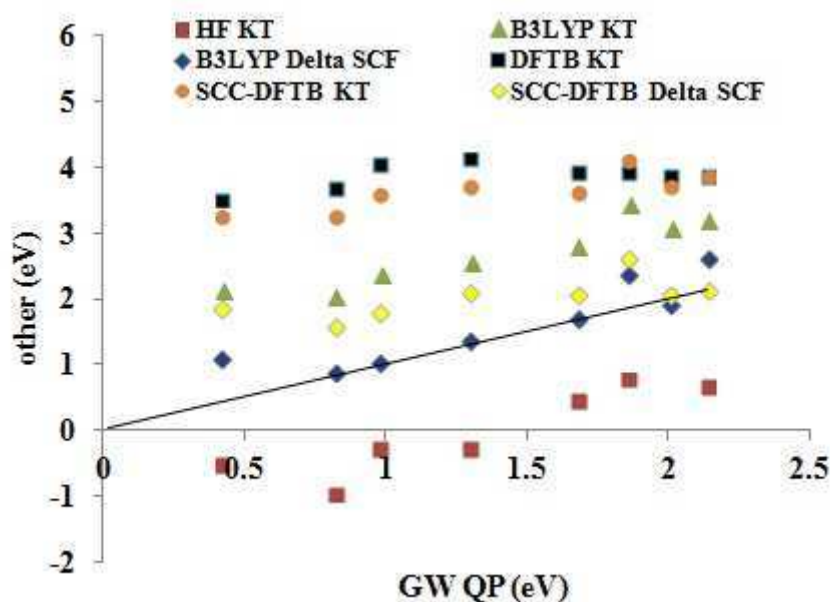


Figure 5.11 – Correlation graph of data from Table 5.5 showing how the DFTB, SCC-DFTB, and other methods (y -axis, eV) compare with GW QP (x -axis, eV) EAs.

KT and Δ SCF values is more in the value of the intercept b than in a change in the slope m . This is consistent with the idea that the KT calculations contain a derivative discontinuity contribution not present in the Δ SCF calculations. As commented earlier, this is not true for the original non-SCC DFTB method where the KT and Δ SCF calculations always give the same result. Furthermore, comparing Tables 5.7 and 5.8, we see that the main difference between the IP and EA B3LYP KT and SCC-DFTB KT fits is also in the intercept b rather than the slope m , also consistent with an important derivative discontinuity effect. Interestingly the IP and EA B3LYP Δ SCF fits show only a small shift of the intercept b while the IP and EA SCC-DFTB Δ SCF fits show a more distinct shift.

5.6 Conclusion

As emphasized, for example, by the Shokley diode model presented in the Appendix and perhaps even better by the Shokley-like model developed in Ref. [5] specifically for organic solar cells, it is important to be able to understand the underlying phenomenology of organic photovoltaics at the atomistic level. However these are complex systems which can benefit from both molecular and solid-state theory and which ultimately are likely to require hybrid approaches which are some-

Table 5.8 – Fitting data for first EAs of the medium-sized BDS molecules: $y = mx + b$, where x is the *GW* EA and y is another theoretical EA, both in eV. HF, Hartree-Fock; OVGF, outer valence Green’s function; LDA, local density approximation; DFTB, density-functional tight binding (without self-consistent charge); SCC-DFTB, self-consistent charge DFTB.

Method	m (unitless)	b (eV)	Δy (eV)	Δx (eV)
Koopmans’ Theorem				
HF ^a	-0.817	1.772	0.181	0.222
HF ^b	1.455	-1.695	0.860	0.591
HF ^c	0.971	-1.289	0.344	0.354
OVGF ^d	1.183	-0.777	0.475	0.402
OVGF ^e	0.948	-0.578	0.487	0.513
LDA	0.801	2.815	0.197	0.246
B3LYP	0.769	1.645	0.218	0.284
DFTB	0.151	3.672	0.195	1.298
SCC-DFTB	0.407	3.089	0.186	0.458
Δ SCF				
HF ^a	1.020	-0.833	0.460	0.451
LDA	0.917	1.107	0.303	0.331
B3LYP	0.926	0.330	0.317	0.342
DFTB	0.150	3.672	0.195	1.298
SCC-DFTB	0.340	1.552	0.252	0.740

^a HF/6-31G**//HF/6-31G* ^b HF/6-31G//B3LYP/6-31G**, except for PCBM which was calculated at the HF/STO-3G//B3LYP/6-31G** level. ^c HF/6-31G//B3LYP/6-31G**, excluding PCBM. ^d OVGF/6-31G//B3LYP/6-31G**, except for PCBM which was calculated at the OVGF/STO-3G//B3LYP/6-31G** level. ^e OVGF/6-31G//B3LYP/6-31G**, excluding PCBM.

where between what is now standard for molecules and what is now standard for inorganic solids. It is a problem, in fact, at the “nanoscale interface” between these two ideological paradigms which is likely to require the modeling the electronic structure and dynamics of ensembles of objects on the order of 1-100 nm in size. As this is beyond the reach of most first principles methods, we have decided to adopt the semi-empirical DFTB approach as a way to try to extend first principles accuracy to larger systems. Naturally this also requires us to accept some loss of accuracy whose magnitude we have tried to evaluate for IPs and EAs of small molecules and of medium-sized molecules of interest for organic electronics.

This paper has presented a test of the accuracy of DFTB and especially of third-order SCC-DFTB. It has been possible to determine this for larger molecules than is usually the case because of our access to recently developed *GW* methodology which itself has been checked against available experimental values. The final result is that DFTB3 with the ob3 parameter set is found to give the first IPs with an accuracy of ± 0.489 eV/ ± 0.326 eV with the SCC-DFTB Δ SCF/KT approaches. To judge from Fig. 5.10, lower IPs may also be determined with a similar accuracy using the SCC-DFTB KT method. The first EAs are found to be accurate to ± 0.740 eV/ ± 0.458 eV with the SCC-DFTB Δ SCF/KT approaches. We find this quite encouraging and expect that one should still be able to answer quite a few well-posed questions in organic electronics with this level of accuracy. There is a caveat however: The reader should keep in mind that results will change if a different implementation of DFTB and/or another parameter set are used.

A perhaps more important observation is that, while it is possible to optimize a semi-empirical method explicitly for IPs and EAs, the parameters in the DFTB method have not been optimized with this end in mind, but rather with the idea of being a well-balanced approximation to DFT. Thus we repeatedly find that DFTB is behaving like DFT rather than, say, a correlated HF-based *ab initio* method. Moreover, though the SCC-DFTB formalism differs significantly in details from the self-consistent solution of the DFT equations, we do find that (much like in DFT) the best way to calculate IPs and EAs is to use the Δ SCF method with SCC-DFT. However, much like in regular DFT calculations, SCC-DFT KT IPs are also found to be a reasonable way to estimate the first several IPs simultaneously and hence to obtain the molecular analogue of band spectra. Such a similarity with DFT, together with the capacity to go to larger and more complex systems, makes DFTB particularly attractive to us as we wish to go well beyond merely studying IPs and EAs to using DFTB to study the details of photochemical processes at the donor-acceptor interface in organic solar cells as all indications point to the details

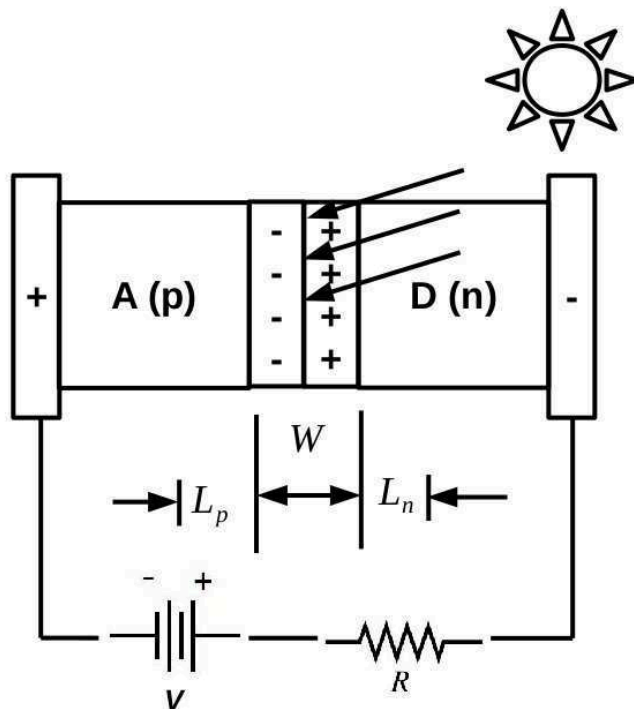


Figure 5.12 – Schematic of an organic solar cell as a Shockley diode.

of polaron pair dissociation as being a key determining step to organic photocell performance [5]. Of course, where possible, we will continue to check our DFTB results against experiment and against good first-principles computational methods as we go along.

Appendix: Brief Review of Shockley Diode Model's for Organic Solar Cells

Though some progress has been made in recent years on developing an improved physical model for organic solar cells [5, 6], the most frequent model used to describe a simple bilayer “Tang” cell involving touching layers of donor (D) and acceptor (A) molecules [103] continues to be the Shockley diode model (pp. 115-117 of Ref. [104]) familiar from the semiconductor device literature. As in Fig. 5.12, the A-D interface is identified with the p-n layer in the Shockley theory. Here V is the applied voltage (represented by the battery symbol) and R is the resistance in series with the applied voltage. According to the depletion approximation (Ref. [105], pp. 159-185), charge transfer already occurs in the unperturbed system (in the dark with $V = 0$ and the

current $I = 0$), creating a dipole bilayer depletion region. Analysis of the current in this region (Ref. [105], pp. 462-470) leads to the diode equation,

$$I = I_L + I_0 \left[1 - \exp \left(\frac{V + RI}{nV_T} \right) \right], \quad (5.43)$$

where $V_T = kT/e$ is the “thermal voltage” and n is the ideality factor [$n \neq 1$ is an empirical correction to include nonideal charge generation and recombination effects (Ref. [105], p. 186)]. The short-circuit voltage is $I_{sc} = I_L$ while the open-circuit voltage is,

$$V_{oc} = nV_T \ln \left(1 + \frac{I_L}{I_0} \right). \quad (5.44)$$

This involves the reverse bias saturation current,

$$\lim_{V \rightarrow -\infty} (I - I_L) = I_0 = eA \left(\frac{D_p p_n}{L_p} + \frac{D_n n_p}{L_n} \right), \quad (5.45)$$

where A is the area of the solar cell cross-section, D_p is the diffusion coefficient for the positive charge carriers, D_n is the diffusion coefficient for the negative charge carriers, L_p and L_n are the corresponding diffusion lengths, n_p is the density of negative carriers in the acceptor half of the solar cell, and p_n is the density of positive carriers in the donor half of the solar cell. The short-circuit current,

$$I_{sc} = e\alpha J_{ph} (L_p + L_n + W) A, \quad (5.46)$$

involves the width W of the depletion region, the photon flux J_{ph} , and the absorption coefficient α which is defined in terms of the variation of optical power in the material, $P_{op}(x) = P_{op}(0) \exp(-\alpha x)$ as a function of the depth, x of light penetration. The diode model presented above could be made more elaborate, but it already captures much of the fundamental physics and is sufficient for present purposes. The diode equation also gives a good empirical fit to experiment in many cases. However it has been criticized on the grounds that the physical quantities used to derive the Shockley model are not the most appropriate ones to describe an organic solar cell and that some phenomena require a different derivation which is more closely tied to the fundamental physics of organic solar cells [5, 6] and that the Shockley model cannot describe certain phenomena such as the S-shaped current-voltage curves sometimes observed in organic solar cells [5, 6, 106, 107]. Either in the context of the Shockley model or, better yet, in terms of some improved model, it is tempting to try to calculate first principles parameters for use in the diode equation for comparison against experiment and, in particular, to seek a better understanding

of how charge separation occurs near the donor-acceptor interface both in the dark and when illuminated.

One thing which is conspicuously missing from the above theory is the notion of an energy gap, E_g . This may be recovered by applying the detailed balance assumption [108] (i) that all absorbed photons create an electron-hole pair and (ii) that every photon whose energy is greater than the fundamental gap E_g is absorbed. In the present case this leads to the intuitively appealing result [109] that,

$$V_{oc} \leq E_g, \quad (5.47)$$

with near equality for ideal solar cells. While $V_{oc} \approx E_g$ is certainly much easier to calculate than using Eq. (5.44), we must remember that this is only an ideal limit. Also, the basic theoretical argument does not specify the nature of the gap, only that every photon is absorbed whose energy exceeds that gap. The nature of this gap in real organic solar cells has been a matter of some discussion. Thus an early paper of Brabec *et al.* argued that the difference between the highest occupied molecular orbital (HOMO) energy of the donor and the lowest unoccupied molecular orbital (LUMO) energy of the acceptor was the dominant determining factor for the gap in organic solar cells [110], in contradiction with earlier work which indicated the importance of the difference of the work functions of the electrodes [111, 112]. This seems to have been resolved by latter work [113] showing that for ohmic contacts,

$$V_{oc} = \frac{1}{e} (\epsilon_{\text{HOMO}}^D - \epsilon_{\text{LUMO}}^A) + \Delta V_b, \quad (5.48)$$

where $\text{IP}_D = -\epsilon_{\text{HOMO}}^D$ is the electron removal energy of the donor, $\text{EA}_A = -\epsilon_{\text{LUMO}}^A$ is the electron attachment energy of the acceptor, and ΔV_b is a correction term for band bending at the electrodes which can presumably be made arbitrarily small for ohmic contacts with small band offsets. Equation (5.48) is written in the language of band theory. Let us emphasize that it is simply an equation involving the donor ionization potential and the acceptor electron affinity,

$$V_{oc} = \frac{1}{e} (\text{EA}_A - \text{IP}_D) + \text{constant}, \quad (5.49)$$

where the “constant” is presumably a function of the nature of the electrode junctions. (See also Ref. [114].)

Acknowledgments

This work is supported, in part, by the ORGAVOLT (ORGAnic solar cell VOLTage by numerical computation) grant ANR-12-MONU-0014-02 of the French *Agence Nationale de la Recherche (ANR) 2012 Programme Modèles Numériques*. ML, PK and DSP acknowledge support from the *Deutsche Forschungsgemeinschaft (DFG)* through the SFB 1083 project and the Spanish MINECO MAT2013-46593-C6-2-P project. DSP and PK acknowledge financial support from projects FIS2013-14481-P from MINECO, the Euroregion Aquitaine-Euskadi program and support from Basque *Departamento de Educación*, UPV/EHU (Grant No. IT-756-13). PK acknowledges financial support from the Fellows Gipuzkoa program of the *Gipuzkoako Foru Aldundia* through the FEDER funding scheme of the European Union. AD would like to thank the French and Irakian governments for support through a Campus France scholarship. WT would like to acknowledge support from the government of Tunisia. Grenoble *Centre d'Expérimentation du Calcul Intensif en Chimie (CE-CIC)* computing resources are gratefully acknowledged as is computing help from Pierre Girard. MEC would like to acknowledge a helpful discussion with Kuntheak Kheng. MEC and AD would like to acknowledge helpful discussions with Mathias Rapacioli. We would also like to thank Thomas A. Niehaus for his comments on an earlier version of this manuscript and for calling our attention to the preprint [14].

Author Contributions

Calculations were carried out by AD (DFTB, DFT, OVGF), WT (DFT), and PK (*GW*) under the direction of MEC (AD), KA (WT), and DSP (ML and PK). Significant programming in the MBPT_LCAO code was done by DF, DSP, ML, and PK. The bulk of manuscript writing was done by MEC with significant contributions from AD, WT, ML, and PK.

Conflicts of Interest

The authors declare no conflict of interest.

Bibliography

- [1] S. M. Sze and K. K. Ng, [Physics of Semiconductor Devices](#), Wiley, Hoboken, New Jersey, third edition, 2007. pages 87, 223

- [2] L. W. Nagel and D. O. Pederson, SPICE ([Simulation Program with Integrated Circuit Emphasis](#)), Memorandum No. ERL-M382, University of California, Berkeley, Apr. 1973; L. W. Nagel, SPICE2: A Computer Program to Simulate Semiconductor Circuits, Memorandum No. ERL-M520, University of California, Berkeley, May 1975. pages 87
- [3] K. Harada et al., [Organic homojunction diodes with a high built-in potential: Interpretation of the current-voltage characteristics by a generalized Einstein relation](#), Phys. Rev. Lett. **94**, 036601 (2005). pages 87
- [4] Y. Vaynzof, Y. Preezant, and N. Tessler, [Current voltage relation of amorphous materials based p n diodes—the effect of degeneracy in organic polymers/molecules](#), J. Appl. Phys. **106**, 084503 (2009). pages 87
- [5] N. C. Giebink, G. P. Wiederrecht, M. R. Wasielewski, and S. R. Forrest, [Ideal diode equation for organic heterojunctions. I. Derivation and application](#), Phys. Rev. B **82**, 155305 (2010). pages 87, 121, 124, 125
- [6] N. C. Giebink, B. E. Lassiter, G. P. Wiederrecht, M. R. Wasielewski, and S. R. Forrest, [Ideal diode equation for organic heterojunctions. II. The role of polaron pair recombination](#), Phys. Rev. B **82**, 155306 (2010). pages 87, 124, 125
- [7] D. C. Tripathi and Y. N. Mohapatra, [Ideal organic homojunction diode obtained using controlled alignment of localized density of states across doped/undoped interface](#), Org. Electronics **13**, 1680 (2012). pages 87
- [8] A. D. D. Dwivedi, [Numerical Simulation and Spice Modeling of Organic Thin Film Transistors \(OTFTs\)](#), Int. J. Adv. Appl. Phys. Res. **1**, 14 (2014). pages 87
- [9] K. Müllen and U. Scherf, editors, [Organic Light-Emitting Devices](#), Springer-Verlag, Berlin, 1990. pages 87, 164
- [10] G. Yu, J. Gao, J. C. Hummelen, F. Wudl, and A. J. Heeger, [Polymer Photovoltaic Cells: Enhanced Efficiencies via a Network of Internal Donor-Acceptor Heterojunctions.](#), Science **270**, 1789 (1995). pages 16, 87
- [11] Y.-S. Huang et al., [Electronic structures of interfacial states formed at polymeric semiconductor heterojunctions](#), Nat. Mat. **7**, 483 (2008). pages 87
- [12] L. Dou et al., [25th anniversary article: A decade of organic/polymer photovoltaic research](#), Adv. Mat. **25**, 6642 (2013). pages 87
- [13] R. Scholz et al., [Topical Review: Quantifying charge transfer energies at donor-acceptor interfaces in small-molecule solar cells with constrained DFTB and spectroscopic methods](#), J. Phys.: Condens. Matter **25**, 473201 (2013). pages 88

- [14] V. Lutsker, B. Aradi, and T. A. Niehaus, [Implementation and benchmark of a long-range corrected functional in the density functional based tight-binding method](#), J. Chem. Phys. **143**, 184107 (2015). pages 88, 95, 127, 171, 235
- [15] T. Niehaus and F. D. Salla, [Range separated functionals in the density functional based tight-binding method: Formalims](#), Phys. Stat. Solidi B **249**, 237 (2012). pages 88, 171, 235
- [16] A. Humeniuk and R. Mitrić, [Long-range correction for tight-binding TD-DFT](#), J. Chem. Phys. **143**, 34120 (2015). pages 88, 171, 172, 173, 228, 235, 239, 241
- [17] L. Hedin, [New Method for Calculating the One-Particle Green's Function with Application to the Electron-Gas Problem](#), Phys. Rev. **139**, A796 (1965). pages 88, 93
- [18] G. Onida, L. Reining, and A. Rubio, [Electronic excitations: Density-functional versus many-body Green's-function approaches](#), Rev. Mod. Phys. **74**, 601 (2002). pages 88
- [19] D. Foerster, P. Koval, and D. Sanchez-Portal, [An \$\mathcal{O}\(N^3\)\$ implementation of Hedin's *GW* approximation for molecules](#), journal=J. Chem. Phys., **135**, 074105 (2011). pages 88, 93, 99, 101
- [20] F. Pilar, [Elementary Quantum Chemistry](#), McGraw-Hill Book Co., New York, 1968. pages 90
- [21] R. G. Parr and W. Yang, [Density-Functional Theory of Atoms and Molecules](#), Oxford University Press, New York, 1989. pages 62, 65, 90, 159, 231
- [22] R. M. Dreizler and E. K. U. Gross, [Density Functional Theory, An Approach to the Quantum Many-Body Problem](#), Springer-Verlag, New York, 1990. pages 90, 159, 231
- [23] W. Koch and M. C. Holthausen, [A Chemist's Guide to Density Functional theory: Introduction to the DFT](#), WILEY-VCH, New York, 2000. pages 90, 159, 231
- [24] K. Burke, [Perspective on density functional theory](#), J. Chem. Phys. **136**, 150901 (2012). pages 90
- [25] A. D. Becke, [Perspective: Fifty years of density-functional theory in chemical physics](#), J. Chem. Phys. **140**, 18A301 (2014). pages 90
- [26] S. R. Whittleton, X. A. S. Vazquez, C. M. Isborn, and E. R. Johnson, [Density-functional errors in ionization potentials with increasing system size](#), J. Chem. Phys. **142**, 184106 (2015). pages 91, 113

- [27] D. Danovich, [Green's function methods for calculating ionization potentials, electron affinities, and excitation energies](#), *Comput. Molec. Sci.* **1**, 377 (2011). pages 93
- [28] W. von Niessen, J. Schirmer, and L. S. Cederbaum, [Computational methods for the one-particle Green's function](#), *Comput. Phys. Reports* **1**, 57 (1984). pages 93
- [29] M. E. Casida and D. P. Chong, [Physical interpretation and assessment of the Coulomb-hole and screened-exchange approximation for molecules](#), *Phys. Rev. A* **40**, 4837 (1989). pages 93
- [30] M. E. Casida and D. P. Chong, [Erratum: "Physical interpretation and assessment of the Coulomb-hole and screened-exchange approximation for molecules"](#), *Phys. Rev. A* **44**, 6151 (1991). pages 93
- [31] M. E. Casida and D. P. Chong, [Simplified Green-function approximations: Further assessment of a polarization model for second-order calculation of outer-valence ionization potentials in molecules](#), *Phys. Rev. A* **44**, 5773 (1991). pages 93
- [32] G. Onida, L. Reining, R. W. Godby, R. Del Sole, and W. Andreoni, [Ab initio calculations of the quasiparticle and absorption spectra of clusters: the sodium tetramer](#), *Phys. Rev. Lett.* **75**, 818 (1995). pages 93
- [33] C. Hu, D. P. Chong, and M. E. Casida, [The parameterized second-order Green function times screened interaction \(pGW2\) approximation for calculation of outer valence ionization potentials](#), *J. Electron Spectr.* **85**, 39 (1997). pages 93
- [34] Y. Shigeta, A. M. Ferreira, V. G. Zakrzewski, and J. V. Ortiz, [Electron propagator calculations with Kohn-Sham reference states](#), *Int. J. Quant. Chem.* **85**, 411 (2001). pages 93
- [35] P. H. Hahn, W. G. Schmidt, and F. Bechstedt, [Molecular electronic excitations from a solid-state approach](#), *Phys. Rev. B* **72**, 245425 (2005). pages 93
- [36] X. Blase, C. Attaccalite, and V. Olevano, [First-principles GW calculations for fullerenes, porphyrins, phtalocyanine, and other molecules of interest for organic photovoltaic applications](#), *Phys. Rev. B* **115**103 (2011). pages 93, 115
- [37] M. E. Casida, [Generalization of the Optimized Effective Potential Model to Include Electron Correlation: A Variational Derivation of the Sham–Schlüter Equation for the Exact Exchange-Correlation Potential](#), *Phys. Rev. A* **51**, 2005 (1995). pages 93
- [38] P. Duffy, D. Chong, M. E. Casida, and D. R. Salahub, [Assessment of Kohn–Sham Density-Functional Orbitals as Approximate Dyson Orbitals for the Calcula-](#)

- tion of Electron-Momentum-Spectroscopy Scattering Cross Sections, *Phys. Rev. A* **50**, 4707 (1994). pages 93
- [39] C. E. Brion, G. Cooper, Y. Zheng, I. V. Litvinyuk, and I. E. McCarthy, [Imaging of orbital electron densities by electron momentum spectroscopy — a chemical interpretation of the binary \(e,2e\) reaction](#), *Chem. Phys.* **270**, 13 (2001). pages 93
- [40] S. Hamel, P. Duffy, M. Casida, and D. Salahub, [Kohn-Sham orbitals and energies: fictitious constructs but good approximations all the same](#), *Journal of Electron Spectroscopy and Related Phenomena*. **123**, 345 (2002). pages 93, 103, 104, 105, 106, 107, 110, 111, 305, 310
- [41] S. Hamel, M. E. Casida, and D. R. Salahub, [Exchange-only optimized effective potential for molecules from resolution-of-the-identity techniques: Comparison with the local density approximation, with and without asymptotic correction](#), *J. Chem. Phys.* **116**, 8276 (2002). pages 94, 108
- [42] R. W. Godby, M. Schlüter, and L. J. Sham, [Self-energy operators and exchange-correlation potentials in semiconductors](#), *Phys. Rev. B* **37**, 10159 (1988). pages 94
- [43] Z. H. Levine and D. C. Allan, [Linear optical response in silicon and germanium including self-energy effects](#), *Phys. Rev. Lett.* **63**, 1719 (1989). pages 94
- [44] X. Gonze and C. Lee, [Dynamical matrices, Born effective charges, dielectric permittivity tensors and interatomic force constants from density-functional perturbation theory](#), *Phys. Rev. B* **55**, 10355 (1997). pages 94
- [45] E. Hückel, [Quantentheoretische Beiträge zum Benzolproblem](#), *Z. Physik* **70**, 204 (1931). pages 94
- [46] E. Hückel, [Quantentheoretische Beiträge zum Benzolproblem II. Quantentheorie der induzierten Polaritäten](#), *Z. Physik* **72**, 310 (1931). pages 94
- [47] E. Hückel, [Quantentheoretische Beiträge zum Problem der aromatischen und ungesättigten Verbindungen. III](#), *Z. Physik* **76**, 628 (1932). pages 94
- [48] J. C. Slater and G. F. Koster, [Simplified LCAO Method for the Periodic Potential Problem](#), *Phys. Rev.* **94**, 1498 (1954). pages 94
- [49] R. Hoffmann, [An extended Hückel theory. I. Hydrocarbons](#), *J. Chem. Phys.* **39**, 1397 (1963). pages 94
- [50] R. Hoffmann, [An extended Hückel theory. II. \$\sigma\$ orbitals in the azines](#), *J. Chem. Phys.* **40**, 2745 (1964). pages 94

- [51] R. Hoffmann, [An extended Hückel theory. III. Compounds of boron and nitrogen](#), J. Chem. Phys. **40**, 2474 (1964). pages 94, 167
- [52] R. Hoffmann, [An extended Hückel theory. IV. Carbonium ions](#), J. Chem. Phys. **40**, 2480 (1964). pages 94, 167
- [53] D. Porezag, T. Frauenheim, T. Köhler, G. Seifert, and R. Kaschner, [Construction of tight-binding-like potentials on the basis of density-functional theory: Application to carbon](#), Phys. Rev. B **51**, 12947 (1995). pages 94, 98, 167, 235
- [54] M. Elstner, [Weiterentwicklung quantenmechanischer Rechenverfahren für organische Moleküle und Polymere](#), PhD thesis, Universität-Gesamthochschule Paderborn, 1998. pages 94
- [55] A. Frauenheim et al., [A self-consistent charge density-functional based tight-binding method for predictive materials simulations in physics, chemistry, and biology](#), Phys. Stat. Sol. B **217**, 41 (2000). pages 94
- [56] P. Koskinen and V. Mäkinen, [Density-functional tight-binding for beginners](#), Comp. Mater. Sci. **47**, 237 (2009). pages 94, 98, 167, 227, 235
- [57] T. Bredow and K. Jug, [Theory and range of modern semiempirical molecular orbital methods](#), Theor. Chem. Acc. **113**, 1 (2005). pages 94, 167, 239
- [58] W. Thiel, [Semiempirical quantum-chemical methods in computational chemistry](#), in *Theory and Applications of Computational Chemistry: The First Forty Years*, edited by C. Dykstra, G. Frenking, K. Kim, and G. Scuseria, chapter 21, pages 559–580, Elsevier, 2005. pages 94
- [59] P. Hohenberg and W. Kohn, [Inhomogeneous electron gas](#), Phys. Rev. **136**, B864 (1964). pages 63, 94, 231
- [60] W. Kohn and L. J. Sham, [Self-consistent equations including exchange and correlation effects](#), Physical Review. **140**, 1133 (1965). pages 66, 94, 159, 164, 231
- [61] M. Elstner et al., [Self-consistent-charge density-functional tight-binding method for simulations of complex materials properties](#), Phys. Rev. B **58**, 7260 (1998). pages 96, 169, 236, 241
- [62] M. Gaus, Q. Cui, and M. Elstner, [DFTB3: Extension of the Self-Consistent-Charge Density-Functional Tight-Binding Method \(SCC-DFTB\)](#), J. Chem. Theory Comput. **7**, 931 (2011). pages 96, 98, 169, 236
- [63] R. Pariser, [An improvement on the \$\pi\$ -electron approximation in LCAO MO theory](#), J. Chem. Phys. **21**, 568 (1953). pages 98, 171
- [64] <http://www.dftb-plus.info/>. pages 99, 240

- [65] M. J. Frisch et al., [GAUSSIAN-09 Revision D.01](#), Gaussian Inc. Wallingford CT 2009. pages 99, 172, 173
- [66] J. M. Soler et al., [The SIESTA method for *ab initio* order- \$N\$ materials simulation](#), J. Phys.: Condens. Matter **14**, 2745 (2002). pages 99, 101
- [67] [Official web page for MBPT_LCAO](#), <http://mbpt-domiprod.wikidot.com/>. pages 99, 101
- [68] W. J. Hehre, L. Radom, P. von R. Schleyer, and J. Pople, [Ab Initio Molecular Orbital Theory](#), Wiley, 1986. pages 99, 173
- [69] <http://www.dftb.org/>. pages 99
- [70] M. Gaus, A. Goez, and M. Elstner, [Parameterization and Benchmark of DFTB3 for Organic Molecules](#), J. Chem. Theory Comput. **9**, 338 (2013). pages 99
- [71] M. Gaus, X. Lu, M. Elstner, and Q. Cui, [Parameterization of DFTB3/3OB for sulfur and phosphorus for chemical and biological applications](#), J. Chem. Theory Comput. **10**, 1518 (2014). pages 99
- [72] W. J. Hehre, R. Ditchfield, and J. Pople, [Self-Consistent Molecular Orbital Methods. XII. Further Extensions of Gaussian-Type Basis Sets for Use in Molecular Orbital Studies of Organic Molecules](#), J. Chem. Phys. **56**, 2257 (1972). pages 100, 173, 240
- [73] P. C. Hariharan and J. A. Pople, [The influence of polarization functions on molecular orbital hydrogenation energies](#), Theor. Chem. Acc. (Theoretica Chimica Acta) **28**, 213 (1973). pages 100, 240
- [74] W. J. Hehre, R. F. Stewart, and J. A. Pople, [Self-Consistent Molecular-Orbital Methods. I. Use of Gaussian Expansions of Slater-Type Atomic Orbitals](#), J. Chem. Phys. **51**, 2657 (1969). pages 100, 173
- [75] S. H. Vosko, L. Wilk, and M. Nusair, [Accurate spin-dependent electron liquid correlation energies for local spin density calculations: a critical analysis.](#), Can. J. Phys. **58**, 1200 (1980). pages 68, 100, 161
- [76] [Becke3LYP Method References and General Citation Guidelines](#), Gaussian NEWS, v. 5, no. 2, summer 1994, p. 2. pages 100
- [77] A. Becke, [Density-functional thermochemistry. III. The role of exact exchange.](#), J. Chem. Phys. **98**, 5648 (1993). pages 100, 161, 162
- [78] R. Krishnan, J. S. Binkley, R. Seeger, and J. A. Pople, [Self-consistent molecular orbital methods. XX. A basis set for correlated wave functions](#), J. Chem. Phys. **72**, 650 (1980). pages 100

- [79] T. Clark, J. Chandrasekhar, and P. V. R. Schleyer, [Efficient diffuse function-augmented basis sets for anion calculations. III. The 3-21+G basis set for first-row elements, Li-F](#), J. Comp. Chem. **4**, 294 (1983). pages 100
- [80] P. Koval, D. Foerster, and D. Sánchez-Portal, [Fully self-consistent *GW* and quasiparticle self-consistent *GW* for molecules](#), Phys. Rev. B **89**, 155417 (2014). pages 102
- [81] C. A. Coulson, [Present state of molecular structure calculations](#), Rev. Mod. Phys. **32**, 170 (1960). pages 104
- [82] J. A. Pople, [Two-dimensional chart of quantum chemistry](#), J. Chem. Phys. **43**, S229 (1965). pages 104
- [83] M. Karplus, [Three-dimensional “Pople diagram”](#), J. Phys. Chem. **94**, 5436 (1990). pages 104
- [84] P. Duffy and D. P. Chong, [Study of transition-state methods in the calculation of vertical ionization potentials by the local density approximation](#), Organic Mass. Spectr. **28**, 321 (1993). pages 107, 112
- [85] M. E. Casida and D. R. Salahub, [Asymptotic correction approach to improving approximate exchange-correlation potentials: Time-dependent density-functional theory calculations of molecular excitation spectra](#), J. Chem. Phys. **113**, 8918 (2000). pages 106
- [86] C. R. Brundle, M. B. Robin, and H. Basch, [Electronic Energies and Electronic Structures of the Fluoromethanes](#), J. Chem. Phys. **53**, 2196 (1970). pages 106
- [87] C. R. Brundle, M. B. Robin, H. Basch, M. Pinsky, and A. Bond, [Experimental and theoretical comparison of the electronic structures of ethylene and diborane](#), J. Am. Chem. Soc. **92**, 3863 (1970). pages 106
- [88] T. Takahashi et al., [Gas and solid-phase photoelectron spectra of 5,6,11,12-tetraphenylanthracene \(rubrene\)](#), Bull. Chem. Soc. Japan **52**, 380 (1979). pages 113, 115
- [89] B. W. D’Andrade et al., [Relationship between the ionization and oxidation potentials of molecular organic semiconductors](#), Organic Electronics **6**, 11 (2005). pages 113
- [90] R. Fitzner et al., [Dicyanovinyl-substituted oligothiophenes: Structure-property relationships and application in vacuum-processed small-molecule organic solar cells](#), Adv. Funct. Mater. **21**, 897 (2011). pages 115, 116
- [91] J. Berkowitz, [Photoelectron spectroscopy of phthalocyanine vapors](#), J. Chem. Phys. **70**, 2819 (1979). pages 115

- [92] D. P. Piet, D. Danovich, H. Zuilhof, and E. J. R. Sudhölter, [Ionization potentials of porphyrins and phthalocyanines. A comparative benchmark study of fast improvements of Koopman's Theorem](#), J. Chem. Soc. Perkin Trans. **2**, 1653 (1999). pages 115
- [93] M. Montalti, A. Credit, L. Prodi, and M. T. Gandolfi, [Handbook of Photochemistry, Third Edition](#), Taylor and Francis, United Kingdom, 2006. pages 25, 115
- [94] A. Tada, Y. Geng, Q. Wei, K. Hashimoto, and K. Tajima, [Tailoring organic heterojunction interfaces in bilayer polymer photovoltaic devices](#), Nature Materials **10**, 450 (2011). pages 115
- [95] N. Sai, M. L. Tiago, J. R. Chelikowsky, and F. A. Reboredo, [Optical spectra and exchange-correlation effects in molecular crystals](#), Phys. Rev. B **77**, 161306 (2008). pages 115, 116
- [96] A. Wilke et al., [Correlation between interface energetics and open circuit voltage in organic photovoltaic cells](#), Appl. Phys. Lett. **101**, 233301 (2012). pages 115, 116
- [97] S. Cook, R. Katoh, and A. Furube, [Ultrafast Studies of Charge Generation in PCBM:P3HT Blend Films following Excitation of the Fullerene PCBM](#), J. Phys. Chem. C **113**, 2547 (2009). pages 115
- [98] L. Crocker, T. B. Wang, and P. Kebarle, [Electron affinities of some polycyclic aromatic hydrocarbons, obtained from electron-transfer equilibria](#), J. Am. Chem. Soc. **115**, 7818 (1993). pages 116
- [99] D. L. Huang, P. D. Dau, H. T. Liu, and L. S. Wang, [High-resolution photoelectron imaging of cold \$C_{60}^-\$ anions and accurate determination of the electron affinity of \$C_{60}\$](#) , J. Chem. Phys. **140**, 224315 (2014). pages 116
- [100] K. Akaike et al., [Ultraviolet photoelectron spectroscopy and inverse photoemission spectroscopy of \[6,6\]-phenyl- \$C_{61}\$ -butyric acid methyl ester in gas and solid phases](#), J. Appl. Phys. **104**, 023710 (2008). pages 116
- [101] S. Siegert, F. Vogeler, C. M. Marian, and R. Weinkauf, [Throwing light on dark states of \$\alpha\$ -oligothiophenes of chain lengths 2 to 6: radical anion photoelectron spectroscopy and excited-state theory](#), Phys. Chem. chem. Phys. **13**, 10350 (2011). pages 116
- [102] B. W. Larson et al., [Electron Affinity of Phenyl- \$C_{61}\$ -Butyric Acid Methyl Ester \(PCBM\)](#), J. Phys. Chem. C **117**, 14958 (2013). pages 116
- [103] C. W. Tang, [Two-layer organic photovoltaic cell.](#), Appl. Phys. Lett. **48**, 183 (1986). pages 15, 124, 224

- [104] S. C. Jain, M. Willander, and V. Kumar, [Conducting Organic Materials and Devices](#), volume 81 of *Semiconductors and Semimetals*, Academic Press, New York, 2007. pages 124
- [105] J. Singh, [Semiconductor Devices: Basic Principles](#), John Wiley and Sons, New York, 2001. pages 124, 125
- [106] J. Wagner et al., [Identification of different origins for s-shaped current voltage characteristics in planar heterojunction solar cells](#), J. Appl. Phys. **111**, 054509 (2012). pages 125
- [107] Y. H. Huh, B. Park, and I. Hwang, [Investigating the origin of S-shaped photocurrent-voltage characteristics of polymer:fullerene bulk-heterojunction organic solar cells](#), J. Appl. Phys. **115**, 124504 (2014). pages 125
- [108] W. Shockley and H. Queisser, [Detailed balance limit of efficiency of \$p-n\$ junction solar cells.](#), J. Appl. Phys. **32**, 510 (1961). pages 17, 19, 126, 309
- [109] P. Baruch, A. D. Vos, P. T. Landsberg, and J. E. Parrott, [On some thermodynamics aspects of photovoltaic solar energy conversion](#), Solar Energy Materials and Solar Cells **36**, 201 (1995). pages 126
- [110] C. J. Brabec et al., [Origin of the Open Circuit Voltage of Plastic Solar Cells](#), Adv. Funct. Mater **11**, 374 (2001). pages 126
- [111] G. Yu, K. Pakbaz, and A. J. Heeger, [Semiconducting polymer diodes: Large size, low cost photodetectors with excellent visible-ultraviolet sensitivity](#), Appl. Phys. Lett. **64**, 3422 (1994). pages 126
- [112] G. Yu and A. J. Heeger, [Charge separation and photovoltaic conversion in polymer composites with internal donor/acceptor heterojunctions](#), J. Appl. Phys. **78**, 4510 (1995). pages 126
- [113] V. D. Mihailetschi, P. W. M. Blom, J. C. Hummelen, and M. T. Rispens, [Cathode dependence of the open-circuit voltage of polymer:fullerene bulk heterojunction solar cells](#), J. Appl. Phys. **94**, 6849 (2003). pages 126
- [114] M. C. Scharber et al., [Design rules for donors in bulk-heterojunction solar cells — Towards 10% energy-conversion efficiency](#), Adv. Mater. **18**, 789 (2006). pages 126

Chapter 6

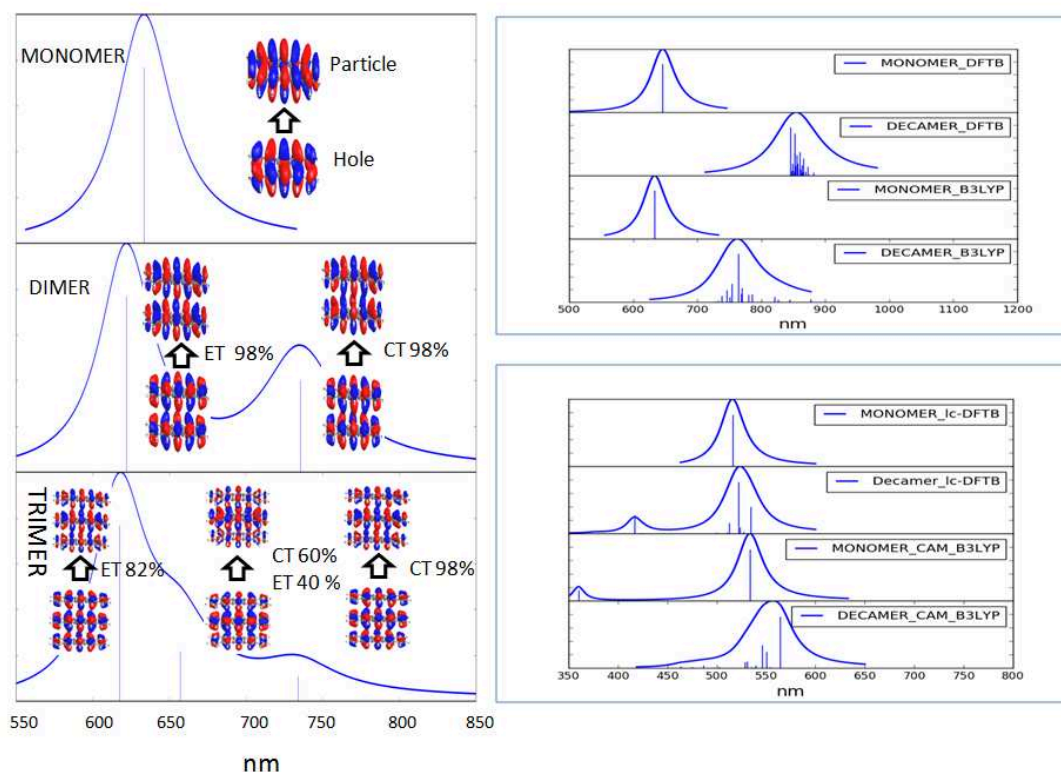
Davydov-Type Excitonic Effects on the Absorption Spectra of Parallel-Stacked and Herringbone Aggregates of Pentacene: Time-Dependent Density-Functional Theory and Time-Dependent Density-Functional Tight Binding

Davydov-Type Excitonic Effects on the Absorption Spectra of Parallel-Stacked and Herringbone Aggregates of Pentacene: Time-Dependent Density-Functional Theory and Time-Dependent Density-Functional Tight Binding

Ala Aldin M. H. M. Darghouth¹, Gabriela Calinao Correa [1]², Sacha Juillard³,
Mark E. Casida⁴,

*Laboratoire de Chimie Théorique, Département de Chimie Moléculaire (DCM),
Institut de Chimie Moléculaire de Grenoble (ICMG), Université Grenoble-Alpes,
301 rue de la Chimie, CS 40700, 38058 Grenoble Cedex 9, France*

Alexander Humeniuk⁵, Roland Mitrić⁶,
*Institut für physikalische und theoretische Chemie, Julius-Maximilians Universität
Würzburg,
Emil-Fischer-Straße 42, D-97074 Würzburg, Germany*



1. ala.darghout@univ-grenoble-alpes.fr
2. gcc73@cornell.edu
3. sachajuillard@univ-savoie.fr
4. mark.casida@univ-grenoble-alpes.fr
5. alexander.humeniuk@gmail.com
6. roland.mitric@uni-wuerzburg.de

Abstract

Exciton formation leads to J-bands in solid pentacene. Describing these exciton bands represents a challenge for both time-dependent (TD) density-functional theory (DFT) and for its semi-empirical analogue, namely for TD density-functional tight binding (DFTB) for three reasons: (i) solid pentacene and pentacene aggregates are bound only by van der Waals forces which are notoriously difficult to describe with DFT and DFTB, (ii) the proper description of the long-range coupling between molecules, needed to describe Davydov splitting, is not easy to include in TD-DFT with traditional functionals and in TD-DFTB, and (iii) mixing may occur between local and charge transfer excitons, which may, in turn, require special functionals. We assess how far TD-DFT and TD-DFTB have progressed towards a correct description of this type of exciton by including both a dispersion correction for the ground state and a range-separated hybrid functional for the excited state. Analytic results for parallel-stacked ethylene are derived which go beyond Kasha's exciton model [Kasha, Rawls, and El-Bayoumi, *Pure Appl. Chem.* **11**, 371 (1965)] in that we are able to make a clear distinction between charge transfer and energy transfer excitons. This is further confirmed when it is shown that range-separated hybrids have a markedly greater effect on charge-transfer excitons than on energy-transfer excitons in the case of parallel-stacked pentacenes. TD-DFT calculations with the CAM-B3LYP functional and TD-lc-DFT calculations lead to negligible excitonic corrections for the herringbone crystal structure, possibly because of an overcorrection of charge-transfer effects. In this case, TD-DFT calculations with the B3LYP functional or TD-DFTB calculations parameterized to B3LYP give the best results for excitonic corrections for the herringbone crystal structure as judged from comparison with experimental spectra and with Bethe-Salpeter equation calculations from the literature. Oddly enough Kasha's original formulation only seems to work when a range-separated functional is used in the case of off-set parallel pentacenes. This is traced back to a lack of consideration of avoided crossings in Kasha's original formulation. Our improved model based upon nearest neighbor interactions does not suffer from this difficulty.

6.1 Introduction

Density-functional theory (DFT) has gained popularity for first-principles calculations of medium- to large-sized molecules or when large numbers of successive calculations are needed such as is the case for molecular dynamics. In fact, DFT has largely supplanted the older Hartree-Fock (HF) theory, except in cases where

HF calculations are followed up by sophisticated post-HF correlated calculations. Although hybrid methods which integrate HF exchange into DFT have become popular, major Achilles heels of DFT have been dispersion forces and charge transfer phenomena. Likewise time-dependent (TD) DFT has become the dominant single-determinant-based approach for describing the excited states of medium- and large-sized molecules. But TD-DFT inherits many of the same problems as DFT, with a few more of its own [2, 3]. Density-functional tight-binding (DFTB) and TD-DFTB are semi-empirical versions, respectively, of DFT and of TD-DFT which (as should be expected from good approximations to DFT and to TD-DFT) inherit many of the problems from their first principles counterparts. General reliability and good scaling would seem to make DFT and TD-DFT (in the first place) and DFTB and TD-DFTB (for still larger systems) excellent choices for atomistic modeling of organic electronics. However dispersion and charge transfer may or may not present real obstacles. The objective of this article is to take a look at the ability of modern DFT, TD-DFT, DFTB, and TD-DFTB to model aggregates of pentacene and solid pentacene. Our focus will be on intermolecular interactions in both the ground and in excited states.

Organic materials are typically bound together by some combination of hydrogen bonding and van der Waals forces. In the case of pentacene, the forces binding the molecules together are purely van der Waals in nature. It is thus imperative to be able to include dispersion forces. Traditional density functionals, such as the local density approximation (LDA), generalized gradient approximations (GGAs), meta-GGAs, and hybrid functionals fail to include the “action at a distance” aspect of dispersion forces because of their inability to give an accurate description of forces between molecules with nonoverlapping densities. Perhaps ironically, C_6 van der Waals coefficients — and hence dispersion forces — may be calculated accurately by TD-DFT. At this time, the most popular way to include dispersion forces in DFT calculations is to add on a semi-empirical correction [4] which is designed to interpolate between the DFT description of the charge density and the TD-DFT description of C_6 coefficients.

Organic electronics relies upon charge transport. However positive and negative carriers may be transported together in a charge-neutral packet called an exciton. From the condensed-matter point of view, excitons are born as local excitations. In fact, it is useful to make a distinction between “exciton structure” and “exciton dynamics” (p. 5 Ref. [5]). Although related to each other, exciton structure is more directly related to absorption spectra — the subject of the present article — while exciton dynamics falls more conveniently under the heading of charge and energy

transport [6]. Even within the seemingly narrow subject of exciton structure, excitons seem to mean different things to different people. In particular, solid-state physicists may seem to require periodic (crystal) boundary conditions [5] in their definition of excitons, while chemists [7, 8] and biochemists [9] do not.

Here we focus on molecular solids where intermolecular interactions are important. Frenkel introduced the term “excitation packets” in his early study of the conversion of light into heat in solids [10, 11]. Unlike molecules which may often be considered to be small enough compared to the size of a photon that the photon may be approximated by an oscillating electric field, a solid is large compared to a photon. Moreover the crystal molecular orbitals should in principle extend over the entire crystal and so must also be large compared to the size of a photon. Yet experimental observations, and indeed common sense, suggests that photons may be absorbed locally. How may this observation be reconciled with the well-established concept of crystal molecular orbitals in periodic systems? Frenkel’s excitation packets resolved this apparent paradox by allowing the nearly degenerate crystal molecular orbitals to form wave packets whose size is on the order of one or several molecules and so for which photon absorption may be treated much like that of a molecule. This, in modern language, is the Frenkel exciton (FR). Another type of exciton — the Wannier-Mott exciton (WM) [12] — may be constructed for metals and semiconductors. Although not critical for the present work, it should be noted that FRs and WMs in periodic systems may be regarded as delocalized crystal states with a high conditional probability that, having specified the position of one charge, the other charge will then be found somewhere in the local neighborhood. The FRs and WMs form limiting cases, with real excitons being somewhere inbetween [5]. Thus, for a solid-state physicist, an exciton is a localized excitation which is small compared to a solid. A variation upon Frenkel excitons are Davydov excitons [13, 14] which will be discussed in the next paragraph.

Physical chemists and chemical physicists seem to have come across the exciton idea in a different way than did solid-state physicists, namely by noticing the appearance of new spectral features when certain dyes aggregate in concentrated solution. If new very narrow peaks appear at lower energies, they are referred to as J-bands [15] (J for Jelly [16, 17] who, along with Scheibe [18, 19] were some of the first to investigate this phenomenon); if the new peaks appear at higher energies, they are referred to as H-bands (H for hypsochromic). Kasha and coworkers were able to give a convincing description of the origin of these bands in terms of the same ideas used by Davydov for solids [7, 8]. In particular, local excitons on different molecules interact in such a way as to lead to Davydov splitting (DS) of otherwise

degenerate excitations. It is thus important to describe, not just *intramolecular* interactions correctly, but also to describe *intermolecular* interactions correctly, if the goal is to model J- or H-band DS. Several ways to improve the description of intermolecular interactions in DFT are available, including GGAs, global hybrids, and range-separated hybrids.

Yet another complication can arise as excitations need not be only within a single molecule (local excitation, LE), but rather may include excitations transferring charge from one molecule to a nearby molecule (charge transfer, CT). As FRs result from interacting LEs, one might think that CT could be ignored when modeling J- or H-bands. However this is not the case when CT and LEs mix, as is thought to occur in crystalline pentacene [20].

Time-dependent DFT with conventional functionals is notorious for underestimating CT excitations. This problem was clearly explained by Dreuw, Weisman, and Head-Gordon in their paper of 2003 [21] but was already apparent in an earlier paper by Tozer *et al.* in 1999 [22]. Later several diagnostic criteria were suggested to know when CT was likely to lead to a problem with TD-DFT with the best known one being the Λ criterion [23, 24, 25, 26, 27, 28, 29].

The situation in solid-state physics evolved somewhat differently beginning with the observation that the exact density functional must have some sort of ultranonlocality if atoms in the middle of a dielectric are to feel the effect of the field induced by charges on the surface of a dielectric. This led, for example, to the incorporation of current into TD-DFT [30]. The lack of ultranonlocality is often invoked to explain why TD-DFT calculations do not show exciton peaks in solid argon [31]. Sharma *et al.* proposed a bootstrap approximation to improve TD-DFT spectra for solids [32]. Ullrich and coworkers have discussed the problem of improving functionals for better description of excitons in crystal spectra [33, 34, 35]. The current recommendation to avoid the underestimation of CT excitations in TD-DFT is to use range-separated hybrids (RSHs) as these can “meet the challenge of CT excitations” [36]. In fact, in their article of 2010, Wong and Hsieh argued strongly for the use of RSHs for the improvement of the description of excitons in the spectra of oligoacenes [37]. While encouraging, that study is also a bit misleading in the present context because it refers to excitons within a single covalently bonded molecule while our concern here is with excitonic effects on the spectra of aggregates held together by van der Waals forces. Nevertheless we concur on the importance of RSHs for describing excitons.

Two other approaches to describing excitonic effects with TD-DFT should be mentioned. This is subsystem TD-DFT [38, 39] which grew out of a little article by Casida and Wesolowski [40] showing how TD-DFT could be done on a subsystem

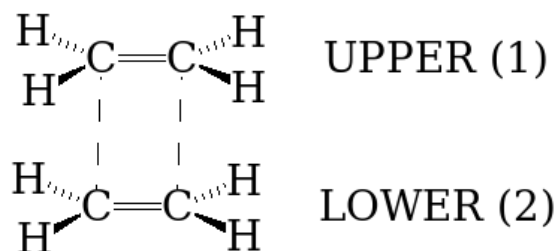


Figure 6.1 – Two vertically-stacked ethylene molecules.

of a larger system. The advantage of this method is that it incorporates the ideas of the exciton model from the very beginning as the system is viewed as made up of interacting chromophores. A different approach, albeit incorporating the exciton model from the very beginning, is used in Ref. [41]. Note, however, that neither of these approaches are used in the present article. Instead, we emphasize obtaining excitonic effects from a supermolecule approach to van der Waals aggregates.

In the interest of future (and on-going) work on large and complex systems, our primary interest is in TD-DFTB. The present study seeks to find out how well state-of-the-art TD-DFTB calculations can mimic state-of-the-art TD-DFT calculations, including dispersion corrections and RSHs, for describing excitonic effects in pentacene aggregates. As an important goal is also understanding, we focus primarily on the overly simple case of parallel stacked pentacene molecules. However we then do go on and extend our tests to the known herringbone structure of solid pentacene which is an old, but still fairly popular, system in organic electronics [42] and which is known to show J-bands.

This paper is organized as follows. The next section reviews a minimum of basic theory needed for this paper. Sec. 6.4 presents the details of how our computations were carried out and Sec. 6.5 presents and discusses our results. Sec. 6.6 concludes.

6.2 Exciton Analysis

We have noticed that there seems to be a great deal of confusion in the literature regarding charge transfer in excitonic systems (e.g., see Ref. [43]). Indeed delocalization of electron density over several molecules does not necessarily imply excitonic charge transfer; what may be taken at first as an indication of charge transfer, may turn out to be a manifestation of energy transfer. For this reason, we wish to be especially careful to define these terms within the context of excitonic theory and,

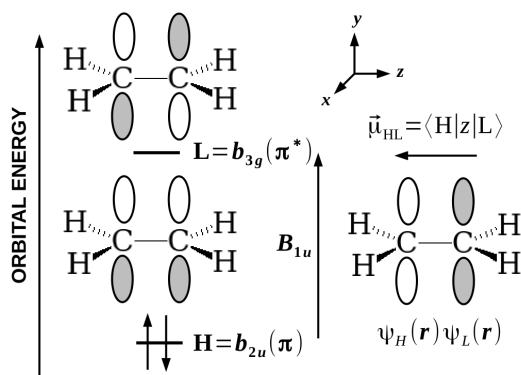


Figure 6.2 – Ethylene highest occupied molecular orbital (H) and lowest unoccupied molecular orbital (L).

in particular, we seek to explain via an algebraic example how excitations described using MOs, delocalized over several molecules in a supermolecule, may be analyzed and understood in terms of the (mainly) pairwise interaction of excitations localized on different molecules to create ET and CT excitons. In particular, we wish to show algebraically and using chemical intuition to what extent Kasha’s exciton model [8] emerges from a linear combination of singly-excited determinants over MOs. For concreteness, we will treat the π system of vertically-stacked molecules of ethylene (Fig. 6.1). This is close enough to the case treated numerically in Sec. 6.5 that we will be able to use the equations developed for vertically-stacked ethylene to help understand the exciton physics of vertically-stacked pentacenes.

6.2.1 Monomer

The MOs of the π system of ethylene are shown in Fig. 6.2. MO symmetries have been assigned following the recommended International Union of Pure and Applied Chemistry (IUPAC) nomenclature [44, 45] and the symmetry of the expected lowest energy excitations have been assigned. Of particular importance for us is the sketch of the transition density $\psi_H(\mathbf{r})\psi_L(\mathbf{r})$ on the right-hand side of the figure with the associated transition dipole moment $\vec{\mu}_{HL}$. Here H stands for the highest occupied molecular orbital, while L stands for the lowest unoccupied molecular orbital.

This is evidently a two-orbital two-electron model (TOTEM, Fig. 6.3) and the excitations may be analyzed in this context. There are four possible one-electron excitations for the TOTEM, but spin symmetry must be taken properly into account. We shall focus on the singlet transition which goes from the ground-state

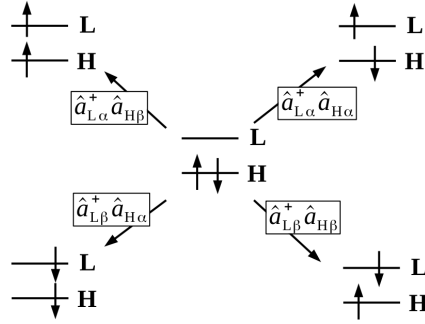


Figure 6.3 – Two-orbital two-electron model (TOTEM).

determinant Φ to the state,

$$^1(H, L) = \frac{1}{\sqrt{2}} \left(\hat{a}_{L\alpha}^\dagger \hat{a}_{H\alpha} + \hat{a}_{L\beta}^\dagger \hat{a}_{H\beta} \right) \Phi, \quad (6.1)$$

where α and β refer to spin states (i.e., spin up and spin down, respectively). In the specific case of the TOTEM, we may just write

$$\begin{aligned} ^1(H, L) &= \frac{1}{\sqrt{2}} (|H, \bar{L}| + |L, \bar{H}|) \\ &= \left[\frac{1}{\sqrt{2}} (H(1)L(2) + L(1)H(2)) \right] \\ &\times \left[\frac{1}{\sqrt{2}} (\alpha(1)\beta(2) - \beta(1)\alpha(2)) \right]. \end{aligned} \quad (6.2)$$

There are also three triplet states which are degenerate in the absence of spin-orbit

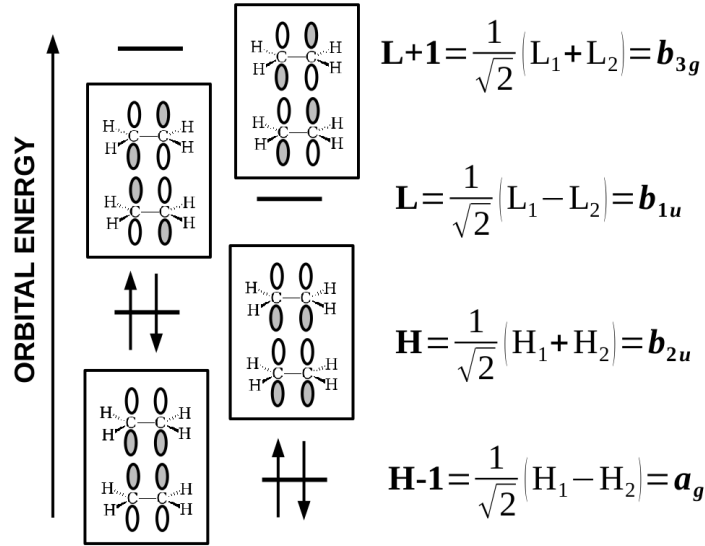


Figure 6.4 – MO diagram for two stacked ethylene molecules. White indicates the positive phase parts of the p functions while grey indicates the negative phase parts. Overlap between the MOs on different molecules have been neglected in normalizing the supermolecule MOs.

coupling,

$$\begin{aligned}
 {}^3(H, L)_{M_S=+1} &= |H, L| \\
 &= \left[\frac{1}{\sqrt{2}} (H(1)L(2) - L(1)H(2)) \right] \\
 &\times [\alpha(1)\alpha(2)] \\
 {}^3(H, L)_{M_S=0} &= \frac{1}{\sqrt{2}} (|H, \bar{L}| - |L, \bar{H}|) \\
 &= \left[\frac{1}{\sqrt{2}} (H(1)L(2) - L(1)H(2)) \right] \\
 &\times \left[\frac{1}{\sqrt{2}} (\alpha(1)\beta(2) + \beta(1)\alpha(2)) \right] \\
 {}^3(H, L)_{M_S=-1} &= |\bar{H}, \bar{L}| \\
 &= \left[\frac{1}{\sqrt{2}} (H(1)L(2) - L(1)H(2)) \right] \\
 &\times [\beta(1)\beta(2)] ,
 \end{aligned} \tag{6.3}$$

which will not concern us here.

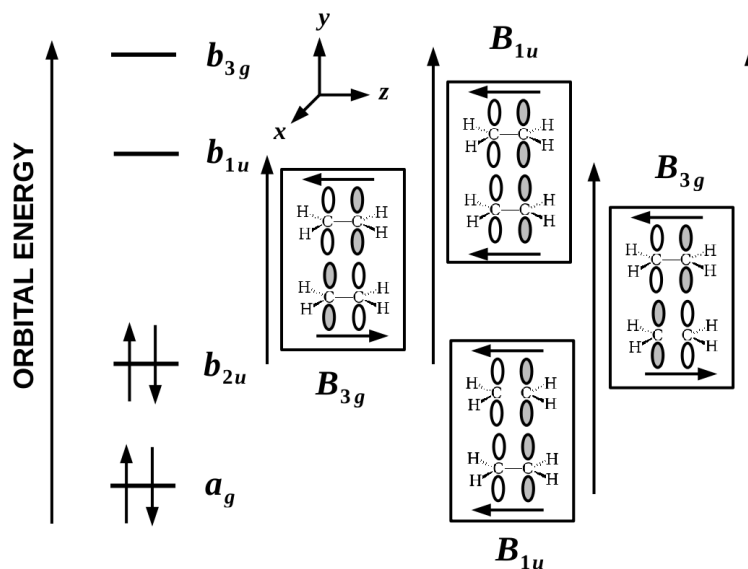


Figure 6.5 – The four transitions in (TOTEM)² and their associated transition dipole moments.

6.2.2 Dimer

We are now ready to treat two interacting stacked ethylene molecules. This system has been studied previously in the context of excitonic effects [46, 47, 48, 49] and at a greater level of sophistication than that needed here. Instead, we try to keep our analysis as simple as possible by assuming weak interactions between the molecules so that we may go to trimers and oligomers. Thus the analysis in the present section is most correct only at large intermolecular distances.

The corresponding dimer MO diagram (Fig. 6.4) under the assumption of weak interactions between the molecules. Here, after ordering MOs by energy, H- n is the n th occupied MO below H and L+ n is the n th unoccupied MO above L. As expected the number of nodal planes also increases with MO energy. Although we might think of this as a four-orbital four-electron model, we would like to think in terms of the exciton model, which we shall refer to as (TOTEM)² for evident reasons. Both energy transfer (ET) and charge transfer (CT) excitons will emerge from our analysis. Figure 6.5 shows the four possible singlet transitions in (TOTEM)² from the point of view of the MOs of the supermolecule composed of the two weakly-interacting ethylene molecules. Exciton analysis means that we want to re-express the description of the excitations so that they are no longer expressed in terms of the MOs of the supermolecule but rather are expressed in terms of ET and CT excitons involving the MOs (H₁ and L₁) of molecule 1 and the MOs (H₂ and L₂) of molecule 2.

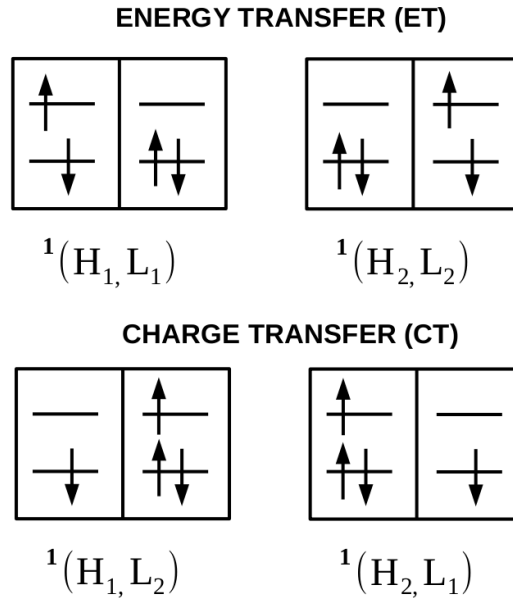


Figure 6.6 – Exciton model classification of transitions in the (TOTEM)² model. In each double box, the left hand side shows the orbital occupancy of the MOs in molecule 1 while the right hand side shows the orbital occupancy of the MOs in molecule 2.

Figure 6.5 shows that the transitions divide neatly into two symmetry types, namely B_{1u} and B_{3g} . This simplifies our analysis as only orbitals of the same symmetry may mix. Physically re-expressing supermolecule excitations in terms of ET and CT excitons on individual molecules can only happen when there are enough degrees of liberty — and, in particular, quasidegenerate states — that delocalized orbitals can be re-expressed in terms of more localized orbitals. This does not happen for the B_{3g} transitions. In fact, the first B_{3g} transition is expected to be heavily dominated by the ${}^1(H, L)$ configuration and the remaining B_{3g} transition should be dominated by the ${}^1(H - 1, L + 1)$ configuration. However the B_{3g} transitions are spectroscopically dark. So we will just go directly on to the B_{1u} orbitals.

The most general B_{1u} transition is of the form,

$$\Psi = c_1 {}^1(H, L + 1) + c_2 {}^1(H - 1, L). \quad (6.4)$$

Expressing the aggregate MOs in terms of the local MOs of molecules 1 and 2 as given in Fig. 6.4 leads to,

$$\Psi = \frac{c_1 + c_2}{\sqrt{2}} \text{ET}_{12} + \frac{c_1 - c_2}{\sqrt{2}} \text{CT}_{12}, \quad (6.5)$$

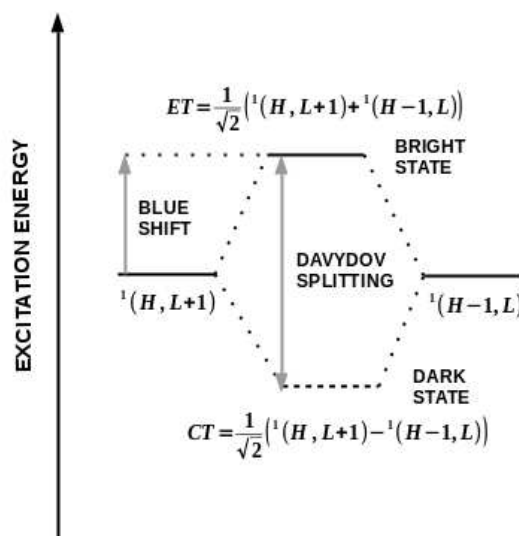


Figure 6.7 – Schematic of Kasha's theory for two parallel stacked molecules.

where,

$$ET_{12} = \frac{1}{\sqrt{2}} [{}^1(H_1, L_1) + {}^1(H_2, L_2)] \quad (6.6)$$

is the pairwise ET exciton and,

$$CT_{12} = \frac{1}{\sqrt{2}} [{}^1(H_1, L_2) + {}^1(H_2, L_1)] \quad (6.7)$$

is the corresponding CT exciton. (See Fig. 6.6. Note that we make no attempt to distinguish between Förster and Dexter ET excitons.) Physically we expect the ${}^1(H-1, L)$ and ${}^1(H, L+1)$ transitions to be quasidegenerate (i.e., $c_1 \approx c_2$) as often happens in organic molecules with a conjugated π system. Kasha's theory is recovered for exact degeneracy (i.e., when $c_1 = \pm c_2 = 1/\sqrt{2}$). As Kasha's theory predicts significant oscillator strength, because of mutual reinforcement of the transition dipole moments of each molecule, we expect to see the monomer absorption peak blue-shifted to the new dimer ET_{12} absorption peak as shown in Fig. 6.7. It is split from dipole-forbidden CT_{12} peak in the dimer spectrum. The difference between the energies of the ET and CT states is the Davydov splitting ($DS = ET - CT$). Kasha's theory may be further developed to show a red shift upon the formation of head-to-tail dimers when the CT state is bright and the ET state is dark [8]. Other configurations yield two peaks with an experimentally observable DS whose relative intensities may be analyzed to give information about the relative orientation of the molecules in the dimer [8].

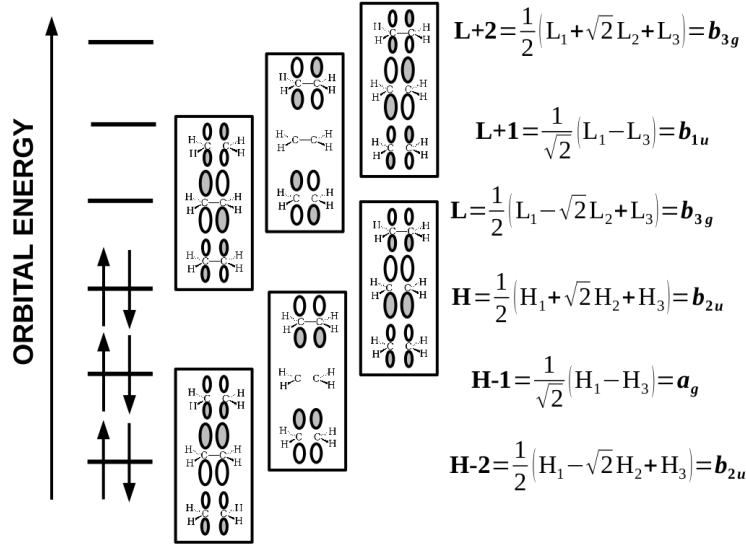


Figure 6.8 – MO diagram for three stacked ethylene molecules. White indicates the positive phase parts of the p functions while grey indicates the negative phase parts. Overlap between the MOs on different molecules have been neglected in normalizing the supermolecule MOs.

6.2.3 Trimer

Three stacked trimers introduce another key level of complexity in the exciton model. We now have an interior molecule interacting with two outer molecules. This asymmetry means that transitions forbidden, and hence dark, in the dimer may now be allowed, and hence bright, in the trimer. Figure 6.8 shows the (TOTEM)³ MOs deduced by analogy with the simple Hückel solution for the propenyl radical.

Figure 6.9 show the nine single excitations. Only the five B_{1u} transitions are symmetry allowed for absorption spectroscopy. Figure 6.10 shows the transition densities for the five symmetry-allowed singlet transitions. We thus restrict our analysis to the linear combination of only these states,

$$\begin{aligned} \Psi = & c_1 {}^1(H, L) + c_2 {}^1(H, L + 2) + c_3 {}^1(H - 1, L + 1) \\ & + c_4 {}^1(H - 2, L) + c_5 {}^1(H - 2, L + 2). \end{aligned} \quad (6.8)$$

Furthermore, we will use chemical intuition to predict the general form of these five allowed transitions. In particular, only the ${}^1(H, L + 2)$, ${}^1(H - 1, L + 1)$, and ${}^1(H - 2, L)$ states are expected to be degenerate enough to mix to form pairwise ET

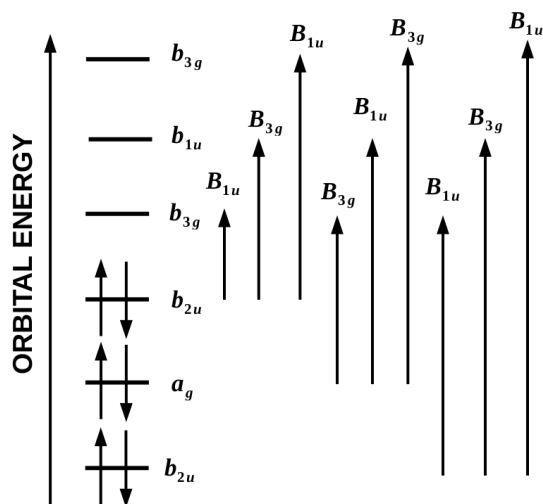


Figure 6.9 – The nine single excitations for three stacked ethylene molecules along with their symmetry assignments.

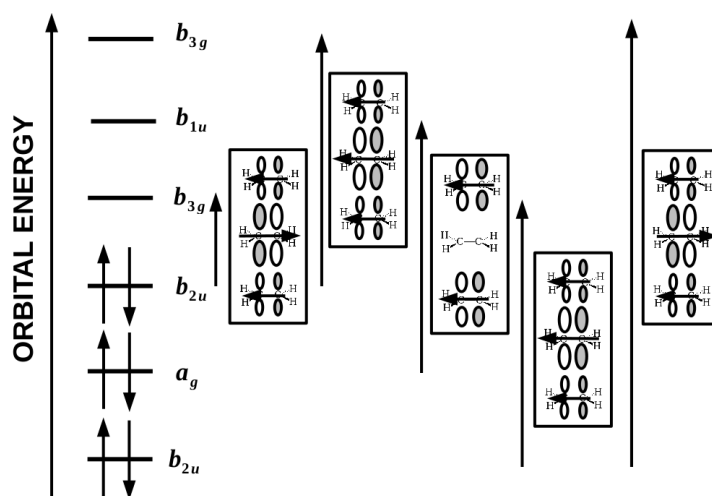


Figure 6.10 – The transition densities for the five symmetry allowed B_{1u} singlet excitations.

and CT excitons. This gives, after some algebra,

$$\begin{aligned}
\Psi = & c_1 {}^1(H, L) \\
& + \frac{3c_2 + 2c_3 + 3c_4}{2\sqrt{6}} \left(\frac{\text{ET}_{12} + \text{ET}_{23}}{\sqrt{3}} \right) \\
& + \sqrt{\frac{2}{3}} c_3 \left\{ \frac{\sqrt{3}}{2} \left[\text{ET}_{13} - \frac{1}{3} (\text{ET}_{12} + \text{ET}_{23}) \right] \right\} \\
& + \frac{c_2 - c_4}{\sqrt{2}} \left(\frac{\text{CT}_{12} + \text{CT}_{23}}{\sqrt{2}} \right) \\
& + \frac{c_2 - 2c_3 + c_4}{2\sqrt{2}} \text{CT}_{13} \\
& + c_5 {}^1(H - 2, L + 2), \tag{6.9}
\end{aligned}$$

where the notation is an obvious generalization of that given in Eqs. (6.6) and (6.7) and where the states have been orthonormalized. To a first approximation, the ${}^1(H, L)$ is too low in energy to mix with the other terms and ${}^1(H - 2, L + 2)$ is too high in energy to mix with the other terms. The ET and CT excitons lie in-between these in energy. Notice, however, that the CT terms vanish if $c_3 = c_4 = c_5$ which is expected to be often approximately the case. Note also that the pairwise ET terms are *not* orthogonal to each other as, for example, $\langle \text{ET}_{12} | \text{ET}_{23} \rangle = \langle {}^1(H_2, L_2) | {}^1(H_2, L_2) \rangle / 2 = 1/2$. However the ET terms have been grouped to reflect the symmetry of the stack and the distance over which energy must be transfered.

As we shall see numerically in Sec. 6.5 for the trimer of stacked pentacene molecules, each term is a reasonably good first approximation to a calculated TD-DFT excitation. Notice the exceptions to Kasha's model: (i) supermolecule MO excitations, such as ${}^1(H, L)$, which are better described in terms of supermolecule MOs than in terms of local MOs and (ii) CT excitons are only expected to cancel approximately in practical calculations. In reality ET and CT terms should mix.

The stacked trimer represents the simplest model where one molecule is interacting with two surrounding molecules. As such, it captures the basic physics of exciton interactions between neighboring molecules ($1 \leftrightarrow 2$ and $2 \leftrightarrow 3$). Equation (6.9) shows that neglect of $1 \leftrightarrow 3$ interactions (i.e., CT_{13} and ET_{13} and their required orthogonalization to the other terms) leads to only a single Davydov splitting into one ET and one CT peak. However a more careful analysis should include $1 \leftrightarrow 3$ interactions and Davydov multiplets may also be expected to be observed.

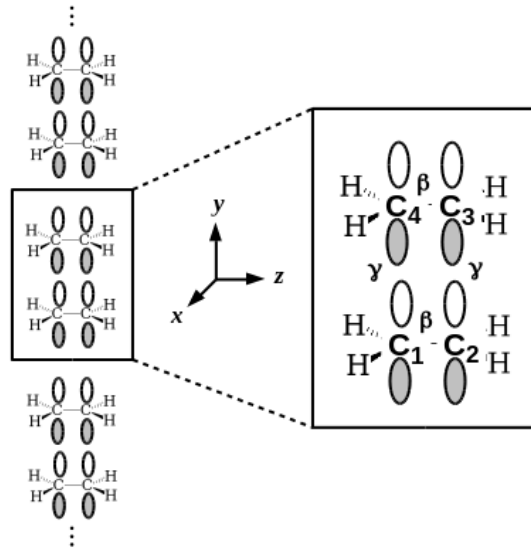


Figure 6.11 – Periodic model labeling and hopping parameters used for our stacked ethylene tight-binding calculation.

6.2.4 Higher Oligomers

The extension of these ideas to $(\text{TOTEM})^N$ for $N > 2$ is in principle straightforward but becomes increasingly complicated. However, it does not seem unreasonable to expect the structure of the spectrum to stabilize after a few layers, because the dominant interactions are expected to be primarily only between adjacent molecules. Thus we may anticipate that the numerical results in Sec. 6.5 should already show most of the qualitatively important features when $N = 3$ that are seen for still larger values of N .

We may explore this further by a back of the envelope tight-binding calculation for the periodic system of stacked ethylenes shown in Fig. 6.11. This is basically just a periodic simple Hückel calculation and so should be largely familiar to Quantum Chemists, even if the precise language and periodic symmetry adapted linear combinations may take a little getting used to.

To carry out our tight-binding calculation, we must include two ethylene molecules in the unit cell. In the exciton model, the MOs of each ethylene molecule $\chi_\mu(\vec{r})$ are looked on much like local AOs (LAOs). Combining them gives us a set of $(\text{TOTEM})^2$ MOs which become local MOs (LMOs)

$$\psi_i(\vec{r}) = \sum_{\mu} \chi_{\mu}(\vec{r}) c_{\mu,i} . \quad (6.10)$$

Periodic symmetry-adapted linear combinations have the form of crystal MOs (CMOs)

$$\psi_i(\vec{r}; \vec{k}) = \sum_{\vec{R}} \psi_i(\vec{r} - \vec{R}) e^{i\vec{k} \cdot \vec{R}}, \quad (6.11)$$

which may also be written as,

$$\psi_i(\vec{r}; \vec{k}) = \sum_{\mu} \chi_{\mu}(\vec{r}; \vec{k}) c_{\mu,i}(\vec{k}), \quad (6.12)$$

in terms of crystal AOs (CAOs),

$$\chi_{\mu}(\vec{r}; \vec{k}) = \frac{1}{\sqrt{N}} \chi_{\mu}(\vec{r} - \vec{R}) e^{i\vec{k} \cdot \vec{R}}. \quad (6.13)$$

The factor N in this formalism represents the number of atoms in a fictitious “finite crystal.” It has been introduced for convenience, but it is not really necessary. The wave vector \vec{k} serves both as a symmetry label and may also be viewed as a sort of electron momentum which can be used in selection rules. The \vec{k} -block of the CMO matrix equation is

$$\mathbf{h}(\vec{k}) \vec{c}_i(\vec{k}) = \epsilon_i(\vec{k}) \mathbf{s}(\vec{k}) \vec{c}_i(\vec{k}), \quad (6.14)$$

where the matrix elements of the overlap matrix are given by,

$$\begin{aligned} s_{\mu,\nu}(\vec{k}) &= \sum_{\vec{R}} s_{\mu,\nu}^{(\vec{R})} e^{i\vec{k} \cdot \vec{R}} \\ s_{\mu,\nu}^{(\vec{R})} &= \int_{V=N\Omega} \chi_{\mu}^*(\vec{r} + \vec{R}) \chi_{\nu}(\vec{r}) d\vec{r}, \end{aligned} \quad (6.15)$$

and the matrix elements of the hamiltonian matrix are given by,

$$\begin{aligned} h_{\mu,\nu}(\vec{k}) &= \sum_{\vec{R}} h_{\mu,\nu}^{(\vec{R})} e^{i\vec{k} \cdot \vec{R}} \\ h_{\mu,\nu}^{(\vec{R})} &= \int_{V=N\Omega} \chi_{\mu}^*(\vec{r} + \vec{R}) \hat{h} \chi_{\nu}(\vec{r}) d\vec{r}. \end{aligned} \quad (6.16)$$

Here Ω is the volume of the unit cell and $N\Omega$ is the volume of the fictitious “finite crystal.”

Our model is subject to several simplifications. For one, the wave vector is a number k since our system is periodic in a single dimension (y). We will follow the common practice of assuming that the overlap matrix $\mathbf{s}(k)$ is the identity. The hamiltonian matrix $\mathbf{h}(k)$ is then constructed from the on-sight (i.e., coulomb) integral α and the hopping (i.e., resonance) integrals β between the p orbitals within

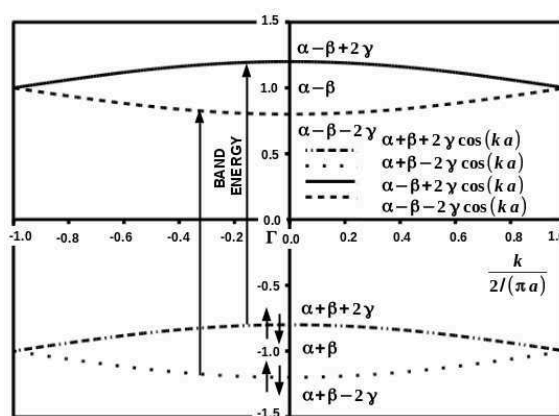


Figure 6.12 – Bands for the stacked ethylene tight-binding model with $\alpha = 0$, $\beta = -1$, and $\gamma = 0.1$. The paired arrows ($\uparrow\downarrow$) are meant to indicate filled bands below the fermi level.

each ethylenes and γ between adjacent p orbitals in different ethylene molecules. Note that $\alpha, \beta < 0$ but that $\gamma > 0$ for this particular configuration. The position vector \vec{R} is Y so that

$$\mathbf{h}(k) = \sum_Y \mathbf{h}^{(Y)} e^{ikY}. \quad (6.17)$$

where,

$$\begin{aligned}
\mathbf{h}^{(Y)} &= \begin{bmatrix} \mathbf{A} & \mathbf{B} \\ \mathbf{C} & \mathbf{A} \end{bmatrix} \\
\mathbf{A} &= \begin{bmatrix} \alpha\delta_{Y,0} & \beta\delta_{Y,0} \\ \beta\delta_{Y,0} & \alpha\delta_{Y,0} \end{bmatrix} \\
\mathbf{B} &= \begin{bmatrix} 0 & \gamma(\delta_{Y,0} + \delta_{Y,+a}) \\ \gamma(\delta_{Y,0} + \delta_{Y,+a}) & 0 \end{bmatrix} \\
\mathbf{C} &= \begin{bmatrix} 0 & \gamma(\delta_{Y,0} + \delta_{Y,-a}) \\ \gamma(\delta_{Y,0} + \delta_{Y,-a}) & 0 \end{bmatrix}, \tag{6.18}
\end{aligned}$$

and a is the y -distance between ethylene molecules as opposed to the unit cell pa-

parameter which is equal to $2a$. Applying Eq. (6.17) to Eq. (6.18) then gives that

$$\begin{aligned} \mathbf{h}(k) &= \begin{bmatrix} \mathbf{A} & \mathbf{B}(k) \\ \mathbf{C}(k) & \mathbf{A} \end{bmatrix} \\ \mathbf{A} &= \begin{bmatrix} \alpha & \beta \\ \beta & \alpha \end{bmatrix} \\ \mathbf{B}(k) &= \begin{bmatrix} 0 & \gamma(1 + e^{i2ka}) \\ \gamma(1 + e^{i2ka}) & 0 \end{bmatrix} \\ \mathbf{C}(k) &= \begin{bmatrix} 0 & \gamma(1 + e^{-i2ka}) \\ \gamma(1 + e^{-i2ka}) & 0 \end{bmatrix}. \end{aligned} \quad (6.19)$$

This has four solutions, namely:

$$\begin{aligned} \epsilon_1(k) = \alpha + \beta + 2\gamma \cos(ka) &\leftrightarrow \vec{c}_1(k) = \begin{pmatrix} 1 \\ 1 \\ +z^*/|z| \\ +z^*/|z| \end{pmatrix} \\ \epsilon_2(k) = \alpha + \beta - 2\gamma \cos(ka) &\leftrightarrow \vec{c}_2(k) = \begin{pmatrix} 1 \\ 1 \\ -z^*/|z| \\ -z^*/|z| \end{pmatrix} \\ \epsilon_3(k) = \alpha - \beta - 2\gamma \cos(ka) &\leftrightarrow \vec{c}_3(k) = \begin{pmatrix} 1 \\ -1 \\ +z^*/|z| \\ -z^*/|z| \end{pmatrix} \\ \epsilon_4(k) = \alpha - \beta + 2\gamma \cos(ka) &\leftrightarrow \vec{c}_4(k) = \begin{pmatrix} 1 \\ -1 \\ -z^*/|z| \\ +z^*/|z| \end{pmatrix}, \end{aligned} \quad (6.20)$$

where,

$$z = 1 + e^{i2ka}. \quad (6.21)$$

The associated band diagram is shown in Fig. 6.12. This is a direct band system. Assuming the Γ point and no momentum transfer to the lattice, then the two allowed transitions are those shown by vertical arrows. The corresponding CMOs (Fig. 6.13)

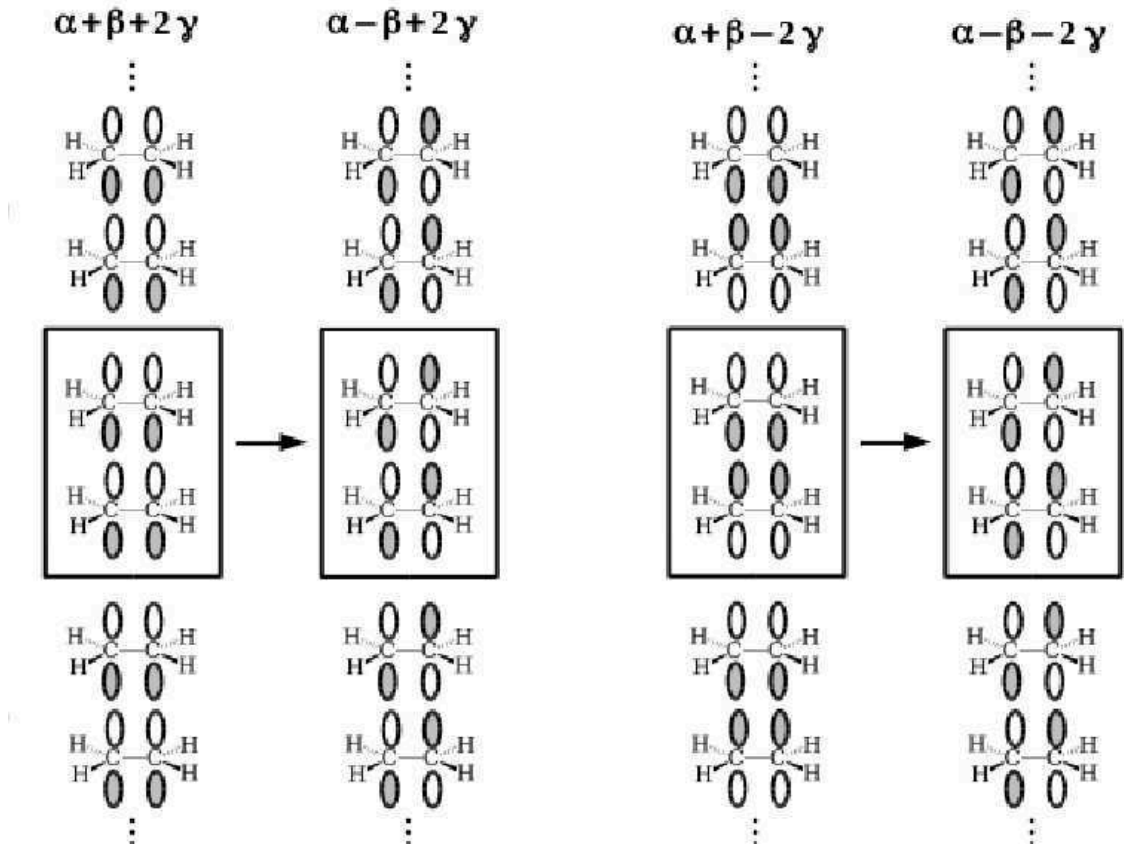


Figure 6.13 – The CMOs for the optically-allowed transitions of $(\text{TOTEM})^N$ at the Γ -point.

bear a close resemblance to the MOs of the $(\text{TOTEM})^2$ dimer (Fig. 6.5), showing that the $(\text{TOTEM})^2$ analysis also applies in the periodic $(\text{TOTEM})^N$ case.

Finally, it is illuminating to apply the same tight-binding model to the $(\text{TOTEM})^2$ dimer. The hamiltonian matrix to be diagonalized is then,

$$\begin{aligned}
 \mathbf{h}(k) &= \begin{bmatrix} \mathbf{A} & \mathbf{B} \\ \mathbf{B} & \mathbf{A} \end{bmatrix} \\
 \mathbf{A} &= \begin{bmatrix} \alpha & \beta \\ \beta & \alpha \end{bmatrix} \\
 \mathbf{B} &= \begin{bmatrix} 0 & \gamma \\ \gamma & 0 \end{bmatrix},
 \end{aligned} \tag{6.22}$$

which has the four solutions,

$$\begin{aligned}
 \epsilon_1 = \alpha + \beta + \gamma &\leftrightarrow \vec{c}_1 = \begin{pmatrix} 1 \\ 1 \\ 1 \\ 1 \end{pmatrix} \\
 \epsilon_2 = \alpha + \beta - \gamma &\leftrightarrow \vec{c}_2 = \begin{pmatrix} 1 \\ 1 \\ -1 \\ -1 \end{pmatrix} \\
 \epsilon_3 = \alpha - \beta - \gamma &\leftrightarrow \vec{c}_3 = \begin{pmatrix} 1 \\ -1 \\ 1 \\ -1 \end{pmatrix} \\
 \epsilon_4(k) = \alpha - \beta + \gamma &\leftrightarrow \vec{c}_4 = \begin{pmatrix} 1 \\ -1 \\ -1 \\ 1 \end{pmatrix}.
 \end{aligned} \tag{6.23}$$

Comparing with the band solution for the periodic system $(\text{TOTEM})^N$, we see that the energy levels are displaced by γ in $(\text{TOTEM})^2$ rather than by 2γ in $(\text{TOTEM})^N$, because each ethylene in $(\text{TOTEM})^2$ is only in contact with a single other ethylene, while each ethylene in $(\text{TOTEM})^N$ is in contact with two other ethylene molecules. However *the key energy differences are the same for $(\text{TOTEM})^2$ and $(\text{TOTEM})^N$* , lending reassurance that the fundamental analysis of the dimer model also applies for larger parallel stacks of ethylene molecules. On the other hand, inclusion of non-nearest neighbor interactions in the model is expected to yield small contributions from higher-order Davydov multiplets, even if our simple model captures the main qualitative aspects of Frenkel excitons in the stack of molecules.

This completes our analytic study of stacked ethylene dimers. In the Sec. 6.5, we will apply this analysis to stacked pentamers and use it to gain a deeper insight into how different variations of TD-DFT and TD-DFTB work.

6.3 (TD-)DFT AND (TD-)DFTB

The previous formal section is important for our study of how well state-of-the-art TD-DFTB calculations can mimic state-of-the-art TD-DFT calculations. In this

section, we will be more specific about what functionals are used in the present (TD-)DFT study and what (TD-)DFTB method was used. As we are testing existant methodology, rather than presenting new methodology, this section is a review section. We will take advantage of this to keep our presentation brief (even just schematic) but will refer the reader back to the original literature or to important review articles. Hartree atomic units ($\hbar = m_e = e = 1$) are used throughout unless otherwise specified.

6.3.1 DFT

Hohenberg-Kohn-Sham DFT [50, 51] is now so well-known that little needs to be said about the basics. For those seeking a deeper understanding of the foundations of DFT, we can recommend Refs. [52, 53, 54]. Our intent here is mainly to go beyond what is found in those references though some mention of the basics is inevitable.

The fundamental idea of DFT is to replace the real system of N interacting electrons in an external potential v_{ext} with a fictitious system of N noninteracting electrons in an effective potential v_s (s for single electron). We will designate the orbitals of the noninteracting system as ψ_i and their associated occupation numbers as n_i . These orbitals are orthonormal,

$$\langle \psi_i | \psi_j \rangle = \delta_{i,j}. \quad (6.24)$$

Normally n_i is zero or one but fractional occupation is also allowed. The density matrix for the noninteracting system is then,

$$\gamma(1, 2) = \sum_i \psi_i(1) n_i \psi_i^*(2), \quad (6.25)$$

where the numeral $i = 1, 2, \dots$ stands for the space and spin coordinates of the i th electron. The density,

$$\rho(1) = \gamma(1, 1). \quad (6.26)$$

is the diagonal element of the density matrix. The electronic energy E is the same for the real and for the interacting systems. It may be written as the sum of three terms,

$$E = E_c + E_H + E_{xc}, \quad (6.27)$$

where the core energy,

$$E_c = \sum_i n_i \langle \psi_i | \hat{h}_c | \psi_i \rangle, \quad (6.28)$$

may be expressed in terms of the core hamiltonian,

$$\hat{h}_c = -\frac{1}{2}\nabla^2 + v_{\text{ext}} , \quad (6.29)$$

the Hartree energy (also called the classical coulomb repulsion energy),

$$E_H = \frac{1}{2} \int \int \rho(1) \left(\frac{1}{r_{1,2}} \right) \rho(2) d1 d2 , \quad (6.30)$$

and the remaining terms needed to make the electronic energy *exact* are included in the exchange-correlation (xc) energy,

$$E_{xc} = E - E_c - E_H . \quad (6.31)$$

This term is approximated in practical calculations. We will consider these approximations very soon. For now, let us note that minimizing E subject to the orthonormality condition [Eq. (6.24)] leads to an orbital equation,

$$\hat{f}\psi_i = \epsilon_i\psi_i , \quad (6.32)$$

where

$$\hat{f} = \hat{h}_c + v_H + v_{xc} . \quad (6.33)$$

Here

$$v_H(1) = \int \left(\frac{1}{r_{12}} \right) \rho(2) d2 \quad (6.34)$$

is the Hartree potential and

$$v_{xc}(1) = \frac{\delta E_{xc}}{\delta \rho(1)} \quad (6.35)$$

is the xc potential. Then it is easy to see that the effective potential of the noninteracting system is,

$$v_s = v_{\text{ext}} + v_H + v_{xc} . \quad (6.36)$$

The orbital equation (6.32) must be solved self-consistently because \hat{f} is orbital dependent. Once self-consistency has been reached, then the energy may be calculated either using Eq. (6.27) or by using the equation

$$E = \sum_i n_i \epsilon_i - \frac{1}{2} E_H + E_{xc} - \int v_{xc}(1) \rho(1) d1 \quad (6.37)$$

This latter form is used as the basis of DFTB.

Thus far the equations are exact, but useless unless approximations are made.

The most common approximation is the local (spin) density approximation (LDA) which assumes that the xc energy density in a nonhomogeneous system such as an atom, molecule, or solid, is the same as the xc energy density in the homogeneous electron gas (HEG),

$$E_{xc}^{\text{LDA}} = \int \epsilon_{xc}^{\text{HEG}}(\rho(1))\rho(1) d1. \quad (6.38)$$

The exchange part of $\epsilon_{xc}^{\text{HEG}}$ has a simple analytic form [55]. We will use the Vosko-Wilk-Nusair parameterization of the correlation part of $\epsilon_{xc}^{\text{HEG}}$ [56] in the present work. Strictly speaking all of our calculations have an explicit dependence on the spin polarization of the local density. That is, we are using spin DFT rather than the original DFT which depended only on the spinless charge density.

The LDA often gives reasonable molecular geometries but is known to overbind. For this reason, it has been useful to include inhomogeneities in the density via generalized gradient approximations (GGAs) of the form,

$$E_{xc}^{\text{GGA}} = \int \epsilon_{xc}^{\text{HEG}}(\rho(1))F_{xc}^{\text{GGA}}(\rho(1), x(1))\rho(1) d1. \quad (6.39)$$

where the enhancement factor F_{xc} depends both on the local density and upon the local reduced gradient,

$$x = \frac{|\vec{\nabla}\rho|}{\rho^{4/3}}. \quad (6.40)$$

Relevant GGAs used in our calculations are Becke's 1988 (B88) exchange GGA [57, 58], Perdew's 1991 correlation GGA [59, 60, 61, 62], and the Lee, Yang, and Parr (LYP) correlation GGA [63].

Thus far, the discussion has been limited to pure density functionals — that is, those that depend only upon the charge density. In 1993, Becke introduced some “exact exchange” into the xc functional [64] (exact exchange is HF exchange evaluated with DFT orbitals.) He did this based upon an adiabatic connection formalism and the improvement in computational results was very striking in that time as they suggested that such (global) hybrid functionals could provide thermochemical accuracy. Of course, this also leaves the framework of formal Hohenberg-Kohn-Sham theory [65] and we must now speak of generalized Kohn-Sham theory. In particular, the xc energy is now a functional of the density matrix $E[\gamma]$ rather than just the density ($E[\rho]$) and the xc potential becomes an xc operator defined by

$$\hat{v}_{xc}\psi(1) = \int \frac{\delta E_{xc}}{\delta \gamma(2, 1)}\gamma(1, 2)\psi_i(2) d2. \quad (6.41)$$

Note that the HF exchange-only operator may be regarded as an extreme case of a

Table 6.1 – Summary of different functionals used in this work. See Eq. (6.47).

Functional	μ	a_0	a_x	a_c
HF ^a	$+\infty$	1	0	0
LDA	0	0	0	1
B3LYP	0	0.20	0.72	0.81
CAM-B3LYP	0.33	0.19	0.46	0.81
LRC-LDA	0.4	0	1	0

^aIn the HF case, we also need to drop the E_c^{VWN80} term.

global hybrid:

$$\begin{aligned}
E_x^{\text{HF}}[\gamma] &= -\frac{1}{2} \int \int \gamma(1,2) \left(\frac{1}{r_{1,2}} \right) \gamma(2,1) d1d2 \\
\frac{\delta E_x^{\text{HF}}[\gamma]}{\delta \gamma(2,1)} &= -\frac{\gamma(1,2)}{r_{1,2}}.
\end{aligned} \tag{6.42}$$

Equation (6.37) still holds but with a nonlocal \hat{v}_{xc} . We use the B3LYP functional in the present work [66]. This is the same as the B3P91 functional originally introduced by Becke [64] but with Perdew's 1991 correlation GGA replaced by the LYP correlation GGA. Specifically,

$$\begin{aligned}
E_{xc} &= E_x^{\text{LDA}} + a_0 (E_x^{\text{HF}} - E_x^{\text{LDA}}) \\
&+ a_x E_x^{\text{B88}} \\
&+ E_c^{\text{LDA}} + a_c (E_c^{\text{LYP}} - E_c^{\text{LDA}}),
\end{aligned} \tag{6.43}$$

where the various functionals have been defined above, $a_0 = 0.20$, $a_x = 0.72$, and $a_c = 0.81$.

We have emphasized that, in TD-DFT, charge-transfer excitations require the use of RSHs [36]. These functionals involve the splitting of the electron repulsion into a short-range (sr) and a long-range (lr) part,

$$\frac{1}{r_{12}} = \left(\frac{1}{r_{12}} \right)^{(\text{sr})} + \left(\frac{1}{r_{12}} \right)^{(\text{lr})}. \tag{6.44}$$

For convenience in a Gaussian orbital-based program, the separation is made using the error function,

$$\text{erf}(\mu r_{12}) = \frac{2}{\sqrt{\pi}} \int_0^{\mu r_{12}} e^{-t^2} dt. \tag{6.45}$$

We will be using the Coulomb attenuated model (CAM) B3LYP functional [67]

where,

$$\begin{aligned} \left(\frac{1}{r_{12}}\right)^{(\text{sr})} &= \frac{1 - [a_0 + a_x \text{erf}(\mu r_{12})]}{r_{12}} \\ \left(\frac{1}{r_{12}}\right)^{(\text{lr})} &= \frac{a_0 + a_x \text{erf}(\mu r_{12})}{r_{12}}, \end{aligned} \quad (6.46)$$

The sr part of the functional is treated by DFT while the lr part is treated by HF. The parameter μ acts as a range-separation parameter. The specific form of the CAM-B3LYP functional is,

$$\begin{aligned} E_{xc} &= E_x^{\text{sr-LDA}} + a_0[E_x^{\text{lr-HF}} - E_x^{\text{sr-LDA}}] \\ &+ a_x E_x^{\text{sr-B88}} \\ &+ E_c^{\text{VWN80}} + a_c[E_c^{\text{LYP88}} - E_c^{\text{VWN80}}], \end{aligned} \quad (6.47)$$

The specific parameters of the CAM-B3LYP functional are given in Table 6.1. Also shown in the table are the values of the parameters which give some of the other functionals used in this paper. The LRC-LDA functional is the LDA form of the long-range corrected (LRC) functional of Iikura, Tsuneda, Yanai, and Harao [68]. This is given because the RSH DFTB used in this paper (*vide infra*) is based upon the LRC family of RSH functionals, rather than upon the CAM-B3LYP form.

The DFT presented thus far still has one very large failure, namely the lack of van der Waals (vdW) forces. This is particularly important in organic electronics because the organic molecules in the condensed phase are primarily held together precisely by these forces. However, to include vdW forces in *ab initio* theory, it is necessary to go beyond HF to at least second order in many-body perturbation theory (MBPT). Designing a density functional that can handle vdW forces has been studied and suggestions usually involve some aspect of MBPT. As TD-DFT resembles a MBPT method, it is perhaps not so remarkable that vdW coefficients for long-range induced-dipole/induced-dipole vdW forces can be calculated reasonably accurately via TD-DFT. The difficulty is then how to use TD-DFT (or some other MBPT approach) and make a computationally efficient method. The present method of choice, and the one used here, is actually a compromise. This is Grimme's D3

correction [4]. It has the semi-empirical form,

$$\begin{aligned}
 E_{\text{vdW}} = & \sum_{A,B} \sum_{n=6,8,10,\dots} s_n \frac{C_n^{A,B}}{R_{A,B}^n \left[1 + 6 \left(\frac{R_{A,B}}{s_{r,n} R_0^{A,B}} \right)^{-\alpha_n} \right]} \\
 - & \sum_{A,B,C} \frac{\sqrt{C_6^{A,B} C_6^{A,C} C_6^{B,C}} (3 \cos \theta_a \cos \theta_b \cos \theta_c + 1)}{(R_{A,B} R_{B,C} R_{C,A})^3 \left[1 + 6 \left(\frac{\bar{R}_{A,B,C}}{s_{r,3} R_0^{A,B}} \right)^{-\alpha_3} \right]}, \tag{6.48}
 \end{aligned}$$

where the C_6 and other vdW coefficients are obtained from TD-DFT [see Ref. [4] for a more detailed description of the D3 correction and the values of the various terms in Eq. (6.48)]. Thus this correction may be seen as an interpolation scheme between DFT and TD-DFT. However E_{vdW} enters as a correction which does not enter into the self-consistent cycle of orbital optimization but instead is added on, after the fact, as a first-order correction to the self-consistent field energy. Derivatives of E_{vdW} are included in force calculations and hence in geometry optimizations.

6.3.2 TD-DFT

TD-DFT is the younger sibling of DFT: The founding papers of DFT [50, 51] were written half a century ago; that of TD-DFT [69] a mere 30 years or so ago. The interested reader can find more information on TD-DFT in the proceedings of two summer schools on the topic [70, 71] as well as in two textbooks [72, 73] and in several recent review articles [74, 75, 76, 2, 77, 78, 79].

The most common application of TD-DFT is to the calculation of electronic absorption spectra via response theory. There are several ways to do this, including real-time TD-DFT, but the classic approach is to use ‘‘Casida’s equation’’ (see, e.g., pp. 145-153 of the recent textbook, Ref. [73], or the original reference [80].) This method is about 20 years old. It consists of solving the pseudo-eigenvalue problem,

$$\begin{bmatrix} \mathbf{A} & \mathbf{B} \\ \mathbf{A}^* & \mathbf{B}^* \end{bmatrix} \begin{pmatrix} \vec{X} \\ \vec{Y} \end{pmatrix} = \omega \begin{bmatrix} \mathbf{1} & \mathbf{0} \\ \mathbf{0} & -\mathbf{1} \end{bmatrix} \begin{pmatrix} \vec{X} \\ \vec{Y} \end{pmatrix}, \tag{6.49}$$

where

$$\begin{aligned}
 A_{ia,jb} &= \delta_{i,j} \delta_{a,b} (\epsilon_a - \epsilon_i) + K_{ia,jb} \\
 B_{ia,bj} &= K_{ia,bj}
 \end{aligned} \tag{6.50}$$

and the indices refer to excitations from occupied (i and j) to unoccupied (a and b) orbitals. The coupling matrix is usually evaluated in the adiabatic approximation, which leads to

$$\begin{aligned} K_{pq,rs} &= \int \int \int \int \psi_p^*(1) \psi_q(2) \\ &\times (f_H(1, 2; 3, 4) + f_{xc}(1, 2; 3, 4)) \\ &\times \psi_r(3) \psi_s^*(4) d1 d2 d3 d4, \end{aligned} \quad (6.51)$$

where,

$$\begin{aligned} f_H(1, 2; 3, 4) &= \delta(1 - 2) \frac{1}{r_{1,3}} \delta(3 - 4) \\ f_{xc}(1, 2; 3, 4) &= \frac{\delta E_{xc}}{\delta \gamma(2, 1) \delta \gamma(4, 3)}. \end{aligned} \quad (6.52)$$

The connection with the formal analysis of the previous section is most easily accomplished within the Tamm-Dancoff approximation (TDA),

$$\mathbf{A} \vec{X} = \omega \vec{X}. \quad (6.53)$$

The TDA makes TD-DFT look like configuration interaction with single excitations (CIS) which is exactly what it is when the TDA is applied to TD-HF. Many of the strengths and shortcomings of TD-DFT can be understood when the TDA is applied to the TOTEM to get the singlet excitation energy, ω_S . In the case of TD-HF,

$$\omega_S = \epsilon_L^{\text{HF}} - \epsilon_H^{\text{HF}} + 2(HL|f_H|LH) - (HH|f_H|LL), \quad (6.54)$$

where

$$(pq|f_H|rs) = \int \int \psi_p^*(1) \psi_q(1) \frac{1}{r_{1,2}} \psi_r^*(2) \psi_s(2) d1 d2. \quad (6.55)$$

As Koopmans' theorem tells us that the HF orbital energies are better suited for describing ionization and electron attachment than for describing excitations, this is not such a good expression for local excitations. However it is well suited for describing CT excitations between two neutral molecules separated by a distance R as Eq. (6.54) becomes roughly the expected formula,

$$\omega_S = I - A - \frac{1}{R}, \quad (6.56)$$

as the ionization potential,

$$I \approx -\epsilon_H^{\text{HF}}, \quad (6.57)$$

and the electron affinity,

$$A \approx -\epsilon_L^{\text{HF}}, \quad (6.58)$$

while,

$$\begin{aligned} \lim_{R \rightarrow \infty} (HL|f_H|LH) &= 0 \\ \lim_{R \rightarrow \text{large}} (HH|f_H|LL) &\approx \frac{1}{R}. \end{aligned} \quad (6.59)$$

In contrast, for pure density functionals (LDA and GGAs),

$$\omega_S = \epsilon_L^{\text{DFT}} - \epsilon_H^{\text{DFT}} + 2(HL|f_H|LH) - (HL|f_{xc}^{\uparrow\uparrow} - f_{xc}^{\uparrow\downarrow}|LH), \quad (6.60)$$

where

$$(pq|f_{xc}|rs) = \int \int \psi_p^*(1)\psi_q(1) \frac{\delta E_{xc}}{\delta \rho(1)\delta \rho(2)} \psi_r^*(2)\psi_s(2) d1d2. \quad (6.61)$$

Since pure DFT orbitals see the same potential, and hence the same number of electrons, for both occupied and unoccupied orbitals, then the orbital energy difference is not a bad first approximation for local excitation energies. This provides an intuitive explanation of why TD-DFT often does better than TD-HF in this case. But, when we consider charge transfer between two widely separated molecules, Eq. (6.60) becomes

$$\lim_{R \rightarrow \text{large}} \omega_S \approx \epsilon_L^{\text{DFT}} - \epsilon_H^{\text{DFT}}, \quad (6.62)$$

which not only has the wrong R dependence but often grossly underestimates the difference between the ionization potential of one molecule and the electron affinity of the other.

Interestingly, exact TD-DFT with pure density functionals circumvents the CT problem by introducing a complicated frequency dependence into the xc kernel $f_{xc}(\omega)$ which imitates spatial nonlocality at particular values of ω . In particular, the time-dependent exchange-only optimized effective potential method gives [81, 3],

$$f_x(\epsilon_a - \epsilon_i) = (ai|f_H|ia). \quad (6.63)$$

While this formal result is highly interesting and can be implemented, the result is basically a very complicated DFT-like form of TD-HF. This suggests that it is better to introduce some exact exchange into our functionals, either through a global hybrid such as B3LYP or via a RSH such as CAM-B3LYP. The astute reader will note that the CAM-B3LYP functional has the wrong asymptotic behavior for CT excitations. Nevertheless, it remains a popular compromise for calculating excitation energies

(e.g., see the DFT popularity poll [82]). However the LRC-type of RSH functional does have the correct asymptotic behavior and is the basis of the lc-DFTB functional described below.

6.3.3 DFTB

DFT scales formally as $\mathcal{O}(N^4)$ with the number of atoms N in the system. Depending upon the functional, its formal scaling may be reduced to $\mathcal{O}(N^3)$, but that still limits the usefulness of DFT. To go to still larger systems or resource intensive dynamics calculations, semi-empirical methods which use only $\mathcal{O}(N^2)$ integrals are useful.

Semi-empirical methods have a long history in quantum chemistry. Originally restricted to the π electrons of conjugated systems, semi-empirical methods had been extended to all the valence electrons of a molecule by 1970 (the date of the classic text of Pople and Beveridge on this subject [83]). Ref. [84] provides a more up-to-date review of semi-empirical methods in quantum chemistry. A constant question with semi-empirical methods has been the physical meaning of the parameters used and how to assign them values. DFTB is specifically designed to approximate DFT with no more than two-centers integrals and no more than valence orbitals. In so doing, “the use of [DFT] removed at a stroke much of the problem of fitting parameters” [85]. The result resembles a less accurate (because less rigorous) form of DFT. Nevertheless the efficiency of DFTB makes it a highly desirable feature and most quantum chemistry packages include some form of DFTB. No attempt is made here to give a thorough review of all the different flavors of DFTB, but we will review the main points and refer the reader to the literature for additional information [86, 87, 88]. In particular, a very nice explanation of DFTB is given in Ref. [86].

The original form of DFTB [89], was a noniterative one-shot calculation resembling Hoffmann’s extended Hückel method [90, 91, 92, 93]. The basis consists of the valence orbitals of isolated atoms calculated in a confining potential to ensure that those atomic orbitals remained local. It is important to keep track of the atom I on which resides the atomic orbital (AO) μ . We will denote this basis function as

$$\chi_{\mu I} = \chi_{\mu \in I}, \quad (6.64)$$

where the left-hand side is a shorter form of the right-hand side. The density is the

superposition of atomic densities,

$$\rho_0 = \sum_I \rho_I^0. \quad (6.65)$$

The nuclear attraction term is separable,

$$v_{\text{ext}}[\rho_0] = \sum_I v_n[\rho_I^0], \quad (6.66)$$

and the Hartree potential is also separable,

$$v_H[\rho_0] = \sum_I v_H[\rho_I^0], \quad (6.67)$$

while the xc potential is assumed separable,

$$v_{xc}[\rho_0] = \sum_I v_{xc}[\rho_I^0], \quad (6.68)$$

which is a reasonable approximation for pure density functionals (LDA and GGAs).

The matrix elements of the orbital hamiltonian (\hat{f}) are calculated as,

$$f_{\mu I, \nu J} = \begin{cases} \langle \chi_{\mu I} | \hat{t} + v_I^{nHxc} | \chi_{\nu I} \rangle = \epsilon_I^0 & ; \ I = J \\ \langle \chi_{\mu I} | \hat{t} + v_I^{nHxc} + v_J^{nHxc} | \chi_{\nu J} \rangle & ; \ I \neq J \end{cases}, \quad (6.69)$$

where

$$\hat{t} = -\frac{1}{2}\nabla^2 \quad (6.70)$$

is the kinetic energy operator and

$$v_I^{nHxc} = v_n[\rho_I^0] + v_H[\rho_I^0] + v_{xc}[\rho_I^0]. \quad (6.71)$$

This is known as the “potential superposition approximation.” A popular alternative is the “density superposition approximation” where $v_{xc}[\rho_I^0] + v_{xc}[\rho_J^0]$ is replaced with $v^{xc}[\rho_I^0 + \rho_J^0]$, hence reducing reliance on the assumption of a separable xc potential. Note that Eq. (6.70) involves only two-center integrals and

$$f_{\mu I, \nu I} = \delta_{\mu, \nu} \epsilon_{\mu I}^0, \quad (6.72)$$

where $\epsilon_{\mu I}$ is the AO energy for the isolated atom. This suffices for setting up the

matrix form of the orbital equation,

$$\mathbf{f}\vec{c}_i = \epsilon_i \mathbf{s}\vec{c}_i, \quad (6.73)$$

and hence to calculate the band structure (BS) part of the total energy,

$$E_{\text{BS}} = \sum_i n_i \epsilon_i. \quad (6.74)$$

Of course, this neglects important terms on the right-hand side of Eq. (6.37), known in DFTB as the repulsion energy,

$$E_{\text{rep}} = -\frac{1}{2}E_H + E_{\text{xc}} - \int v_{xc}(1)\rho(1) d1. \quad (6.75)$$

It is a fundamental tenant of DFTB that this energy can be expanded as a set of pairwise potentials between different atom types,

$$E_{\text{rep}} = \sum_{I < J} V_{I,J}(R_{I,J}). \quad (6.76)$$

Finding and tabulating good transferable pair repulsion potentials $V_{I,J}(R_{I,J})$ is a major part of DFTB.

An important extension of DFTB is the addition of a self-consistent charge (SCC) term, E_{coul} , accounting for charge density corrections $\delta\rho$ beyond the original superposition of atomic densities approximation ρ_0 . This correction may be through second- [94] or third-order [95]. For simplicity, we describe only the second-order correction here. We seek a semi-empirical approximation to

$$E_{\text{coul}} = \frac{1}{2} \int \int \delta\rho(1) (f_H(1,2) + f_{xc}(1,2)) \delta\rho(2) d1d2. \quad (6.77)$$

This is accomplished by extensive use of two approximations. The first is Mulliken's approximation for use in approximating electron repulsion integrals (ERIs) [96],

$$\chi_{\mu I}^*(1)\chi_{\nu J}(1) \approx \frac{S_{\mu I, \nu J}}{2} (\chi_{\mu I}^*(1)\chi_{\mu I}(1) + \chi_{\nu J}^*(1)\chi_{\nu J}(1)), \quad (6.78)$$

which leads to

$$\psi_r^*(1)\psi_s(1) \approx \sum_{\mu I} q_{\mu I}^{r,s} \chi_{\mu I}^*(1)\chi_{\mu I}(1), \quad (6.79)$$

where

$$q_{\mu I}^{r,s} = \frac{1}{2} \sum_{\nu J} (c_{\mu I, r}^* S_{\mu I, \nu J} c_{\nu J, s} + c_{\mu I, s} S_{\mu I, \nu J} c_{\nu J, r}^*) \quad (6.80)$$

is a Mulliken transition charge. The second approximation is the gamma approximation

$$\chi_{\mu I}^*(1)\chi_{\mu I}(1) \approx g_I(1), \quad (6.81)$$

where g_I is an s -type function centered on atom I . The restriction to s -type functions is needed to solve a classic rotational invariance problem in semi-empirical theories (pp. 60-63 of Ref. [83]). (In more recent programs, g_I may be replaced with s -type functions g_{II} , allowing g_{II} to be different for different values of the angular momentum quantum number of $\chi_{\mu I}$ [97].) Together Mulliken's ERI approximation and the gamma approximation lead to the auxiliary-function expansion

$$\psi_r^*(1)\psi_s(1) \approx \sum_I q_I^{r,s} g_I(1), \quad (6.82)$$

where

$$q_I^{r,s} = \sum_{\mu \in I} q_{\mu I}^{r,s}. \quad (6.83)$$

The name “gamma approximation” comes from the integral,

$$\gamma_{I,J} = \int \int g_I(1) (f_H(1,2) + f_{xc}(1,2)) g_I(2) d1d2, \quad (6.84)$$

where,

$$\begin{aligned} f_H(1,2) &= \frac{1}{r_{1,2}} \\ f_{xc}(1,2) &= \frac{\delta^2 E_{xc}}{\delta \rho(1) \delta \rho(2)}, \end{aligned} \quad (6.85)$$

which means that the density is

$$\rho(1) = \sum_i n_i \psi_i^*(1)\psi_i(1) \approx \sum_I q_I g_I(1), \quad (6.86)$$

where the Mulliken charge on atom I is

$$q_I = \sum_{\mu \in I} q_{\mu I}^{i,i} n_i. \quad (6.87)$$

The second-order SCC becomes

$$E_{\text{coul}}(\mathbf{R}) = \frac{1}{2} \sum_{I,J} \gamma_{I,J}(R_{I,J}) \Delta q_I \Delta q_J. \quad (6.88)$$

where Δq_I is the Mulliken charge fluctuation on atom I because

$$\delta\rho(1) \approx \sum_I \Delta q_I g_I(1). \quad (6.89)$$

Sometimes the diagonal elements $\gamma_{I,I}$ are calculated using some variation on Parisser's observation [98] that it should be equal to the difference between the ionization potential and electron affinity of atom I . This suggests that DFTB may work particularly well for calculating ionization potentials and electron affinities and this does seem to be the case [99], although the cited reference points out that DFTB was not parameterized to fit a single specific property, but rather to behave like DFT across a broad range of properties.

The SCC correction to the orbital hamilonian matrix,

$$f_{\mu I, \nu J} = \frac{s_{\mu I, \nu J}}{2} \sum_K (\gamma_{J,K} + \gamma_{K,I}) \Delta q_K, \quad (6.90)$$

is obtained in the usual way by variational minimization of the energy,

$$E = E_{\text{BS}} + E_{\text{rep}} + E_{\text{coul}} + E_{\text{vdW}}. \quad (6.91)$$

Note that we have added Grimme's D3 vdW correction to the DFTB energy formula as this is an important addition used in the present paper. Adding in this vdW term requires no essential changes in the DFTB formalism.

The construction of global hybrid and RSH versions of DFTB is now straightforward with appropriate modifications of the gamma integral. For example, to make the HF form of DFTB, both the xc parts of $E_{\text{BS}}[\rho_0]$ and of $E_{\text{rep}}[\delta\rho]$ must be replaced by the semi-empirical forms:

$$\begin{aligned} \gamma_{I,J} &= \int \int g_I(1) f_H(1,2) g_J(2) d1 d2, \\ J &= \sum_{i,j} n_i (ii | f_H | jj) n_j = \sum_{I,J} q_I \gamma_{I,J} q_J, \\ K &= \sum_{i,j} n_i (ij | f_H | ji) n_j = \sum_{I,J} \gamma_{I,J} \left(\sum_{i,j} n_k q_I^{i,j} q_J^{j,i} n_j \right). \end{aligned} \quad (6.92)$$

The first version of RSH DFTB seems to be that of Niehaus and Della Sella [100]. This was followed by an implementation by Niehaus [101] (see also Ref. [102]) and by Humeniuk and Mitrić [103, 104]. We will be using the latter form which was

parameterized to behave like a LRC version of their DFTB method which, itself, was parameterized to behave like PBE DFT. We will refer to the resultant method as lc-DFTB following Humeniuk and Mitić and we will see that it behaves not unlike CAM-B3LYP DFT. The long-range γ -matrix is given by,

$$\gamma_{I,J}^{\text{lr}}(R_{I,J}; \mu) = \text{erf}(\mu R_{I,J}) \gamma_{I,J}(R_{I,J}), \quad (6.93)$$

where $\mu = 1/R_{\text{max}}$ is the usual range-separation parameter. Humeniuk and Mitić also neglect the long-range contribution to E_{BS} on the grounds that the zero-order system “already accounts for all interactions between electrons in the neutral atoms” [104].

6.3.4 TD-DFTB

Niehaus *et al.* were the first to extend DFTB to TD-DFTB [105, 97, 106, 107]. This is greatly facilitated by the observation that the TD-DFT coupling matrix is already approximated in the E_{coul} term of TD-DFTB. This allows the **A** and **B** matrices in Casida’s equation to be written out in TD-DFTB form. The TD-DFTB coupling matrix is given by

$$K_{pq,rs} = \sum_{I,J} q_I^{p,q} \gamma_{I,J} q_J^{s,r}, \quad (6.94)$$

with $\gamma_{I,J}$ defined as in Eq. (6.84). For a detailed treatment of spin and separation into singlet and triplet blocks, see e.g., Ref. [108]. The dipole matrix elements needed to calculate oscillator strengths are calculated as

$$\langle \psi_p | \vec{r} | \psi_q \rangle = \sum_I \vec{R}_I q_I^{p,q}. \quad (6.95)$$

Other implementations include that of Ref. [109]. We will be using the TD-lc-DFTB described in Refs. [103, 104].

6.4 Computational Details

Two programs were used to carry out the calculations reported in this paper, namely GAUSSIAN09 [110] for DFT and TD-DFT calculations and DFTBABY [103, 104] for DFTB and TD-DFTB calculations. Note that, although GAUSSIAN09 does have the ability to carry out DFTB calculations, only DFTBABY allows us to carry out state-of-the-art TD-lc-DFTB calculations. We will first describe the options used

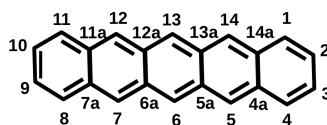


Figure 6.14 – Pentacene carbon numbering.

with each program in more detail. We will then go on to describe how the programs were used in structural and spectral studies.

GAUSSIAN09 [110] calculations may be described in terms of a “theoretical model” (p. 5, Ref. [111]) which is fully specified, in our case, by indicating for an excited-state (i.e., TD) calculation, the choice of functional and the orbital basis set. This is conveniently expressed in expanded notation as

$$(TD-)DFA1/Basis1//DFA2/Basis2$$

(p. 96, Ref. [111]), where DFA2 is the density-functional approximation used for the geometry optimization and Basis2 is the corresponding basis set used for the geometry optimization, and DFA1 is the density-functional approximation used for the TD-DFT calculation and Basis1 is the corresponding orbital basis used in the TD-DFT calculation. The density-functionals used (LDA, B3LYP, HF, CAM-B3LYP with or without Grimme’s D3 correction) were described in the previous section. Two orbital basis sets were used here, namely the minimal STO-3G basis set [112, 113] and the much more flexible 6-31G(d,p) split-valence (hydrogen [114], carbon [115]) plus polarization basis set [116]. An example of the expanded notation is that TD-CAM-B3LYP/6-31G(d,p)//D3-CAM-B3LYP/6-31G(d,p) means that the geometry of the molecule was optimized using the 6-31G(d,p) basis set using the CAM-B3LYP functional with the D3 dispersion correction. Then a TD-DFT calculation was carried out at that geometry using the 6-31G(d,p) orbital basis set and the CAM-B3LYP functional. Often we will use a shorter nomenclature when the details of the theoretical model are clear from context.

DFTBABY [103, 104] was used to carry out lc-DFTB and TD-lc-DFTB calculations. The values for the confinement radius r_0 and the Hubbard parameter U_H that were used to parameterize the electronic part of DFTB are shown in Table I of Ref. [103]. The parameter for the lc correction was set to $R_{lc} = 3.03$ bohr so $\mu = 1/R_{lc} = 0.33$, which is a reasonable compromise between $\mu = 0.33$ used in the CAM-B3LYP functional and $\mu = 0.4$ used in the LRC family of functionals.

Our structural calculations started with initial x-ray crystallography geometries taken from the Crystallography Open Database (COD) [117, 118]. We will use the

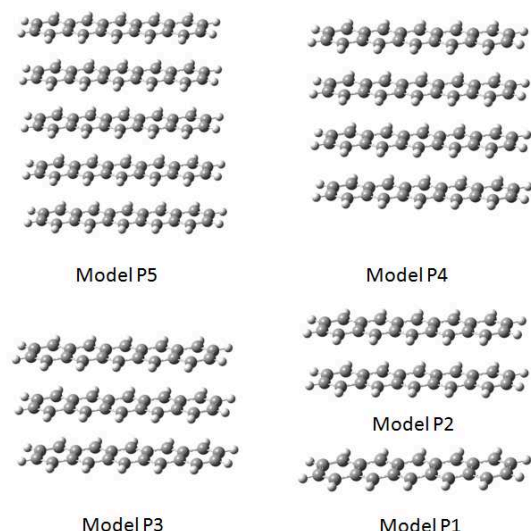


Figure 6.15 – The configurations of the five models of parallel stacked pentacene (P_n stands for n parallel stacked pentacenes).

standard numbering of pentacene carbon shown in Fig. 6.14. We first optimized the *monomer* geometry and calculated its absorption spectrum at each level. Vibrational frequencies were calculated to make sure that the optimized structures were true minima. We then went on to study an ideal *parallel stacked* model in which B3LYP/6-31G(d,p) optimized monomers were π -stacked vertically face-to-face with a fixed distance R between them (Fig. 6.15). The distance R was optimized for the tetramer using different methods and then this distance was used in studying stacks of different sizes. Finally we studied calculated absorption spectra for cluster models cut out of the experimental *herringbone* structure without any geometry optimization.

6.5 Results

Our goal in this section is to evaluate state-of-the-art (TD-)DFTB calculations of excitons in pentacene aggregates with state-of-the-art (TD-)DFT calculations on the same systems. We would also like to get a feeling for the relative importance of ET versus CT excitons. This involves three levels of calculation on three classes of systems. The three levels of calculation are first high-quality (TD-)DFT/6-31G(d,p) calculations aimed at obtaining good quality reference calculations which can be compared to experiment as a reality check. The second type of calculation consists of minimum basis set (TD-)DFT/STO-3G calculations as our ultimate goal is to evaluate the third method,

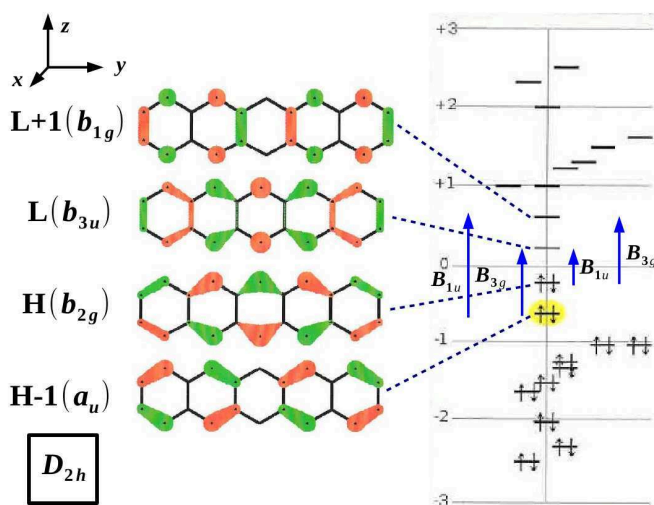


Figure 6.16 – Simple Hückel molecular orbital theory results for the pentacene monomer.

namely the minimal basis set semi-empirical (TD-)DFTB method. The systems considered are first an isolated gas phase pentacene molecule, second a series of parallel stacked pentacene molecules as these parallel the theory already presented in Sec. 6.2, and lastly a subunit of the known structure of crystalline pentacene.

6.5.1 Monomer

Although our primary interest here is in the absorption spectrum of the monomer, it is useful to begin with a review of the molecular orbitals (MOs). Figure 6.16 shows the result of a simple Hückel MO calculation with the SHMO calculator [119]. MO symmetries have been assigned following the recommended IUPAC nomenclature [44, 45] and the symmetry of the expected lowest energy excitations have been assigned.

The monomer geometry has been optimized at the LDA/STO-3G, LDA/6-31G(d,p), B3LYP/STO-3G, B3LYP/6-31G(d,p), CAM-B3LYP/STO-3G, CAM-B3LYP/6-31G(d,p), DFTB, and lc-DFTB levels of theory. The orbitals at the resultant optimized geometries have been visualized (e.g., Fig. 6.17) and are found to be qualitatively similar to those obtained from simple Hückel MO theory. This is important as it is then relatively easy to make a connection between the results of stacked pentacene molecules and the theoretical discussion of Sec. 6.2 for stacked ethylene molecules.

Figure 6.18 compares the calculated monomer absorption spectra with the experimental spectrum measured in tetrahydrofuran (data obtained by plot digitization [120] of Fig. 1 of Ref. [121]). Note that TD-DFT and TD-DFTB (and TD-lc-DFTB) calculations give qualitatively similar spectra in terms of the number and spacing of

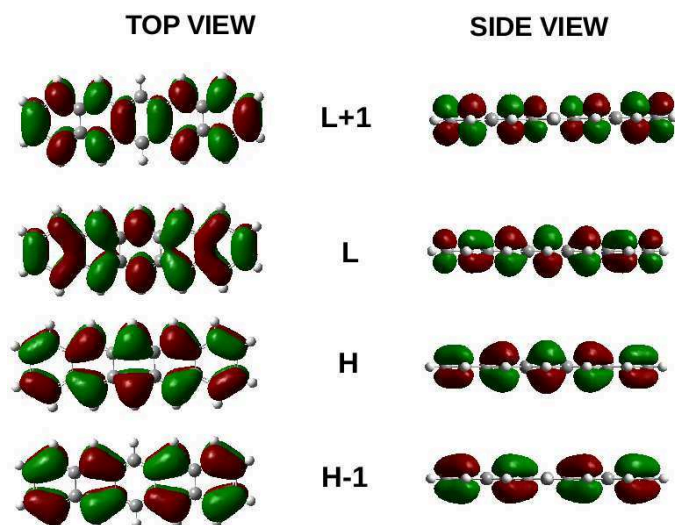


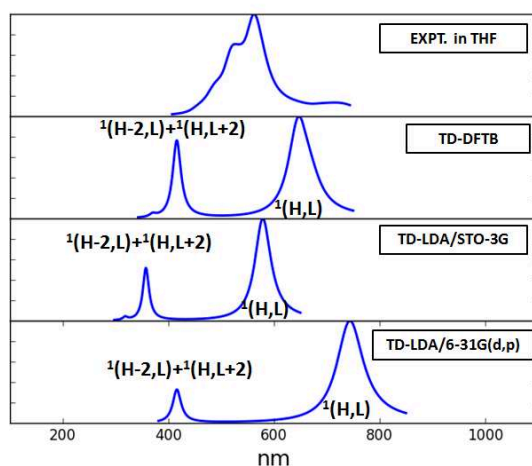
Figure 6.17 – Pentacene monomer B3LYP/6-31G(d,p) MOs.

peaks, though not all peaks are shown in Fig. 6.18. Our concern is primarily with the lowest energy (i.e., longest wavelength) transitions.

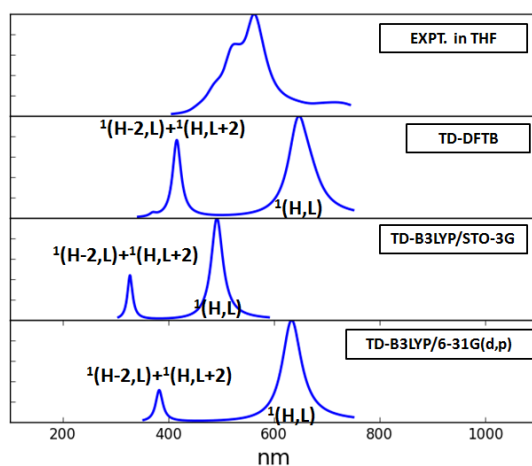
Let us first look at the TD-DFT calculations with the 6-31G(d,p) basis set using different functionals. The TD-LDA/6-31G(d,p) spectrum is red-shifted with respect to the experimental spectrum. The TD-B3LYP/6-31G(d,p) spectrum, which includes some HF exchange via a global hybrid, brings us closer to the experimental spectrum. Finally the TD-CAM-B3LYP/6-31G(d,p) spectrum, which includes even more HF exchange to describe the long-range part of the electron-electron repulsion, matches the experimental spectrum very well. Of course, this should be taken with a certain amount of scepticism because the experimental spectrum is measured in solution while the theoretical calculations are for the gas phase and neglect any vibrational contributions.

Let us now turn to the TD-DFTB and TD-lc-DFTB calculations. Since these are semi-empirical calculations, they are expected to be similar to TD-DFT/STO-3G calculations in that DFTB calculations are parameterized assuming a minimal basis set. This might be expected to show up in the number of underlying degrees of freedom and hence in the complexity of the calculated absorption spectra. Indeed this does seem to be the case in that the longest wavelength TD-CAM-B3LYP/6-31G(d,p) peak shows more complexity than does the longest wavelength TD-lc-DFTB or TD-DFTB peak. (This difference is *not* visible in Fig. 6.18, but rather in the underlying stick spectra.) However the TD-lc-DFTB and TD-DFTB spectra are red-shifted compared to the correspondingly TD-DFT/STO-3G spectra. This brings the TD-DFTB spectrum in remarkably good correspondence with the TD-

a)



b)



c)

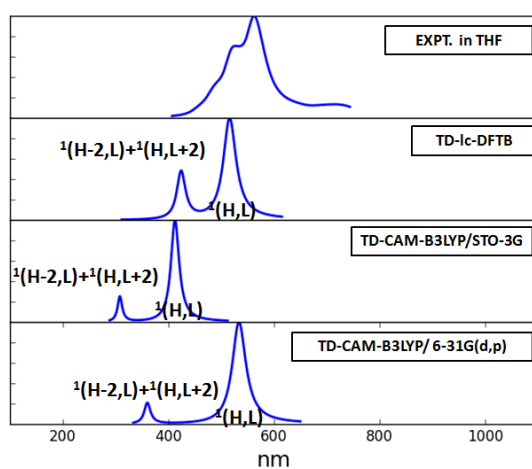


Figure 6.18 – Pentacene monomer absorption spectra: (a) TD-LDA, TD-DFTB, and experiment; (b) TD-B3LYP, TD-DFTB, and experiment; (c) TD-CAM-B3LYP, TD-lc-DFTB, and experiment. The experimental curve is a spectrum measured in tetrahydrofuran. Intensities are in arbitrary units.

Table 6.2 – Monomer lowest energy peak $^1(\text{H,L})$ calculated with various methods.

Method			
State	f (unitless)	λ (nm)	ΔE (eV)
TD-LDA/6-31G(d,p)//LDA/6-31G(d,p)			
1^1B_{1u}	0.0234	744	1.67
TD-LDA/STO-3G//LDA/STO-3G			
1^1B_{1u}	0.0325	579	2.14
TD-B3LYP/6-31G(d,p)//B3LYP/6-31G(d,p)			
1^1B_{1u}	0.0415	633	1.96
TD-B3LYP/STO-3G//B3LYP/STO-3G			
1^1B_{1u}	0.0596	492	2.52
TD-DFTB//DFTB			
1^1B_{1u}	0.1594	646	1.92
TD-CAM-B3LYP/6-31G(d,p)//B3LYP/6-31G(d,p)			
1^1B_{1u}	0.0750	534	2.32
TD-CAM-B3LYP/STO-3G//CAM-B3LYP/STO-3G			
1^1B_{1u}	0.1070	412	3.01
TD-lc-DFTB//lc-DFTB			
1^1B_{1u}	0.3212	515	2.40
HF/6-31G(d,p)//B3LYP/6-31G(d,p)			
1^1B_{1u}	0.1436	491	2.53
HF/STO-3G//B3LYP/6-31G(d,p)			
1^1B_{1u}	0.2279	357	3.47

B3LYP/6-31G(d,p) spectrum and the TD-lc-DFTB spectrum in remarkably good correspondence with the TD-CAM-B3LYP/6-31G(d,p) spectrum.

Some rough assignments are given, based upon MO contributions to the TD-DFT and TD-DFTB (or TD-lc-DFTB) coefficients. The lowest energy peaks (Table 6.2) are singlet HOMO \rightarrow LUMO transitions [$^1(\text{H,L})$]. The $^1(\text{H,L})$ TD-CAM-B3LYP/6-31G(d,p) peak is at 534 nm, which may be compared with the corresponding experimental value of about 540 nm from gas phase spectroscopy [122] and spectroscopy of isolated pentacene molecules in rare gas matrices [123]. The next lowest energy peaks have mixed $^1(\text{H-2,L})$ and $^1(\text{H,L+2})$ character as we have mentioned (Sec. 6.2) often occurs in the excitation spectra of π -conjugated molecules.

It is especially important to confirm our $^1(\text{H,L})$ peak assignment. Figure 6.19 shows the natural transition orbitals (NTOs) associated with the lower energy peak in the spectrum. Comparison with the nodal structure in Figs. 6.16 and 6.17 confirms that this is indeed the $^1(\text{H,L})$ transition.

Notice that there is a close analogy between the TOTEM model in ethylene and that of pentacene. In particular, the part of the H and L MOs on carbons 6 and 13 in pentacene (see Fig. 6.14) corresponds to a $\pi^* \rightarrow \pi$. This is sufficiently analogous to

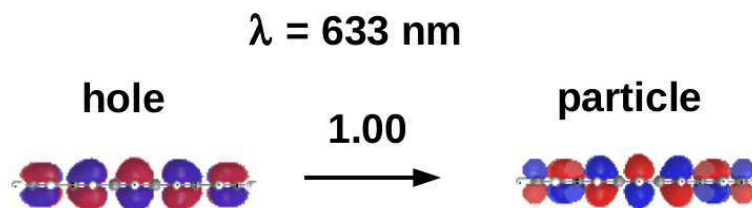


Figure 6.19 – Monomer NTOs and renormalized coefficient: TD-B3LYP/6-31G(d,p)//B3LYP/6-31G(d,p) 633 nm.

the $\pi \rightarrow \pi^*$ transition in ethylene that essentially the same theoretical analysis goes through for pentacene as for ethylene and we will make great use of this observation in the next subsection.

6.5.2 Stacking

We are concerned with the model of equally-spaced stacked pentacenes shown in Fig. 6.15. This model, though far from the observed herringbone structure of solid pentacene, is interesting because of its obvious analogy to graphite and because it may be readily compared with the model of equally-spaced stacked ethylenes discussed in the previous section.

6.5.2.1 Intermolecular forces

Equally-spaced parallel stacked pentacenes were prepared by optimizing the intermolecular distance for stacked tetramers without reoptimizing the individual molecules. The tetramer stacked structure is expected to be bound together by van der Waals forces at a distance similar to that in graphene, namely about 3 Å [124].

Figure 6.20 shows the resultant PES for molecules without dispersion correction. As a general rule, DFT can only describe forces between atoms in regions of space where the electron density is significant. Uncorrected DFT is usually unable to describe van der Waals binding as such binding takes place at intermolecular distances where the molecular densities do not overlap significantly. As seen in Fig. 6.20, LDA/6-31G(d,p) shows an accidental minimum at about 3.65 Å but LDA/STO-3G does not bind. The other functionals do not bind whichever basis is used. DFTB also does not bind, but it is less repulsive than the other calculations shown here.

Figure 6.21 shows the improved curves obtained using Grimme's D3 dispersion correction. The minima are located at about 3.7 Å for B3LYP+D3, at about 3.72 Å for CAM-B3LYP+D3, and at about 3.1 Å for DFTB+D3. Optimized intermolecular distances are summarized in Table 6.3.

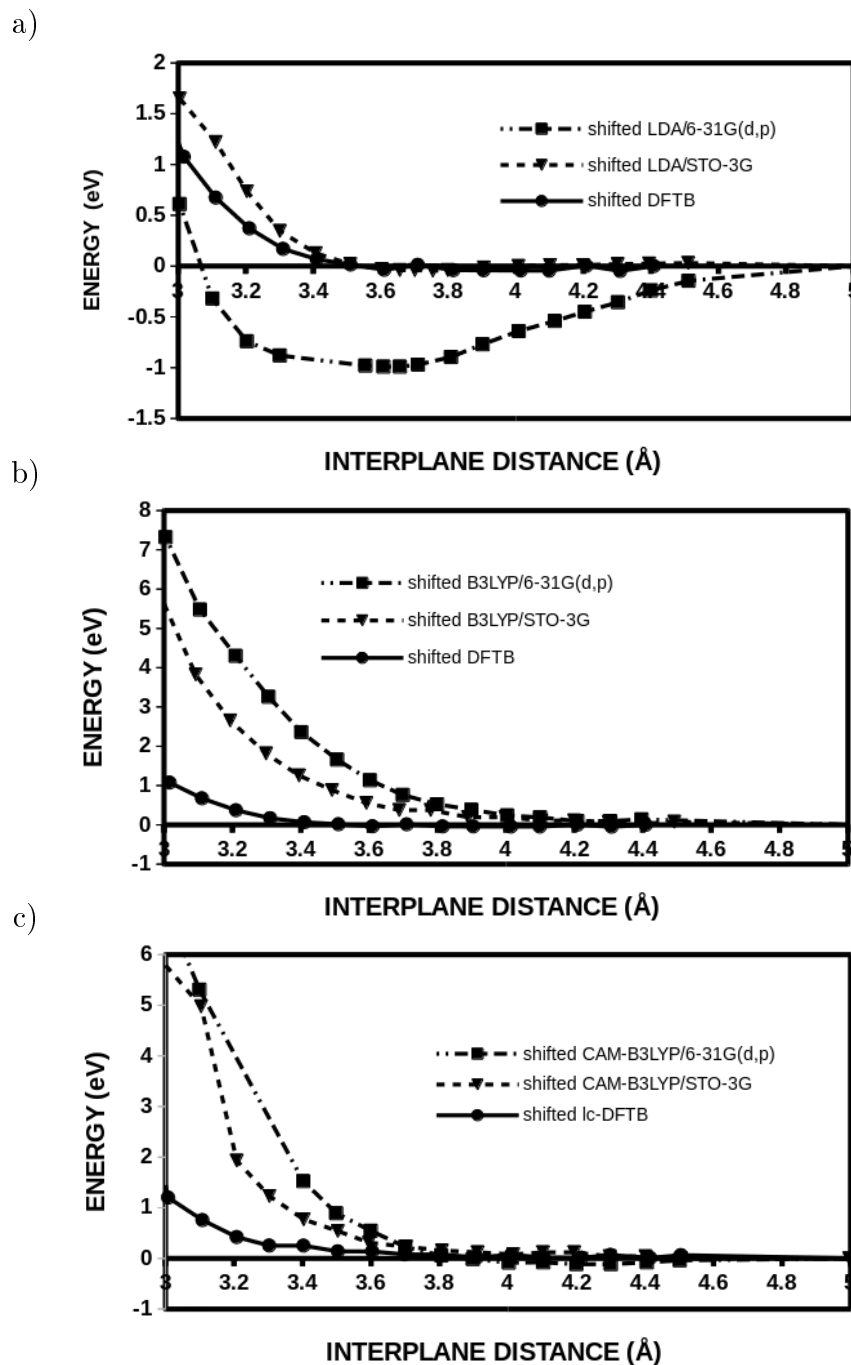


Figure 6.20 – Pentacene tetramer potential energy surfaces without dispersion correction: (a) LDA and DFTB; (b) B3LYP and DFTB; (c) CAM-B3LYP, lc-DFTB.

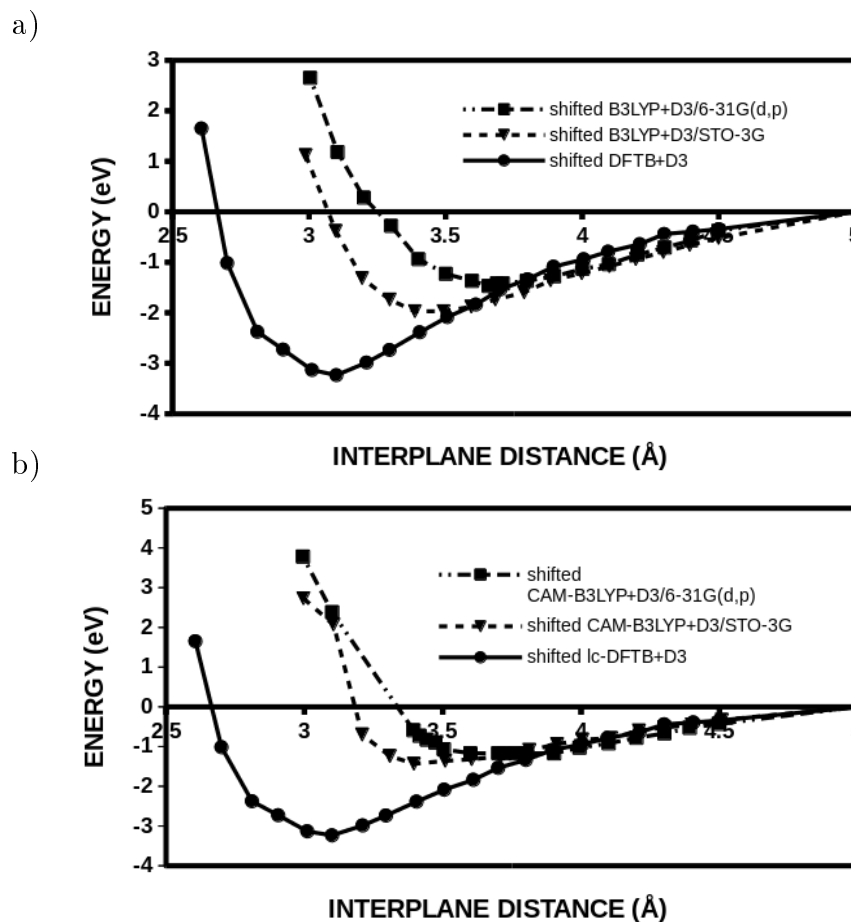


Figure 6.21 – Pentacene tetramer potential energy surfaces without dispersion correction: (a) B3LYP+D3 and DFTB+D3; (b) CAM-B3LYP+D3, lc-DFTB+D3.

Table 6.3 – Intermolecular distances obtained for the tetramer of parallel stacked pentacene molecules.

Method	Distance (Å)
LDA/STO-3G	3.7
LDA/6-31G(d,p)	3.6
B3LYP+D3/STO-3G	3.5
B3LYP+D3/6-31G(d,p)	3.68
CAM-B3LYP+D3/STO-3G	3.5
CAM-B3LYP+D3/6-31G(d,p)	3.72
DFTB+D3	3.1
lc-DFTB+D3	3.1

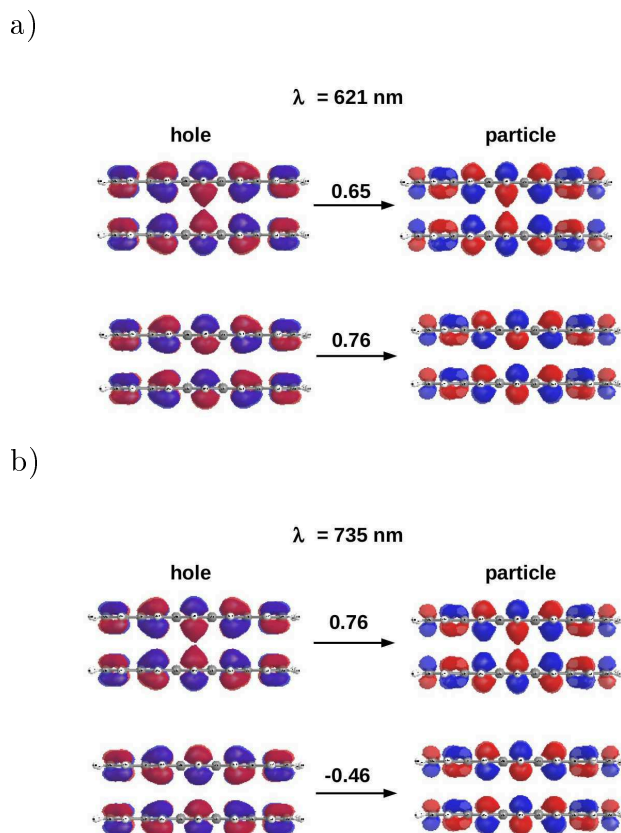


Figure 6.22 – Dimer NTOs and renormalized coefficients: (a) TD-B3LYP/6-31G(d,p)//D3-B3LYP/6-31G(d,p) 621 nm, (b) TD-B3LYP/6-31G(d,p)//D3-B3LYP/6-31G(d,p) 735 nm.

6.5.2.2 Energy versus charge transfer

Now that we have determined an optimal stacking distance (namely 3.71 Å), we can use the analogy to stacked ethylenes developed in the previous section to estimate the relative contributions of CT versus ET in the exciton model. This is possible by concentrating on the central part (carbons 6 and 13 of Fig. 6.14) of the $H(b_{2g})$ and $L(b_{3u})$ MOs in Fig. 6.16. This part of the pentacene $H(b_{2g})$ MO resembles the ethylene π^* MO while the pentacene $L(b_{3u})$ MO resembles the ethylene π MO (Fig. 6.2). Figure 6.19 shows a side view of the pentacene $H \rightarrow L$ transition. Looked at this way, the only important difference between the MOs for stacked pentacenes and the MOs for stacked ethylenes is that one MO diagram is the inverse of the other (i.e., bonding and antibonding orbitals have been interchanged).

Figure 6.22 shows the stacked pentacene dimer MOs which may be compared with the stacked ethylene dimer MOs (Fig. 6.4). It is easy to identify the coefficient c_1 for the $^1(H, L + 1)$ configuration and the coefficient c_2 for the $^1(H - 1, L)$ con-

Table 6.4 – Relative percentages of CT and ET excitonic transitions to the principle transition for two parallel stacked pentacenes as a function of method. See Eq. (6.5). DS is the Davydov splitting between the CT and ET excitonic transitions.

Method					
State	f (unitless)	λ (nm)	ΔE (eV)	ET ^a	CT ^b
TD-LDA/6-31G(d,p)//LDA/6-31G(d,p)					
1^1B_{1u}	0.0002	1033	1.20	0.3%	99.9%
2^1B_{1u}	0.0322	733	1.69	99.9%	0.3%
DS ₂ = 0.49 eV					
TD-LDA/STO-3G//LDA/STO-3G					
1^1B_{1u}	0.0000	818	1.52	0.005%	99.9%
2^1B_{1u}	0.0499	572	2.17	99.9%	0.005%
DS ₂ = 0.65 eV					
TD-B3LYP/6-31G(d,p)//B3LYP+D3/6-31G(d,p)					
1^1B_{1u}	0.0005	735	1.69	2%	98.9%
2^1B_{1u}	0.0576	621	2.00	98.9%	2%
DS ₂ = 0.31 eV					
TD-B3LYP/STO-3G//B3LYP+D3/STO-3G					
1^1B_{1u}	0.0000	604	2.05	0.02%	99.9%
2^1B_{1u}	0.0897	484	2.56	99.9%	0.02%
DS ₂ = 0.51 eV					
TD-DFTB//DFTB+D3					
1^1B_{1u}	0.0001	872	1.42	0.05%	99.9%
2^1B_{1u}	0.2831	634	1.96	99.9%	0.06%
DS ₂ = 0.54 eV					
TD-CAM-B3LYP/6-31G(d,p)//B3LYP+D3/6-31G(d,p)					
1^1B_{1u}	0.1036	523	2.37	97.9%	3.9%
2^1B_{1u}	0.0033	489	2.54	3.9%	97.9%
DS ₂ = -0.17 eV					
TD-CAM-B3LYP/STO-3G//CAM-B3LYP+D3/STO-3G					
1^1B_{1u}	0.0004	423	2.93	0.2%	99.9%
2^1B_{1u}	0.1628	404	3.07	99.9%	0.2%
DS ₂ = 0.14 eV					
TD-lc-DFTB//lc-DFTB+D3					
1^1B_{1u}	0.5782	495	2.50	99.8%	0.24%
2^1B_{1u}	0.0013	451	2.75	0.21%	99.8%
DS ₂ = -0.25 eV					
TD-HF/6-31G(d,p)//B3LYP+D3/6-31G(d,p)					
1^1B_{1u}	0.2087	474	2.62	99.9%	0.07%
2^1B_{1u}	0.0002	332	3.73	0.06%	99.9%
DS ₂ = -1.11 eV					
TD-HF/STO-3G//B3LYP+D3/6-31G(d,p)					
1^1B_{1u}	0.3557	347	3.58	99.9%	0.01%
2^1B_{1u}	0.0001	282	4.40	0.01%	99.9%
DS ₂ = -0.82 eV					

$$^a(c_1 + c_2)^2/2. \quad ^b(c_1 - c_2)^2/2.$$

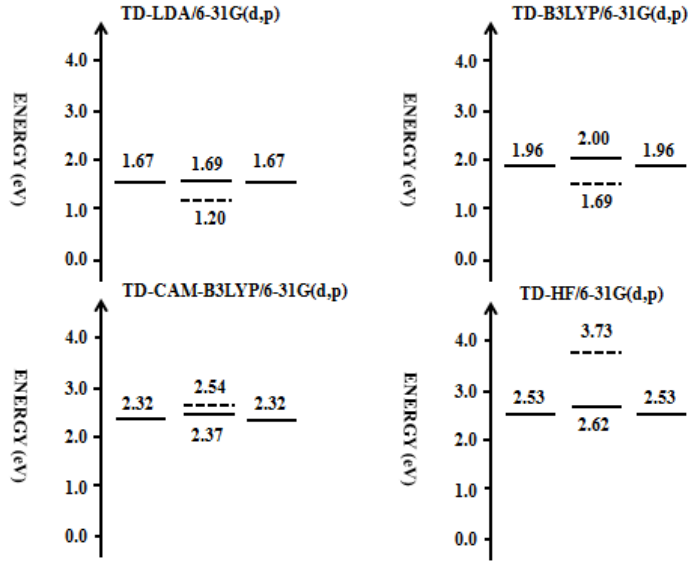


Figure 6.23 – Comparison of exciton diagrams for different functionals using the data from Tables 6.2 and 6.4.

figuration. Table 6.4 shows how the excitations split into a bright ET exciton and a much darker CT exciton. The energy splitting $DS = ET - CT$ is the Davydov splitting. Kasha's exciton model (Fig. 6.7) predicts a positive DS and this is exactly what is seen in our TD-LDA/6-31G(d,p), TD-LDA/STO-3G, TD-B3LYP/6-31G(d,p), TD-B3LYP/STO-3G, TD-CAM-B3LYP/STO-3G, and TD-DFTB calculations. However, improving the description of charge transfer by adding more HF exchange leads to negative values of DS in the TD-CAM-B3LYP/6-31G(d,p), TD-HF/6-31G(d,p), TD-HF/STO-3G, and TD-lc-DFTB models and a very different picture of exciton coupling (Fig. 6.23). Careful rereading of the classic exciton theory article of Kasha, Rawls, and El-Bayoumi [8] reveals that they took into account only dipole-dipole interactions but not charge transfer effects. As these charge transfer effects are implicit in our calculations, we may explain the observation that Hartree-Fock exchange leads to CT excitonic states of higher energy than ET states by the large amount of energy needed to separate charges. Interestingly the DS obtained from TD-DFTB//D3-DFTB resembles most closely that obtained with the TD-B3LYP/STO-3G//D3-B3LYP/STO-3G or TD-LDA/STO-3G//D3-LDA/STO-3G, consistent with the idea that the DS is primarily determined by the overlap which is too small when a minimal basis set is used. The situation changes markedly in going to the long-range corrected functionals. Here the TD-lc-DFTB DS is closer to the TD-CAM-DFTB/6-31G(d,p) DS than to the TD-CAM-DFTB/STO-3G DS.

Tables 6.5, 6.6, 6.7, 6.8, and 6.9 apply the analysis of Sec. 6.2 to the equally-spaced

Table 6.5 – Relative percentages of CT and ET excitonic transitions to the principle transition for three parallel stacked pentacenes as a function of method. See Eq. (6.8). DS is the Davydov splitting between the lowest energy CT and the highest energy ET excitonic transitions.

Method			
State	f (unitless)	λ (nm)	ΔE (eV)
TD-LDA/6-31G(d,p)//LDA/6-31G(d,p)			
1^1B_{1u}	0.0000	2444	0.51
Analysis			
		100%	$^1(\text{H,L})$
		0% ^a	$(\text{ET}_{12}+\text{ET}_{23})/\sqrt{3}$
		0% ^b	$(\sqrt{3}/2)[\text{ET}_{13}-(1/3)(\text{ET}_{12}+\text{ET}_{23})]$
		0% ^c	$(\text{CT}_{12}+\text{CT}_{23})/\sqrt{2}$
		0% ^d	CT_{13}
		0%	$^1(\text{H-2,L+2})$
2^1B_{1u}	0.0002	1040	1.20
Analysis			
		0%	$^1(\text{H,L})$
		8.9% ^a	$(\text{ET}_{12}+\text{ET}_{23})/\sqrt{3}$
		2.9% ^b	$(\sqrt{3}/2)[\text{ET}_{13}-(1/3)(\text{ET}_{12}+\text{ET}_{23})]$
		81.9% ^c	$(\text{CT}_{12}+\text{CT}_{23})/\sqrt{2}$
		6.3% ^d	CT_{13}
		0%	$^1(\text{H-2,L+2})$
3^1B_{1u}	0.0003	950	1.30
Analysis			
		0%	$^1(\text{H,L})$
		1.2% ^a	$(\text{ET}_{12}+\text{ET}_{23})/\sqrt{3}$
		34.2% ^b	$(\sqrt{3}/2)[\text{ET}_{13}-(1/3)(\text{ET}_{12}+\text{ET}_{23})]$
		7.6% ^c	$(\text{CT}_{12}+\text{CT}_{23})/\sqrt{2}$
		54.6% ^d	CT_{13}
		2.3%	$^1(\text{H-2,L+2})$
4^1B_{1u}	0.0405	730.	1.70
Analysis			
		0%	$^1(\text{H,L})$
		80.6% ^a	$(\text{ET}_{12}+\text{ET}_{23})/\sqrt{3}$
		19.1% ^b	$(\sqrt{3}/2)[\text{ET}_{13}-(1/3)(\text{ET}_{12}+\text{ET}_{23})]$
		0.3% ^c	$(\text{CT}_{12}+\text{CT}_{23})/\sqrt{2}$
		0.02% ^d	CT_{13}
		0%	$^1(\text{H-2,L+2})$
DS ₃ = 0.50 eV			
TD-LDA/STO-3G//LDA/STO-3G			
1^1B_{1u}	0.0000	1024	1.21
Analysis			
		88.4%	$^1(\text{H,L})$
		0.1% ^a	$(\text{ET}_{12}+\text{ET}_{23})/\sqrt{3}$
		3.5% ^b	$(\sqrt{3}/2)[\text{ET}_{13}-(1/3)(\text{ET}_{12}+\text{ET}_{23})]$
		2.3% ^c	$(\text{CT}_{12}+\text{CT}_{23})/\sqrt{2}$
		5.7% ^d	CT_{13}
		0%	$^1(\text{H-2,L+2})$
2^1B_{1u}	0.0000	816	1.52
Analysis			
		0%	$^1(\text{H,L})$
		0.3% ^a	$(\text{ET}_{12}+\text{ET}_{23})/\sqrt{3}$
		7.3% ^b	$(\sqrt{3}/2)[\text{ET}_{13}-(1/3)(\text{ET}_{12}+\text{ET}_{23})]$
		79.7% ^c	$(\text{CT}_{12}+\text{CT}_{23})/\sqrt{2}$
		12.7% ^d	CT_{13}
		0%	$^1(\text{H-2,L+2})$
3^1B_{1u}	0.0000	754	1.64
Analysis			
		7.2%	$^1(\text{H,L})$
		0.1% ^a	$(\text{ET}_{12}+\text{ET}_{23})/\sqrt{3}$
		39.2% ^b	$(\sqrt{3}/2)[\text{ET}_{13}-(1/3)(\text{ET}_{12}+\text{ET}_{23})]$
		22.8% ^c	$(\text{CT}_{12}+\text{CT}_{23})/\sqrt{2}$
		4.1% ^d	CT_{13}
		26.7%	$^1(\text{H-2,L+2})$
4^1B_{1u}	0.0664	571	2.17
Analysis			
		0%	$^1(\text{H,L})$
		78.5% ^a	$(\text{ET}_{12}+\text{ET}_{23})/\sqrt{3}$
		21.4% ^b	$(\sqrt{3}/2)[\text{ET}_{13}-(1/3)(\text{ET}_{12}+\text{ET}_{23})]$
		0.05% ^c	$(\text{CT}_{12}+\text{CT}_{23})/\sqrt{2}$
		0.05% ^d	CT_{13}
		0%	$^1(\text{H-2,L+2})$
DS ₃ = 0.65 eV			

$$^a(3c_2 + 2c_3 + 3c_4)^2/24. \quad ^b2c_3^2/3. \quad ^c(c_2 - c_4)^2/2. \quad ^d(c_2 - 2c_3 + c_4)^2/8.$$

Table 6.6 – Relative percentages of CT and ET excitonic transitions to the principle transition for three parallel stacked pentacenes as a function of method. See Eq. (6.8). DS is the Davydov splitting between the lowest energy CT and the highest energy ET excitonic transitions.

Method			
State	f (unitless)	λ (nm)	ΔE (eV)
TD-B3LYP/6-31G(d,p)//B3LYP+D3/6-31G(d,p)			
1^1B_{1u}	0.0001	1220	1.02
		Analysis	
		100.0%	$^1(\text{H,L})$
		0% ^a	$(\text{ET}_{12}+\text{ET}_{23})/\sqrt{3}$
		0% ^b	$(\sqrt{3}/2)[\text{ET}_{13}-(1/3)(\text{ET}_{12}+\text{ET}_{23})]$
		0% ^c	$(\text{CT}_{12}+\text{CT}_{23})/\sqrt{2}$
		0% ^d	CT_{13}
		0%	$^1(\text{H-2,L+2})$
		734	1.69
		2^1B_{1u}	0.0006
Analysis			
0%	$^1(\text{H,L})$		
0.8% ^a	$(\text{ET}_{12}+\text{ET}_{23})/\sqrt{3}$		
0% ^b	$(\sqrt{3}/2)[\text{ET}_{13}-(1/3)(\text{ET}_{12}+\text{ET}_{23})]$		
98.8% ^c	$(\text{CT}_{12}+\text{CT}_{23})/\sqrt{2}$		
0.3% ^d	CT_{13}		
0%	$^1(\text{H-2,L+2})$		
657	1.89		
3^1B_{1u}	0.0012		
		Analysis	
		0%	$^1(\text{H,L})$
		0.6% ^a	$(\text{ET}_{12}+\text{ET}_{23})/\sqrt{3}$
		39.7% ^b	$(\sqrt{3}/2)[\text{ET}_{13}-(1/3)(\text{ET}_{12}+\text{ET}_{23})]$
		0.2% ^c	$(\text{CT}_{12}+\text{CT}_{23})/\sqrt{2}$
		59.5% ^d	CT_{13}
		0%	$^1(\text{H-2,L+2})$
		618	2.01
		4^1B_{1u}	0.0723
Analysis			
0%	$^1(\text{H,L})$		
82.9% ^a	$(\text{ET}_{12}+\text{ET}_{23})/\sqrt{3}$		
15.8% ^b	$(\sqrt{3}/2)[\text{ET}_{13}-(1/3)(\text{ET}_{12}+\text{ET}_{23})]$		
0.9% ^c	$(\text{CT}_{12}+\text{CT}_{23})/\sqrt{2}$		
0.4% ^d	CT_{13}		
0%	$^1(\text{H-2,L+2})$		
DS ₃ = 0.32 eV			
TD-B3LYP/STO-3G//B3LYP+D3/STO-3G			
1^1B_{1u}	0.0001	801	1.55
		Analysis	
		100%	$^1(\text{H,L})$
		0% ^a	$(\text{ET}_{12}+\text{ET}_{23})/\sqrt{3}$
		0% ^b	$(\sqrt{3}/2)[\text{ET}_{13}-(1/3)(\text{ET}_{12}+\text{ET}_{23})]$
		0% ^c	$(\text{CT}_{12}+\text{CT}_{23})/\sqrt{2}$
		0% ^d	CT_{13}
		0%	$^1(\text{H-2,L+2})$
		602	2.06
		2^1B_{1u}	0.0000
Analysis			
0%	$^1(\text{H,L})$		
0.0% ^a	$(\text{ET}_{12}+\text{ET}_{23})/\sqrt{3}$		
0% ^b	$(\sqrt{3}/2)[\text{ET}_{13}-(1/3)(\text{ET}_{12}+\text{ET}_{23})]$		
100.0% ^c	$(\text{CT}_{12}+\text{CT}_{23})/\sqrt{2}$		
0.0% ^d	CT_{13}		
0%	$^1(\text{H-2,L+2})$		
539	2.30		
3^1B_{1u}	0.0003		
		Analysis	
		0%	$^1(\text{H,L})$
		7.0% ^a	$(\text{ET}_{12}+\text{ET}_{23})/\sqrt{3}$
		79.6% ^b	$(\sqrt{3}/2)[\text{ET}_{13}-(1/3)(\text{ET}_{12}+\text{ET}_{23})]$
		0.0% ^c	$(\text{CT}_{12}+\text{CT}_{23})/\sqrt{2}$
		13.4% ^d	CT_{13}
		0%	$^1(\text{H-2,L+2})$
		482	2.57
		4^1B_{1u}	0.1180
Analysis			
0%	$^1(\text{H,L})$		
82.9% ^a	$(\text{ET}_{12}+\text{ET}_{23})/\sqrt{3}$		
17.1% ^b	$(\sqrt{3}/2)[\text{ET}_{13}-(1/3)(\text{ET}_{12}+\text{ET}_{23})]$		
0.0% ^c	$(\text{CT}_{12}+\text{CT}_{23})/\sqrt{2}$		
0.0% ^d	CT_{13}		
0%	$^1(\text{H-2,L+2})$		
DS ₃ = 0.51 eV			

$$^a(3c_2 + 2c_3 + 3c_4)^2/24. \quad ^b2c_3^2/3. \quad ^c(c_2 - c_4)^2/2. \quad ^d(c_2 - 2c_3 + c_4)^2/8.$$

Table 6.7 – Relative percentages of CT and ET excitonic transitions to the principle transition for three parallel stacked pentacenes as a function of method. See Eq. (6.8). DS is the Davydov splitting between the lowest energy CT and the highest energy ET excitonic transitions.

		Method	
State	f (unitless)	λ (nm)	ΔE (eV)
TD-DFTB//DFTB+D3			
1^1B_{1u}	0.0000	1606	0.772
		Analysis	
		86.9%	$^1(\text{H,L})$
		1.6% ^a	$(\text{ET}_{12}+\text{ET}_{23})/\sqrt{3}$
		6.6% ^b	$(\sqrt{3}/2)[\text{ET}_{13}-(1/3)(\text{ET}_{12}+\text{ET}_{23})]$
		0% ^c	$(\text{CT}_{12}+\text{CT}_{23})/\sqrt{2}$
2^1B_{1u}	0.0002	4.9% ^d	CT_{13}
		0%	$^1(\text{H-2,L+2})$
		872	1.42
		Analysis	
		0%	$^1(\text{H,L})$
		0.01% ^a	$(\text{ET}_{12}+\text{ET}_{23})/\sqrt{3}$
3^1B_{1u}	0.0004	0% ^b	$(\sqrt{3}/2)[\text{ET}_{13}-(1/3)(\text{ET}_{12}+\text{ET}_{23})]$
		99.9% ^c	$(\text{CT}_{12}+\text{CT}_{23})/\sqrt{2}$
		0.03% ^d	CT_{13}
		0%	$^1(\text{H-2,L+2})$
		819	1.51
		Analysis	
4^1B_{1u}	0.4122	0%	$^1(\text{H,L})$
		6.0% ^a	$(\text{ET}_{12}+\text{ET}_{23})/\sqrt{3}$
		39.8% ^b	$(\sqrt{3}/2)[\text{ET}_{13}-(1/3)(\text{ET}_{12}+\text{ET}_{23})]$
		7.5% ^c	$(\text{CT}_{12}+\text{CT}_{23})/\sqrt{2}$
		46.7% ^d	CT_{13}
		0%	$^1(\text{H-2,L+2})$
DS ₃ = 0.57 eV			
TD-CAM-B3LYP/6-31G(d,p)//B3LYP+D3/6-31G(d,p)			
1^1B_{1u}	0.0005	764	1.62
		Analysis	
		94.5%	$^1(\text{H,L})$
		0.7% ^a	$(\text{ET}_{12}+\text{ET}_{23})/\sqrt{3}$
		2.7% ^b	$(\sqrt{3}/2)[\text{ET}_{13}-(1/3)(\text{ET}_{12}+\text{ET}_{23})]$
		0% ^c	$(\text{CT}_{12}+\text{CT}_{23})/\sqrt{2}$
2^1B_{1u}	0.1301	2.0% ^d	CT_{13}
		0%	$^1(\text{H-2,L+2})$
		520	2.38
		Analysis	
		0%	$^1(\text{H,L})$
		74.4% ^a	$(\text{ET}_{12}+\text{ET}_{23})/\sqrt{3}$
3^1B_{1u}	0.0074	20.6% ^b	$(\sqrt{3}/2)[\text{ET}_{13}-(1/3)(\text{ET}_{12}+\text{ET}_{23})]$
		4.9% ^c	$(\text{CT}_{12}+\text{CT}_{23})/\sqrt{2}$
		0.06% ^d	CT_{13}
		0%	$^1(\text{H-2,L+2})$
		489	2.53
		Analysis	
4^1B_{1u}	0.0001	0%	$^1(\text{H,L})$
		4.5% ^a	$(\text{ET}_{12}+\text{ET}_{23})/\sqrt{3}$
		0% ^b	$(\sqrt{3}/2)[\text{ET}_{13}-(1/3)(\text{ET}_{12}+\text{ET}_{23})]$
		94.0% ^c	$(\text{CT}_{12}+\text{CT}_{23})/\sqrt{2}$
		1.5% ^d	CT_{13}
		0%	$^1(\text{H-2,L+2})$
DS ₃ = -0.15 eV			
4^1B_{1u}	0.0001	435	2.85
		Analysis	
		4.2%	$^1(\text{H,L})$
		2.0% ^a	$(\text{ET}_{12}+\text{ET}_{23})/\sqrt{3}$
		22.9% ^b	$(\sqrt{3}/2)[\text{ET}_{13}-(1/3)(\text{ET}_{12}+\text{ET}_{23})]$
		7.9% ^c	$(\text{CT}_{12}+\text{CT}_{23})/\sqrt{2}$
4^1B_{1u}	0.0001	40.3% ^d	CT_{13}
		22.7%	$^1(\text{H-2,L+2})$
		Analysis	
		4.2%	$^1(\text{H,L})$
		2.0% ^a	$(\text{ET}_{12}+\text{ET}_{23})/\sqrt{3}$
		22.9% ^b	$(\sqrt{3}/2)[\text{ET}_{13}-(1/3)(\text{ET}_{12}+\text{ET}_{23})]$
4^1B_{1u}	0.0001	7.9% ^c	$(\text{CT}_{12}+\text{CT}_{23})/\sqrt{2}$
		40.3% ^d	CT_{13}
		22.7%	$^1(\text{H-2,L+2})$
		Analysis	
		4.2%	$^1(\text{H,L})$
		2.0% ^a	$(\text{ET}_{12}+\text{ET}_{23})/\sqrt{3}$
4^1B_{1u}	0.0001	22.9% ^b	$(\sqrt{3}/2)[\text{ET}_{13}-(1/3)(\text{ET}_{12}+\text{ET}_{23})]$
		7.9% ^c	$(\text{CT}_{12}+\text{CT}_{23})/\sqrt{2}$
		40.3% ^d	CT_{13}
		22.7%	$^1(\text{H-2,L+2})$
		Analysis	
		4.2%	$^1(\text{H,L})$

$$^a(3c_2 + 2c_3 + 3c_4)^2/24. \quad ^b2c_3^2/3. \quad ^c(c_2 - c_4)^2/2. \quad ^d(c_2 - 2c_3 + c_4)^2/8.$$

Table 6.8 – Relative percentages of CT and ET excitonic transitions to the principle transition for three parallel stacked pentacenes as a function of method. See Eq. (6.8). DS is the Davydov splitting between the lowest energy CT and the highest energy ET excitonic transitions.

		Method	
State	f (unitless)	λ (nm)	ΔE (eV)
TD-CAM-B3LYP/STO-3G//CAM-B3LYP+D3/STO-3G			
$1^1 B_{1u}$	0.0006	544	2.28
		Analysis	
		93.0%	$^1(\text{H,L})$
		4.1% ^a	$(\text{ET}_{12} + \text{ET}_{23})/\sqrt{3}$
		1.7% ^b	$(\sqrt{3}/2)[\text{ET}_{13} - (1/3)(\text{ET}_{12} + \text{ET}_{23})]$
		0% ^c	$(\text{CT}_{12} + \text{CT}_{23})/\sqrt{2}$
		1.2% ^d	CT_{13}
		0%	$^1(\text{H-2,L+2})$
$2^1 B_{1u}$	0.0000	423	2.93
		Analysis	
		0%	$^1(\text{H,L})$
		4.4% ^a	$(\text{ET}_{12} + \text{ET}_{23})/\sqrt{3}$
		0% ^b	$(\sqrt{3}/2)[\text{ET}_{13} - (1/3)(\text{ET}_{12} + \text{ET}_{23})]$
		89.7% ^c	$(\text{CT}_{12} + \text{CT}_{23})/\sqrt{2}$
		5.9% ^d	CT_{13}
		0%	$^1(\text{H-2,L+2})$
$3^1 B_{1u}$	0.2165	402	3.08
		Analysis	
		0%	$^1(\text{H,L})$
		79.6% ^a	$(\text{ET}_{12} + \text{ET}_{23})/\sqrt{3}$
		20.3% ^b	$(\sqrt{3}/2)[\text{ET}_{13} - (1/3)(\text{ET}_{12} + \text{ET}_{23})]$
		0.03% ^c	$(\text{CT}_{12} + \text{CT}_{23})/\sqrt{2}$
		0.1% ^d	CT_{13}
		0%	$^1(\text{H-2,L+2})$
$4^1 B_{1u}$	0.0001	371	3.34
		Analysis	
		0%	$^1(\text{H,L})$
		3.4% ^a	$(\text{ET}_{12} + \text{ET}_{23})/\sqrt{3}$
		23.9% ^b	$(\sqrt{3}/2)[\text{ET}_{13} - (1/3)(\text{ET}_{12} + \text{ET}_{23})]$
		0.7% ^c	$(\text{CT}_{12} + \text{CT}_{23})/\sqrt{2}$
		45.1% ^d	CT_{13}
		26.8%	$^1(\text{H-2,L+2})$
DS ₃ = 0.15 eV			
TD-lc-DFTB//lc-DFTB+D3			
$1^1 B_{1u}$	0.0028	705	1.76
		Analysis	
		88.4%	$^1(\text{H,L})$
		1.5% ^a	$(\text{ET}_{12} + \text{ET}_{23})/\sqrt{3}$
		5.8% ^b	$(\sqrt{3}/2)[\text{ET}_{13} - (1/3)(\text{ET}_{12} + \text{ET}_{23})]$
		0% ^c	$(\text{CT}_{12} + \text{CT}_{23})/\sqrt{2}$
		4.4% ^d	CT_{13}
		0%	$^1(\text{H-2,L+2})$
$2^1 B_{1u}$	0.8238	487	2.54
		Analysis	
		0%	$^1(\text{H,L})$
		29.6% ^a	$(\text{ET}_{12} + \text{ET}_{23})/\sqrt{3}$
		26.0% ^b	$(\sqrt{3}/2)[\text{ET}_{13} - (1/3)(\text{ET}_{12} + \text{ET}_{23})]$
		14.2% ^c	$(\text{CT}_{12} + \text{CT}_{23})/\sqrt{2}$
		30.2% ^d	CT_{13}
		0%	$^1(\text{H-2,L+2})$
$3^1 B_{1u}$	0.0018	452	2.74
		Analysis	
		0%	$^1(\text{H,L})$
		0.01% ^a	$(\text{ET}_{12} + \text{ET}_{23})/\sqrt{3}$
		0% ^b	$(\sqrt{3}/2)[\text{ET}_{13} - (1/3)(\text{ET}_{12} + \text{ET}_{23})]$
		100.0% ^c	$(\text{CT}_{12} + \text{CT}_{23})/\sqrt{2}$
		0.003% ^d	CT_{13}
		0%	$^1(\text{H-2,L+2})$
$4^1 B_{1u}$	0.0007	409	3.03
		Analysis	
		0%	$^1(\text{H,L})$
		3.8% ^a	$(\text{ET}_{12} + \text{ET}_{23})/\sqrt{3}$
		15.2% ^b	$(\sqrt{3}/2)[\text{ET}_{13} - (1/3)(\text{ET}_{12} + \text{ET}_{23})]$
		0% ^c	$(\text{CT}_{12} + \text{CT}_{23})/\sqrt{2}$
		11.4% ^d	CT_{13}
		69.5%	$^1(\text{H-2,L+2})$
DS ₃ = -0.20 eV			

$$^a(3c_2 + 2c_3 + 3c_4)^2/24. \quad ^b2c_3^2/3. \quad ^c(c_2 - c_4)^2/2. \quad ^d(c_2 - 2c_3 + c_4)^2/8.$$

Table 6.9 – Relative percentages of CT and ET excitonic transitions to the principle transition for three parallel stacked pentacenes as a function of method. See Eq. (6.8). DS is the Davydov splitting between the lowest energy CT and the highest energy ET excitonic transitions.

Method			
State	f (unitless)	λ (nm)	ΔE (eV)
TD-HF/STO-3G//B3LYP+D3/6-31G(d,p)			
1^1B_{1u}	0.0051	417	2.97
		Analysis	
		77.8%	$^1(\text{H,L})$
		0.2% ^a	$(\text{ET}_{12}+\text{ET}_{23})/\sqrt{3}$
		8.4% ^b	$(\sqrt{3}/2) \text{ET}_{13}-(1/3)(\text{ET}_{12}+\text{ET}_{23}) $
		1.4% ^c	$(\text{CT}_{12}+\text{CT}_{23})/\sqrt{2}$
		9.6% ^d	CT_{13}
		6.9%	$^1(\text{H-2,L+2})$
2^1B_{1u}	0.4703	343	3.62
		Analysis	
		0%	$^1(\text{H,L})$
		89.4% ^a	$(\text{ET}_{12}+\text{ET}_{23})/\sqrt{3}$
		21.2% ^b	$(\sqrt{3}/2) \text{ET}_{13}-(1/3)(\text{ET}_{12}+\text{ET}_{23}) $
		0.02% ^c	$(\text{CT}_{12}+\text{CT}_{23})/\sqrt{2}$
		0.02% ^d	CT_{13}
		0%	$^1(\text{H-2,L+2})$
3^1B_{1u}	0.0001	283	4.38
		Analysis	
		4.3%	$^1(\text{H,L})$
		0.65% ^a	$(\text{ET}_{12}+\text{ET}_{23})/\sqrt{3}$
		0% ^b	$(\sqrt{3}/2) \text{ET}_{13}-(1/3)(\text{ET}_{12}+\text{ET}_{23}) $
		91.1% ^c	$(\text{CT}_{12}+\text{CT}_{23})/\sqrt{2}$
		0.22% ^d	CT_{13}
		3.7%	$^1(\text{H-2,L+2})$
4^1B_{1u}	0.0000	270	4.59
		Analysis	
		18.3%	$^1(\text{H,L})$
		1.3% ^a	$(\text{ET}_{12}+\text{ET}_{23})/\sqrt{3}$
		9.5% ^b	$(\sqrt{3}/2) \text{ET}_{13}-(1/3)(\text{ET}_{12}+\text{ET}_{23}) $
		9.5% ^c	$(\text{CT}_{12}+\text{CT}_{23})/\sqrt{2}$
		17.8% ^d	CT_{13}
		48.4%	$^1(\text{H-2,L+2})$
DS ₃ = -0.76 eV			
TD-HF/6-31G(d,p)//B3LYP+D3/6-31G(d,p)			
1^1B_{1u}	0.0025	662	1.87
		Analysis	
		81.0%	$^1(\text{H,L})$
		0.2% ^a	$(\text{ET}_{12}+\text{ET}_{23})/\sqrt{3}$
		7.1% ^b	$(\sqrt{3}/2) \text{ET}_{13}-(1/3)(\text{ET}_{12}+\text{ET}_{23}) $
		3.1% ^c	$(\text{CT}_{12}+\text{CT}_{23})/\sqrt{2}$
		13.9% ^d	CT_{13}
		0%	$^1(\text{H-2,L+2})$
2^1B_{1u}	0.2682	468	2.65
		Analysis	
		0%	$^1(\text{H,L})$
		89.0% ^a	$(\text{ET}_{12}+\text{ET}_{23})/\sqrt{3}$
		21.8% ^b	$(\sqrt{3}/2) \text{ET}_{13}-(1/3)(\text{ET}_{12}+\text{ET}_{23}) $
		0.11% ^c	$(\text{CT}_{12}+\text{CT}_{23})/\sqrt{2}$
		0.003% ^d	CT_{13}
		0%	$^1(\text{H-2,L+2})$
3^1B_{1u}	0.0002	334	3.71
		Analysis	
		4.0%	$^1(\text{H,L})$
		1.5% ^a	$(\text{ET}_{12}+\text{ET}_{23})/\sqrt{3}$
		0% ^b	$(\sqrt{3}/2) \text{ET}_{13}-(1/3)(\text{ET}_{12}+\text{ET}_{23}) $
		90.6% ^c	$(\text{CT}_{12}+\text{CT}_{23})/\sqrt{2}$
		5.1% ^d	CT_{13}
		3.4%	$^1(\text{H-2,L+2})$
4^1B_{1u}	0.0004	315	3.94
		Analysis	
		18.1%	$^1(\text{H,L})$
		1.1% ^a	$(\text{ET}_{12}+\text{ET}_{23})/\sqrt{3}$
		14.7% ^b	$(\sqrt{3}/2) \text{ET}_{13}-(1/3)(\text{ET}_{12}+\text{ET}_{23}) $
		11.5% ^c	$(\text{CT}_{12}+\text{CT}_{23})/\sqrt{2}$
		25.1% ^d	CT_{13}
		36.8%	$^1(\text{H-2,L+2})$
DS ₃ = -1.06 eV			

$$^a(3c_2 + 2c_3 + 3c_4)^2/24. \quad ^b2c_3^2/3. \quad ^c(c_2 - c_4)^2/2. \quad ^d(c_2 - 2c_3 + c_4)^2/8.$$

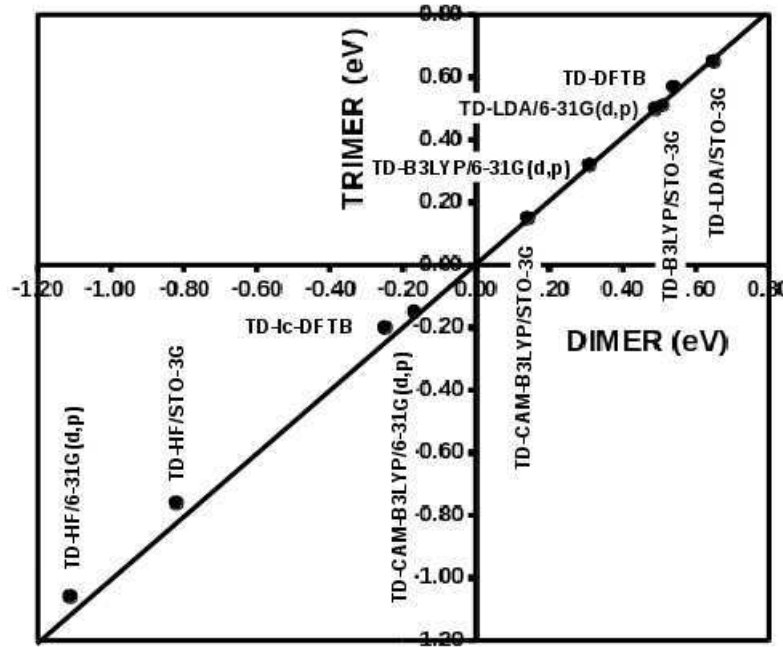


Figure 6.24 – Graph comparing the Davydov splittings, $E(ET)-E(CT)$, of the trimer and dimer. The 45° line indicates perfect agreement between dimer and trimer Davydov splittings.

parallel stacked trimer. As expected, instead of a Davydov pair of ET and CT excitations, we find a Davydov triplet corresponding to the 2^1B_{1u} , 3^1B_{1u} , and 4^1B_{1u} states. When the Davydov pairs can be identified, we have highlighted their assignment in terms of nearest neighbor interactions in the tables. Cases where the Davydov pairs are clear are: TD-LDA/6-31G(d,p)//LDA/6-31G(d,p), TD-LDA/STO-3G//LDA/STO-3G, TD-B3LYP/6-31G(d,p)//B3LYP+D3/6-31G(d,p), TD-B3LYP/STO-3G//B3LYP+D3/STO-3G, TD-DFTB//DFTB+D3. In these cases, the $(ET_{12}+ET_{23})$ -dominated state is the highest energy transition of the Davydov triplet and also has the highest oscillator strength while the $(CT_{12}+CT_{23})$ -dominated state is the lowest energy transition of the Davydov triplet and has significantly less oscillator strength. A third contribution to the Davydov triplet lies between the two other states and also has only a feeble transition energy. This assignment is a bit less clear in the TD-DFTB//DFTB+D3 case because there is significant mixing between $ET_{12}+ET_{23}$ and ET_{13} in the brightest configuration. Henceforth we shall simply assume that the peak with the highest oscillator strength is an $(ET_{12}+ET_{23})$ -dominated state. Figure 6.24 shows that calculations with these methods give essentially the same Davydov splitting for the dimer and for the trimer, and that the dimer (DS_2) and trimer (DS_3) splittings are very similar for TD-DFTB and for TD-B3LYP/6-31G(d,p), as well as being very similar for TD-lc-DFT and for TD-CAM-B3LYP/6-

31G(d,p).

6.5.2.3 Spectra

Calculations beyond the trimer become increasingly complicated to analyze but we may compare calculated spectra for increasingly large numbers of parallel stacked pentacene molecules. The tight-binding calculation in Sec. 6.2 is based upon the hope that nearest neighbor interactions dominate excitonic effects in spectra. The comparison of dimer and trimer DSs seem to at least partially confirm this. We may make a further check by seeing how the spectra change as more and more pentacene molecules are stacked. These spectra are shown in Fig. 6.25. All of the spectra show a main peak (i.e., the ET peak) which blue shifts as the pentacene stack grows. More specifically, the graphs show a main peak which undergoes the largest shift in going from the monomer to the dimer, a smaller shift in going from the dimer to the trimer and then shifts very little in going to higher oligomers, consistent with the suppositions behind the tight-binding model.

Our TD-DFT and TD-lc-DFTB calculations led us to become aware of a problem already reported in Ref. [104]. It is in the spirit of semi-empirical approaches to make simplifying approximations which allow the treatment of larger molecules than would otherwise be possible. This is why DFTBABY restricts the space of active orbitals, but it is still up to the user to decide how to use this option. One way would be to increase the size of the active space until converged spectra are achieved. But this ideal approach is not really practical when going to larger and larger aggregates of molecules. Instead, the first idea that comes to mind is to use the largest active space for which calculations are possible. In practice, this means using the same number of occupied and unoccupied orbitals in the active space, independent of the number of molecules. We call doing this a calculation with a *fixed active space*. However it has the important drawback when describing size-dependent trends that fixed active space calculations have more basis functions per molecule for smaller aggregates than for larger aggregates and so invariably describe smaller aggregates better than larger aggregates with the introduction of corresponding systematic errors in the resultant size-dependent properties. The other approach is to keep the number of occupied and unoccupied orbitals in the active space proportional to the number of molecules. In this way, we hope to obtain a better description of size-dependent trends, albeit at some cost of accuracy for smaller aggregates. We call this doing a calculation with a *size-consistent active space*. (There is some confusion in the literature between the terms “size-consistent” and “size-extensive.” Both terms are arguably correct here, but we shall stick to “size-consistent.”) Figures 6.26 and 6.27 compare fixed and

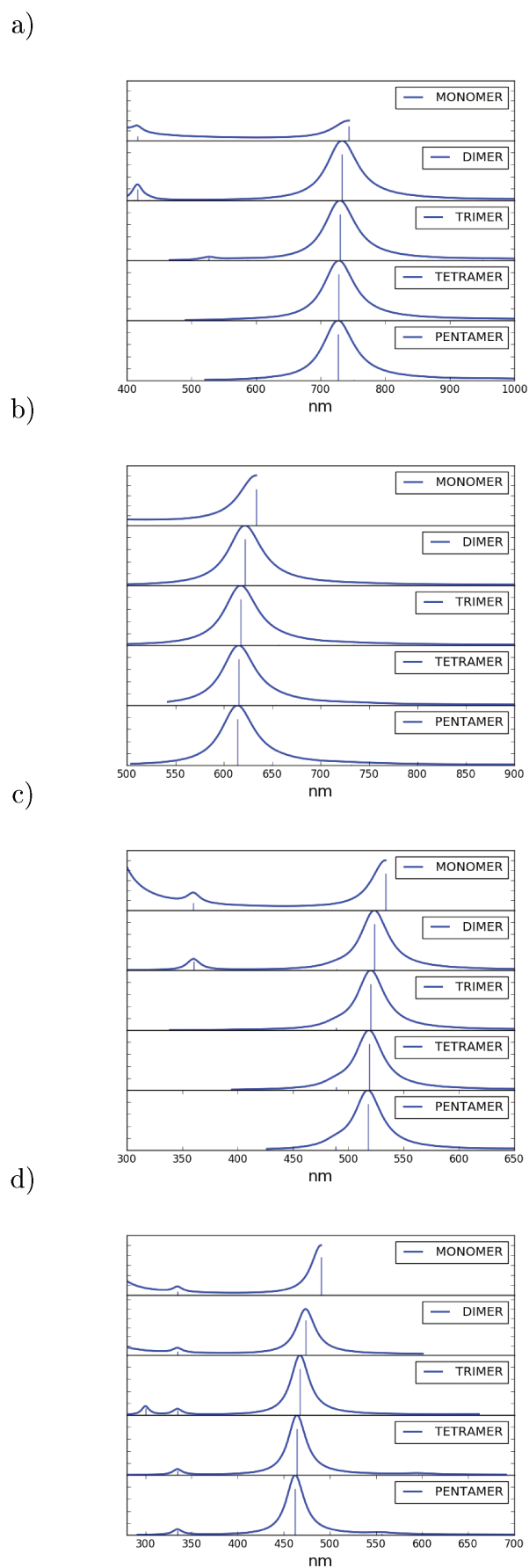
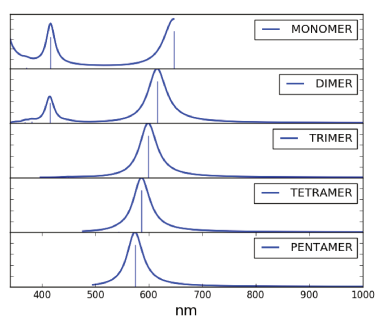


Figure 6.25 – Convergence of spectra as a function of number of pentacene molecules in the stack: (a) TD-LDA/6-31G(d,p), (b) TD-B3LYP/6-31G(d,p), (c) TD-CAM-B3LYP/6-31G(d,p), and (d) TD-HF/6-31G(d,p).

a)



b)

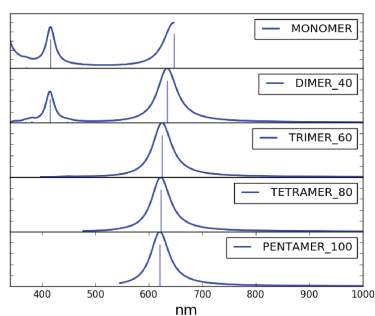
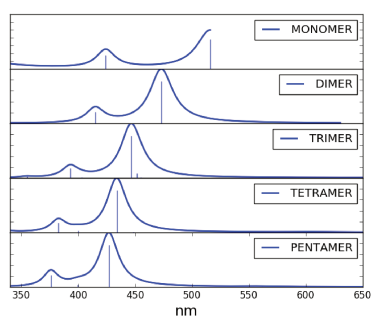


Figure 6.26 – TD-DFTB spectra of stacked pentacene: (a) with a fixed active space, (b) with a size-extensive active space.

a)



b)

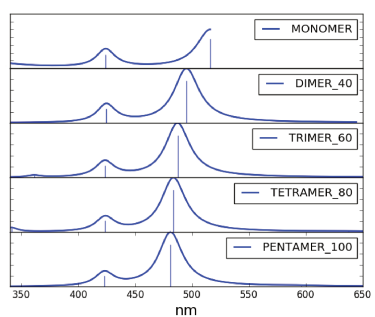


Figure 6.27 – TD-ic-DFTB spectra of stacked pentacene: (a) with a fixed active space, (b) with a size-consistent active space.

size-consistent active space calculations. The fixed active space calculations use 20 occupied orbitals and 20 unoccupied orbitals per aggregate. The size-consistent active space calculations use 20 occupied and 20 unoccupied orbitals per pentacene molecule. As the figure shows, the calculations with fixed active space blue shifts much more than do the calculations with self-consistent active space as the number of pentacene molecules increases. TD-DFT calculations of excitation energies are variational in the Tamm-Dancoff approximation and pseudo-variational in the sense that full linear response calculations often give similar results to using the Tamm-Dancoff approximation. For the monomer the fixed active space and size-consistent active space calculations are identical; however for the aggregates, the size-consistent active space is larger than the fixed active space calculations, leading to lower excitation energies in the size-consistent active space calculations. One would hope that the larger basis set would give better answers and that this is the case is shown in Fig. 6.28 where it is seen that TD-DFTB and TD-B3LYP/6-31G(d,p) spectral peak locations differ by only about 10 nm. Figure 6.26 shows that the difference between the TD-DFTB and TD-B3LYP/6-31G(d,p) calculations would have been more like 50 nm had the fixed active space been used. Figure 6.28 also shows that the differences between TD-lc-DFTB and TD-CAM-B3LYP/6-31G(d,p) spectra are larger than for the TD-DFTB and TD-B3LYP/6-31G(d,p) case when the size-extensive active space is used, with the main peak in this part of the spectrum having an energy difference of around 30 nm between the two calculations. Interestingly both show qualitatively similar Davydov multiplets. Figure 6.27 shows that the difference between the TD-lc-DFTB and TD-CAM-B3LYP(d,p) calculations would have been more like 80 nm had the fixed active space been used. This is why, except for Figs. 6.26 and 6.27, we have been careful to use a size-consistent active space consisting of 20 occupied and 20 unoccupied orbitals per molecule in all the TD-DFTB and TD-lc-DFTB reported in this paper.

6.5.3 Herringbone

The main objective of the present work has been to evaluate the ability of TD-DFTB and TD-lc-DFTB to simulate, respectively, the results of TD-B3LYP/6-31G(d,p) and TD-CAM-B3LYP/6-31G(d,p) calculations. While this has been largely satisfied by our study of parallel stacked pentacene molecules, the case of parallel stacked molecules is too artificial to allow comparison against experiment (except for the monomer.) In order to have a reality check, we have also carried out calculations for cluster models of pentacene crystals. The experimental spectrum of the molecule and of the crystal are available both from experiment [126, 121, 127]

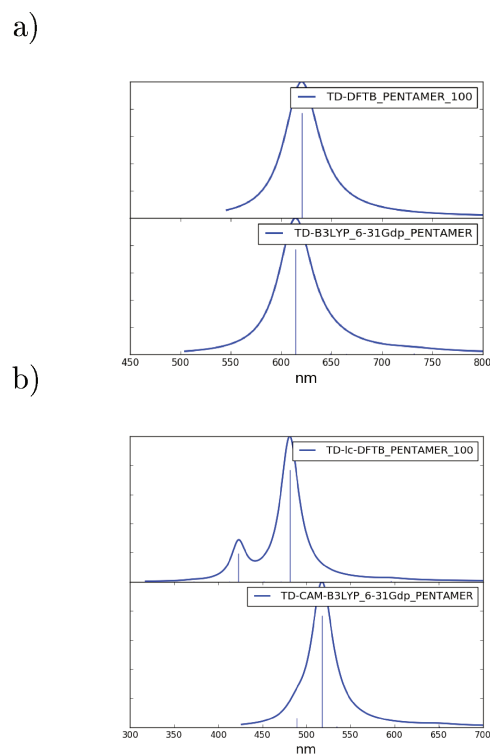


Figure 6.28 – Comparison of pentacene spectra: (a) TD-DFTB and TD-B3LYP/6-31G(d,p) and (b) TD-lc-DFTB and TD-CAM-B3LYP/6-31G(d,p).

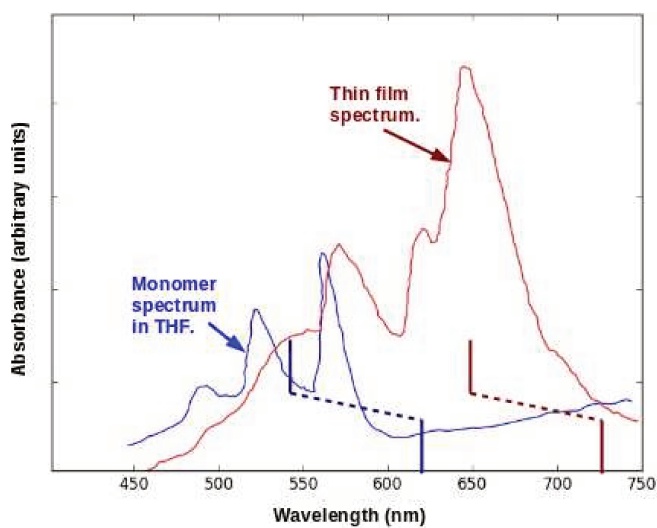


Figure 6.29 – Excitonic effects on the absorption spectrum of pentacene: curves, pentacene in tetrahydrofuran (THF) and as a thin film (from Ref. [121]); stick spectra, lower are the position of unshifted monomer and crystal peaks calculated using the Bethe-Salpeter equation (BSE) while the upper stick spectra have been shifted to match the experiment (from Ref. [20].) See also Ref. [125].

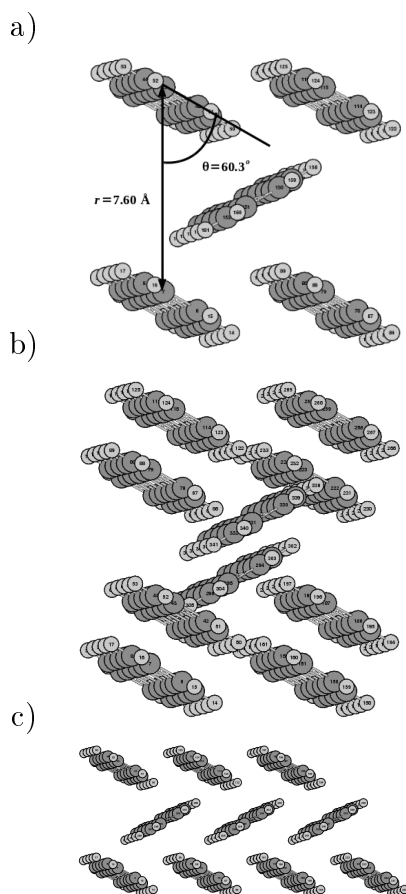


Figure 6.30 – Herringbone cluster models used in this work. All are portions of the x-ray crystal structure: (a) pentamer, (b) “vertical” decamer, and (c) “horizontal” decamer.

and from state-of-the-art theoretical calculations [125, 128, 129, 130, 20]. These are shown in Fig. 6.29. This time excitonic shifts lead to a red shift, rather than a blue shift. The structure of the spectrum suggests that both CT and ET transitions contribute to the spectrum. As we shall see, charge transfer is more important for describing excitonic effects in the absorption spectrum than is the case for parallel stacked pentamers.

We carried out calculations for the cluster models shown in Fig. 6.30 obtained by cutting out different portions of the x-ray crystal structure [117, 118] without any subsequent relaxation. Unless otherwise indicated all of the results reported below are for the “horizontal” decamer model. The picture of the horizontal model makes it clear that the crystal is made up of layers of tilted stacks of pentamers whose tilt angles alternate from layer to layer to provide a herringbone structure.

Figure 6.31 shows the herringbone spectra calculated at various levels and compared with the thin film spectrum. Both the TD-LDA/6-31G(d,p) and the TD-

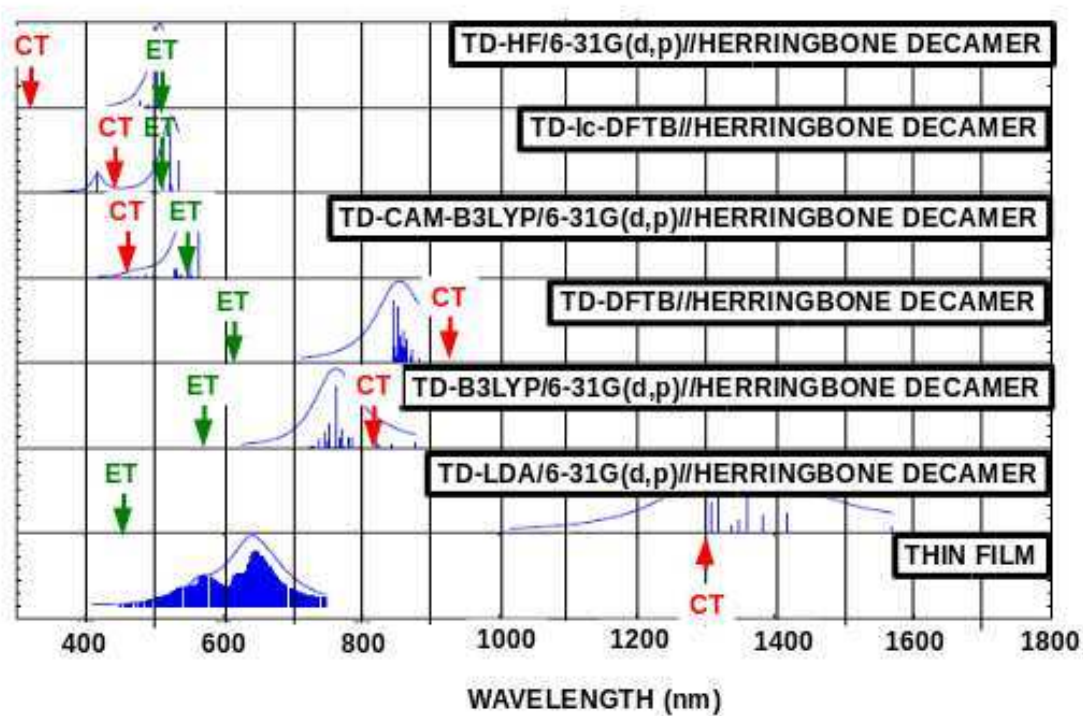


Figure 6.31 – Comparisons of calculations using various methods with the thin film absorption spectrum from Ref. [121]. The CT and ET excitation energies were calculated from Kasha's exciton model using Eq. (6.97).

B3LYP/6-31G(d,p) calculations are red shifted compared to the thin film experiment with the TD-LDA/6-31G(d,p) red shift being quite dramatic. This is consistent with the idea that the TD-LDA/6-31G(d,p) exciton is delocalized over too many molecules while the inclusion of some HF exchange in the TD-B3LYP/6-31G(d,p) helps to increase the excitation energy by localizing the exciton over fewer molecules. The TD-DFTB calculation is in semi-quantitative agreement with the TD-B3LYP/6-31G(d,p) but are slightly red-shifted. In contrast, the TD-CAM-B3LYP/6-31G(d,p) and TD-HF/6-31G(d,p) calculations are blue shifted compared to the thin film experiment. The TD-lc-DFTB calculation is in semi-quantitative agreement with the TD-CAM-B3LYP/6-31G(d,p) calculation but is slightly blue shifted. It is difficult to say from this figure which of the two calculations — TD-B3LYP/6-31G(d,p) or TD-CAM-B3LYP/6-31G(d,p) — is a better description of the experiment.

The level of agreement with experiment is best judged by Fig. 6.32. Here we see that the TD-B3LYP/6-31G(d,p) and TD-DFTB results are in reasonable qualitative agreement with experiment. However the TD-CAM-B3LYP/6-31G(d,p) and TD-lc-DFTB results, while in good agreement with each other, do not at all provide a good description of exciton effects. We assume that this is because of the importance of CT which may be over corrected at the TD-CAM-B3LYP/6-31G(d,p) and TD-lc-DFTB levels compared with the TD-B3LYP/6-31G(d,p) and TD-DFTB levels.

6.5.4 Re-examination of Kasha's Model

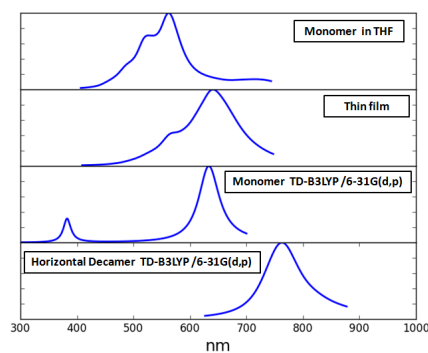
There is some hope in the literature that you only need a single crystal plane to calculate the Davydov splitting of the crystal [131, 132, 133]. In their recent work [133], Meyenburg *et al.* give the formula [their Eq. (5) rewritten in atomic units],

$$\Delta E = \frac{2|\vec{D}|^2}{\epsilon r^3} [\cos(\phi) - 3 \cos(\alpha_1) \cos(\alpha_2)] , \quad (6.96)$$

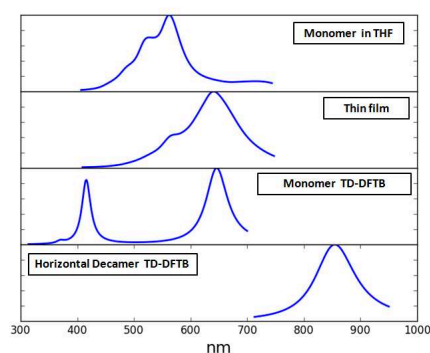
where the angles are defined in Fig. 3 of their paper. [Equation (6.96) is a generalization of a formula given in the paper of Kasha, Rawls, and El-Bayoumi [8] (resulting in Fig. 4 of their article).] We translate this the following relationship between the DS of the herringbone model DS_{HB} and of the parallel stack model DS_{PS} :

$$\begin{aligned} DS_{HB} &= DS_{PS} \left(\frac{\epsilon_{PS}}{\epsilon_{HB}} \right) \left(\frac{r_{PS}}{r_{HB}} \right)^3 \\ &\times [\cos(\phi) - 3 \cos(\alpha_1) \cos(\alpha_2)] . \end{aligned} \quad (6.97)$$

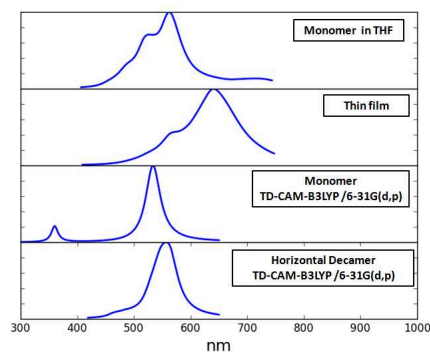
a)



b)



c)



d)

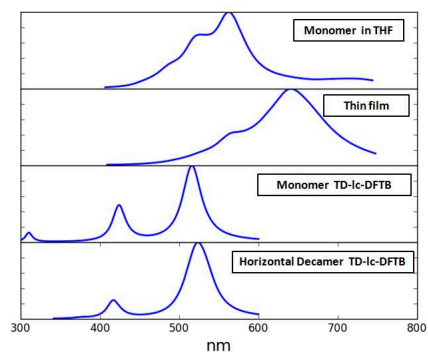


Figure 6.32 – Comparison of theoretical and experimental exciton shifts: (a) TD-B3LYP/6-31G(d,p), (b) TD-DFTB, (c) TD-CAM-B3LYP/6-31G(d,p), and (d) TD-Id-DFTB.

The values $\alpha_1 = 98.19^\circ$, $\alpha_2 = 22.98^\circ$, $\phi = 58.83^\circ$, and $r = 4.835 \text{ \AA}$ were taken from the experimental crystal structure. The ratio $\epsilon_{\text{PS}}/\epsilon_{\text{HB}}$ is not something that we can really determine *a priori* and so we just use it as a fitting factor (equal to 10.64 in our calculations). We can use this, together with DS_2 to predict the DS_{HB} that we would expect from various models. These results are shown by arrows in Fig. 6.31. Something very remarkable has happened: The locations of the TD-lc-DFTB, TD-HF, and TD-CAM-B3LYP main peaks are well produced, as expected, by the ET peak. In contrast, the location of the TD-DFTB, TD-B3LYP, and TD-LDA main peaks has been generated unexpectedly, from the CT peak, which was expected to be relatively dark compared to the ET peak.

This leads us to take a closer look at how Kasha's exciton model works in our (TD-)DFT and (TD-)DFTB calculations. We have done this by looking at two parallel-stacked pentacenes. This corresponds to a simplification of Eq. (6.97), namely

$$\Delta E = \frac{2|\vec{D}|^2}{r^3} (1 - 3 \cos^2 \theta) , \quad (6.98)$$

with $\epsilon = 1$. Figure 6.33 summarizes what we expect to see on the basis of the original exciton model for excitation energies and oscillator strengths. This is a simple theory which gives simple curves. Above $\theta = 55^\circ$, the main oscillator strength is in the higher energy (lower wavelength) ET state; below $\theta = 55^\circ$, the main oscillator strength is in the lower energy (higher wavelength) ET state which has crossed the CT state. However the original theory did not anticipate avoided crossings. For the herringbone structure, $\theta \approx 60^\circ$ and the prediction is that the brighter state should be the higher wavelength state. This is indeed what is seen in all the calculations in Fig. 6.31, but the assignment of the longer wavelength peak depends upon the method.

Let us turn now to Fig. 6.34 which shows results from our TD-B3LYP/6-31G(d,p)//B3LYP+D3/6-31G(d,p) calculations. This more realistic calculation gives more complicated results. Rather than seeing a simple crossing of energy levels at about $\theta = 55^\circ$ as in Fig. 6.33(b), we see evidence of configuration mixing as the oscillator strength is transferred from one state to another with maximum transfer near $\theta = 55^\circ$ (i.e., at $\theta = 45^\circ$) as the two energy levels mix and move apart at $\theta = 55^\circ$. This seems even more clear in the 3D plot [part (c) of Fig. 6.34] where the two curves behave in a way very consistent with an avoided crossing of two diabatic states (one with high and one with low oscillator strength) around 50° . Later, at a much lower value of $\theta = 20^\circ$, there appears to be a real crossing, but this is of little importance for understanding the herringbone results. Comparing with the TD-DFTB, TD-B3LYP, and TD-LDA herringbone spectra in Fig. 6.31, we realize that the assignment of the

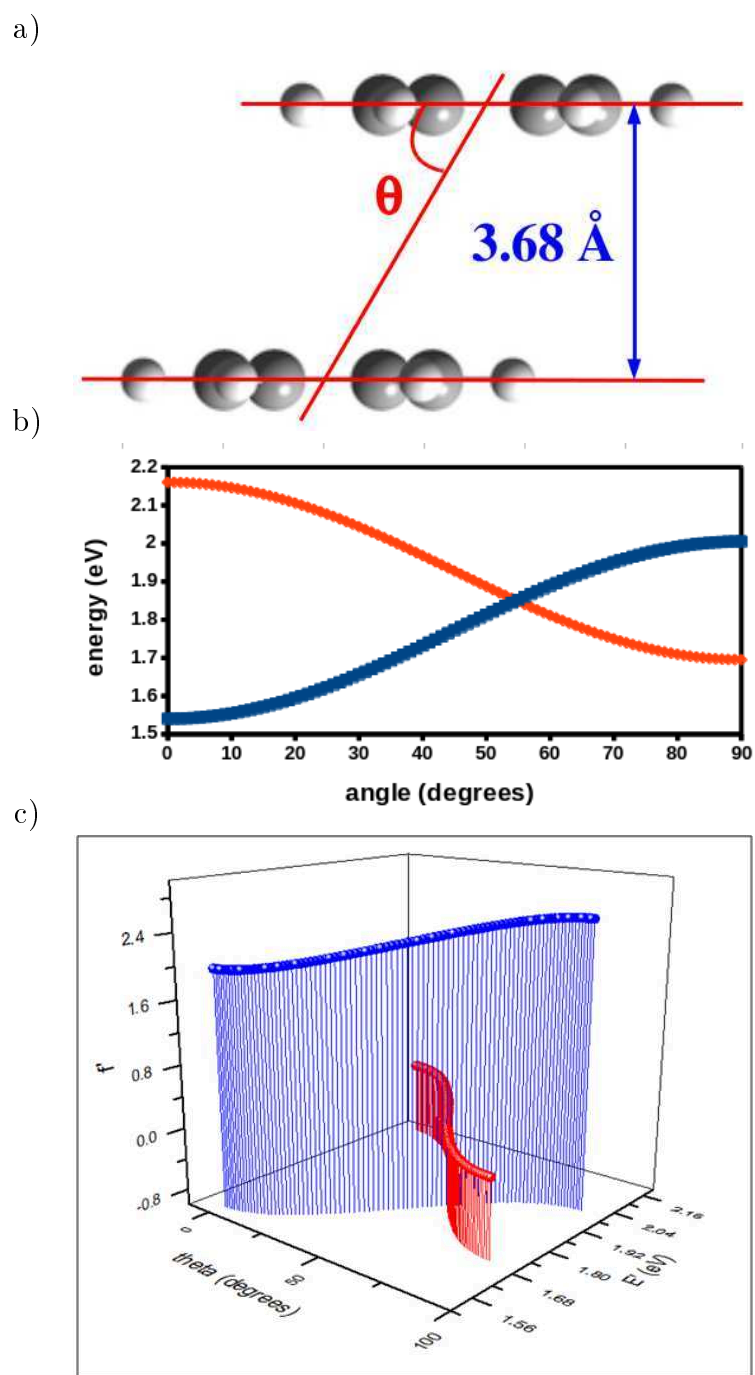
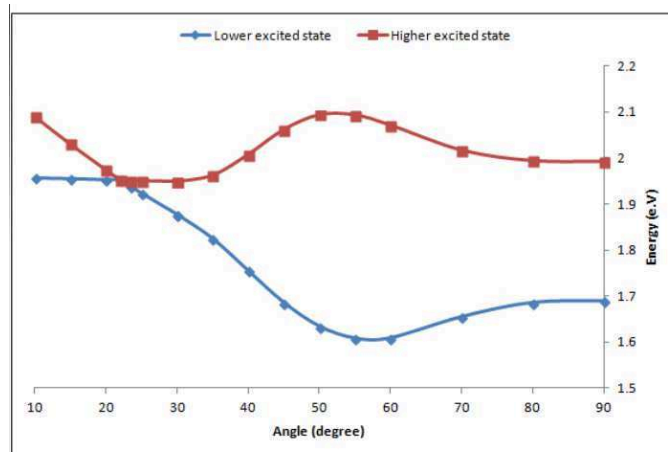
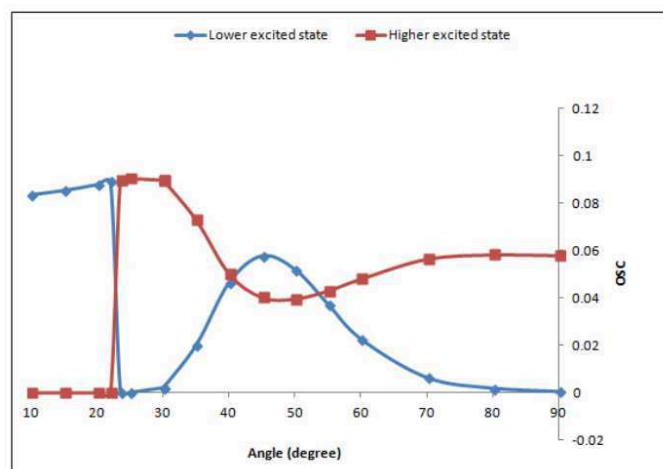


Figure 6.33 – Ideal Kasha figures for co-planar inclined transition dipole moments: (a) laterally shifted parallel stacked pentacene dimer, (b) Kasha plot of excitation energies as a function of the angle θ , (c) 3D plot of Kasha's model for oscillator strengths and excitation energies.

a)



b)



c)

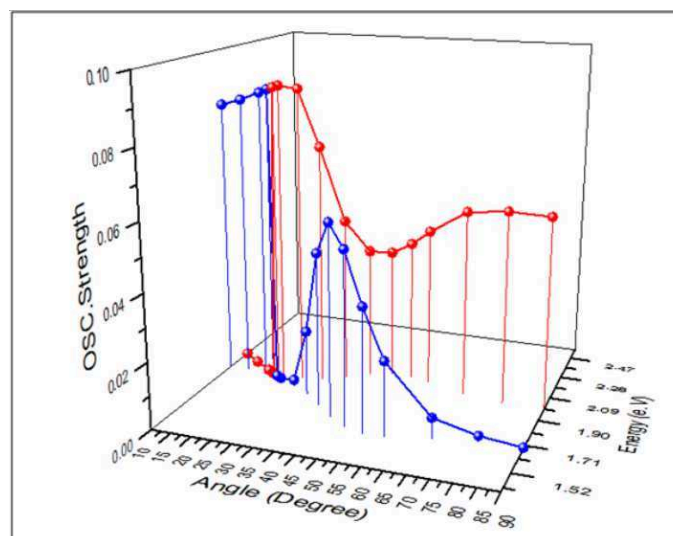


Figure 6.34 – TD-B3LYP/6-31G(d,p)//B3LYP+D3/6-31G(d,p) Kasha figures for co-planar inclined transition dipole moments: (a) excitation energies as a function of the angle θ , (b) 2D plot of oscillator strengths, (c) 3D plot of oscillator strengths and excitation energies,

longer wavelength peak as CT is misleading as most likely there is a great deal of mixing between the ET and CT states. Figure 6.35 shows what happens for a RSH. In particular, TD-CAM-B3LYP/6-31G(d,p)//CAM-B3LYP+D3/6-31G(d,p) results are shown. There is also some evidence of an avoided crossing here, but the lower energy (longer wavelength) state keeps most of the oscillator strength. At $\theta = 90^\circ$, it is of ET type, but shows some mixing between CT and ET type at around $\theta = 65^\circ$. Comparing with the TD-lc-DFTB, TD-HF, and TD-CAM-B3LYP herringbone spectra in Fig. 6.31, we realize that the assignment of the longer wavelength peak as ET is reasonable in this case.

Despite these criticisms that Kasha's exciton model is missing many of the subtleties of our more elaborate calculations, we must conclude that the exciton model allows us to extrapolate remarkably well from intramolecular interactions between pairs of molecules to larger aggregates, but only when a RSH is used.

6.6 Conclusion

The aggregation of dye molecules leads to additional spectral features which have long been explained by Kasha's exciton model [8]. This model provides a simple explanation of H-bands such as those found in our calculations of parallel stacked pentacene molecules and of J-bands such as those associated with the experimentally-known herringbone structure of crystalline pentacene. We have re-examined Kasha's exciton model in terms of state-of-the-art TD-DFT and TD-DFTB calculations. Our calculations include Grimme's D3 dispersion correction which we confirm is absolutely necessary in order to have van der Waals binding beyond the LDA level (which, however, "accidentally" binds when an extensive-enough basis set is used). We have also included some HF exchange either in the form of the global B3LYP hybrid functional or in the form of the range-separated CAM-B3LYP hybrid functional. Corresponding TD-DFTB calculations have also been performed with DFTBABY which we find does very well at mimicking the two functionals (depending upon whether or not the long-range correction is used).

Perhaps not surprisingly we find that the hybrid functionals give better spectra than the TD-LDA. We also find that, while the TD-DFTB spectra have the structural simplicity of STO-3G minimum basis set TD-DFT spectra, the TD-DFTB spectral peak energies are placed more like the TD-DFT calculations with larger basis used in the semi-empirical parameterization. This is reassuring. However care must be taken when doing TD-DFTB calculations on aggregates to do them size consistently or results can be misleading — that is, the size of the active space must

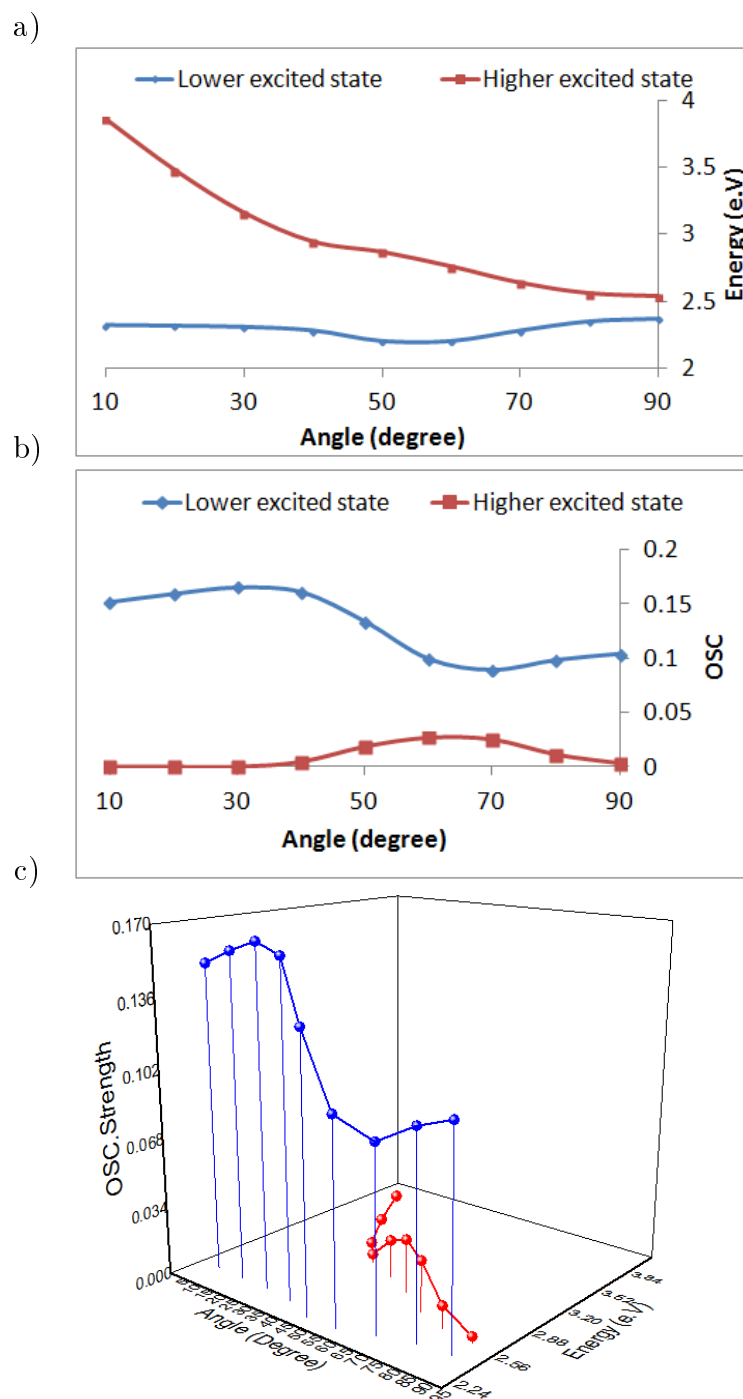


Figure 6.35 – TD-CAM-B3LYP/6-31G(d,p)//CAM-B3LYP+D3/6-31G(d,p) Kasha figures for co-planar inclined transition dipole moments: (a) excitation energies as a function of the angle θ , (b) 2D plot of oscillator strengths, (c) 3D plot of oscillator strengths and excitation energies,

increase in proportion to the number of molecules in the aggregate.

On the other hand, Fig. 6.32 is definitely telling us that the Davydov splitting for the herringbone model is reasonable and close to the experimental value at the TD-B3LYP and TD-DFTB levels, even if the spectral peaks are shifted, but that the Davydov splitting is practically nonexistent and therefore wrong at the CAM-TD-B3LYP and TD-lc-DFTB levels. For this reason, we cannot recommend using either of these latter two approaches for calculating excitonic effects on the spectra of polyoligocenes and recommend instead the use of TD-B3LYP or TD-DFTB carefully carried out on aggregates.

Also, in light of arguments regarding the extent and nature of exciton delocalization (e.g., Refs. [43, 134]), it is interesting that our analysis shows that a more sophisticated version of Kasha's exciton model, based only on nearest neighbor interactions but including both ET and CT as well as avoided crossings, works very well. In contrast, Kasha's original model fails for displaced parallel pentacene dimers unless RSHs are used because of failure to take proper account of avoided crossings.

6.7 acknowledgments

This work is supported, in part, by the ORGAVOLT (ORGAnic solar cell VOLTage by numerical computation) Grant ANR-12-MONU-0014-02 of the French *Agence Nationale de la Recherche (ANR) 2012 Programme Modèles Numériques*. Ala Aldin M. H. M. Darghouth would like to thank the French and Iraq governments for support through a Campus France scholarship. Gabriela Calinao Correa was an American iREU (International Research Experience for Undergraduates) scholar who acknowledges support from Chemistry (CHE) Grant Number 1263336 of the American National Science Foundation (NSF) and the Labex Arcane ANR-11-LABX-0003-01 French Grant. Mark E. Casida and Ala Aldin M. H. M. Darghouth would like to acknowledge helpful discussions with Mathias Rapacioli. Mark E. Casida and Ala Aldin M. H. M. Darghouth would also like to acknowledge a useful trip to Würzburg funded by the German GRK 2112 Project "Biradicals."

6.8 Author Contributions

This project began with a two month research project under the direction of Mark E. Casida during the summer of 2013 when Sacha Juillard, then a first-year Masters student in Chemistry, explored the possibilities for using DFTB to model polymers in organic photovoltaic cells. The project continued with calculations carried out by Ala

Aldin M. H. M. Darghouth as part of his PhD project with Mark E. Casida. Major coding was done by Alexander Humeniuk and by Roland Mitrić in their TD-DFTB program. Gabriela Calinao Correa contributed to expanding the understanding of those of us in Grenoble of the TD-DFTB code via her work analysing and applying DFTBABY. The bulk of the manuscript writing was done by Mark E. Casida with contributions from Gabriela Calinao Correa and major contributions from Ala Aldin M. H. M. Darghouth.

6.9 Conflicts of Interest

The authors declare no conflict of interest.

6.10 Abbreviations

For the reader's convenience, we have collected together the abbreviations used in this paper:

AO Atomic orbital.

B88 Becke's 1988 exchange GGA

BS Band structure.

BSE Bethe-Salpeter equation.

CAM Coulomb attenuated model.

CAO Crystal atomic orbital.

CIS Configuration interaction with single excitations.

CMO Crystal molecular orbital.

CT Charge transfer.

D3 Grimme's 3-parameter vdW energy correction.

DFT Density-functional theory.

DFTB Density-functional tight binding.

DS (= ET - CT) Davydov splitting.

ERI Electron repulsion integral.

ET Energy transfer.

FR Frenkel.

GGA Generalized gradient approximation.

- H-bands** Hypsochromatic bands, high energy spectral peaks due to aggregation.
- H** Highest-occupied molecular orbital.
- H- n** n th level below the HOMO.
- HEG** Homogeneous electron gas.
- HF** Hartree-Fock.
- HOMO** Highest-occupied molecular orbital.
- IUPAC** International Union of Pure and Applied Chemistry.
- J-bands** Jelly bands (also known as Scheibe bands), low energy spectral peaks due to aggregation.
- L** Lowest-unoccupied molecular orbital.
- L+ n** n th level above the LUMO.
- LAO** Localized atomic orbital.
- LDA** Local density approximation.
- LE** Local excitation.
- LMO** Localized molecular orbital.
- lr** Long range.
- LRC** Long-range corrected.
- LUMO** Lowest-unoccupied molecular orbital.
- LYP** Lee-Yang-Parr correlation GGA.
- MBPT** Many-body perturbation theory.
- MO** Molecular orbital.
- NTO** Natural transition orbital.
- PES** Potential energy surface (also, somewhat abusively, used to mean a potential energy curve).
- RSH** Range-separated hybrid.
- SCC** Self-consistent charge.
- sr** Short range.
- TD** Time-dependent
- TDA** Tamm-Dancoff approximation.
- TD-DFT** Time-dependent density-functional theory.
- TD-DFTB** Time-dependent density-functional tight binding.

THF Tetrahydrofuran.

TOTEM Two-orbital two-electron model.

(TOTEM)ⁿ *n* stacked TOTEMs.

vdW Van der Waals.

WM Wannier-Mott.

xc Exchange correlation.

Bibliography

- [1] Present address: Doctoral student in the Department of Materials Science, Cornell University, Ithaca, New York. pages 138
- [2] M. E. Casida and M. Huix-Rotllant, [Progress in Time-Dependent Density-Functional Theory](#), *Annu. Rev. Phys. Chem.* **63**, 287 (2012). pages 140, 164, 233, 241
- [3] M. E. Casida and M. Huix-Rotllant, [Many-Body Perturbation Theory \(MBPT\) and Time-Dependent Density-Functional Theory \(TD-DFT\): MBPT Insights About What is Missing in, and Corrections to, the TD-DFT Adiabatic Approximation](#), in [Density-Functional Methods for Excited States](#), edited by N. Ferré, M. Filatov, and M. Huix-Rotllant, Topics in Current Chemistry, Springer, 2015. pages 140, 166
- [4] S. Grimme, J. Antony, S. Ehrlich, and H. Krieg, [A consistent and accurate *ab initio* parameterization of density functional dispersion correction \(DFT-D\) for the 94 elements H-Pu](#), *J. Chem. Phys.* **132**, 154104 (2010). pages 140, 164, 228, 238, 241
- [5] R. S. Knox, [Theory of Excitons](#), volume 5 of *Solid State Physics*, Academic Press, New York, 1963. pages 140, 141
- [6] V. May and O. Kühn, [Charge and Energy Transfer Dynamics in Molecular Systems: A Theoretical Introduction](#), Wiley-VCH, Berlin, 2000. pages 141, 228
- [7] M. Kasha, [Relation between Exciton Bands and Conduction Bands in Molecular Lamellar Systems](#), *Rev. Mod. Phys.* **31**, 162 (1959). pages 141
- [8] M. Kasha, H. R. Rawls, and A. El-Bayoumi, [The exciton model in molecular spectroscopy](#), *Pure Appl. Chem.* **11**, 371 (1965). pages 141, 144, 149, 184, 198, 203
- [9] H. van Amerongen, L. Valkunas, and R. van Grondelle, [Photosynthetic Excitons](#), World Scientific, Singapore, 2000. pages 141
- [10] J. Frenkel, [On the Transformation of light into Heat in Solids. I](#), *Phys. Rev.* **37**, 17 (1931). pages 141
- [11] J. Frenkel, [On the Transformation of light into Heat in Solids. II](#), *Phys. Rev.* **37**, 1276 (1932). pages 141
- [12] G. H. Wannier, [The structure of electronic excitation levels in insulating crystals](#), *Phys. Rev.* **52**, 191 (1937). pages 141
- [13] A. S. Davydov, [The theory of molecular excitons](#), *Sov. Phys. Usp.* **7**, 145 (1964). pages 141

- [14] A. S. Davydov, [Theory of Absorption Spectra of Molecular Crystals](#), translated and reprinted from *zh. eksp. teor. fiz.* **18**, 210 (1948)., Ukr. J. Phys. **53**, 65 (2008). pages 141
- [15] D. Möbius, [Scheibe aggregates](#), Adv. Mat. **7**, 437 (1995). pages 141
- [16] E. E. Jelley, [Spectral Absorption and Fluorescence of Dyes in the Molecular State](#), **138**, 1009 (1936). pages 141
- [17] E. E. Jelley, [Molecular, Nematic and Crystal States of 1:1'-Diethyl- \$\psi\$ -Cyanine Chloride](#), **139**, 631 (1937). pages 141
- [18] G. Scheibe, [Über die Veränderlichkeit der Absorptionsspektren in Lösungen und die Nebenvalezen als ihre Ursache](#), Angew. Chem. **50**, 212 (1937). pages 141
- [19] F. Würthner, T. E. Kaiser, and C. R. Saha-Möller, [J-aggregates: From serendipitous discover to suprmolecular engineering of functional dye materials](#), Angew. Chem. Int. Ed. **50**, 3376 (2011). pages 141
- [20] P. Cudazzo, F. Sottile, A. Rubio, and M. Gatti, [Topical Review: Exciton dispersion in molecular solids](#), J. Phys.: Condens. Matter **27**, 113204 (2015). pages 142, 195, 196, 313
- [21] A. Dreuw, J. L. Weisman, and M. Head-Gordon, [Long-range charge-transfer excited states in time-dependent density functional theory require non-local exchange](#), J. Chem. Phys. **119**, 2943 (2003). pages 142, 234
- [22] D. J. Tozer, R. D. Amos, N. C. Handy, B. O. Roos, and L. Serrano-Andrés, [Does density functional theory contribute to the understanding of excited states of unsaturated organic compounds?](#), Mol. Phys. **97**, 859 (1999). pages 142, 234
- [23] M. J. G. Peach, P. Benfield, T. Helgaker, and D. J. Tozer, [Excitation energies in density functional theory: an evaluation and a diagnostic test](#), J. Chem. Phys. **128**, 044118 (2008). pages 142, 234
- [24] M. J. G. Peach and D. J. Tozer, [Illustration of a TDDFT spatial overlap diagnostic by basis function exponent scaling](#), J. Mol. Struct.: THEOCHEM **914**, 110 (2009). pages 142, 234
- [25] M. J. G. Peach, C. R. L. Sueur, K. Ruud, M. Guillaume, and D. J. Tozer, [TDDFT diagnostic testing and functional assessment for triazene chromophores](#), Phys. Chem. Chem. Phys. **11**, 4465 (2009). pages 142, 234
- [26] T. S. Kuhlman, K. V. Mikkelsen, K. B. Møller, and T. L. Sølling, [Charge-resonance excitations in symmetric molecules — Comparison of linear response DFT with CC3 for the excited states of a model dimer](#), Chem. Phys. Lett. **478**, 127 (2009). pages 142, 234

- [27] P. Wiggins, J. A. G. Williams, and D. J. Tozer, [Excited state surfaces in density functional theory: A new twist on an old problem](#), J. Chem. Phys. **131**, 091101 (2009). pages 142, 234
- [28] A. D. Dwyer and D. J. Tozer, [Effect of chemical change on TDDFT accuracy: orbital overlap perspective of the hydrogenation of retinal](#), Phys. Chem. Chem. Phys. **12**, 2816 (2010). pages 142, 234
- [29] S. S. Leang, F. Zahariev, and M. S. Gordon, [Benchmarking the performance of time-dependent density functional methods](#), J. Chem. Phys. **136**, 104101 (2012). pages 142, 234
- [30] G. Vignale and W. Kohn, [Current-dependent exchange-correlation potential for dynamical linear response theory](#), Phys. Rev. Lett. **77**, 2037 (1996). pages 142
- [31] F. Sottile, M. Marsili, V. Olevano, and L. Reining, [Efficient *ab initio* calculations of bound and continuum excitons in the absorption spectra of semiconductors and insulators](#), Phys. Rev. B **76**, 161103(R) (2007). pages 142
- [32] S. Sharma, J. K. Dewhurst, A. Sanna, and E. K. U. Gross, [Bootstrap Approximation for the Exchange-Correlation Kernel of Time-Dependent Density-Functional Theory](#), Phys. Rev. Lett. **107**, 186401 (2011). pages 142
- [33] V. Turkowski, A. Leonardo, and C. A. Ulrichs, [Time-dependent density-functional approach for exciton binding energies](#), Phys. Rev. B **79**, 233201 (2009). pages 142
- [34] Z. Yang and C. A. Ullrich, [Direct calculation of exciton binding energies with time-dependent density-functional theory](#), Phys. Rev. B **87**, 195204 (2013). pages 142
- [35] C. A. Ullrich and Z. Yang, [Excitons in Time-Dependent Density-Functional Theory](#), in *Density-Functional Methods for Excited States*, volume 368 of *Topics in Current Chemistry*, page 185, Springer, New York, 2016. pages 142
- [36] S. Kümmel, [Charge-transfer excitations: A challenge for time-dependent density functional theory that has been met](#), Adv. Energy Mat. **7**, 1700440 (2017). pages 142, 162
- [37] B. M. Wong and T. H. Hsieh, [Optoelectronic and Excitonic Properties of Oligoacenes: Substantial Improvements from Range-Separated Time-Dependent Density Functional Theory](#), J. Chem. Theory. Comput. **6**, 3704 (2010). pages 142
- [38] C. R. Jacob and J. Neubegauer, [Subsystem density-functional theory](#), WIREs Comp. Molec. Sci. **4**, 325 (2014). pages 142

- [39] P. Ramos and M. Pavenello, [Constrained subsystem density functional theory](#), Phys. Chem. Chem. Phys. **18**, 21172 (2016). pages 142
- [40] M. E. Casida and T. A. Wesolowski, [Generalization of the Kohn-Sham Equations with Constrained Electron Density \(KSCED\) Formalism and its Time-Dependent Response Theory Formulation](#), Int. J. Quant. Chem. **96**, 577 (2004). pages 142
- [41] A. A. Kocherzhenko, X. A. S. Vasquez, J. M. Milanese, and C. M. Isborn, [Absorption spectra for disordered aggregates of chromophores using the exciton model](#), J. Chem. Theory. Comput. **13**, 3787 (2017). pages 143
- [42] J. E. Anthony, [The Larger Acenes: Versatile Organic Semiconductors](#), Angew. Chem. Int. Ed. **47**, 452 (2008). pages 143, 225
- [43] P. M. Zimmerman, F. Bell, D. Casanova, and M. Head-Gordon, [Mechanism for singlet fission in pentacene and tetracene from single exciton to two triplets](#), J. Am. Chem. Soc. **133**, 19944 (2009). pages 143, 205
- [44] R. S. Mulliken, [Report on Notation for the Spectra of Polyatomic Molecules](#), J. Chem. Phys. **23**, 1997 (1955). pages 144, 175
- [45] R. S. Mulliken, [Erratum : Report on Notation for the Spectra of Polyatomic Molecules](#), J. Chem. Phys. **24**, 1118(E) (1956). pages 144, 175
- [46] J. Koutecký and J. Paldus, [A study of interaction of two ethylene molecules by the semiempirical complete configuration interaction method in \$\pi\$ -electron approximation](#), Theoret. chim. Acta (Berl.) **1**, 268 (1963). pages 147
- [47] G. D. Scholes and K. P. Ghiggino, [Rate expressions for excitation transfer I. Radiationless transition theory perspective](#), J. Chem. Phys. **101**, 1251 (1994). pages 147
- [48] R. D. Harcourt, G. D. Scholes, and K. P. Ghiggino, [Rate expressions for excitation transfer II. Electronic considerations of direct and through-configuration exciton resonance interactions](#), J. Chem. Phys. **101**, 10521 (1994). pages 147
- [49] G. D. Scholes, R. D. Harcourt, and K. P. Ghiggino, [Rate expressions for excitation transfer III. An ab initio study of electronic factors in excitation transfer and exciton resonance interactions](#), J. Chem. Phys. **102**, 9574 (1995). pages 147
- [50] P. Hohenberg and W. Kohn, [Inhomogeneous electron gas](#), Phys. Rev. **136**, B864 (1964). pages 159, 164
- [51] W. Kohn and L. J. Sham, [Self-consistent equations including exchange and correlation effects](#), Phys. Rev. **140**, A1133 (1965). pages 66, 94, 159, 164, 231
- [52] R. G. Parr and W. Yang, [Density-Functional Theory of Atoms and Molecules](#), Oxford University Press, New York, 1989. pages 62, 65, 90, 159, 231

- [53] R. M. Dreizler and E. K. U. Gross, [Density Functional Theory, An Approach to the Quantum Many-Body Problem](#), Springer-Verlag, New York, 1990. pages 90, 159, 231
- [54] W. Koch and M. C. Holthausen, [A Chemist's Guide to Density Functional Theory](#), Wiley-VCH, New York, 2000. pages 90, 159, 231
- [55] P. A. M. Dirac, [Note on exchange phenomena in the Thomas-Fermi atom](#), Proc. Cambridge Phil. Roy. Soc. **26**, 376 (1930). pages 161
- [56] S. H. Vosko, L. Wilk, and M. Nusair, [Accurate spin-dependent electron liquid correlation energies for local spin density calculations: a critical analysis](#), Can. J. Phys. **58**, 1200 (1980). pages 68, 100, 161
- [57] A. D. Becke, [Density-functional exchange-energy approximation with correct asymptotic behavior](#), Phys. Rev. A **38**, 3098 (1988). pages 161
- [58] L. Fan and T. Ziegler, [The influence of self-consistency on nonlocal density functional calculations](#), J. Chem. Phys. **94**, 6057 (1991). pages 161
- [59] J. P. Perdew et al., [Atoms, molecules, solids, and surfaces: Applications of the generalized gradient approximation for exchange and correlation](#), Phys. Rev. B **46**, 6671 (1992). pages 161
- [60] J. P. Perdew et al., [Erratum: "Atoms, molecules, solids, and surfaces: Applications of the generalized gradient approximation for exchange and correlation"](#), Phys. Rev. B **48**, 4978 (1993). pages 161
- [61] J. P. Perdew, K. Burke, and Y. Wang, [Generalized gradient approximation for the exchange-correlation hole of a many-electron system](#), Phys. Rev. B **54**, 16533 (1996). pages 161
- [62] J. P. Perdew, K. Burke, and Y. Wang, [Erratum: "Generalized gradient approximation for the exchange-correlation hole of a many-electron system"](#), Phys. Rev. B **57**, 14999 (1996). pages 161
- [63] C. Lee, W. Yang, and R. G. Parr, [Development of the Colle-Salvetti correlation energy formula into a functional of the electron density](#), Phys. Rev. B **37**, 785 (1988). pages 68, 161, 240
- [64] A. D. Becke, [A new mixing of Hartree-Fock and local density functional theories](#), J. Chem. Phys. **98**, 1372 (1993). pages 100, 161, 162
- [65] P. M. W. Gill, [Obituary: Density-functional theory \(1927-1993\)](#), Aust. J. Chem. **54**, 661 (2001). pages 161, 232
- [66] [Becke3LYP Method References and General Citation Guidelines](#), Gaussian NEWS, v. 5, no. 2, summer 1994. pages 162, 240

- [67] T. Yanai, D. P. Tew, and N. C. Handy, [A new hybrid exchange-correlation functional using the Coulomb-attenuating method \(CAM-B3LYP\)](#), Chem. Phys. Lett. **393**, 51 (2004). pages 162, 241
- [68] H. Iikura, T. Tsuneda, T. Yanai, and K. Hirao, [A long-range correction scheme for generalized-gradient-approximation exchange functionals](#), J. Chem. Phys. **115**, 3540 (2001). pages 163
- [69] E. Runge and E. K. U. Gross, [Density-functional theory for time-dependent systems](#), Phys. Rev. Lett. **52**, 997 (1984). pages 164, 233
- [70] M. A. L. Marques, C. Ullrich, F. Nogueira, A. Rubio, and E. K. U. Gross, editors, [Time-Dependent Density-Functional Theory](#), volume 706 of *Lecture Notes in Physics*, Springer, Berlin, 2006. pages 164, 233
- [71] M. A. L. Marques, N. Maitra, F. Nogueira, E. K. U. Gross, and A. Rubio, editors, [Fundamentals of Time-Dependent Density-Functional Theory](#), volume 837 of *Lecture Notes in Physics*, Springer, Berlin, 2011. pages 164, 233
- [72] G. D. Mahan and K. R. Subbaswamy, [Local Density Theory of Polarizability](#), Plenum, New York, 1990. pages 87, 164
- [73] C. A. Ullrich, [Time-Dependent Density-Functional Theory](#), Oxford University Press, New York, 2012. pages 164, 233
- [74] K. Burke, J. Werschnik, and E. K. U. Gross, [Time-dependent density functional theory: Past, present, and future](#), J. Chem. Phys. **123**, 062206 (2005). pages 164
- [75] M. E. Casida, [Review: Time-Dependent Density-Functional Theory for Molecules and Molecular Solids](#), J. Mol. Struct. (Theochem) **914**, 3 (2009). pages 164, 233, 241
- [76] D. Jacquemin, V. Wathelet, E. A. Perpète, and C. Adamo, [Extensive TD-DFT benchmark: Singlet-excited states of organic molecules](#), J. Chem. Theory Comput. **5**, 2420 (2009). pages 164, 233
- [77] C. Adamo and D. Jacquemin, [The calculations of excited-state properties with time-dependent density functional theory](#), Chem. Soc. Rev. **42**, 845 (2013). pages 164, 233, 241
- [78] A. D. Laurent and D. Jacquemin, [TD-DFT benchmarks: A review](#), Int. J. Quant. Chem. **113**, 2019 (2013). pages 164, 233
- [79] N. T. Maitra, [Perspective: Fundamental aspects of time-dependent density functional theory](#), J. Chem. Phys. **144**, 220901 (2016). pages 164, 233

- [80] M. E. Casida, [Time-dependent density-functional response theory for molecules](#), in *Recent Advances in Density Functional Methods, Part I*, edited by D. P. Chong, page 155, World Scientific, Singapore, 1995. pages 164, 233, 234, 241
- [81] X. Gonze and M. Scheffler, [Exchange and correlation kernels at the resonance frequency: implications for excitation energies in density-functional theory](#), Phys. Rev. Lett. **82**, 4416 (1999). pages 166
- [82] M. Swart, F. M. Bickelhaupt, and M. Duran, [DFT2016 poll](#), <http://www.marcelswart.eu/dft-poll/news2016.pdf>, last accessed: 21 January 2018. pages 167
- [83] J. A. Pople and D. L. Beveridge, [Approximate Molecular Orbital Theory](#), McGraw-Hill, New York, 1970. pages 167, 170
- [84] T. Bredow and K. Jug, [Theory and range of modern semiempirical molecular orbital methods](#), Theor. Chem. Acc. **113**, 1 (2005). pages 94, 167, 239
- [85] A. Horsfield, [Where does tight binding go from here?](#), Phys. Status Solidi B **249**, 231 (2012). pages 167
- [86] P. Koskinen and V. Mökinen, [Density-functional tight-binding for beginners](#), Comput. Mater. Sci. **47**, 237 (2009). pages 94, 98, 167, 227, 235
- [87] A. Oliveira, G. Seifert, T. Heine, and H. Duarte, [Density-functional based tight-binding: An approximate DFT method](#), J. Braz. Chem. Soc. **20**, 1193 (2009). pages 167, 227, 235
- [88] M. Elstner and G. Seifert, [Density functional tight binding](#), Philos. Trans. R. Soc. A **372**, 20120483 (2014). pages 167, 227, 235
- [89] D. Porezag, T. Frauenheim, T. Köhler, G. Seifert, and R. Kaschner, [Construction of tight-binding-like potentials on the basis of density-functional theory: Application to carbon](#), Phys. Rev. B **51**, 12947 (1995). pages 94, 98, 167, 235
- [90] R. Hoffmann, [An extended Hückel theory. I. Hydrocarbons](#), J. Chem. Phys. **39**, 1397 (1963). pages 167
- [91] R. Hoffmann, [An extended Hückel theory. II. \$\sigma\$ orbitals in the azines](#), J. Chem. Phys. **40**, 2745 (1964). pages 94, 167
- [92] R. Hoffmann, [An extended Hückel theory. III. Compounds of boron and nitrogen](#), J. Chem. Phys. **40**, 2474 (1964). pages 94, 167
- [93] R. Hoffmann, [An extended Hückel theory. IV. Carbonium ions](#), J. Chem. Phys. **40**, 2480 (1964). pages 167
- [94] M. Elstner et al., [Self-consistent-charge density-functional tight-binding method for simulations of complex materials properties](#), Phys. Rev. B **58**, 7260 (1998). pages 96, 169, 236, 241

- [95] M. Gaus, Q. Cui, and M. Elstner, [DFTB3: Extension of the self-consistent-charge density-functional tight-binding method \(SCC-DFTB\)](#), J. Chem. Theory Comput. **7**, 931 (2011). pages 96, 98, 169, 236
- [96] R. S. Mulliken, [Report on Molecular Orbital Theory](#), Journal de Chimie Physique et de Physico-Chimie Biologique **497** (1949). pages 169, 237
- [97] T. Frauenheim et al., [Atomistic simulations of complex materials: ground-state and excited-state properties](#), J. Phys.: Condens. Matter **14**, 3015 (2002). pages 170, 172, 227, 235
- [98] R. Pariser, [An improvement on the \$\pi\$ -electron approximation in LCAO MO theory](#), J. Chem. Phys. **21**, 568 (1953). pages 98, 171
- [99] A. M. H. M. Darghouth et al., [Assessment of density-functional tight-binding ionization potentials and electron affinities of molecules of interest for organic solar cells against first-principles *GW* calculations](#), Computation **3**, 616 (2015). pages 171, 227
- [100] T. Niehaus and F. Della Sala, [Range separated functionals in the density functional tight-binding method](#), Phys. Status Solidi B **2**, 237 (2012). pages 88, 171, 235
- [101] V. Lutsker, B. Aradi, and T. A. Niehaus, [Implementation and benchmark of a long-range corrected functional in the density functional based tight-binding method](#), J. Chem. Phys. **143**, 184107 (2015). pages 88, 95, 127, 171, 235
- [102] V. Q. Vuong et al., [Parameterization and benchmark of long-range corrected DFTB2 for organic molecules](#), J. Chem. Theory Comput. **14**, 115 (2018). pages 171, 235
- [103] A. Humeniuk and R. Mitrić, [Long-range correction for tight-binding TD-DFT](#), J. Chem. Phys. **143**, 134120 (2015). pages 88, 171, 172, 173, 228, 235, 239, 241
- [104] A. Humeniuk and R. Mitrič, [DFTBABY: A software package for non-adiabatic molecular dynamics simulations based on long-ranged corrected tight-binding TD-DFT\(B\)](#), Comp. Phys. Comm. **221**, 174 (2017). pages 171, 172, 173, 191, 227, 235, 239, 240, 241, 242
- [105] T. Niehaus et al., [Tight-binding approach to time-dependent density-functional response theory](#), Phys. Rev. B **63**, 085108 (2001). pages 172, 227, 235
- [106] D. Heringer, T. A. Niehaus, M. Wanko, and T. Frauenheim, [Analytical excited state forces for the time-dependent density-functional tight-binding method](#), J. Comput. Chem. **28**, 2589 (2007). pages 172, 227, 235

- [107] T. A. Niehaus, [Approximate time-dependent density functional theory](#), J. Molec. Struct.: THEOCHEM **914**, 38 (2009). pages 172, 227, 235
- [108] T. A. Niehaus et al., [Tight-binding approach to time-dependent density-functional response theory](#), Phys. Rev. B **63**, 085108 (2001). pages 172
- [109] F. Trani et al., [Time-dependent density-functional tight binding: New formulation and benchmark of excited states](#), J. Chem. Theory Comput. **7**, 3304 (2011). pages 172
- [110] M. J. Frisch et al., [GAUSSIAN 09 Revision D.01](#), Gaussian Inc. Wallingford CT 2009. pages 99, 172, 173
- [111] W. J. Hehre, L. Radom, P. v. R. Schleyer, and J. A. Pople, [Ab Initio Molecular Orbital Theory](#), John Wiley and Sons, New York, 1986. pages 99, 173
- [112] W. J. Hehre, R. F. Stewart, and J. A. Pople, [Self-Consistent Molecular-Orbital Methods. I. Use of Gaussian Expansions of Slater-Type Atomic Orbitals](#), J. Chem. Phys. **51**, 2657 (1969). pages 100, 173
- [113] W. J. Hehre, R. Ditchfield, R. F. Stewart, and J. A. Pople, [Self-Consistent Molecular Orbital Methods. IV. Use of Gaussian Expansions of Slater-Type Orbitals. Extension to Second-Row Molecules](#), J. Chem. Phys. **52**, 2769 (1970). pages 173
- [114] R. Ditchfield, W. J. Hehre, and J. A. Pople, [Self-Consistent Molecular-Orbital Methods. IX. An Extended Gaussian-Type Basis for Molecular-Orbital Studies of Organic Molecules](#), J. Chem. Phys. **54**, 724 (1971). pages 173
- [115] W. J. Hehre, R. Ditchfield, and J. A. Pople, [Self-Consistent Molecular Orbital Methods. XII. Further Extensions of Gaussian-Type Basis Sets for Use in Molecular Orbital Studies of Organic Molecules](#), J. Chem. Phys. **56**, 2257 (1972). pages 100, 173, 240
- [116] P. C. Harihan and J. A. Pople, [The effect of *d*-functions on molecular orbital energies for hydrocarbons](#), Chem. Phys. Lett. **16**, 217 (1972). pages 173
- [117] D. L. Dorset and M. P. McCourt, [Disorder and the molecular packing of C₆₀ buckminsterfullerene: A direct electron-crystallographic analysis](#), Acta Crystallogr. Sect. A **50**, 344 (1994). pages 173, 196, 240
- [118] S. Schiefer, M. Huth, A. Dobrinevski, and B. Nickel, [Determination of the Crystal Structure of Substrate-Induced Pentacene Polymorphs in Fiber Structured Thin Films](#), J. Am. Chem. Soc. **129**, 10316 (2007). pages 173, 196, 240
- [119] A. Rauk, [Interactive Simple Hückel Molecular Orbital \(SHMO\) Theory Calculator](#), <http://www.ucalgary.ca/rauk/shmo>, accessed 22 July 2016. pages 175

- [120] J. A. Huwaldt, [PLOT DIGITIZER, version 2.6.8](#), [//http://plotdigitizer.sourceforge.net/](http://plotdigitizer.sourceforge.net/), accessed 28 June 2017. pages 175
- [121] A. Maliakal, K. Raghavachari, H. Katz, E. Chandross, and T. Siegrist, [Photochemical stability of pentacene and a substituted pentacene in solution and in thin films](#), Chem. Mater. **16**, 4980 (2004). pages 175, 194, 195, 197, 313
- [122] E. Heinecke, D. Hartmann, R. Müller, and A. Hese, [Laser spectroscopy of free pentacene molecules \(I\): The rotational structure of the vibrationless \$S_1 \leftarrow S_0\$ transition](#), J. Chem. Phys. **109**, 906 (1998). pages 178
- [123] T. M. Halasinski, D. M. Hudgins, F. Salama, L. J. Allamandola, and T. Bally, [Electronic absorption spectra of neutral pentacene \(\$C_{22}H_{14}\$ \) and its positive and negative ions in Ne, Ar, and Kr matrices](#), J. Chem. Phys. A **104**, 7484 (2000). pages 178
- [124] M. S. Alam, J. Lin, and M. Saito, [First-principles calculation of the interlayer distance of the two-layer graphene](#), Jap. J. Appl. Phys. **50**, 080213 (2011). pages 179
- [125] M. L. Tiago, J. E. Northrup, and S. G. Louie, [Ab initio calculation of the electronic and optical properties of solid pentacene](#), Phys. Rev. B **67**, 115212 (2003). pages 195, 196, 313
- [126] L. Sebastian, G. Weiser, and H. Bässler, [Charge transfer transitions in solid tetracene and pentacene studied by electroabsorption](#), Chem. Phys. **61**, 125 (1981). pages 194
- [127] N. J. Hestand et al., [Polarized absorption in crystalline pentacene: Theory vs experiment](#), J. Phys. Chem. **119**, 22137 (2015). pages 194
- [128] C. Ambrosch-Draxl, D. Nabok, P. Puschnig, and C. Meisenbichler, [The role of polymorphism in organic thin films: oligoacenes investigated from first principles](#), New J. Phys. **11**, 125010 (2009). pages 196
- [129] P. Cudazzo, M. Gatti, A. Rubio, and F. Sottile, [Frenkel versus charge-transfer exciton dispersion in molecular crystals](#), Phys. Rev. B **88**, 195152 (2013). pages 196
- [130] S. Sharifzadeh, P. Darancet, L. Kronk, and J. B. Neaton, [Low-energy charge-transfer excitons in organic solids from first-principles: The case of pentacene](#), J. Phys. Chem. Lett. **4**, 2197 (2013). pages 196
- [131] M. R. Philpott, [Planewise summation of point dipole-dipole interactions for some aromatic hydrocarbon crystals](#), J. Chem. Phys. **58**, 588 (1973). pages 198

-
- [132] H. Yamagata et al., [The nature of singlet excitons in oligoacene molecular crystals](#), J. Chem. Phys. **134**, 204703 (2011). pages 198
- [133] I. Meyenburg et al., [Temperature-resolved optical spectroscopy of pentacene polymorphs: variation of herringbone angles in single-crystals and interface-controlled thin films](#), Phys. Chem. Chem. Phys. **18**, 3825 (2016). pages 198
- [134] S. A. Mewes, F. Plasser, and A. Dreuw, [Universal exciton size in organic polymers is determined by nonlocal exchange in time-dependent density functional theory](#), J. Phys. Chem. Lett. **8**, 1205 (2017). pages 205

Chapter 7

How Long Do Energy and Charge
Transfer Take? Tully-Type Mixed
Time-Dependent Tight-Binding
Density-Functional/Classical
Trajectory Surface Hopping Study of
a Model

Buckminsterfullerene/Pentacene
Heterojunction with and without
Long-Range Correction

How Long Do Energy and Charge Transfer Take? Tully-Type Mixed Time-Dependent Tight-Binding Density-Functional/Classical Trajectory Surface Hopping Study of a Model Buckminsterfullerene/Pentacene Heterojunction with and without Long-Range Correction

Ala Aldin M. H. M. Darghouth¹, Mark E. Casida²,

Laboratoire de Chimie Inorganique Rédox (CIRE), Département de Chimie
Moléculaire (DCM),

Institut de Chimie Moléculaire de Grenoble (ICMG), Université Grenoble-Alpes,
301 rue de la Chimie, CS 40700, 38058 Grenoble Cedex 9, France

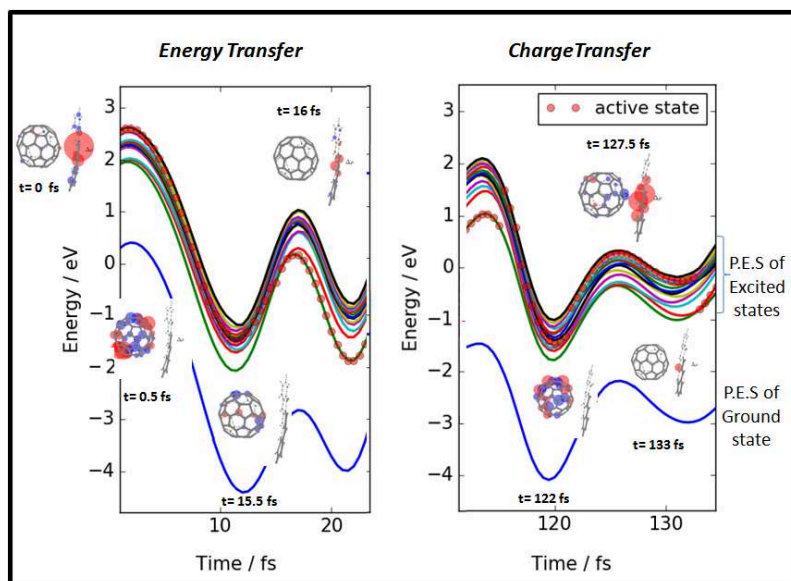
Xi Zhu (朱熹) [1]³, Bhaarithi Natarajan⁴, Haibin Su (蘇海斌) [2]⁵

Division of Materials Science, Nanyang Technical University, 50 Nanyang 639789,
Singapore

Alexander Humeniuk⁶ and Roland Mitrić⁷

Institut für Physikalische und Theoretische Chemie,
Julius-Maximilians-Universität Würzburg,
Emil-Fischer-Straße 42, D-97074 Würzburg, Germany

Abstract



1. ala.darghout@univ-grenoble-alpes.fr
2. mark.casida@univ-grenoble-alpes.fr
3. 0220ustc@gmail.com
4. phyever@gmail.com
5. hbsu@ntu.edu.sg
6. alexander.humeniuk@gmail.com
7. roland.mitric@uni-wuerzburg.de

Six Step Model	
(i)	Exciton formation via photon absorption
(ii)	Exciton diffusion to the heterojunction
(iii)	Exciton dissociation into closely-bound charge-transfer (CT) states at the heterojunction
(iv)	Dissociation of these CT states into charge-separated states composed of free mobile charges
(v)	Charge transport away from the heterojunction
(vi)	Charge collection at the electrodes

Table 7.1 – The generally accepted model for organic heterojunction solar cells [3].

Tully-type mixed time-dependent long-range corrected density-functional tight-binding /classical surface-hopping photodynamics is used to investigate the nature of and time scales for energy and charge transfer in the simplest model of an organic photovoltaic heterojunction, namely a single molecule of buckminsterfullerene (C_{60}) together with a single molecule of pentacene. The distinction between energy and charge transfer is more difficult to make in practical calculations than might at first seem to be the case, but several criteria are used to make a clear distinction between these two phenomena. It is found that the excitation fluctuates from one molecule to the other, with the first change within about 20 fs. However it is only after 188 ± 28 fs that real charge transfer occurs. This is commensurate with what is known from experiment and very different from the severe under-estimate obtained when the same calculation is repeated without a long-range correction. Of course, our system is not large enough for the charge transfer to occur irreversibly and so the charge does not remain on the acceptor indefinitely but instead must return to the donor. We believe that these encouraging results obtained with time-dependent long-range corrected density-functional tight-binding/classical surface-hopping photodynamics may, because of their intrinsic computational efficiency compared with time-dependent long-range corrected density-functional theory/classical surface-hopping photodynamics may open the way to investigating a larger variety of increasingly realistic model organic photovoltaic heterojunctions.

7.1 Introduction

So far, solar cell technology is dominated by silicon-based solar cells as these provide excellent energy output for the amount of energy obtained per amount of money spent. Part of the reason for this is, of course, the result of many years devoted to understanding and engineering silicon-based electronics [4]. However organic electronics

is a rapidly developing technology based upon similar, but different, principles [5]. It is increasingly able to compete with traditional silicon-based technologies for niche applications, especially where ease of fabrication (including the possibility to print circuits with only minor modification of existant printing technology), lightness, and flexibility are concerned. And one of the very interesting niche applications of organic electronics is organic solar cells [also known as organic photovoltaics (OPV)] [6, 7, 8, 9, 3, 10]. According to the American National Renewable Energy Lab's best energy efficiencies [11], crystalline silicon solar cell technology achieves between 25% and 30% efficiency, approaching the theoretical Shockley-Queisser efficiency of 33.16% [12]. In contrast, organic solar cells are currently limited to 10% to 12% efficiency at best. It is a challenge to know if this is close to some intrinsic limit of organic materials or whether significant increases in organic solar cell efficiency are still possible. Theoretical investigation of the fundamental mechanism of organic solar cell operation is likely to be helpful here. The accepted model of power conversion in the popular bulk heterojunction configuration is summarized in Table 7.1. These steps highlight the importance of the heterojunction between an electron acceptor and an electron donor phase. Experimental evidence indicates that step (iii) occurs on a time scale on the order of about 100 fs (e.g., 200 fs for APFO3/PCBM [13], 70-100 fs for pentacene/C₆₀ [14], \leq 100 fs for MDMO-PPV/PC₇₀BM and for PCPDTBT/PC₇₀BM [15], and 82 fs for p-DTS(FBTTh₂)₂/PC₇₁BM [16].) This short time scale has sometimes been used by certain researchers (particularly those coming from a solid-state physics background) to neglect nuclear displacements during the CT process. However key photochemical events involving nuclear motion often occur on time scales of this same order of magnitude. This has led us to model the bulk heterojunction excitation dissociation event using techniques from the photochemical modeler's toolbox, in particular mixed Tully-type quantum chemical/classical surface hopping photodynamics. Our specific objective is to obtain a better understanding of the types of photochemical phenomena that are occurring, and how quickly they are occurring, on the scale of a few hundred fs.

Charge separation in organic solar cells has been intensively studied and several review articles may be found in the literature [6, 7, 8, 9, 17, 3, 10, 18]. The previously-mentioned six step model focusing on events at, or in the vicinity of, the heterojunction gradually emerged after Ching Tang's key demonstration in the 1980s that the excitations which ultimately lead to charge separation originate on average at no more than 10 nm from the heterojunction [19]. Central questions inspired by this model concern the time scales and efficiencies of different steps. Step (v) is often mentioned as particularly puzzling. Indeed a back-of-the-envelope calculation based

upon the idea of the formation of a dipole layer at the heterointerface suggests that the charges should be bound to the interface by on the order of 0.1-0.5 eV which may be compared to the amount of available thermal energy which is on the order of 0.025 eV [18], leading to the question of how organic heterojunction solar cells can work at all? Experimental techniques have provided some illumination, but are usually time-scale specific. Thus ultrafast spectroscopic methods can probe excited-state dynamics on subpicosecond time scales [20, 21, 22, 15, 23], pump-probe electron field-induced second harmonic (EFISH) generation experiments [24] can probe excited-state dynamics on ps to ns time scales, and electrical methods can probe free carrier motion on ns to ms time scales. As it stands, step (iii) of the model is known experimentally to take place on a time scale of the order of 100 fs, while step (iv) is known experimentally to take place on a ps time scale. The exact mechanism of step (iv) might be explained by “simple” diffusion in a hopping model [24] but several other factors are likely to contribute or may provide better explanations [18]. As we shall see, our simulations are too short and our model is too small to address the question of how independent charge carriers form. However we may gain insight into the initial charge separation event (iii).

Several considerations were taken into account in choosing a model heterojunction. Rather than focusing on components of the most efficient solar cells, we chose to focus on two well-studied components, namely pentacene (Pent) and buckminsterfullerene (C_{60}) as well as devices made with them as components. Pentacene belongs to the family of acenes which has been reviewed in Ref. [25]. It is the largest conveniently synthesized member of the family and is a good choice as electron donor (D). Buckminsterfullerene is an excellent electron acceptor (A) and its derivatives are frequently found in organic solar cells [26]. These molecules have been extensively studied both experimentally and theoretically. They have also been combined to make interesting A/D devices, including field-effect transistors [27] and solar cells [28, 29]. C_{60} /Pent devices have also been investigated in the context of singlet fission [14, 29]. How pentacene molecules align themselves on a surface should depend both upon the type of surface and perhaps also upon sample preparation. There is experimental evidence that pentacene aligns in a head-on configuration with silicon oxide corresponding to a (001) cut of the pentacene crystal [30] but aligns itself in a flat-side configuration on graphene corresponding to a (010) cut of the pentacene crystal [31]. This is consistent with the general chemistry concept of “like-likes-like” that is often used to explain solubility and phase separation. The stability of different cuts of a pentacene crystal interfaced with crystalline C_{60} has been investigated theoretically with the conclusion that the head-on configuration formed by a (001)

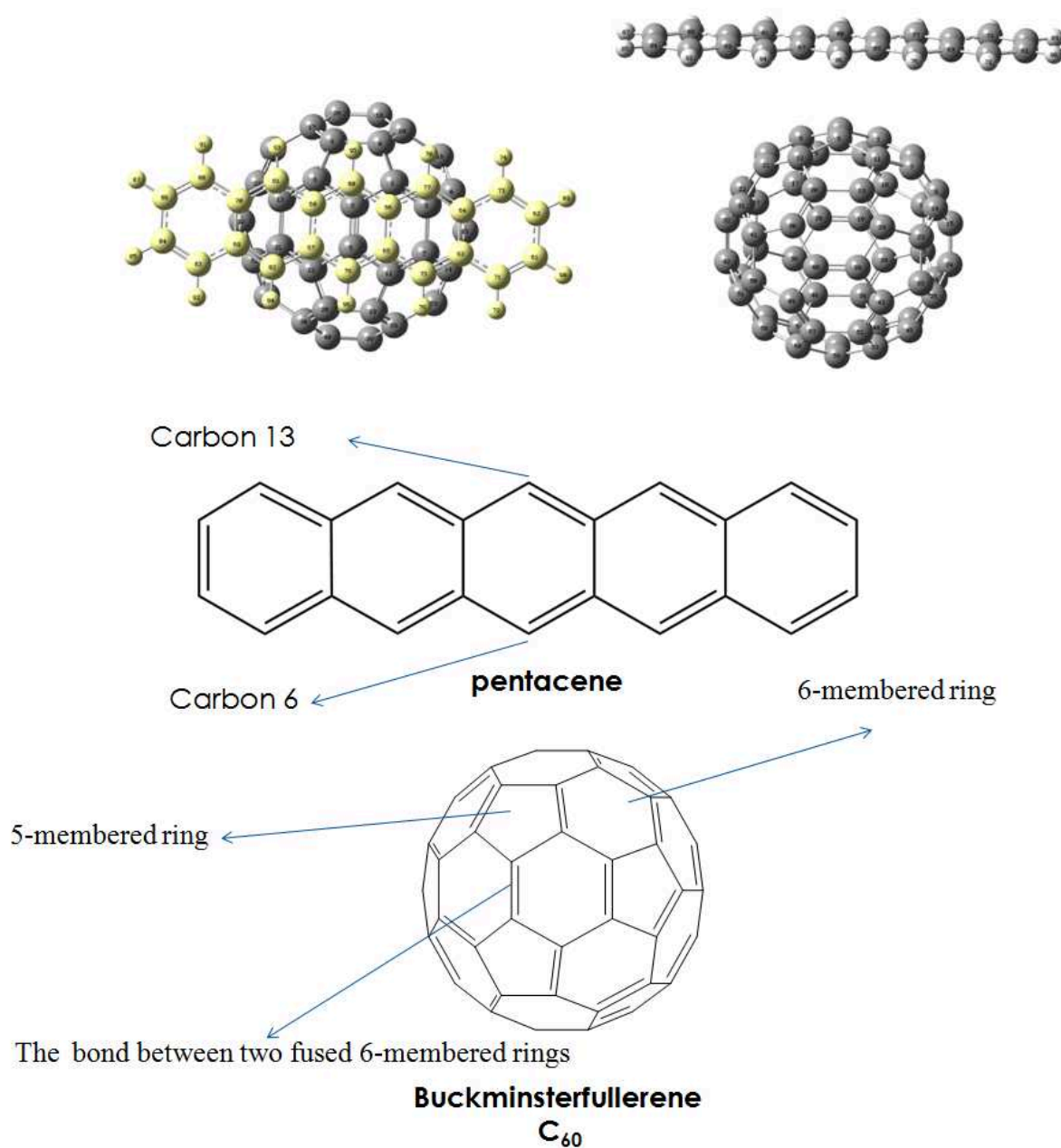


Figure 7.1 – The initial orientations of pentacene and buckminsterfullerene in the model of organic solar cells studied in this work.

cut of the pentacene crystal is likely to be more stable than the flat-side configuration formed by a (010) cut of the pentacene crystal [32]. This might suggest that we should orient Pent in a head-on configuration with C_{60} in our model as has been done in several previous articles focusing on excitation energies without dynamical modeling [33, 34, 35]. However other studies have chosen to focus on both the head-on and flat-side configurations [36, 37]. Indeed we find it interesting that the flat-side configuration is known to undergo an electrocyclic addition reaction [38] (though no indication of such a reaction was found in our photochemical simulations.) After investigating the energetics of a single buckminsterfullerene acceptor molecule together with a single pentacene acceptor molecule, we chose a low energy model consisting of a single buckminsterfullerene acceptor molecule together with a single pentacene acceptor molecule with the central 6,13 carbons in pentacene centred over a the π -bond between two fused 6-membered rings in C_{60} as shown in Fig. 7.1. This corresponds to Model 1 in Ref. [36].

We have chosen to study the photodynamics of our system using mixed Tully-type quantum chemical/classical surface hopping photodynamics [39, 40, 41, 42]. This is versatile enough to describe nonadiabatic surface hopping processes where the system can change from electronic states of different character (e.g., charge localized to charge transfer type) and, if enough trajectories are run, can give an idea of branching ratios for different photochemical processes. The difficulty with this method is that the choice of quantum chemical method must be efficient enough to do many trajectories and many time steps for each trajectory. One approach is to use time-dependent (TD) density-functional theory (DFT). Mixed Tully-type TD-DFT/classical surface hopping photodynamics was first introduced by Tapavicza, Tavernelli, and Roethlisberger in 2007 [43] (Refs. [44, 45] provide reviews). As the model system studied here is getting to be too large for mixed TD-DFT/classical surface hopping calculations, further approximations are necessary. We have chosen to replace DFT with density-functional tight-binding (DFTB) [46, 47, 48] which is a semiempirical approximation to DFT. TD-DFTB was introduced by Niehaus *et al.* [49, 50, 51, 52] and is now well established. Naturally we have to expect some loss of accuracy, but DFTB is now sufficiently tested that we know that it is reasonably accurate for, for example, obtaining trends in the ionization potentials and electron affinities of molecules important for organic electronics [53] and that TD-DFTB is able to effectively mimic excitonic effects in TD-DFT calculations of molecular aggregates [54]. Mitrić and coworkers were apparently the first to develop mixed Tully-type TD-DFTB/classical surface hopping photodynamics [55, 56, 57] and this is what we use here in the recent program DFTBABY [58]. We note that this

includes both Grimme’s empirical van der Waals correction [59] which is important for describing intermolecular forces between organic molecules and the (TD-)DFTB version of a long-range corrected (also known as a range-separated hybrid) [(TD-)lc-DFTB] [60] which is needed for a correct description of CT excitations. Indeed previous work indicates that TD-lc-DFTB gives similar results to those obtained in TD-CAM-B3LYP calculations [54].

A complete description of exciton energy transfer (EET) and of charge transfer (CT) requires taking into account not only the molecule(s) of interest but also their environment [61]. Our model neglects environmental effects and has 88 atoms. It is large enough to demand significant computational resources for the relatively long photodynamics calculations reported here, but it is small enough that we must expect recurrences. At the beginning of the calculation, the overlap with the initial state is expected to diminish in a process known as dephasing (p. 81, Ref. [61]). According to the Poincaré recurrence theorem, we should expect to see any finite size dynamical system return arbitrary close to its starting point after some time interval. That is, in another jargon (p. 81, Ref. [61]), the system will rephase. The result is that we should expect to see energy and charge sloshing (most likely) nonperiodically back and forth between C₆₀ and Pent. In the case of EET, additional mechanisms such as Foerster or Dexter energy transfer could be invoked to describe how the process occurs. However we shall not be concerned with this level of detail here, only with the fact that EET does indeed occur. Our interest is focused on discovering typical times for EET in this system. We will also see CT but, because of rephasing, it will not be a permanent separation of charges as that would require adding an environment capable of carrying away the charges. Nevertheless, our calculations should provide a lower estimate of how long charge separation should take at a bulk heterojunction. As our A/D system is C₆₀/Pent, we expect electrons to be transferred from Pent to C₆₀.

This article is organized as follows: The next section provides a brief review of the basic theory used in this paper. Section 7.3 provides computational details and our results are presented in Sec. 7.4. Section 7.5 contains our concluding discussion.

7.2 Theoretical methods

This is a review section whose intent is to keep this article reasonably self-contained. As photochemical modeling techniques have been reviewed in several places [44, 45, 62], we will focus only on the specific techniques needed to understand this article.

Following Tully [39], we use a mixed quantum mechanical/classical trajectory

surface hopping model where the nuclear dynamics is assumed to be classical while the electron dynamics is described by quantum mechanics. Thus, the k th nucleus with mass M_k and position $\vec{R}_k(t)$ follows Newton's equation,

$$M_k \frac{d^2 \vec{R}_k(t)}{dt^2} = -\vec{\nabla}_k V_I(\mathbf{R}(t)), \quad (7.1)$$

where $\mathbf{R} = [\vec{R}_1, \vec{R}_2, \dots, \vec{R}_M]$ is the matrix of nuclear position (column) vectors and V_I is the adiabatic potential energy function for the I th electronic state. In contrast, electron dynamics is governed by the time-dependent field due to the classical nuclei,

$$\hat{H}_e(\mathbf{r}; \mathbf{R}(t)) \Psi(\mathbf{x}, t) = i \frac{d}{dt} \Psi(\mathbf{x}, t), \quad (7.2)$$

where \hat{H}_e is the usual electronic Hamiltonian, $\mathbf{r} = [\vec{r}_1, \vec{r}_2, \dots, \vec{r}_N]$, $\vec{x} = (\vec{r}, \sigma)$ includes both space and spin, and $\mathbf{x} = [\vec{x}_1, \vec{x}_2, \dots, \vec{x}_N]$. Such a model cannot be derived from first principles, but is physically appealing even if quantum effects of nuclear motion are lost. The probability that a classical particle, following a classical trajectory on the potential energy hypersurface of the I th electronic state hops to the hypersurface for the J th electronic state is governed by the quantum mechanical evolution of the electronic state. Tully [39, 40] proposed an efficient way to calculate the hopping probability known as fewest switches surface hopping (FSSH).

7.2.1 FSSH

To determine the probability that a classical trajectory describing nuclear motion hops to a new trajectory on another potential energy surface, we expand

$$\Psi(\mathbf{x}, t) = \sum_I \Psi_I(\mathbf{x}; \mathbf{R}(t)) C_I(t), \quad (7.3)$$

in solutions of the time-independent electronic Schrödinger equation,

$$\hat{H}_e \Psi_I(\mathbf{x}; \mathbf{R}(t)) = E_I(\mathbf{R}(t)) \Psi_I(\mathbf{x}; \mathbf{R}(t)). \quad (7.4)$$

The probability of finding the system on potential energy surface m is then given by

$$P_I(t) = |C_I(t)|^2. \quad (7.5)$$

The coefficients $C_I(t)$ are found by integrating the first-order differential equation,

$$\frac{dC_I(t)}{dt} = -iE_I(t) - \sum_J d_{I,J} C_J(t), \quad (7.6)$$

where the nonadiabatic coupling element,

$$\begin{aligned} d_{I,J}(\mathbf{R}(t)) &= \langle \Psi_I(\mathbf{R}(t)) | \frac{d\Psi_J(\mathbf{R}(t))}{dt} \rangle \\ &= \frac{d\vec{R}(t)}{dt} \cdot \vec{F}_{I,J}(\mathbf{R}(t)), \end{aligned} \quad (7.7)$$

is related to the derivative coupling matrix,

$$\vec{F}_{I,J}(\mathbf{R}(t)) = \langle \Psi_I(\mathbf{R}(t)) | \vec{\nabla}_{\mathbf{R}(t)} | \Psi_J(\mathbf{R}(t)) \rangle. \quad (7.8)$$

Note that this last quantity is both a function of the nuclear coordinates, a vector with respect to the nuclear coordinates, and a matrix with respect to the electronic degrees of freedom. ($\langle \dots \rangle$ refers only to integration over the electronic degrees of freedom.) We have arrived at this point at a very nice physical picture of swarms of trajectories of particles hopping between multiple potential energy surfaces with the relative number of trajectories on each potential energy surface giving the probability of finding the system in that electronic state at any given time.

We have to go a bit further in order to make our model well-defined and to overcome some technical problems. For one thing, we must be careful to conserve energy during the calculation. This is accomplished by rescaling the classical velocities after a hop from one surface to another so that the potential plus kinetic energies of the classical particle always remains constant. The element $d_{m,n}(\mathbf{R}(t))$ may at first seem hard to calculate, but in fact may be calculated numerically as,

$$\begin{aligned} d_{I,J}(\mathbf{R}(t + \frac{\Delta}{2})) &= \frac{1}{2\Delta} [\langle \Psi_I(\mathbf{R}(t)) | \Psi_J(\mathbf{R}(t + \Delta)) \rangle \\ &\quad - \langle \Psi_I(\mathbf{R}(t + \Delta)) | \Psi_J(\mathbf{R}(t)) \rangle]. \end{aligned} \quad (7.9)$$

A more difficult problem becomes evident when the derivative coupling matrix is rewritten as,

$$\vec{F}_{I,J}(\mathbf{R}) = \frac{\langle \Psi_I | \vec{\nabla} \hat{H}_e(\mathbf{R}) \Psi_J \rangle - \delta_{I,J} \vec{\nabla} E_I(\mathbf{R})}{E_J(\mathbf{R}) - E_I(\mathbf{R})}. \quad (7.10)$$

which shows that numerical difficulties can appear near conical intersections when $E_I(\mathbf{R}) \approx E_J(\mathbf{R})$. This difficulty is usually solved by switching from adiabatic to diabatic surfaces and following diabatic dynamics [63]. However the major problem

with this sort of model is that surface hopping at every time step rapidly becomes unmanageable.

Tully [39, 40] solved this problem by coming up with an especially efficient Monte Carlo procedure to carry out the above calculation, namely the FSSH procedure. The hopping probability from the m th to the n th potential energy surface during a time interval of duration Δt is given by,

$$g_{I \rightarrow J}(t, \Delta t) = \frac{(dP_{I,J}(t)/dt)\Delta t}{P_{I,I}(t)}, \quad (7.11)$$

where,

$$P_{I,J}(t) = C_I(t)C_J^*(t). \quad (7.12)$$

A random number ξ is generated with uniform probability over the interval $(0, 1)$. The transition $m \rightarrow n$ only occurs if

$$P_J^{(I-1)} < \xi < P_J^I, \quad (7.13)$$

where

$$P_J^{(I)} = \sum_{K=1,I} P_{J,K} \quad (7.14)$$

is the sum of the transition probabilities for the first m states.

7.2.2 TD-DFT FSSH

The calculations in the present model are based upon the ground state density-functional tight binding (DFTB) method and upon time-dependent (TD) DFTB. As these are semi-empirical versions of density functional theory (DFT) and of TD-DFT, we must first give a brief description of DFT and of TD-DFT as well as of TD-DFT FSSH.

DFT [64, 65] is now so well known that little needs to be said except to introduce notation. (Refs. [66, 67, 68] provide an introduction to DFT.) The basic idea of the Kohn-Sham formulation is to replace the real system of N interacting electrons in an external potential v_{ext} , with a fictitious system of noninteracting electrons moving in a new potential,

$$v_s = v_{\text{ext}} + v_H + v_{xc}. \quad (7.15)$$

Here

$$v_H(\vec{r}_1) = \int \frac{\rho(\vec{r}_2)}{r_{1,2}} d\vec{r}_2 \quad (7.16)$$

is the Hartree (also known as the classical coulomb) potential,

$$\rho(\vec{r}) = \sum_i n_i |\psi_i(\vec{r})|^2 \quad (7.17)$$

is the charge density, and

$$v_{xc}(\vec{r}) = \frac{\delta E_{xc}[\rho]}{\delta \rho(\vec{r})} \quad (7.18)$$

is the exchange-correlation (xc) potential. (Hartree atomic units $m_e = e = \hbar = 1$ are used throughout unless otherwise indicated.) The Kohn-Sham molecular orbitals (MOs) ψ_i with associated occupation number n_i satisfy the orbital Schrödinger equation,

$$\left(-\frac{1}{2}\nabla^2 + v_s\right)\psi_i = \epsilon_i\psi_i, \quad (7.19)$$

and the exact ground-state electronic energy for the real system may be written as,

$$\begin{aligned} E_0 &= \sum_i n_i \epsilon_i + G \\ G &= -\frac{1}{2} \iint \frac{\rho(\vec{r}_1)\rho(\vec{r}_2)}{r_{1,2}} d\vec{r}_1 d\vec{r}_2 + E_{xc} - \int v_{xc}(\vec{r})\rho(\vec{r}) d\vec{r}, \end{aligned} \quad (7.20)$$

where E_{xc} is the xc energy.

Thus far the theory is exact but impractical. To make it practical, we must introduce density functional approximations (DFAs) for the xc energy. We are not very concerned in the present article about the details of different DFAs with the exception of DFAs which introduce some orbital-dependent Hartree-Fock exchange. The first such DFA was a “global hybrid,” introduced by Becke in order to achieve near thermochemical accuracy [69]. This was clearly no longer pure Kohn-Sham theory [70] and has been properly rebaptized as a generalized Kohn-Sham theory [71]. In particular, molecular orbital energies in generalized Kohn-Sham theory will behave differently from those in traditional Kohn-Sham theory. In recent years, global hybrids are being replaced with “range-separated hybrids” [also called “long-range corrected hybrids” (lc)] where the electron repulsion is separated into a short-range

(sr) part and a long range (lr) part,

$$\begin{aligned}\frac{1}{r_{1,2}} &= \left(\frac{1}{r_{1,2}}\right)_{sr} + \left(\frac{1}{r_{1,2}}\right)_{lr} \\ \left(\frac{1}{r_{1,2}}\right)_{sr} &= \frac{\text{erfc}(\mu r_{12})}{r_{1,2}} \\ \left(\frac{1}{r_{1,2}}\right)_{lr} &= \frac{\text{erf}(\mu r_{12})}{r_{1,2}},\end{aligned}\quad (7.21)$$

where erf is the error function and erfc is the complementary error function. These become especially important for a correct description of charge-transfer corrections in TD-DFT.

TD-DFT is generally said to be based upon the Runge-Gross theorem [72]. It has been extensively reviewed in two recent proceedings [73, 74] and in one single author book [75] as well as in several recent review articles [76, 77, 78, 79, 80, 81]. The most common application of TD-DFT is to solve for excitation energies and oscillator strengths for UV-Vis spectra (usually) using Casida's linear-response equation [82],

$$\begin{bmatrix} \mathbf{A} & \mathbf{B} \\ \mathbf{B}^* & \mathbf{A}^* \end{bmatrix} \begin{pmatrix} \vec{X}_I \\ \vec{Y}_I \end{pmatrix} = \omega_I \begin{bmatrix} \mathbf{1} & \mathbf{0} \\ \mathbf{0} & -\mathbf{1} \end{bmatrix} \begin{pmatrix} \vec{X}_I \\ \vec{Y}_I \end{pmatrix} \quad (7.22)$$

in the TD-DFT adiabatic approximation,

$$v_{xc}[\rho](\vec{r}, t) = \frac{\delta E_{xc}[\rho_t]}{\delta \rho_t(\vec{r})}, \quad (7.23)$$

where $\rho_t(\vec{r}) = \rho(\vec{r}, t)$ is a function of \vec{r} at a particular t . The definition of the \mathbf{A} and \mathbf{B} matrices requires extending DFT to include spin (indicated by σ and τ). We may then write that,

$$\begin{aligned}A_{ia\sigma,jb\tau} &= \delta_{i,j}\delta_{a,b}\delta_{\sigma,\tau}(\epsilon_{a\sigma} - \epsilon_{i\sigma}) + K_{ia\sigma,jb\tau} \\ B_{ia\sigma,jb\tau} &= K_{ia\sigma,jb\tau},\end{aligned}\quad (7.24)$$

where the coupling matrix is defined by,

$$\begin{aligned}K_{ia\sigma,jb\tau} &= \int \int \psi_{i\sigma}^*(\vec{r}_1) \psi_{a\sigma}(\vec{r}_1) \\ &\quad \times f_{Hxc}^{\sigma,\tau}(\vec{r}_1, \vec{r}_2) \psi_{j\tau}^*(\vec{r}_2) \psi_b(\vec{r}_2) d\vec{r}_1 d\vec{r}_2 \\ f_{Hxc}^{\sigma,\tau}(\vec{r}_1, \vec{r}_2) &= \frac{1}{r_{1,2}} + \frac{\delta^2 E_{xc}[\rho_\alpha, \rho_\beta]}{\delta \rho_\sigma(\vec{r}_1) \delta \rho_\tau(\vec{r}_2)}.\end{aligned}\quad (7.25)$$

The indices i and j are reserved for occupied orbitals while a and b are used for

unoccupied orbitals.

Thus far the TD-DFT linear response equations have been written here for conventional (pure) DFAs. It is now well-established that TD-DFT with conventional DFAs works best for localized low-energy excitations without too much charge transfer. On the other hand, charge-transfer excitations may be underestimated by one or two electron volts [83, 84]. Peach and co-workers defined the Λ criterion to detect when a TD-DFT excited state is likely to suffer from CT errors [85, 86, 87, 88, 89, 90, 91].

$$\begin{aligned}\Lambda &= \frac{\sum_{i,a} \kappa_{ia}^2 O_{ia}}{\sum_{i,a} \kappa_{ia}^2} \\ \kappa_{ia} &= X_{ia} + Y_{ia} \\ O_{ia} &= \int |\psi_i(\vec{r})|^2 |\psi_a(\vec{r})|^2 d\vec{r}.\end{aligned}\tag{7.26}$$

The best solution to date is to use TD-lc-DFT [92, 93, 94, 95, 96, 97].

The energy of the I th electronic excited state is then,

$$E_I = E_0 + \omega_I.\tag{7.27}$$

As it is now known how to take gradients of both the ground-state energy E_0 and of the excitation energy ω_I [98, 99, 100, 101, 102, 103, 104, 105], dynamics becomes possible on the potential energy hypersurface for the n th excited state, opening up the way for the TD-DFT FSSH method.

The first implementation of TD-DFT FSSH was due to Tapavicza, Tavernelli, and R  thlisberger in 2007 [43] in a development version of the CPMD code. They proposed that the nonadiabatic coupling be calculated using Casida's *Ansatz* which was originally intended as an aid for assigning TD-DFT excited states [82]. Specifically, an excited-state wave function

$$\Psi_I = \sum_{i,a,\sigma} \Phi_{i\sigma}^{a\sigma} C_{ia\sigma},\tag{7.28}$$

made up of singly excited determinants $\Phi_{i\sigma}^{a\sigma}$ (corresponding to the $i\sigma \rightarrow a\sigma$ excitation) is postulated and it is argued that

$$C_{ia\sigma}^I = \sqrt{\frac{\epsilon_{a\sigma} - \epsilon_{i\sigma}}{\omega_I}} F_{ia\sigma}^I,\tag{7.29}$$

where

$$\vec{F}_I \propto (\mathbf{A} - \mathbf{B})^{-1/2} \left(\vec{X}_I + \vec{Y}_I \right),\tag{7.30}$$

is renormalized so that,

$$\vec{F}_I^\dagger \vec{F}_I = 1. \quad (7.31)$$

This was followed by an application to the photochemical ring opening of oxirane [106] which showed that the nonexistence of a proper conical intersection in conventional TD-DFT [107] was not a serious practical problem of TD-DFT FSSH. TD-DFT FSSH has also been implemented in a version of TURBOMOL capable of calculating nonadiabatic coupling elements analytically [108] and this has been applied to study the photochemistry of vitamin-D [109].

7.2.3 TD-DFTB FSSH

As TD-DFT FSSH requires many repeated electronic structure calculations, it rapidly becomes computationally resource intensive. For example, we did try to use NEWTON-X [110] to carry out TD-DFT FSSH calculations for the Pent/C₆₀ system, but we found such calculations to be too resource intensive to be practical for the long run times reported in this paper. Instead we make use of a semi-empirical version of TD-DFT, known as TD-DFTB. (Other related TD-DFTB and DFTB methods for photochemical dynamics have also been developed [111, 112, 113, 114] but are not of direct importance for the present work.) DFTB is reviewed in Refs. [46, 47, 48]. Like other semi-empirical quantum chemistry theories, DFTB uses an atom-centered minimal basis set which treats only the valence electrons. The core electrons are included as an ionic potential within v_{ext} . Approximations are made so that no more than two-center integrals need be evaluated. For invariance reasons, the two-center integrals are generally restricted to integrals over s -type functions, albeit different s -type functions for different values of the angular momentum quantum number l . In recent years, the theory has been extended to TD-DFTB [49, 50, 51, 52, 115], to lc-DFTB [116, 60, 117, 118], to TD-lc-DFTB, and most recently to TD-lc-DFTB FSSH [58]. The basic theory is only very briefly reviewed here, so the reader is referred to the original literature for additional information.

The original form of DFTB [119] was noninterative. We will denote the μ th basis function on atom I by,

$$\chi_{\mu I} = \chi_{\mu \in I}, \quad (7.32)$$

where the left-hand side is just a shorter form of the right-hand side. The density is the superposition of atomic densities,

$$\rho_0 = \sum_I \rho_I^0, \quad (7.33)$$

and the Hxc part of the Kohn-Sham potential is assumed separable,

$$v_{Hxc}[\rho] = \sum_I v_{Hxc}[\rho_I]. \quad (7.34)$$

The matrix elements of the Kohn-Sham hamiltonian (\hat{f}) are calculated as,

$$f_{\mu I, \nu J} = \begin{cases} \delta_{\mu, \nu} \langle \chi_{\mu I} | \hat{t} + v_s[\rho_I] | \chi_{\nu J} \rangle & ; \ I = J \\ \langle \chi_{\mu I} | \hat{t} + v_s[\rho_I] + v_{Hxc}[\rho_J] | \chi_{\nu J} \rangle & ; \ I \neq J \end{cases}, \quad (7.35)$$

where \hat{t} is the kinetic energy operator. Frequently $v_{Hxc}[\rho_I] + v_{Hxc}[\rho_J]$ is replaced with $v_{Hxc}[\rho_I + \rho_J]$ in modern implementations of DFTB. It then suffices to solve the matrix form of the Kohn-Sham equation,

$$\mathbf{f}^0 \vec{c}_i^0 = \epsilon_i^0 \mathbf{s} \vec{c}_i^0, \quad (7.36)$$

to be able to find the “band structure” (BS) part of the DFTB total energy,

$$E_{\text{BS}} = \sum_i n_i \epsilon_i^0. \quad (7.37)$$

Here

$$s_{\mu I, \nu J} = \langle \chi_{\mu I} | \chi_{\nu J} \rangle \quad (7.38)$$

is the usual overlap matrix and the superscript ⁰ is a reminder that these quantities are evaluated in a one-shot procedure with unperturbed atomic densities.

An examination of the expression for the DFT total energy (7.20) shows that the BS part of the energy is only the first term. This term must be corrected by the G term plus the repulsion between the core potentials. This is the so-called “repulsive potential” which, in DFTB, is assumed to be expandable as a set of pairwise potentials between different types of atom types,

$$E_{\text{rep}} = \sum_{I < J} V_{I,J}(R_{I,J}). \quad (7.39)$$

Probably the most difficult part of DFTB is developing and tabulating these pairwise potentials.

The theory presented thus far is not yet suitable for response theory calculations as we must still be able to take into account the effect of distortions of atomic densities due to external potentials such as those due to other atoms in a molecule. The extension of the theory may be through second- [120] or third-order [121], but

only the second-order theory will be described here. In particular the DFTB total energy is completed with a self-consistent charge (SCC) coulomb (coul) correction

$$E = E_{BS} + E_{rep} + E_{coul} , \quad (7.40)$$

where, in principle,

$$\begin{aligned} E_{coul} &= \frac{1}{2} \int \int \delta\rho(\vec{r}_1) (f_H(\vec{r}_1, \vec{r}_2) \\ &+ f_{xc}(\vec{r}_1, \vec{r}_2)) \delta\rho(\vec{r}_2) d\vec{r}_1 d\vec{r}_2 . \end{aligned} \quad (7.41)$$

However this expression is replaced by a new semi-empirical expression by making two approximations. The first is Mulliken's approximation, developed for use in approximating electron repulsion integrals [122]. This gives,

$$\psi_r^*(\vec{r})\psi_s(\vec{r}) = \sum_{\mu,I} q_{\mu I}^{r,s} \chi_{\mu I}^*(\vec{r})\chi_{\nu J}(\vec{r}) , \quad (7.42)$$

after a bit of algebra, where

$$q_{\mu I}^{r,s} = \frac{1}{2} (c_{\mu I,r}^* s_{\mu I,\nu J} c_{\nu J,s} + c_{\mu I,s} s_{\mu I,\nu J} c_{\nu J,r}^*) \quad (7.43)$$

is a Mulliken transition charge and the $c_{\mu I,r}$ are the coefficients obtained from expanding the MOs in terms of atomic orbitals. The second approximation is an approximate expansion in terms of s -type functions g_I ,

$$\chi_{\mu I}^*(\vec{r})\chi_{\mu I}(\vec{r}) = g_I(\vec{r}) . \quad (7.44)$$

It leads to the monopole expansion,

$$\psi_r^*(\vec{r})\psi_s(\vec{r}) = \sum_{\mu I} q_{\mu I}^{r,s} \chi_{\mu I}^*(\vec{r}) \quad (7.45)$$

Equation (7.44) might be called the “gamma approximation” because it allows us to define the integrals,

$$\begin{aligned} \gamma_{I,J} &= \int g_I(\vec{r}) (f_H(\vec{r}_1, \vec{r}_2) \\ &+ f_{xc}(\vec{r}_1, \vec{r}_2)) g_J(\vec{r}) d\vec{r}_1 d\vec{r}_2 . \end{aligned} \quad (7.46)$$

As the Mulliken charge on atom I ,

$$q_I = \sum_i q_I^{i,i} n_i, \quad (7.47)$$

then the coulomb energy [Eq. (7.41)] becomes

$$E_{\text{coul}} = \frac{1}{2} \sum_{I,J} \Delta q_I \gamma_{I,J} \Delta q_J \quad (7.48)$$

in these approximations, because

$$\delta \rho(\vec{r}) = \sum_I \Delta q_I g_I(\vec{r}) \quad (7.49)$$

in terms of the Mulliken charge fluctuations on each atom. In practice, in this work, we will add one more term to the DFTB energy, namely Grimme's D3 correction for van der Waals interactions [59].

Comparing Eqs. (7.25) and (7.46) makes it fairly clear that Casida's equation may be solved in DFTB. In particular, we need only replace the TD-DFT expression for the coupling matrix with the new expression,

$$K_{ia\sigma,jb\tau} = \sum_{I,J} q_I^{ia} \gamma_{I,J}^{\sigma,\tau} q_I^{jb}. \quad (7.50)$$

where the transition charges are

$$q_I^{ia} = \sum_{\mu \in I} q_{\mu I}^{ia}. \quad (7.51)$$

and $\gamma_{I,J}^{\sigma,\tau}$ takes on the spin indices σ and τ because we now include a spin dependence in

$$f_{xc}^{\sigma,\tau}(\vec{r}_1, \vec{r}_2) = \frac{\delta_{xc}^E}{\delta \rho_\sigma(\vec{r}_1) \delta \rho_\tau(\vec{r}_2)}. \quad (7.52)$$

Note that Grimme's D3 correction for van der Waals interactions does not enter into either TD-DFT or TD-DFTB calculations except indirectly through an initial ground-state geometry optimization.

As (TD-)DFTB is a semi-empirical approximation to (TD-)DFT, we can expect (TD-)DFTB to inherit the problems of (TD-)DFT—notably the underestimation of CT excitation energies. Unfortunately the Λ criterion [Eq. (7.26)] is difficult to evaluate directly within (TD-)DFTB. Instead, use is made of the monopole expansion

[Eq. (7.45)] to approximate,

$$O_{ia} = \sum_{I,J} q_I^{r,r} \int g_I(\vec{r}) g_J(\vec{r}) d\vec{r} q_I^{s,s}. \quad (7.53)$$

Additional details may be found in Ref. [60].

Of course, the better approach would be to develop the (TD)-lc-DFTB method. The obvious difficulty here is that the introduction of the semi-empirical equivalent of Hartree-Fock exchange means a return to traditional semi-empirical quantum chemistry techniques [123] whose somewhat less rigorous approximations have so far been avoided in DFTB. It also highlights a fundamental difficulty with DFTB, namely the need for extensive reparameterization each time a new DFA is used. This is avoided in the method of Humeniuk and Mitrić (used in the present article) where a long-range correction for exchange is added with

$$\gamma_{I,J}^{lr}(R_{I,J}) = \text{erf}(\mu R_{I,J}) \gamma_{I,J}(R_{I,J}) \quad (7.54)$$

and no reparameterizations. Furthermore Humeniuk and Mitrić neglect the lr contribution to the BS energy on the grounds that the zero-order system “already accounts for all interactions between electrons in the neutral atoms” [58]. In practice, the resultant (TD)-lc-DFTB method appears to behave very much like the (TD)-CAM-B3LYP method [54].

As TD-DFTB is very closely analogous to TD-DFT, it should not be too surprising that the advent of TD-DFTB FSSH quickly followed the advent of TD-DFT FSSH [56, 55, 124, 57]. The main difficulties to be overcome involved the development of analytic derivatives and the calculation of the nonadiabatic coupling matrix element $d_{I,J}(\mathbf{R}(t))$. In the implementation used in this article, the calculation of $d_{I,J}(\mathbf{R}(t))$ is accomplished by Casida’s wave function *Ansatz* [Eqs. (7.28) and (7.29)] combined with Eq. (7.9). This leads to a linear combination of overlap terms between two Slater determinants at different times which is evaluated using the observation [125] that

$$\begin{aligned} \left\langle \Phi_{i\alpha}^{a\alpha}(\mathbf{R}(t)) | \Phi_{j\beta}^{b\beta}(\mathbf{R}(t + \Delta)) \right\rangle &= \det(\mathbf{AB}) \\ &= (\det \mathbf{A})(\det \mathbf{B}), \end{aligned} \quad (7.55)$$

for a system of $N = 2n$ electrons where

$$\mathbf{A} = \begin{bmatrix} \langle \psi_1 | \psi'_1 \rangle & \cdots & \langle \psi_1 | \psi'_j \rangle & \cdots & \langle \psi_1 | \psi'_n \rangle \\ \vdots & \ddots & \vdots & \ddots & \vdots \\ \langle \psi_i | \psi'_1 \rangle & \cdots & \langle \psi_i | \psi'_j \rangle & \cdots & \langle \psi_i | \psi'_n \rangle \\ \vdots & \ddots & \vdots & \ddots & \vdots \\ \langle \psi_n | \psi'_1 \rangle & \cdots & \langle \psi_n | \psi'_j \rangle & \cdots & \langle \psi_n | \psi'_n \rangle \end{bmatrix} \quad (7.56)$$

is the determinant of overlaps of spin α orbitals and

$$\mathbf{B} = \begin{bmatrix} \langle \psi_1 | \psi'_1 \rangle & \cdots & \langle \psi_1 | \psi'_b \rangle & \cdots & \langle \psi_1 | \psi'_n \rangle \\ \vdots & \ddots & \vdots & \ddots & \vdots \\ \langle \psi_a | \psi'_1 \rangle & \cdots & \langle \psi_a | \psi'_b \rangle & \cdots & \langle \psi_a | \psi'_n \rangle \\ \vdots & \ddots & \vdots & \ddots & \vdots \\ \langle \psi_n | \psi'_1 \rangle & \cdots & \langle \psi_n | \psi'_b \rangle & \cdots & \langle \psi_n | \psi'_n \rangle \end{bmatrix} \quad (7.57)$$

is the determinant of overlaps of spin β orbitals. Unprimed and primed orbitals are evaluated at times t and $t + \Delta$ respectively. The merger of TD-lc-DFTB with TD-DFTB FSSH has only been achieved very recently and is used in this work [58]. The interested reader who is further interested in the technical details of this method should see that reference.

7.3 Computational Details

Three different programs were used to carry out the calculations reported in this paper: GAUSSIAN09 [126] was used to construct start geometries and to carry out some single-point spectra calculations. DFTB+ [127] was used to prepare an initial ensemble of trajectories. DFTBABY [58] was used to carry out Tully-type TD-lc-DFTB/classical trajectory surface hopping calculations.

GAUSSIAN09 was used to generate start geometries and for some single-point spectra calculations. Start geometries for the individual Pent and C₆₀ molecules were obtained by gas-phase optimization of initial crystal geometries taken from the Crystallography Open Database (COD) [128, 129, 130] and then optimized at the B3LYP/6-31G(d,p) level — that is, with the B3LYP functional (i.e., Becke's B3P functional [69] with Perdew's correlation generalized gradient approximation (GGA) replaced with the Lee-Yang-Parr GGA [131] without further optimization [132]) [133, 69] using the 6-31G(d,p) basis set [134, 135].

The start geometry of the Pent/C₆₀ van der Waals complex as obtained from the minimum of the potential energy curve for the unrelaxed molecules as a function of the intermolecular distance using the orientation shown in the upper left-hand corner of Fig. 7.1. These curves were calculated at the CAM-B3LYP-D3/6-31G(d,p) level — that is, the range-separated CAM-B3LYP [136] was supplemented with Grimme’s semi-empirical van der Waals correction [59].

A few single point time-dependent (TD) DFT calculations [82, 137, 138] were carried out at the TD-CAM-B3LYP/6-31G(d,p) level for the individual Pent and C₆₀ molecules.

DFTB+ was used to take the start geometries and to generate a thermal distribution of 30 start configurations for our FSSH calculations. It is not entirely clear whether it is best to use a thermal distribution or one which approximates a quantum distribution of vibrational states or, perhaps, something taking into account both thermal and quantum effects. We believe that the choice of thermal distribution used here is best for the Pent-C₆₀ intermolecular coordinate, but may lead to overly narrow distributions for the intramolecular coordinates of the monomers [139]. Calculations were performed at the DFTB2/mio-0-1 level [120] using a Lennard-Jones dispersion correction [140] and equilibrated at $T = 300$ K using the Nosé-Hoover thermostat and a time step of 0.5 fs. The system was judged to be equilibrated after 1000 fs (Fig. 7.2) and geometrical coordinates for the start geometries began to be collected after 1050 fs.

DFTBABY was used to carry out mixed TD-lc-DFTB/classical trajectory surface hopping using the FSSH algorithm. Each molecule from the 300K ensemble was excited to the excited state having the highest oscillator strength. This corresponds very roughly to broad band absorption in a solar cell. A different method of sample preparation (not used here), appropriate for excitation in a laser experiment, would be to use an excitation energy window.

The use of a range-separated hybrid has been previously investigated and shown to be important when calculating TD-DFT spectra of Pent/C₆₀ systems [33, 34, 37, 36, 35] in order to correct the well-known underestimation of charge-transfer excitations (for reviews of difficulties encountered with traditional TD-DFT and suggestions for correcting them see Refs. [76, 77, 79].) We used the TD-lc-DFTB as formulated by Humeniuk and Mitić [60] and used in their mixed TD-lc-DFTB/classical trajectory surface hopping program DFTBABY [58].

Calculations were carried out with a nuclear time step of 0.5 fs for trajectories

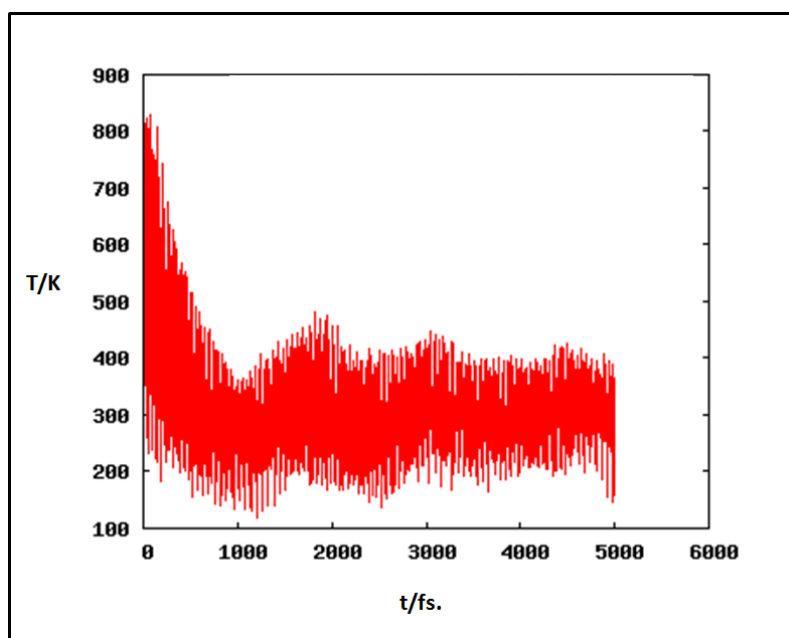


Figure 7.2 – Convergence of temperature with time during the DFTB+ equilibration.

as long as 500 fs. At least ten excited states, in addition to the ground state, have been followed during each trajectory calculation. (Similar mixed TD-DFT/classical trajectory calculations were tried using the NEWTON-X program [141], but were found to be too demanding of local computer resources to be practical.) Excited state gradients were calculated analytically (Appendix B of Ref. [58].) Adiabatic energies and scalar non-adiabatic couplings were interpolated linearly when integrating the electronic Schrödinger equation between nuclear time steps. Although decoherence effects can be important [142], no decoherence correction was used in the present calculations. Hops from a lower to a higher state were rejected if the kinetic energy was less than the energy gap between the states so as not to violate the principle of conservation of energy. Velocities were uniformly scaled after an allowed hop so that the total (kinetic plus potential) energy was conserved. It is known that artifacts can occur when integrating the electronic Schrödinger equation in an adiabatic basis near a photochemical funnel. This problem was avoided using a locally diabatic basis [63] which avoids numerical instabilities due to “trivial crossings.” Although it is conceivable that interatomic distances might have occurred for which DFTBABY was not parameterized, this situation was not encountered in practice.

7.4 Results

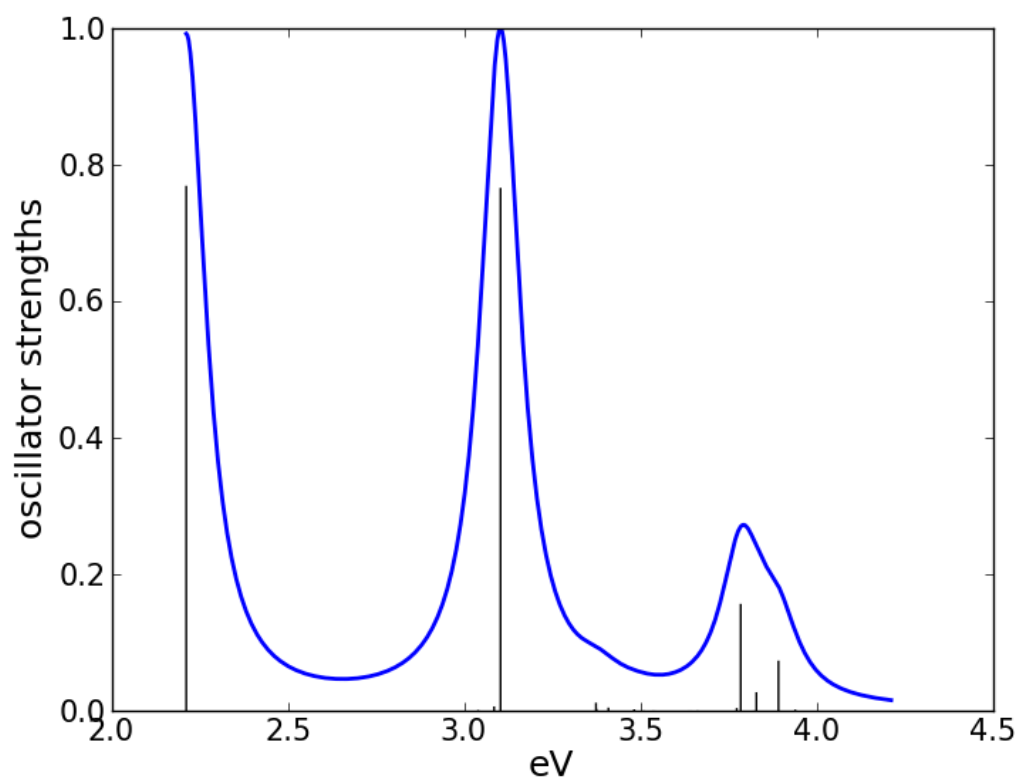
Photodynamics calculations were run with and without the long-range correction. The results *without* the long-range correction showed a CT excitation much too quickly (as will be briefly discussed at the end of this section) compared to the expectation of roughly 100 fs based upon experimental results. For this reason, we concentrate on the results with long-range correction. These results are divided into four subsections. The first subsection describes the assignment of absorption spectra obtained from a single ground-state optimized geometry. The next subsection explains how the initial excited states were prepared in our photodynamics simulation and classifies the resultant states. This is followed by a discussion of exciton energy transfer (EET) which is seen on a relatively short time scale and then by a subsection discussing CT which is seen on a longer time scale, comparable to what is expected based upon experimental results. A final subsection comments on the CT times that we see when the same simulation is done without any long-range correction.

7.4.1 Assignment of Absorption Spectra

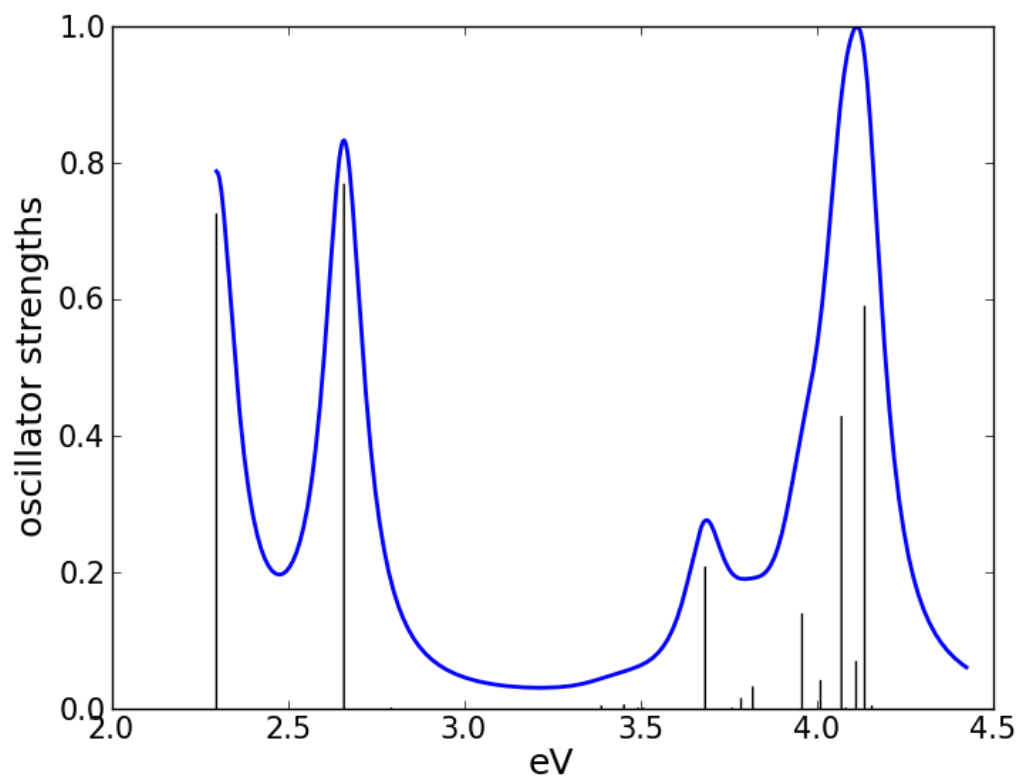
Replacing a first-principles method such as TD-DFT with a semi-empirical approximation implies a trade-off between accuracy and computational efficiency. We look at calculated absorption spectra in this section in order to obtain a better understanding of the implications of this trade-off.

The initial model geometry has been used to calculate the absorption spectrum of thirty excited states by using both the TD-lc-DFTB and TD-CAM-B3LYP/6-31G(d,p) methods. The resultant spectra are shown in Fig. 7.3. At first glance, the TD-lc-DFTB and TD-CAM-B3LYP/6-31G(d,p) spectra may seem very different. However the peaks do lie between 2.2 and 4.1 eV in both cases, both have significant absorption between 3.3 and 4.2 eV and two intense peaks between 2.1 and 3.3 eV.

Figure 7.4 shows the MO analysis of the 4 most intense peaks in the TD-CAM-B3LYP absorption spectra. Note the remarkable qualitative similarity of the lc-DFTB and CAM-B3LYP hole and particle MOs. The exception is the second major peak in the TD-CAM-B3LYP spectrum at 2.66 eV with oscillator strength $f = 0.0495$. Here we could not find a corresponding TD-lc-DFT peak based upon the MO analysis. Instead we compared against the energetically closest TD-lc-DFT peak which lies at 3.03 eV and has a very small oscillator strength of $f = 0.0000001$. The 2.66 eV TD-CAM-B3LYP is a $\text{Pent} \rightarrow \text{C}_{60}$ CT excitation, while the 3.03 eV TD-lc-DFT peak is a local excitation on Pent. Other than this peak mismatch, the two spectra are in good qualitative agreement. Note that the replacement of



TD-lc-DFTB



TD-CAM-B3LYP/6-31G(d,p)

Figure 7.3 – Calculated absorption spectra using lc methods.

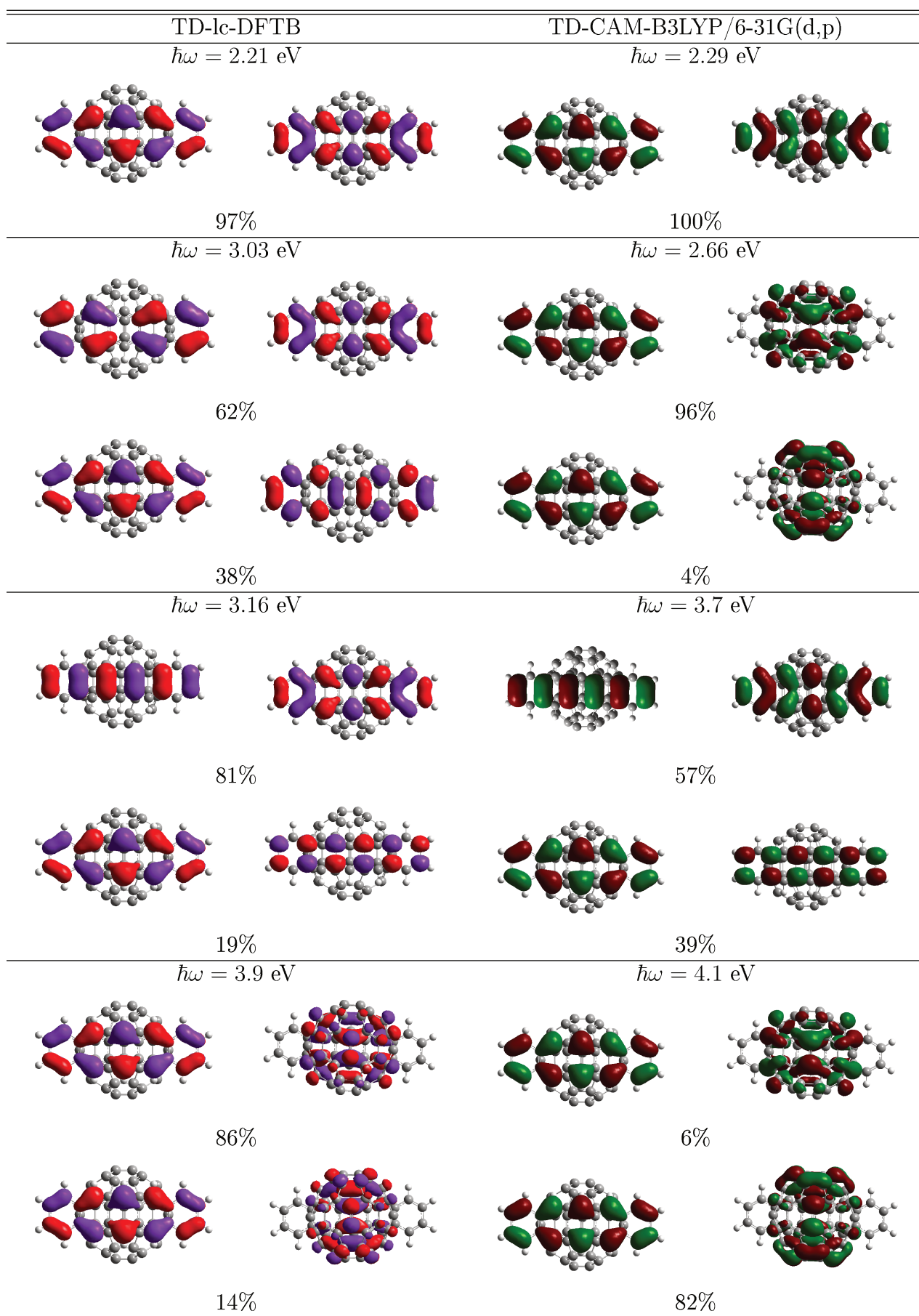


Figure 7.4 – Dominant particle \rightarrow hole contributions and excitation energies showing the correspondence between the most intense TD-CAM-B3LYP/6-31G(d,p) absorption peak and the corresponding TD-lc-DFTB absorption peak.

Excitation Energies (eV)		
Method	Pent	CT
Present Work		
TD-CAM-B3LYP	2.29/3.7	2.66/4.1
TD-lc-DFTB	2.21/3.03/3.16	3.9
Ref. [36]		
TD-LC-BLYP	2.55	3.33
TD-LC- ω PBE	2.52	3.36
TD- ω B97X	2.44	3.16
TD- ω B97XD	2.31	2.48
TD-OPT-LC-BLYP	2.22	2.33
TD-OPT-LC- ω PBE	2.23	2.25
TD-OPT- ω B97X	2.23	2.30
TD-OPT- ω B97XD	2.24	2.31

Table 7.2 – Comparison of the excitation energies of the present work with those of Model 1 in given in Table 3 of Ref. [36].

quantitative agreement with a more qualitative picture is, of course, the “price” we pay for using a semi-empirical method. However, it should be emphasized that the type of dynamics calculations reported here for molecules of this size and on this time scale are extremely difficult to do without making approximations.

As our model is essentially the same as Model 1 in Ref. [36], we have compared our excitation energies with those reported in that article. Our results appear to us to be in good agreement with those obtained with lc functionals in Ref. [36] — certainly well within the variations observed for excitations obtained with different lc functionals.

7.4.2 Initial Excited States

Having discussed the (static vertical) absorption spectrum, we now proceed to describe our photodynamics calculation and what results it gave. We ran thirty TD-lc-DFTB FSSH trajectories (numbered Traj 1, Traj 2, ..., Traj 30) whose initial states were obtained by exciting from an ensemble of molecules with different geometries equilibrated at 300 K to the singlet excited state with the highest oscillator strength *at that geometry*. This led to an initial ensemble of states which will be described in this subsection.

The energetic gap between the first several singlet excited states is much smaller than that between the ground state (S_0) and the first excited singlet state (S_1). For this reason, it is perhaps not surprising that only 36.7% of the Trajs began from

S_1 . Moreover only an additional 16.7% of the initial states are accounted for by the next four states ($S_2 - S_5$), leaving 46.6% of the initial states in still higher states. Note however that the ordering of these energetically dense states is sensitive to the geometry of the molecules which is different for the initial states of different Trajs.

Some programs, such as NEWTON-X [141, 110] have special routines (CALCDEN and THEODORE in the case of NEWTON-X) which allow the automatic assignment of state character [143, 144, 145, 146]. DFTBABY is less advanced in this respect, but is more advanced in its implementation of the lc-DFTB needed for the present study. In the present case, the physical nature of the initial states was determined by direct visualisation of the MOs involved in each excitation. An example of this analysis is shown in Fig. 7.5. Two types of excited states were found. Excitations localized on Pent are designated as P-type while those excited states which are delocalized over both Pent and C_{60} are designated as DL. Of course, there is an element of subjectivity in this analysis. However no amount of automation seems likely to be able to totally eliminate the fuzzy boundary between what is a localized and what is a delocalized excitation. In practice, we found it fairly clear how to label the states. For example, although Traj 18 is partly of $P \rightarrow DL$ character, it is clear that the dominant contribution is of P-type (i.e., $P \rightarrow P$ character.)

In total, there were 16 initial excited states of P-type and 14 initial excited states of DL-type. To some extent, these two types of excitations are associated with particular orbitals. For example, all but three of the P-type initial states are dominated by the $^1(H, L)$ transition. The exceptions are Traj 18 which is still about 33% $^1(H, L)$ and Trajs 4 and 6 which are predominantly $^1(H, L + 1)$. However caution should be taken when basing assignments on orbital ordering as this can change when the molecules are deformed from one geometry to another. All of the 14 DL-type initial states are dominated by the $^1(H, L + 3)$ transition.

7.4.3 Exciton Energy Transfer Dynamics

The 30 initial excited states were propagated for 500 fs. To do this, it is necessary to specify for how many other excited states surface hopping will be allowed. In general this number was varied from 10 (if the initial state was low in energy) to 17 (if the initial state was higher in energy.) It is also necessary to use multiple criteria when analysing the character of the electronic states during the photodynamics simulations. We have mainly followed three properties of the active state over time, namely (i) the transition dipole moment (TDM), (ii) the oscillator strength f , and (iii) the degree of spatial overlap between occupied and virtual orbitals as measured by Λ . Note that two of these properties are closely related (but not proportional)

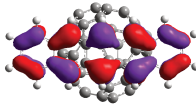
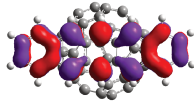
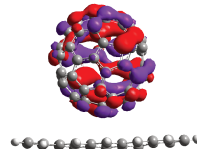
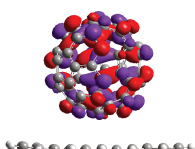
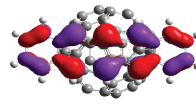
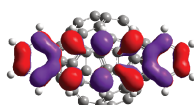
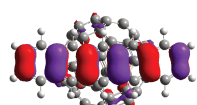
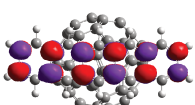
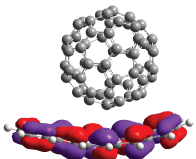
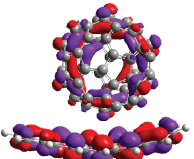
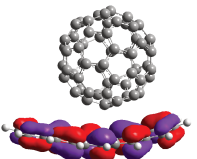
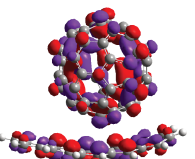
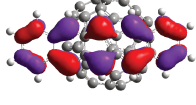
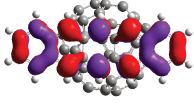
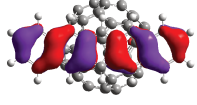
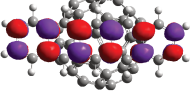
Major Component		Minor Component	
Traj 1			
			
86.6% HOMO \rightarrow LUMO+3		13.4% HOMO-5 \rightarrow LUMO+4	
Traj 2			
			
97% HOMO \rightarrow LUMO		3% HOMO-8 \rightarrow LUMO+8	
Traj 18			
			
67.1% HOMO \rightarrow LUMO+2		3% HOMO \rightarrow LUMO	
Traj 6			
			
96.5% HOMO \rightarrow LUMO+1		3.5% HOMO-7 \rightarrow LUMO+8	

Figure 7.5 – Assignment of the physical character of the initial excitation of several trajectories based upon the two most important MO contributions to the singlet excitation: Traj 1, DL-type; Traj 2, P-type; Traj 18, P-type; Traj 6, P-type.

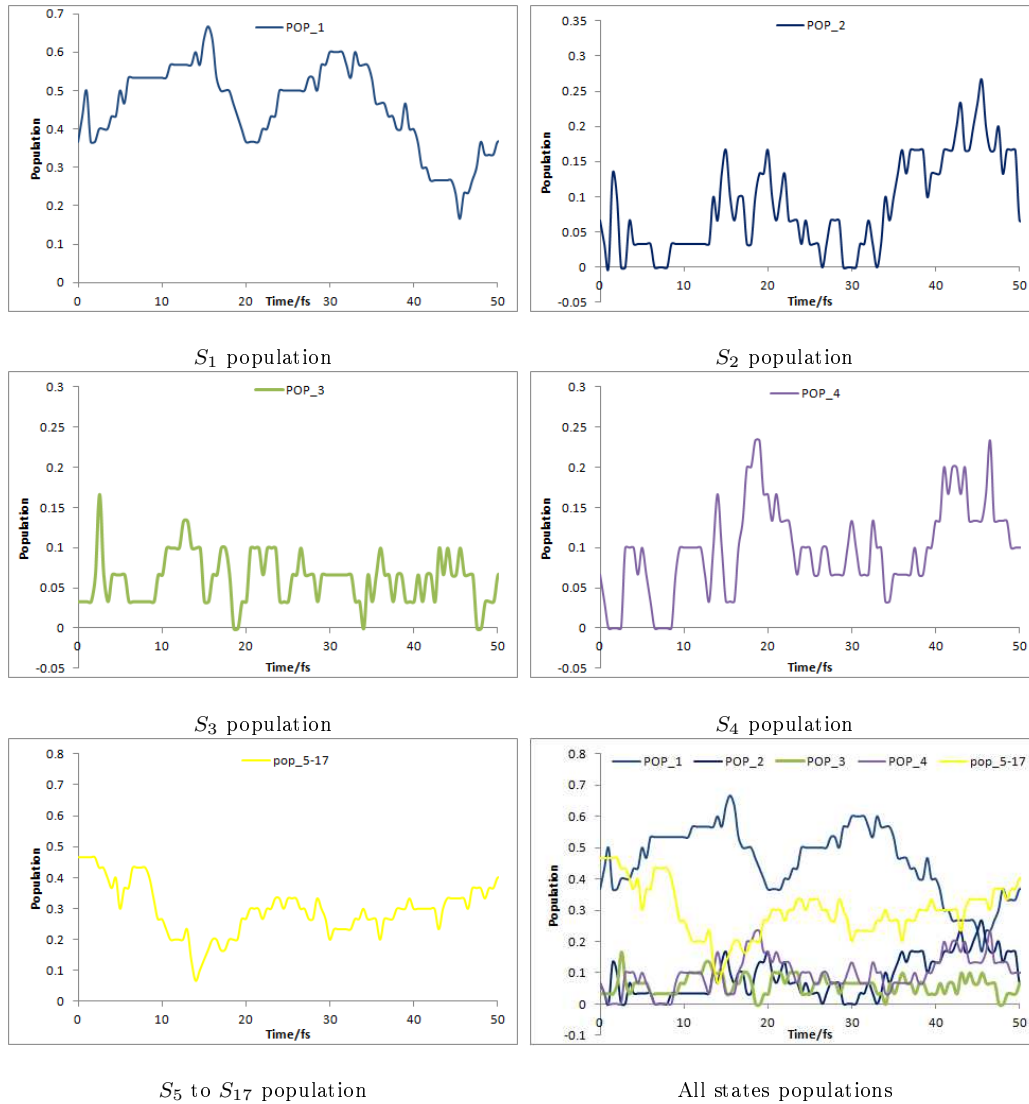


Figure 7.6 – Variation of state populations during the first 50 fs of the simulation.

because the oscillator strength f_I for a transition with excitation energy ω_I is related to the TDM

$$\mu_{I \leftarrow 0} = |\langle \Psi_I | \vec{r} | \Psi_0 \rangle|, \quad (7.58)$$

by

$$f_I = \frac{2}{3} \omega_I \mu_{I \leftarrow 0}^2. \quad (7.59)$$

In addition this was accompanied by looking at (iv) the molecular orbital contributions to the active excited state and (v) visualization of the particle-hole charge distribution or (vi) particle-hole charge density difference. As noted above, the MO contributions can be misleading because the ordering of the MOs may change during the simulation. However this was only one of several criteria examined.

We found that exciton energy transfer (EET) happens very quickly. So our discussion of EET focuses on what happens on the a short-time scale, on the order of 50 fs or less. As shown in Fig. 7.6, S_1 and S_4 dominate during the first 50 fs, but other excited states are present. This is because the manifold of singlet excited states is quite dense compared to their energetic separation from the ground state.

MO analysis of the 30 trajectories (Supplementary Information) shows that all but one of the P-type initial-state trajectories follow the pathway $P \rightarrow P \rightarrow C_{60}$. (The exception follows the pathway $P \rightarrow DL \rightarrow C_{60}$.) All but one of the DL-type initial state trajectories follows the $DL \rightarrow C_{60} \rightarrow P$ pathway. (The exception follows the pathway $DL \rightarrow P \rightarrow C_{60}$.)

The results are shown for some initial P-type trajectories in Fig. 7.7. It is immediately obvious that something dramatic is happening at around 20 fs because there is a dramatic fall in oscillator strength and in the related quantity, the TDM. The effect is somewhat less dramatic for Λ but is also present. The hole-particle charge analysis (Supplementary Information) shows that the excitation is moving from a P-type excitation to become a C_{60} -type excitation. The results are shown for some initial DL-type trajectories in Fig. 7.8. The situation is less dramatic here, but something is clearly happening 10-20 fs into each run as all three properties move up to a maximum. The particle-hole analysis (Supplementary Information) show that a localization procedure is taking place followed by movement of the localized excitation from one molecule to another. While these results may at first seem puzzling, they are in fact consistent with the well-known process of energy transfer. The natural direction is from the donor (D) to the (A) acceptor,

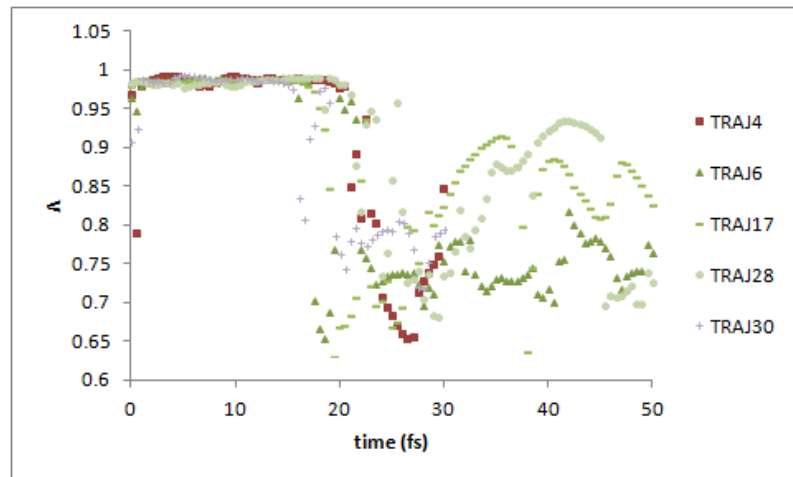


Such an energy transfer has been explained via electron exchange (i.e., Dexter's mechanism) or via a coulombic mechanism [i.e., Förster resonance energy transfer (FRET) [147]]. But, because the system is finite, recurrances will occur, so we also see the excitation being passed back again,

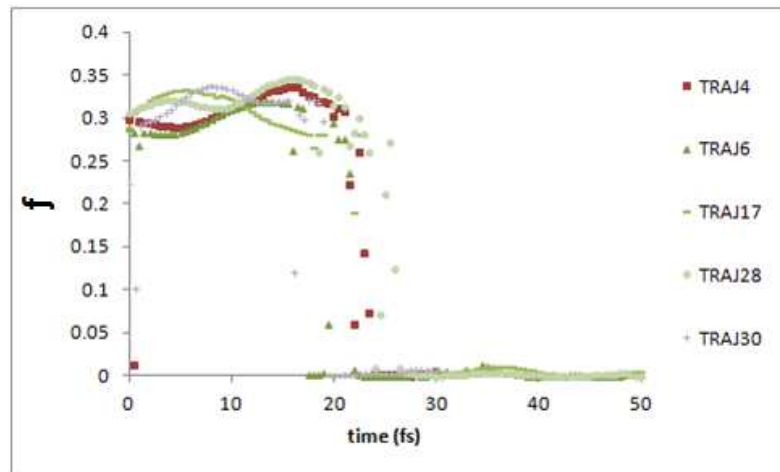


Let us try to summarize the main conclusion of this subsection: We are seeing excitonic energy transfer on a very short time scale: 17 ± 11 fs for P-type initial-state Trajs and 13 ± 5 fs for DL-type initial-state Trajs. Such a time is too short for the nuclei to move very much. Nevertheless, some change in molecular geometry is apparent as the pentacene forms a crescent shape around C_{60} (Supplementary

(a)



(b)



(c)

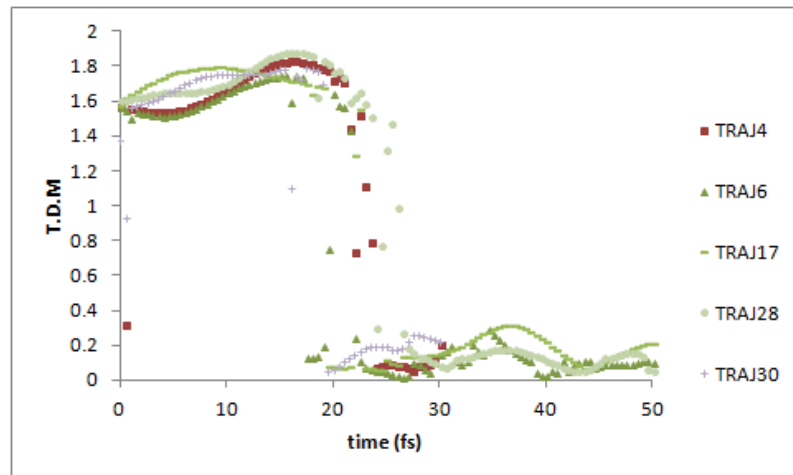
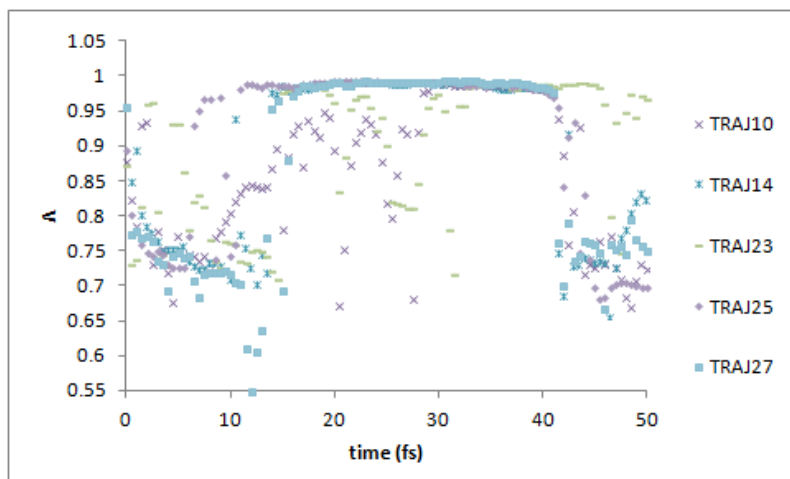
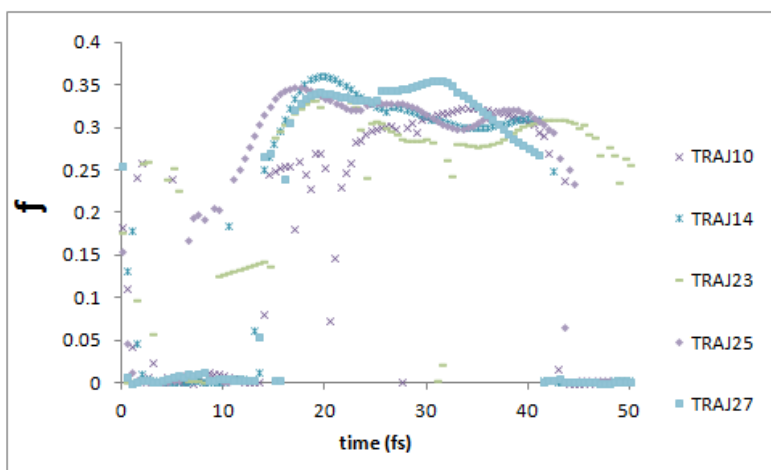


Figure 7.7 – Temporal variation of properties for the active state of five initially P-type trajectories (trajectory numbers 4, 6, 17, 28, and 30): (a) Λ , (b) oscillator strength, and (c) transition dipole moment.

(a)



(b)



(c)

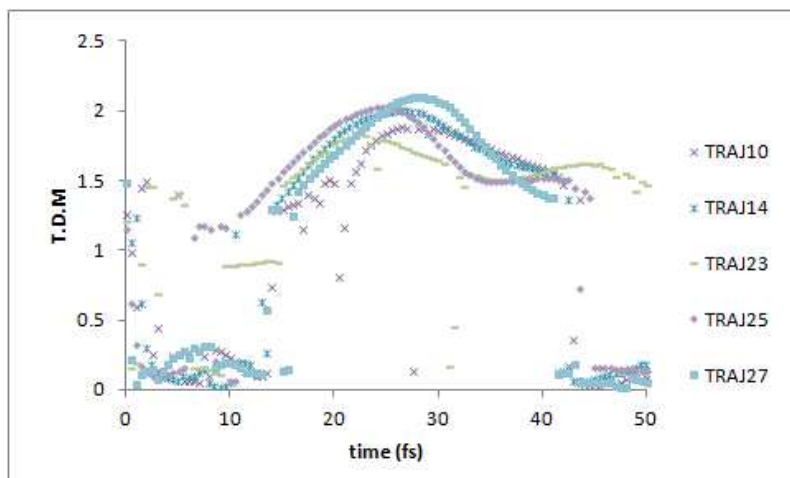


Figure 7.8 – Temporal variation of properties for the active state of five initially DL-type trajectories (trajectory numbers 10, 14, 23, 25, and 27): (a) Λ , (b) oscillator strength, and (c) transition dipole moment.

Information.) Such a shape enhances the van der Waals bonding between the two fragments, thereby making exciton energy transfer easier than it might otherwise have been.

7.4.4 Charge Transfer Dynamics

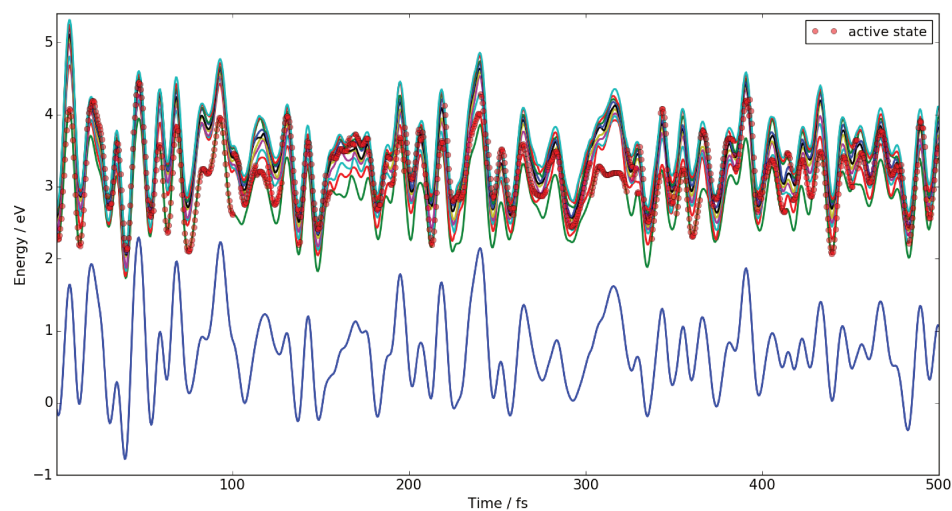
At the heart of the modern OPVs is charge separation at the heterointerface. This is something we see in six out of 30 of Trajs at 188 ± 28 fs. Of these Trajs, two had P-type initially-excited states and the other four had DL-type initially-excited states. As we shall illustrate by taking an in-depth look at two typical Trajs, it is only by carefully examining images of particle-hole charge distributions that we were able to establish what value of Λ is low enough to indicate CT. We have chosen to discuss the charge separation process in detail by focusing on Traj 6 which is an initially P-type excited state and on Traj 27 which is an initially DL-type excited state.

7.4.4.1 Traj 6: Example of a P-type initial state

Figure 7.9 shows the evolution of the active state in time for Traj 6 as it hops from one state to another. It is clear that the excited states form a close-packed manifold well-separated from the ground state. This leads to a high probability of surface hopping as is confirmed in Fig. 7.10. Now let us follow in detail what is happening for the active state along its trajectory. Figure 7.11 shows the particle and hole MOs involved in the excited state and 7.12 shows the particle-hole charge density difference for several snapshots of the active state. The initial state is S_4 , a P-type state, consisting mainly of $H \rightarrow L+1$ (96.5%) with a little bit of $H-7 \rightarrow L+8$ (3.5%). At the time of this hopping from the S_1 state, the active state becomes a linear combination of two transitions (86.3% $H \rightarrow L$ + 13.7% $H-1 \rightarrow L+1$). All the particle and hole MOs of these transitions are located mainly on the pentacene.

At 17.5 fs, there is a sudden change in properties (Fig. 7.13). The active state has become S_8 which is a C_{60} -type state [(2) in Fig. 7.12]. The MO analysis of the active state shows a major (88.7%) $H-1 \rightarrow L+2$ component and a minor (11.3%) $H-2 \rightarrow L+3$ component. All these MOs are localized on C_{60} . Hence the 17.5 fs transition is the first exciton energy transfer. Values of Λ , TDM, and Osc are high for P-type excitations. For C_{60} -type excitations, Λ falls considerably and values of both the TDM and Osc fall nearly to zero. These values (Fig. 7.13) are initially high, drop at 17.5 fs, and then rise again at 20 fs. They subsequently drop at 22 fs and remain low until 56 fs before they rise up again. They remain high for another 13 fs, and then drop again at 69 fs, indicating that the active state has changed its nature.

(a)



(b)

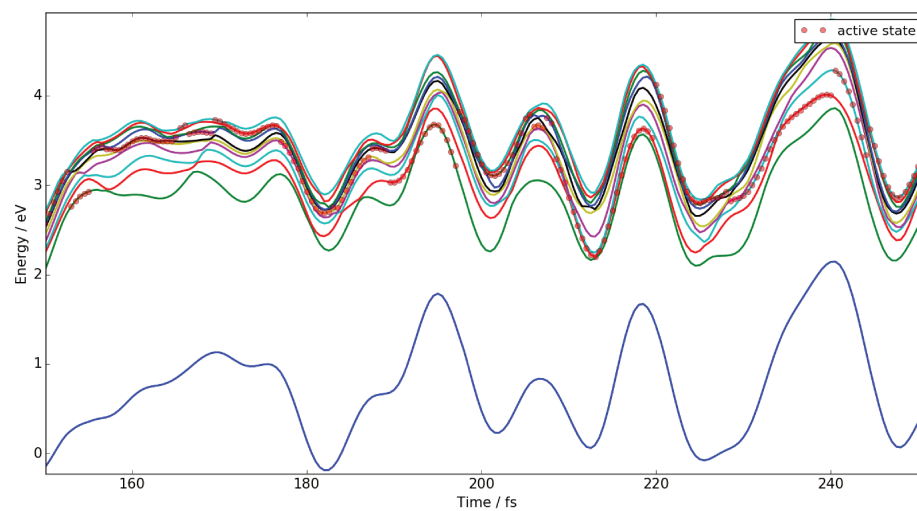


Figure 7.9 – Traj 6: Ground and excited state energies as a function of time: (a) first 500 fs, (b) zoom to 150-250 fs. The active state is marked by red bullets.

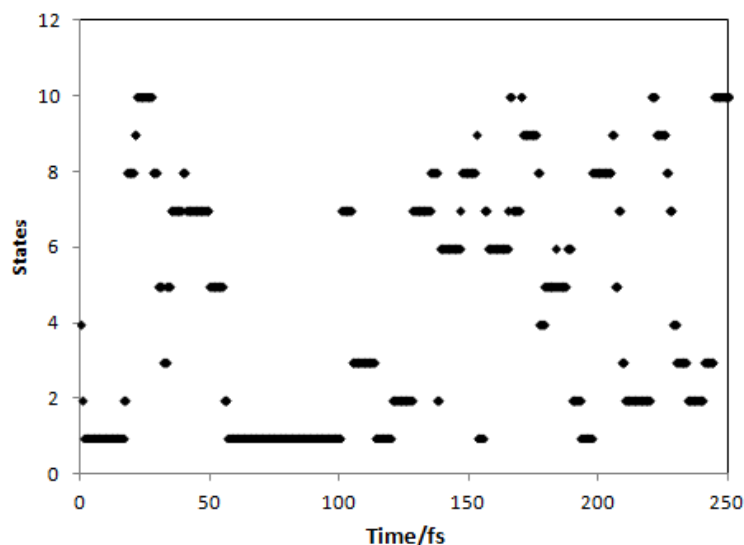


Figure 7.10 – Traj. 6: Surface hopping during the first 250 fs of the trajectory.

These oscillations are very tricky to analyze as they occur for both exciton energy transfer and for charge transfer. However the MO analysis (Fig. 7.11) and particle-hole charge density difference (Fig. 7.12) indicates that the active state changes its nature at 20 fs from local on C_{60} to local on pentacene and then, 2 fs later, local on C_{60} . At 56 fs, the active state is once again a local excitation on pentacene. This exciton energy transfer continues up to 69 fs and beyond — up to 157 fs.

At 157.5 fs, there is a dramatic change in the nature of the excited state from a C_{60} -type state to a charge transfer state with a hole on the C_{60} and an extra electron on pentacene [(8) in Fig. 7.11 and (8) in Fig. 7.12]. This qualitatively different change is *not* visible in the f or in the TDM graphs, and it is only visible in the Λ graph as a particularly low value of Λ (i.e., ≤ 0.5). The MO analysis shows a major H-6 \rightarrow L component (67.4%) with a minor H-3 \rightarrow L component (32.6%). Both the major and minor components show particles and holes located on different fragments, thus confirming the charge-transfer nature of the 157.5 fs active state. Interestingly the charge transfer is happening from C_{60} to pentacene, which is not the intuitively expected direction. However there is sufficient energy for this to happen in our finite system and the charge separation only lasts about 1.5 fs before becoming localized once again on C_{60} [(10) of Fig. 7.11 and (10) of Fig. 7.12].

At 210 fs, the hole and particle become delocalized over both molecules and this leads to another charge-transfer state at 221 fs, this time with the hole on the pentacene and an extra electron on C_{60} . This is confirmed by examination of the MOs involved in the H \rightarrow L+1 (57.9%) excitation and in the particle-hole charge

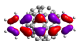
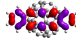
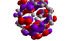
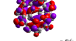


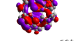
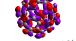

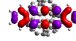
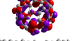
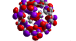
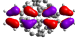
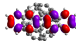
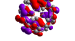
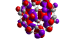

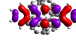
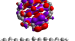
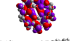
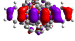
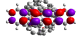
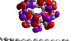
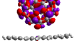
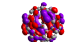
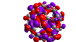
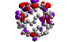
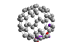
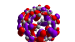
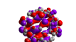
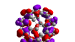

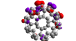
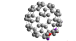
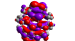
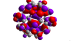

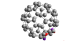

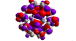
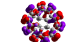
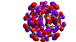
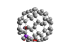
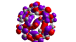
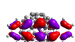
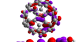
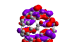
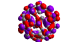
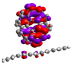
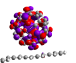
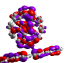
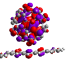
Major Component	Minor Component	Major Component	Minor Component
1) 0 fs, S_4		2) 17.5 fs, S_8	
			
			
96.5% H \rightarrow L+1	3.5% H-7 \rightarrow L+8	88.7% H-1 \rightarrow L+2	11.3% H-2 \rightarrow L+3
3) 20 fs, S_8		4) 22 fs, S_{10}	
			
			
98.4% H \rightarrow L+3	1.6% H-6 \rightarrow L+7	58.4% H-1 \rightarrow L+4	41.6% H-4 \rightarrow L+1
5) 56 fs, S_2		6) 69 fs, S_1	
			
			
96.7% H \rightarrow L	3.3% H-8 \rightarrow L+8	73.2% H-1 \rightarrow L+1	26.8% H-2 \rightarrow L+2
7) 157 fs, S_5		8) 157.5 fs, S_6	
			
			
73% H-1 \rightarrow L+2	27% H-4 \rightarrow L+1	67.4% H-6 \rightarrow L	32.6% H-3 \rightarrow L
9) 158.5 fs, S_6		10) 166.5 fs, S_{10}	
			
			
73.5% H-6 \rightarrow L	25.6% H-3 \rightarrow L	62.9% H-1 \rightarrow L+3	37.1% H-3 \rightarrow L+3
11) 210 fs, S_2		12) 221 fs, S_{10}	
			
			
52.4% H -2 \rightarrow L+2	47.6% H \rightarrow L	57.9% H \rightarrow L+1	42.1% H-1 \rightarrow L+6
13) 222 fs, S_9			
			
71% H-1 \rightarrow L+4		29% H-8 \rightarrow L+1	

Figure 7.11 – Traj. 6: Snapshots of the principle particle and hole MOs characterizing the active state.

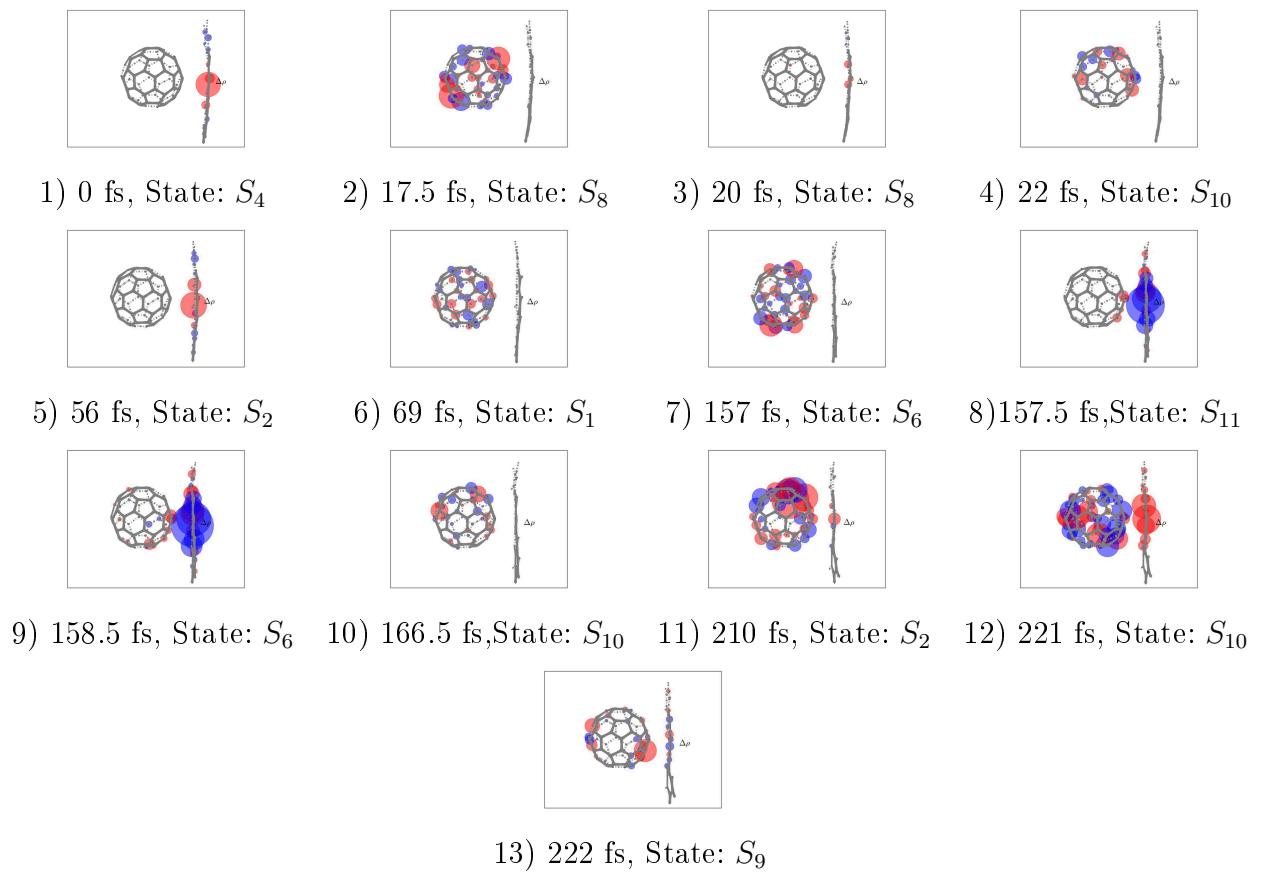
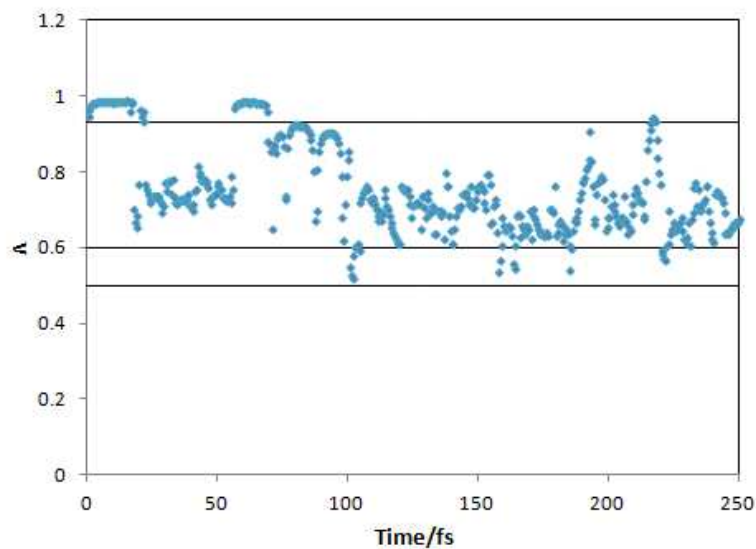
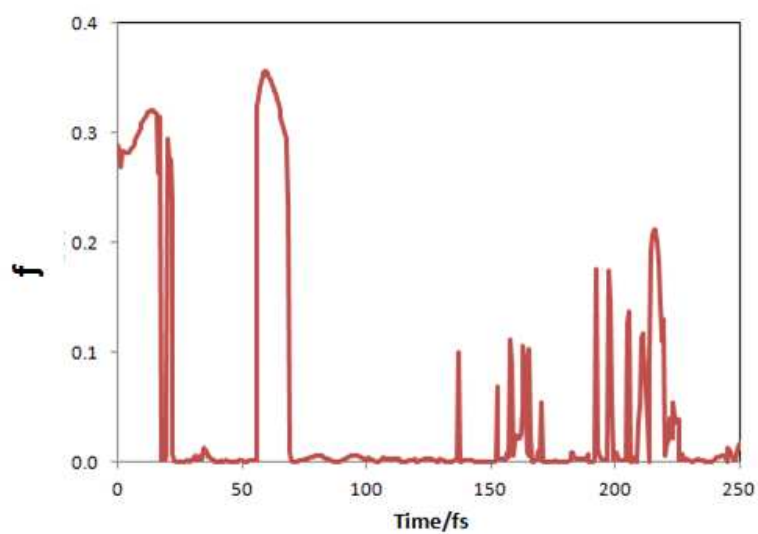


Figure 7.12 – Traj. 6: Snapshots of the particle-hole charge density difference for the active state.

(a)



(b)



(c)

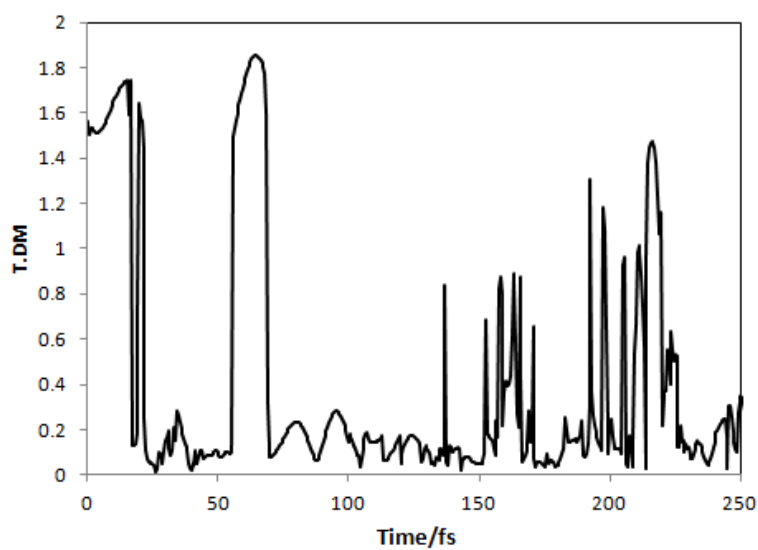


Figure 7.13 – Evolution of some properties of the Traj. 6 active state: (a) Λ , (b) oscillator strength, and (c) transition dipole moment.

density difference for the active S_{10} state. Once again, the this charge transfer state is transitory and after only 1 fs it has become a local excitation on C_{60} . There is no particular reason for charge transfer to be permanent in such a small system.

7.4.4.2 Traj 27: Example of a DL-type initial state

We carry out a similar analysis to that for the initially P-type Traj. 6, but this time for the initially DL-type Traj 27. Figures 7.14 and 7.15 show the evolution of the active state. It generally stays among the lower energy singlet excited states—especially S_1 and S_2 —but does not remain exclusively in these states.

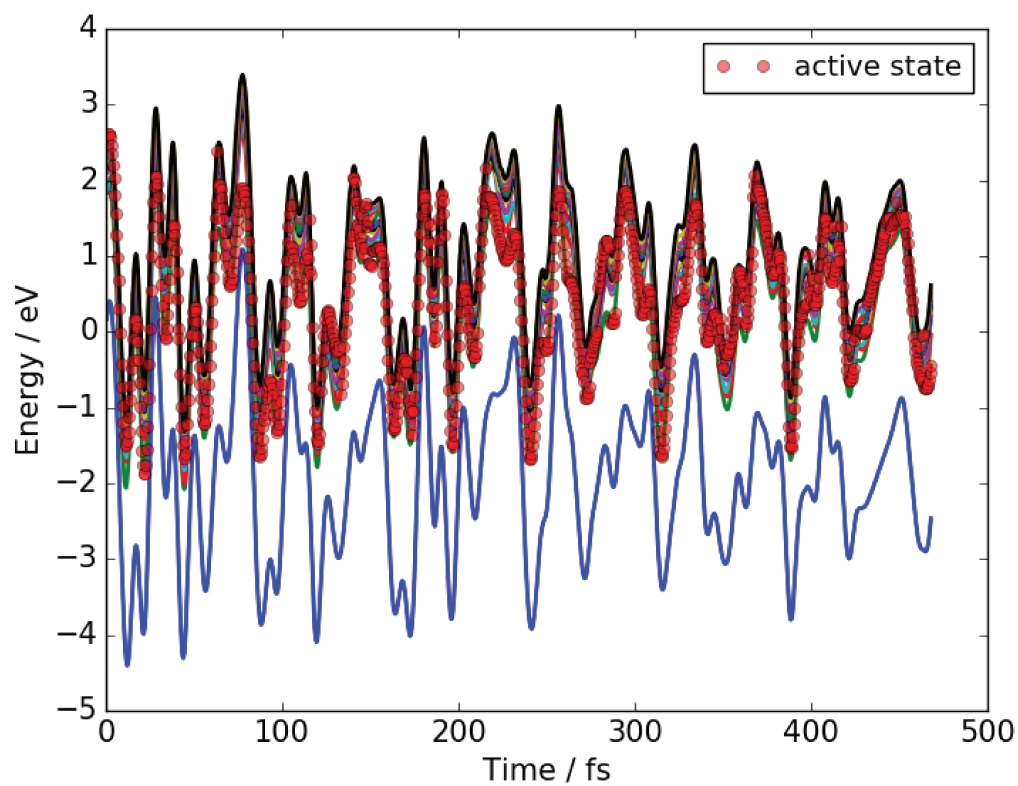
Now let us follow in detail what is happening for the active state along its trajectory. Figures 7.16 and 7.17 show the particle and hole molecular orbitals (MOs) involved in and the particle-hole charge density difference for several snapshots of the active state. The initial state is S_{13} , a DL-type state which passes to S_{12} after 3 fs, returns to S_{11} for 1.5 fs more, then hops to S_9 for 1 fs before hopping to S_6 for 5.5 fs, and then passes through S_3 and S_4 , staying on each for about 0.5 fs, until finally relaxing to the lowest excited state S_1 after 15 fs.

Figure 7.18 shows the same sort of oscillations that we have seen in the case of Traj 6. Indeed the MO analysis of the active state shown in Fig. 7.16 indicates that we are once more seeing excitonic energy sloshing back and forth between pentacene and C_{60} , with the first exciton energy transfer happening at 16 fs. This process continues without the development of significant charge transfer until 127.5 fs, when the Λ value falls below 0.5, which appears to us to be a critical value for intermolecular charge transfer. This is an important point: Higher values of Λ such as $\Lambda = 0.6$ generally also indicate charge transfer but only intramolecular charge transfer within one or the other molecule. To have intermolecular charge transfer, Λ must fall lower still and the value that we have found to correlate with intermolecular transfer is $\Lambda \leq 0.5$. Figures 7.16 and 7.17 indicate that true intermolecular charge transfer is indeed happening at 127.5 fs. Once again, this intermolecular charge transfer is only short lived but is expected to reoccur were we to run the simulation for long enough.

7.4.4.3 Summary of all six CT times

Figure 7.19 provides a summary in terms of charge density difference maps of what CT looks like for the six trajectories where it was observed. We note that the CT may take place either from Pent to C_{60} or from C_{60} to Pent, but that, whichever the direction of CT, the opposite CT will take place in the opposite direction for this finite system. The Fig.7.19 shows that precisely this phenomenon has been observed

(a)



(b)

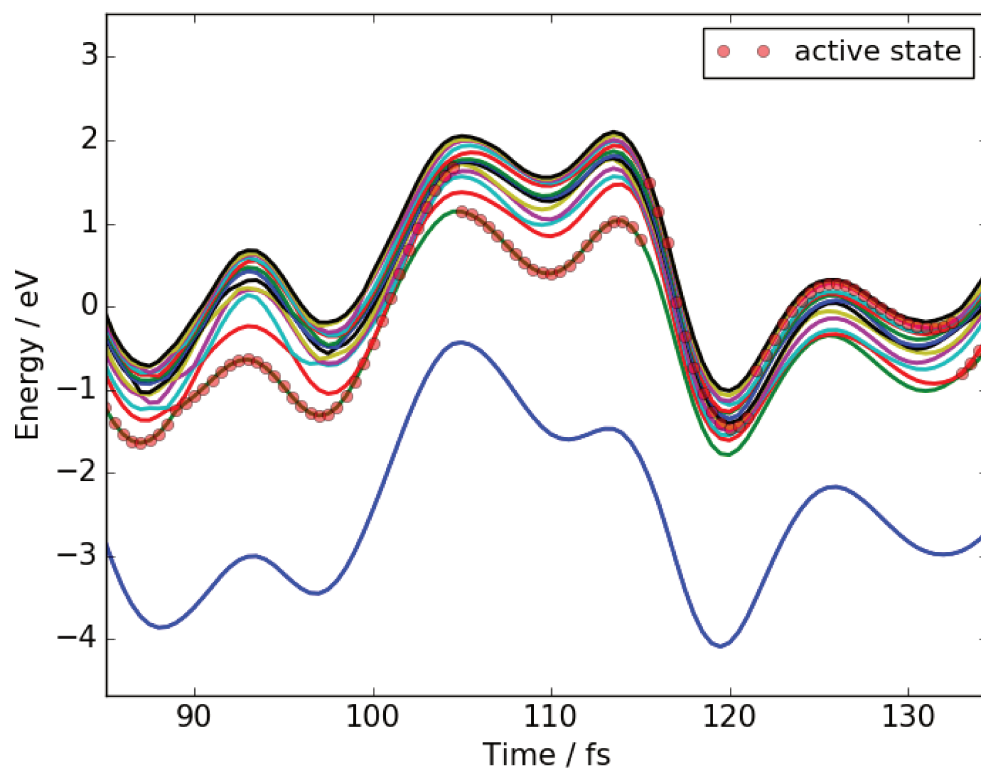


Figure 7.14 – Traj 27: Ground and excited state energies as a function of time: (a) first 500 fs, (b) zoom to 85-135 fs. The active state is marked by red bullets.

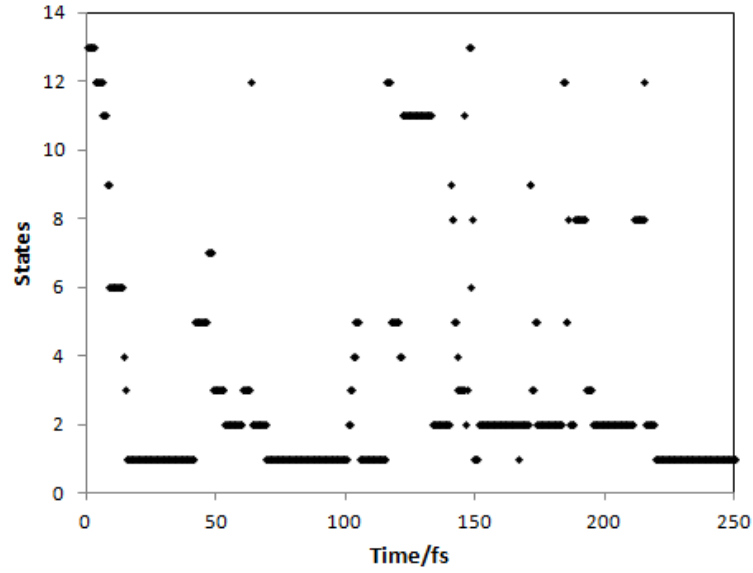


Figure 7.15 – Traj. 27: Surface hopping during the first 250 fs of the trajectory.


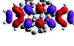
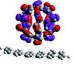
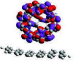
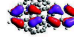
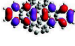
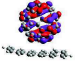
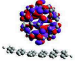
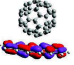
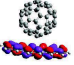
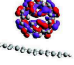
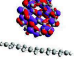
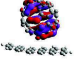
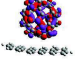
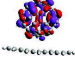
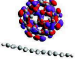
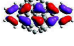
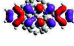
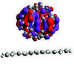
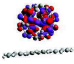
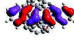
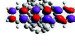
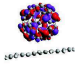
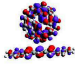
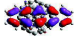
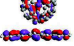
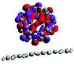
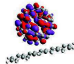
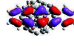
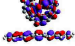
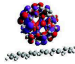
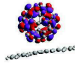
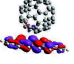
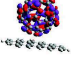
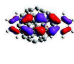
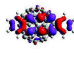
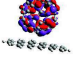
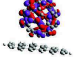
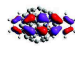
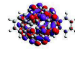
Major Component	Minor Component	Major Component	Minor Component
1) 0 fs, S_{13}		2) 0.5 fs, S_{13}	
			
			
97.9% $H \rightarrow L+3$	2.1% $H-6 \rightarrow L+7$	56.2% $H-4 \rightarrow L+5$	43.8% $H-1 \rightarrow L+6$
3) 16 fs, S_1		4) 41.5 fs, S_5	
			
			
89.4% $H \rightarrow L$	10.6% $H-1 \rightarrow L+1$	84.2% $H-3 \rightarrow L+1$	15.8% $H-4 \rightarrow L+1$
5) 89.5 fs, S_1		6) 105 fs, S_1	
			
			
96.3% $H \rightarrow L$	3.7% $H-6 \rightarrow L+8$	92% $H-1 \rightarrow L+1$	8% $H-2 \rightarrow L+1$
7) 118 fs, S_5		8) 122 fs, S_{11}	
			
			
63.8% $H \rightarrow L+1$	36.2% $H \rightarrow L+1$	74.2% $H-4 \rightarrow L+3$	28.8% $H-5 \rightarrow L+2$
9) 127.5 fs, S_{11}		10) 133 fs, S_2	
			
			
67.2% $H \rightarrow L+1$	32.8% $H-4 \rightarrow L+3$	90.7% $H \rightarrow L$	9.3% $H \rightarrow L+1$

Figure 7.16 – Traj. 27: Snapshots of the principle particle and hole MOs characterizing the active state.

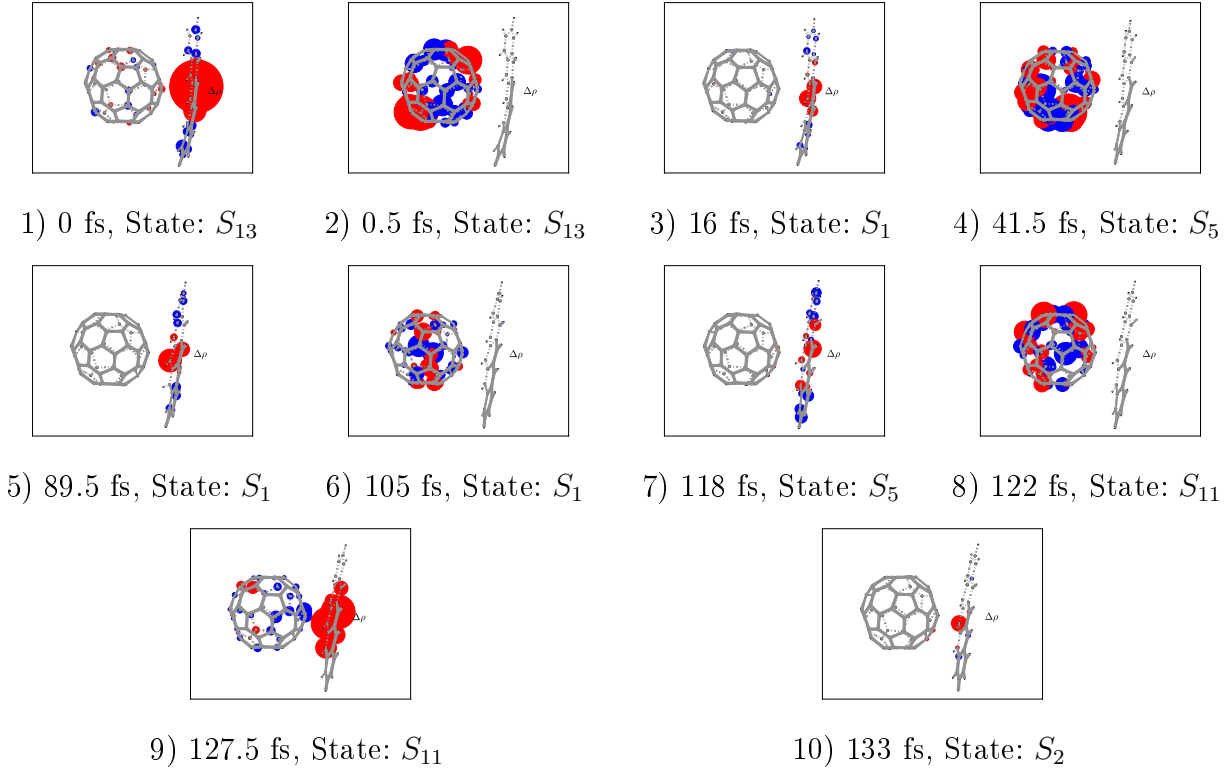


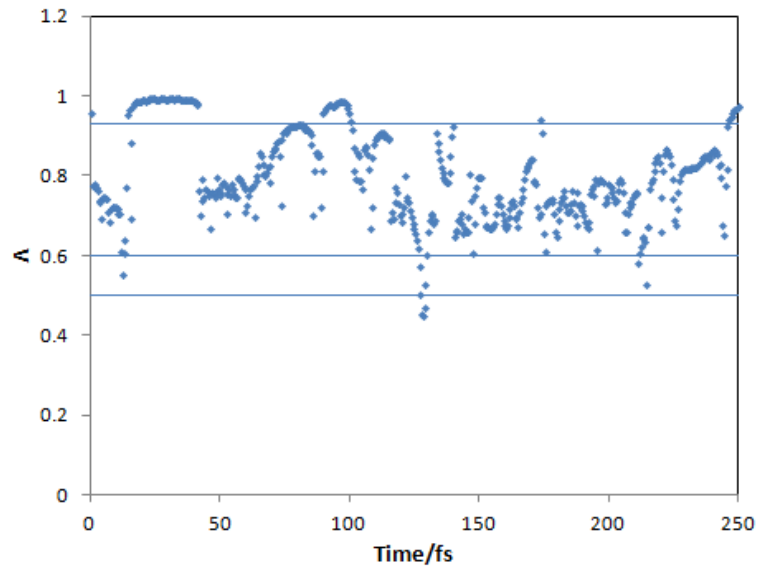
Figure 7.17 – Traj 27: Snapshots of the particle-hole charge density difference for the active state.

in our calculations for both Trajs 6 and 14. An especially important point is that our observation of a CT time of 188 ± 28 fs is commensurate with experimental observations of CT times at heterojunctions in OPV devices (i.e., 200 fs for APFO3/PCBM [13], 70-100 fs for pentacene/ C_{60} [14], ≤ 100 fs for MDMO-PPV/ $PC_{70}BM$ and for PCPDTBT/ $PC_{70}BM$ [15], and 82 fs for p-DTS(FBTTh₂)₂/ $PC_{71}BM$ [16].)

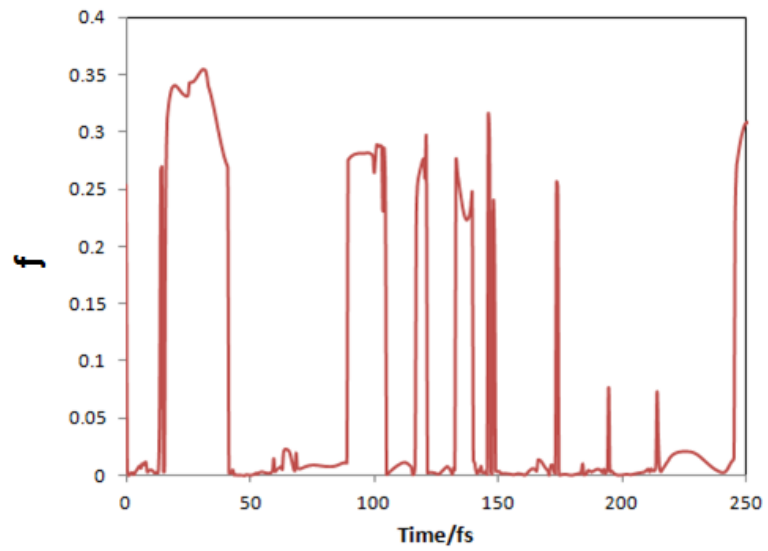
7.4.5 Charge Transfer Dynamics without Long-Range Correction

As we had also done the same type of TD-DFTB FSSH calculations with DFT-BABY *without any long-range correction*, we can see the importance of the lc. Details are reported in the Supplementary Information. All 30 Trajs show at least one CT and we have found two CTs in most cases. The first CT occurs extremely quickly at 3 ± 3 fs. The second CT takes place at 16 ± 11 fs. Obviously neither of these is commensurate with the experimental observations of CT times at OPV heterojunctions cited above. This confirms the importance of including a lc when calculating CT times.

(a)



(b)



(c)

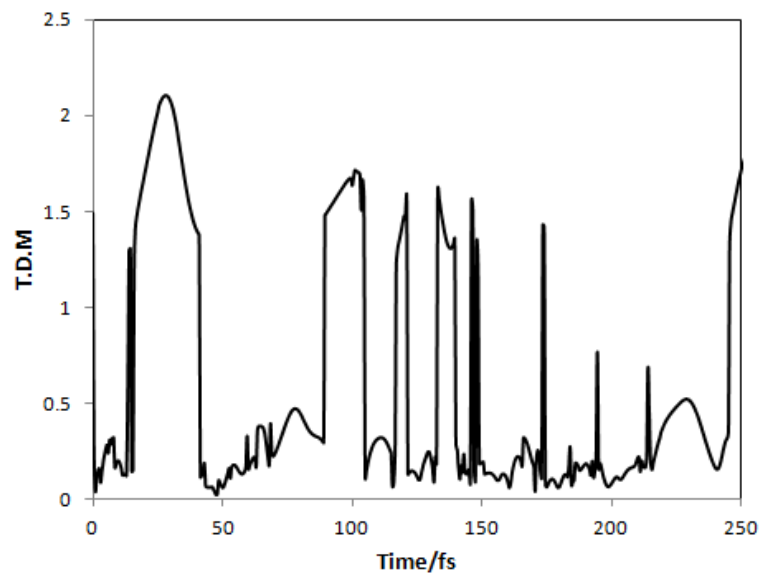


Figure 7.18 – Evolution of some properties of the Traj 27 active state: (a) Λ , (b) oscillator strength, and (c) transition dipole moment.

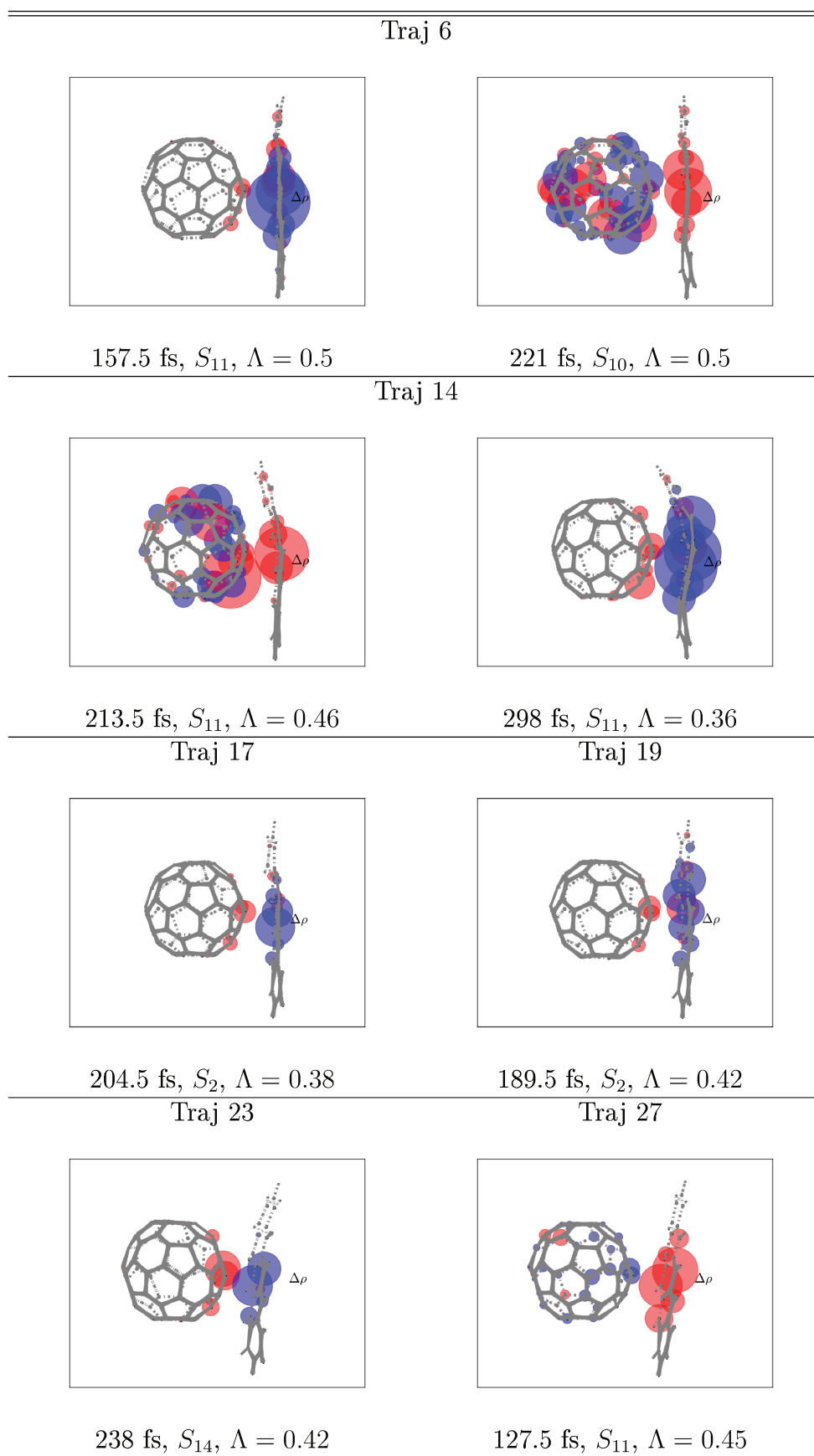


Figure 7.19 – Charge density difference maps and CT times for the six trajectories where CT was observed.

7.5 Conclusion

We have carried out Tully-type mixed time-dependent long-range-corrected density-functional tight binding/classical trajectory surface hopping calculations on a van der Waals complex consisting of a single buckminsterfullerene (C_{60}) molecule together with a single pentacene ($C_{22}H_{14}$) molecule. Calculations for an ensemble of 30 trajectories were run for significantly more than 100 fs for this 96 atom system and were carefully analyzed to see what processes were happening on different time scales. Although several approximations have been made — including taking only two molecules into account in our dynamics, the use of the semi-empirical TD-lc-DFTB approach, and the use of Tully’s semi-classical approximation — there is a certain satisfaction that is obtained from being able to follow the photodynamical process in such detail. Excitations were made, not from a single geometry, but from a thermally-equilibrated ensemble of ground state geometries. The initial excited state lay anywhere within a bundle of closely-spaced states lying well above the ground state. Both nuclei and electrons were free to move, though the nuclei did not move very far in 100 fs. Nevertheless, pentacene was found to twist and to wrap itself around C_{60} , offering ample symmetry reduction to mix different excited states. Generally speaking, the molecules soon relaxed to the lowest excited states, but they did not generally remain in the lowest excited state. Nor was there time for the system to go all the way to the ground state and, indeed, the ground state was not our hoped-for objective anyway. Instead we expected to see charge separation and the production of some sort of precursor to a conducting state as befits a model for the heterojunction of an organic solar cell.

What we actually observed on a short time scale was a localized excited state on one molecule transforming into a localized excited state on another molecule and then going back again, with the first energy transfer occurring within less than about 20 fs. This is a known phenomenon though we have found that it is rarely mentioned in the organic solar cell literature. As the system is finite, recurrence are inevitable, so that the energy continues to go back and forth. However Fourier transforming various properties showed no particular periodicity in the sloshing back and forth of energy. The literature does talk about excimer trapping at the interface, which would prevent the exciton from departing very quickly from the interface. Our model van der Waals complex consisting of only one pentacene and one C_{60} is too small to conclude regarding the formation of an excimer, but the rapidity of the movement of energy from one molecule to the next raises the question of whether the geometry at the interface can relax fast enough to catch the exciton before it diffuses away from the interface or whether the energy is simply sloshing back and forth within

an excimer potential energy well?

A sudden change in oscillator strength was found to be a good indication of EET. The best criterion that we found for CT was when Λ fell below about 0.5.

Assuming the energy remains trapped at the interface, our calculations show that charge separation takes place after 188 ± 28 fs. This is quite encouraging in so far as this is the order of magnitude of the time-scale reported in the literature for charge separation at organic solar cell bulk heterojunction interfaces based upon experimental results. We also carried out calculations *without* the long-range correction and found significantly shorter CT times which are in no way consistent with experiment. *This emphasizes the importance of using a long-range corrected theory not just for calculating spectra but also in photodynamics simulations.* As our system is finite, CT also recurs. That is, the charges recombine so that they can separate again at some later time. Recombination could be prevented if the system were large enough to allow charge to diffuse away from the interface.

Shortly before submitting this article, we became aware of a recently published paper by Joseph, Ravva, and Bredas [148] reporting results of TD- ω B97XD FSSH calculations on the same system. Although the details of their simulation and their preparation of the initial ensemble of excited states is different from ours, we may hope that they would find similar CT times in their simulation with a long-range corrected functional as we did in our simulation using TD-lc-DFTB. This is confirmed by their reporting of a 25 fs CT time.

All of these points to the need for simulations on model systems composed of larger numbers of molecules and, eventually, varying the types of molecules. We believe that such future studies will be aided by the present study in so far as we have done the pioneering work applying state-of-the-art TD-lc-DFTB FSSH to fs CT dynamics. As TD-lc-DFTB FSSH has a better scaling than TD- ω B97XD FSSH, we may hope to be able to treat still larger systems in the future. At the same time, we are also fully aware of the need to explore other methods for preparing the ensemble of initial excited states and of the limitations of the analytic tools that we have used to characterize CT. While we believe our results to be improvable, we believe that they have already shown beyond any serious doubt the importance of including long-range corrections in studies of CT at OPV heterojunctions.

7.6 Acknowledgements

This work has been supported in part by the French National Research Agency (*Agence Nationale de la Recherche*, ANR) ORGAVOLT (ORGANic solar cell VOLT-

age) project ANR-12-MONU-0014-02. AMMD acknowledges a Franco-Iraqi PhD scholarship administered via the French agency *Campus France*. The authors wish to acknowledge the support from Grenoble Alps University's ICMG (*Institut de Chimie Moléculaire de Grenoble*) Chemistry Nanobio Platform PCECIC (*Plateau du Centre d'Expérimentation et de Calcul Intensif en Chimie*) on which this work has been performed. Pierre Girard is gratefully acknowledged for his help and support using this platform. The work in Singapore is supported in part by Society of Interdisciplinary Research (SOIRÉE). Mark E. Casida and Ala Aldin M. H. M. Darghouth would also like to acknowledge a useful trip to Würzburg funded by the German GRK 2112 Project "Biradicals," as well as useful discussions with Drs. Mathias Rapacioli and Hemanadhan Myneni. Ala Aldin M. H. M. Darghouth acknowledges having followed an advanced course taught by Prof. Mario Barbatti on "Theoretical Aspects of Organic Femtochemistry" together with a tutorial on the NEWTON-X program. We are grateful to Mario Barbatti for his extensive comments on an early version of this manuscript. A. H. and R. M. acknowledge the financial support within the ERC Consolidator Grant DYNAMO (Grant Nr. 646737).

Author Contributions

This project began when Bhaarathi Natarajan, a former Ph.D. student of Mark E. Casida, left Grenoble to do postdoctoral work with Haibin Su in Singapore using software from Roland Mitrić's lab. The project was continued from that small, but important, beginning first by Xi Zhu with Haibin Su in Singapore and then as part of the Ph.D. project of Ala Aldin M. H. M. Darghouth under the direction of Mark E. Casida in Grenoble. Major coding was done by Alexander Humeniuk and by Roland Mitrić in their TD-DFTB program. The bulk of the manuscript writing was done by Mark E. Casida and Ala Aldin M. H. M. Darghouth.

Conflicts of Interest

The authors declare no conflict of interest.

Supplemental

The supplemental information for this paper contains the following:

- Short-time analysis for the 16 states initially localized on pentacene.

- Short-time analysis for the 14 states initially delocalized over pentacene and buckminsterfullerene.
- CT analysis of TD-DFTB FSSH calculations.

Abbreviations

For the reader's convenience, we have collected together the abbreviations used in this chapter:

Λ Degree of spatial overlap between occupied and virtual orbitals

A Acceptor.

BS Band structure.

C₆₀ Buckminsterfullerene.

coul Coulomb.

CT Charge transfer.

D Donor.

DFA Density-functional approximation.

DFT Density-functional theory.

DFTB Density-functional tight binding.

DL Delocalized.

D_{KI} Nonadiabatic coupling.

E Energy.

EFISH Electric field-induced second harmonic.

erf Error function.

erfc Complementary error function.

ET Energy transfer.

ETT Exciton energy transfer.

FRET Förster resonance energy transfer.

FSSH Fewest switches surface hopping.

fs Femtoseconds.

f Oscillator strength.

GGA Generalized gradient approximation.

H Highest-occupied molecular orbital.

H- n n th level below the HOMO.

HOMO Highest-occupied molecular orbital.

HF Hartree-Fock.

L Lowest-unoccupied molecular orbital.

L+ n n th level above the LUMO.

LUMO Lowest-unoccupied molecular orbital.

HOMO Highest-occupied molecular orbital.

L Lowest-unoccupied molecular orbital.

L+ n n th level above the LUMO.

lc Long-range corrected.

lc-DFTB long-range corrected Density-functional tight binding.

lr Long range.

LUMO Lowest-unoccupied molecular orbital.

MO Molecular orbital.

ms Milliseconds.

ns Nanoseconds.

NTO Natural transition orbital.

OPV Organic photovoltaics.

P Pentacene.

Pent Pentacene.

ps Picoseconds.

rep Repulsion.

S Singlet.

SCC Self-consistent charge.

sr Short range.

TD Time-dependent

TD-DFT Time-dependent density-functional theory.

TD-DFTB Time-dependent density-functional tight binding.

TD-lc-DFTB long-range corrected time dependent Density-functional tight binding.

TDM Transition dipole moment.

Traj Trajectory.

UV-Vis Ultraviolet-visible.

xc Exchange-correlation.

Bibliography

- [1] Present address: The Chinese University of Hong Kong, Shenzhen, No. 2001 Longxiang Blvd., Longgang Dist., Shenzhen, Guangdong, China, 518172. pages 222, 282
- [2] Present address: Department of Chemistry, The Hong Kong University of Science and Technology, Hong Kong, China. pages 222, 282
- [3] G. Li, R. Zhu, and Y. Yang, [Polymer solar cells.](#), Nat. Photonics **6**, 153 (2012). pages 223, 224, 306
- [4] S. M. Sze and K. K. Ng, [Physics of Semiconductor Devices](#), Wiley, 3rd edition, 2007. pages 87, 223
- [5] M. Pope and C. Z. Swenberg, [Electronic Processes in Organic Crystals and Polymers](#), Oxford University Press, Oxford, 1999. pages 224
- [6] B. Maennig et al., [Organic p-i-n solar cells](#), Applied Physics A: Materials Science and Processing **79**, 1 (2004). pages 224
- [7] J. Bredas, J. E. Norton, J. Cornil, and V. Coropceanu, [Molecular understanding of organic solar cells: the challenges.](#), Acc. Chem. Res. **42**, 1691 (2009). pages 21, 224
- [8] X. Y. Zhu, Q. Yang, and M. Muntwiler, [Charge-transfer excitons at organic semiconductor surfaces and interfaces.](#), Acc. Chem. Res. **42**, 1779 (2009). pages 21, 224
- [9] T. M. Clarke and J. R. Durrant, [Charge photogeneration in organic solar cells.](#), Chem. Rev. **110**, 6736 (2010). pages 21, 224
- [10] A. Mishra and P. Bäuerle, [Small molecule organic semiconductors on the move: Promises for future solar energy technology.](#), Angew. Chem. Int. Ed. **51**, 2020 (2012). pages 224
- [11] [Best Research-Cell Efficiencies](#), https://www.nrel.gov/pv/assets/pdfs/cell_efficiency_explanatory_notes.pdf and <https://www.nrel.gov/pv/assets/images/efficiency-chart.png>, last accessed 22 February 2018. pages 224
- [12] S. Rühle, [Tabulated values of the Shockley-Queisser limit for single junction solar cells](#), Solar Energy , 139 (2016). pages 224

- [13] S. De et al., [Geminate charge recombination in alternating polyfluorene copolymer/fullerene blends](#), J. Am. Chem. Soc. **129**, 8466 (2007). pages 224, 262
- [14] W. Chan et al., [Observing the multiexciton state in singlet fission and ensuing ultrafast multielectron transfer](#), Science **334**, 1541 (2011). pages 224, 225, 262
- [15] A. A. Bakulin et al., [The role of driving energy and delocalized states for charge separation in organic semiconductors.](#), Science. **335**, 1340 (2012). pages 224, 225, 262
- [16] S. Gelinas et al., [Ultrafast Long-Range Charge Separation in Organic Semiconductor Photovoltaic Diodes](#), Science **343**, 512 (2014). pages 224, 262
- [17] C. Deibel and V. Dyakonov, [Polymer-fullerene bulk heterojunction solar cells](#), Rep. Prog. Phys. **73**, 9 (2010). pages 224
- [18] S. Few, J. M. Frost, and J. Nelson, [Models of charge pair generation in organic solar cells](#), Phys. Chem. Chem. Phys. **17**, 2311 (2015). pages 6, 224, 225
- [19] C. W. Tang, [Two-layer organic photovoltaic cell](#), Appl. Phys. Lett. **48**, 183 (1986). pages 15, 124, 224
- [20] I. G. Scheblykin, A. Yartsev, T. Pullerits, V. Gulbinas, and V. Sunderström, [Excited state and charge photogeneration dynamics in conjugated polymers](#), J. Phys. Chem. B **111**, 6303 (2017). pages 225
- [21] J. Guo, H. Ohkita, H. Benten, and S. Ito, [Near-IR femtosecond transient absorption spectroscopy of ultrafast polaron and triplet exciton formation in polythiophene films with different regioregularities](#), J. Am. Chem. Soc. **131**, 16869 (2009). pages 225
- [22] R. A. Marsch, J. M. Hodgkiss, S. Albert-Seifried, and R. H. Friend, [Effect of annealing on P3HT:PCBM charge transfer and nanoscale morphology probed by ultrafast spectroscopy](#), Nano Lett. **10**, 923 (2010). pages 225
- [23] G. Grancini et al., [Hot exciton dissociation in polymer solar cells](#), Nat. Mater. **12**, 29 (2013). pages 225
- [24] D. A. Vithanage et al., [Visualizing charge separation in bulk heterojunction organic solar cells](#), Nature Comm. **4**, 2334 (2013). pages 225
- [25] J. E. Anthony, [The Larger Acenes: Versatile Organic Semiconductors](#), Angew. Chem. Int. Ed. **47**, 452 (2008). pages 143, 225
- [26] M. S. Dresselhaus and G. Dresselhaus, [Fullerenes and fullerene-derived solids as electronic materials](#), Ann. Rev. Mater. Sci. **25**, 487 (1995). pages 225
- [27] H. Yan, T. Kagata, and H. Okuzaki, [Ambipolar pentacene/C₆₀-based field-effect transistors with high hole and electron mobilities in ambient temperature](#), Appl. Phys. Lett. **94**, 023305 (2009). pages 225

- [28] S. Yoo, B. Domercq, and B. Kippelen, [Efficient thin-film organic solar cells based on pentacene/C₆₀ heterojunctions](#), Appl. Phys. Lett. **85**, 5427 (2004). pages 225
- [29] D. N. Congreve et al., [External quantum efficiency above 100% in a singlet-fission-based organic photovoltaic cell](#), Science **340**, 334 (2013). pages 225
- [30] S. C. B. Mannsfeld, A. Virkar, C. Reese, M. F. Toney, and Z. Bao, [Precise structure of pentacene monolayers on amorphous silicon oxide and relation to charge transport](#), Adv. Mater. **21**, 2294 (2009). pages 225
- [31] K. Berke et al., [Current transport across the pentacene/CVD-grown graphene interface for diode applications](#), J. Phys.: Condens. Matter. **24**, 255802 (2012). pages 225
- [32] Y. Fu, C. Risko, and J. Brédas, [Intermixing at the pentacene-fullerene bilayer interface: A molecular dynamics study](#), Adv. Mater. **25**, 878 (2013). pages 227
- [33] T. Minami, M. Nakano, and F. Castet, [Nonempirically tuned long-range corrected density functional theory study on local and charge-transfer excitations in a pentacene/C₆₀ model complex](#), J. Phys. Chem. Lett. **2**, 1725 (2011). pages 227, 241
- [34] T. Minami, S. Ito, and M. Nakano, [Functional dependence of excitation energy for pentacene/C₆₀ model complex in the nonempirically tuned long-range corrected density functional theory](#), Int. J. Quantum Chem. **113**, 252 (2013). pages 227, 241
- [35] Z. Zheng, J.-L. Brédas, and V. Coropceanu, [Description of the Charge Transfer States at the Pentacene/C₆₀ Interface: Combining Range-Separated Hybrid Functionals with the Polarizable Continuum Model](#), Phys. Chem. Lett. **7**, 2616 (2016). pages 227, 241
- [36] C. Zhang et al., [Theoretical Study of the Local and Charge-Transfer Excitations in Model Complexes of Pentacene-C₆₀ Using Tuned Range-Separated Hybrid Functionals](#), J. Chem. Theory Comput. **10**, 2379 (2014). pages 227, 241, 246, 307
- [37] B. Yang et al., [Impact of Electron Delocalization on the Nature of the Charge-Transfer States in Model Pentacene/C₆₀ Interfaces : A Density Functional Theory Study](#), J. Phys. Chem. C **118**, 27648 (2014). pages 227, 241
- [38] Y. Murata, N. Kato, K. Fujiwara, and K. Komatsu, [Solid-State \[4+2\] Cycloaddition of Fullerene C₆₀ with Condensed Aromatics Using a High-Speed Vibration Milling Technique](#), J. Org. Chem. **64**, 3483 (1999). pages 227

- [39] J. C. Tully, [Molecular dynamics with electronic transitions.](#), J. Chem. Phys. **93**, 1061 (1990). pages 227, 228, 229, 231
- [40] S. Hammes-Schiffer and J. C. Tully, [Proton transfer in solution: Molecular dynamics with quantum transitions.](#), J. Chem. Phys. **101**, 4657 (1994). pages 227, 229, 231
- [41] U. Werner, [Simulation of Nonadiabatic Dynamics and Time-Resolved Photoelectron Spectra in the Frame of Time-Dependent Density Functional Theory.](#), PhD thesis, Humboldt University of Berlin, 2011. pages 227
- [42] F. Plasser et al., [Surface Hopping Dynamics with Correlated Single-Reference Methods: 9H-Adenine as a Case Study.](#), J. Chem. Theory Comput. **10**, 1395 (2014). pages 227
- [43] E. Tapavicza, I. Tavernelli, and U. Roethlisberger, [Trajectory surface hopping within linear response time-dependent density functional theory](#), Phys. Rev. Lett. **98**, 023001 (2007). pages 227, 234
- [44] N. Doltsinis and D. Marx, [First principles molecular dynamics involving excited states and non-adiabatic transitions.](#), J. Theor. Comput. Chem. **1**, 319 (2002). pages 227, 228
- [45] M. E. Casida, B. Natarajan, and T. Deutsch, [Non-Born-Oppenheimer dynamics and conical intersections](#), in *Fundamentals of Time-Dependent Density-Functional Theory*, edited by M. Marques, N. Maitra, F. Noguiera, E. K. U. Gross, and . Rubio, volume 837 of *Lecture Notes in Physics*, page 279, Springer Verlag, Berlin, 2011. pages 227, 228
- [46] P. Koskinen and V. Mäkinen, [Density-functional tight-binding for beginners](#), Comp. Mater. Sci. **47**, 237 (2009). pages 94, 98, 167, 227, 235
- [47] A. Oliveira, G. Seifert, T. Heine, and H. Duarte, [Density-functional based tight-binding: An approximate DFT method](#), J. Braz. Chem. Soc. **20**, 1193 (2009). pages 167, 227, 235
- [48] M. Elstner and G. Seifert, [Density functional tight binding](#), Philos. Trans. R. Soc. A **372**, 20120483 (2014). pages 167, 227, 235
- [49] T. Niehaus et al., [Tight-binding approach to time-dependent density-functional response theory](#), Phys. Rev. B **63**, 085108 (2001). pages 172, 227, 235
- [50] T. Frauenheim et al., [Atomistic simulations of complex materials: ground-state and excited-state properties](#), J. Phys.: Condens. Matter **14**, 3015 (2002). pages 170, 172, 227, 235

- [51] D. Heringer, T. A. Niehaus, M. Wanko, and T. Fraunheim, [Analytical excited state forces for the time-dependent density-functional tight-binding method](#), J. Comput. Chem. **28**, 2589 (2007). pages 172, 227, 235
- [52] T. A. Niehaus, [Approximate time-dependent density functional theory](#), J. Molec. Struct.: THEOCHEM **914**, 38 (2009). pages 172, 227, 235
- [53] A. A. M. H. M. Darghouth et al., [Assessment of Density-Functional Tight-Binding Ionization Potentials and Electron Affinities of Molecules of Interest for Organic Solar Cells Against First-Principles GW Calculations](#), Computation **3**, 616 (2015). pages 171, 227
- [54] A. A. M. H. M. Darghouth et al., [Davydov-Type Excitonic Effects on the Absorption Spectra of Parallel-Stacked and Herringbone Aggregates of Pentacene: Time-Dependent Density-Functional Theory and Time-Dependent Density-Functional Tight Binding](#), J. Chem. Phys., submitted 11 February 2018, <https://arxiv.org/abs/1803.00056>. pages 227, 228, 239
- [55] U. Werner, R. Mitrić, T. Suzuki, and V. Bonačić-Koutecký, [Nonadiabatic dynamics within the time dependent density functional theory: Ultrafast photodynamics in pyrazine](#), Chem. Phys. **349**, 319 (2008). pages 227, 239
- [56] R. Mitrić, U. Werner, and V. Bonačić-Koutecký, [Nonadiabatic dynamics and the simulation of time-resolved photoelectron spectra within time-dependent density functional theory: Ultrafast photoswitching in benzilydeneaniline](#), J. Chem. Phys. **129**, 164118 (2008). pages 227, 239
- [57] M. Barbatti et al., [Nonadiabatic dynamics of pyrrole: Dependence of deactivation mechanisms on the excitation energy](#), Chem. Phys. **375**, 26 (2010). pages 227, 239
- [58] A. Humeniuk and R. Mitrić, [DFTBABY: A software package for non-adiabatic molecular dynamics simulations based on long-ranged corrected tight-binding TD-DFT\(B\)](#), Comp. Phys. Comm. **221**, 174 (2017). pages 171, 172, 173, 191, 227, 235, 239, 240, 241, 242
- [59] S. Grimme, J. Antony, S. Ehrlich, and H. Krieg, [A consistent and accurate ab initio parameterization of density functional dispersion correction \(DFT-D\) for the 94 elements H-Pu.](#), J. Chem. Phys. **132**, 154104 (2010). pages 140, 164, 228, 238, 241
- [60] A. Humeniuk and R. Mitrić, [Long-range correction for tight-binding TD-DFT](#), J. Chem. Phys. **143**, 134120 (2015). pages 88, 171, 172, 173, 228, 235, 239, 241

- [61] V. May and O. Kühn, [Charge and Energy Transfer Dynamics in Molecular Dynamics](#), Wiley-VCH, New York, 2000. pages 141, 228
- [62] W. Domcke, D. R. Yarkony, and H. Nöppel, [Conical Intersections: Electronic Structure, Dynamics and Spectroscopy](#), World Scientific, Singapore, 2004. pages 228
- [63] G. Granucci, M. Persico, and A. Toniolo, [Direct semiclassical simulation of photochemical processes with semiempirical wave functions](#), J. Chem. Phys. **114**, 10608 (2001). pages 230, 242
- [64] P. Hohenberg and W. Kohn, [Inhomogeneous electron gas](#), Phys. Rev.B. **136**, 864 (1964). pages 63, 94, 231
- [65] W. Kohn and L. J. Sham, [Self-consistent equations including exchange and correlation effects](#), Phys. Rev. **140**, 1133 (1965). pages 66, 94, 159, 164, 231
- [66] R. G. Parr and W. Yang, [Density-Functional Theory of Atoms and Molecules](#), Oxford University Press, Oxford, 1989. pages 62, 65, 90, 159, 231
- [67] R. M. Dreizler and E. K. U. Gross, [Density Functional Theory, An Approach to the Quantum Many-Body Problem](#), Springer-Verlag, New York, 1990. pages 90, 159, 231
- [68] W. Koch and M. C. Holthausen, [A Chemist's Guide to Density Functional theory: Introduction to the DFT](#), Wiley-VCH, New York, 2000. pages 90, 159, 231
- [69] A. D. Becke, [Density-functional thermochemistry. III. The role of exact exchange](#), J. Chem. Phys. **98**, 5648 (1993). pages 232, 240
- [70] P. M. W. Gill, [Obituary: Density-Functional Theory \(1927-1993\)](#), Aust. J. Chem. **54**, 661 (2001). pages 161, 232
- [71] A. Seidl, A. Görling, P. Vogl, J. A. Majewski, and M. Levy, [Generalized Kohn-Sham schemes and the band-gap problem](#), Phys. Rev. B **53**, 3764 (1996). pages 232
- [72] E. Runge and E. K. U. Gross, [Density-functional theory for time-dependent systems](#), Phys. Rev. Lett. **52**, 997 (1984). pages 164, 233
- [73] M. A. L. Marques, C. Ullrich, F. Nogueira, A. Rubio, and E. K. U. Gross, editors, [Time-Dependent Density-Functional Theory](#), volume 706 of *Lecture Notes in Physics*, Springer, Berlin, 2006. pages 164, 233
- [74] M. A. L. Marques, N. Maitra, F. Nogueira, E. K. U. Gross, and A. Rubio, editors, [Fundamentals of Time-Dependent Density-Functional Theory](#), volume 837 of *Lecture Notes in Physics*, Springer, Berlin, 2011. pages 164, 233

- [75] C. A. Ullrich, [Time-Dependent Density-Functional Theory](#), Oxford University Press, New York, 2012. pages 164, 233
- [76] M. Casida, [Time-dependent density-functional theory for molecules and molecular solids.](#), J. Mol. Struct.: THEOCHEM. **914**, 3 (2009). pages 164, 233, 241
- [77] M. E. Casida and M. Huix-Rotllant, [Progress in Time-Dependent Density-Functional Theory](#), Annu. Rev. Phys. Chem. **63**, 287 (2012). pages 140, 164, 233, 241
- [78] D. Jacquemin, V. Wathelet, E. A. Perpete, and C. Adamo, [Extensive TD-DFT benchmark: Singlet-excited states of organic molecules](#), J. Chem. Theory Comput. **5**, 2420 (2009). pages 164, 233
- [79] C. Adamo and D. Jacquemin, [The calculations of excited-state properties with Time-Dependent Density Functional Theory](#), Chem. Soc. Rev. **42**, 845 (2013). pages 164, 233, 241
- [80] A. D. Laurent and D. Jacquemin, [TD-DFT benchmarks: A review](#), Int. J. Quant. Chem. **113**, 2019 (2013). pages 164, 233
- [81] N. T. Maitra, [Perspective: Fundamental aspects of time-dependent density functional theory](#), J. Chem. Phys. **144**, 220901 (2016). pages 164, 233
- [82] M. E. Casida, [Time-dependent density-functional response theory for molecules](#), in *Recent Advances in Density Functional Methods, Part I*, edited by D. Chong, page 155, World Scientific, Singapore, 1995. pages 164, 233, 234, 241
- [83] D. J. Tozer, R. D. Amos, N. C. Handy, B. O. Roos, and L. Serrano-Andrés, [Does density functional theory contribute to the understanding of excited states of unsaturated organic compounds?](#), Mol. Phys. **97**, 859 (1999). pages 142, 234
- [84] A. Dreuw, J. L. Weisman, and M. Head-Gordon, [Long-range charge-transfer excited states in time-dependent density functional theory require non-local exchange](#), J. Chem. Phys. **119**, 2943 (2003). pages 142, 234
- [85] M. J. Peach, P. Benfield, T. Helgaker, and D. J. Tozer, [Excitation energies in density functional theory: An evaluation and a diagnostic test](#), J. Chem. Phys. **128**, 044118 (2008). pages 142, 234
- [86] M. J. Peach and D. J. Tozer, [Illustration of a TDDFT spatial overlap diagnostic by basis function exponent scaling](#), J. Mol. Struct.: THEOCHEM **914**, 110 (2009). pages 142, 234
- [87] M. J. G. Peach, C. R. L. Sueur, M. Guillaume, and D. J. Tozer, [TDDFT diagnostic testing and functional assessment for triazene chromophores](#), Phys. Chem. Chem. Phys. **11**, 4465 (2009). pages 142, 234

- [88] T. S. Kuhlman, K. V. Mikkelsen, K. B. Møller, and T. I. Sølling, [Charge-resonance excitations in symmetric molecules - Comparison of linear response DFT with CC3 for the excited states of a model dimer](#), Chem. Phys. Lett. **478**, 127 (2009). pages 142, 234
- [89] P. Wiggins, J. A. G. Williams, and D. J. Tozer, [Excited state surfaces in density functional theory: A new twist on an old problem](#), J. Chem. Phys. **131**, 091101 (2009). pages 142, 234
- [90] A. D. Dwyer and D. J. Tozer, [Effect of chemical change on TDDFT accuracy: orbital overlap perspective of the hydrogenation of retinal](#), Phys. Chem. Chem. Phys. **12**, 2816 (2010). pages 142, 234
- [91] S. S. Leang, F. Zahariev, and M. S. Gordon, [Benchmarking the performance of time-dependent density functional methods](#), J. Chem. Phys. **136**, 104101 (2012). pages 142, 234
- [92] Y. Tawada, T. Tsuneda, S. Yanagisawa, T. Yanai, and K. Hirao, [A long-range-corrected time-dependent density functional theory](#), J. Chem. Phys. **120**, 8425 (2004). pages 234
- [93] S. Totura, T. Tsuneda, and K. Hirao, [Long-range-corrected time-dependent density functional study on electronic spectra of five-membered ring compounds and free-base porphyrin](#), J. Theor. Comput. Chem. **5**, 925 (2006). pages 234
- [94] O. A. Vydrov and G. E. Scuseria, [Assessment of a long-range corrected hybrid functional](#), J. Chem. Phys. **125**, 234109 (2006). pages 234
- [95] M. J. G. Peach, E. I. Tellgren, P. Salek, T. Helgaker, and D. J. Tozer, [Structural and Electronic Properties of Polyacetylene and Polyynes from Hybrid and Coulomb-Attenuated Density Functionals](#), J. Phys. Chem. A **111**, 11930 (2007). pages 234
- [96] E. Livshits and R. Baer, [A well-tempered density functional theory of electrons in molecules](#), Phys. Chem. Chem. Phys. **9**, 2932 (2007). pages 234
- [97] E. L. and R. Baer, [A Density Functional Theory for Symmetric Radical Cations from Bonding to Dissociation](#), J. Phys. Chem. A **112**, 12789 (2008). pages 234
- [98] C. V. Caillie and R. E. Amos, [Geometric derivatives of excitation energies using SCF and DFT](#), Chem. Phys. Lett. **308**, 249 (1999). pages 234
- [99] C. V. Caillie and R. E. Amos, [Geometric derivatives of density functional theory excitation energies using gradient-corrected functionals](#), Chem. Phys. Lett. **317**, 159 (1999). pages 234
- [100] F. Furche and R. Ahlrichs, [Adiabatic time-dependent density functional methods for excited state properties](#), J. Chem. Phys. **117**, 7433 (2002). pages 234

- [101] J. Hutter, [Excited state nuclear forces from the Tamm-Dancoff approximation to time-dependent density functional theory within the plane wave basis set framework](#), J. Chem. Phys. **118**, 3928 (2003). pages 234
- [102] N. L. Doltsinis and D. S. Kosov, [Plane wave/pseudopotential implementation of excited state gradients in density functional linear response theory: A new route via implicit differentiation](#), J. Chem. Phys. **112**, 144101 (2005). pages 234
- [103] D. Rappoport and F. Furche, [Analytical time-dependent density functional derivative methods within the RI- \$J\$ approximation, an approach to excited states of large molecules](#), J. Chem. Phys. **112**, 064105 (2005). pages 234
- [104] M. Chiba, T. Tsuneda, and K. Hirao, [Excited state geometry optimizations by analytical energy gradient of long-range corrected time-dependent density functional theory](#), J. Chem. Phys. **124**, 144106 (2006). pages 234
- [105] G. Scalmani et al., [Geometries and properties of excited states in the gas phase and in solution: Theory and application of a time-dependent density functional theory polarizable continuum model](#), J. Chem. Phys. **124**, 094107 (2006). pages 234
- [106] E. Tapavicza, I. Tavernelli, U. Rothlisberger, C. Filippi, and M. E. Casida, [Mixed time-dependent density-functional theory/classical surface hopping study of oxirane photochemistry](#), J. Chem. Phys. **129**, 124108 (2008). pages 235
- [107] B. G. Levine, C. Ko, J. Quenneville, and T. J. Martínez, [Conical intersections and double excitations in time-dependent density functional theory](#), Mol. Phys. **104**, 1039 (2006). pages 235
- [108] R. Send and F. Furche, [First-order nonadiabatic couplings from time-dependent hybrid density functional response theory: Consistent formalism, implementation, and performance](#), J. Chem. Phys. **132**, 044107 (2010). pages 235
- [109] E. Tapavicza, A. M. Meyer, and F. Furche, [Unravelling the details of vitamin D photosyntheses by non-adiabatic molecular dynamics simulations](#), Phys. Chem. Chem. Phys. **13**, 20986 (2011). pages 235
- [110] [NEWTON-X web page](#), [http://http://www.newtonx.org/](http://www.newtonx.org/). pages 235, 247
- [111] Y. Lei, S. Yuan, Y. Dou, Y. Wang, and Z. Wen, [Detailed dynamics of the nonradiative deactivation of adenine: A semiclassical dynamics study](#), J. Phys. Chem. A **112**, 8497 (2008). pages 235
- [112] J. Jakowski and K. Morokuma, [Liouville-von Neumann molecular dynamics](#), J. Chem. Phys. **130**, 224106 (2009). pages 235

- [113] X. Gao, Q. Peng, Y. Niu, D. Wang, and Z. Shuai, [Theoretical insight into the aggregation induced emission phenomena of diphenyldibenzofulvene: a nonadiabatic molecular dynamics study](#), *Phys. Chem. Chem. Phys.* **14**, 14207 (2012). pages 235
- [114] S. Pal et al., [Nonadiabatic molecular dynamics for thousand atom systems: A tight-binding approach toward PYXAID](#), *J. Chem. Theory Comput.* **12**, 1436 (2016). pages 235
- [115] A. Domínguez, B. Aradi, T. Frauenheim, V. Lutsker, and T. A. Niehaus, [Extensions of the time-dependent density functional based tight-binding approach](#), **9**, 4901 (2013). pages 235
- [116] T. Niehaus and F. Della Sala, [Range separated functionals in the density functional tight-binding method](#), *Phys. Status Solidi B* **2**, 237 (2012). pages 88, 171, 235
- [117] V. Lutsker, B. Aradi, and T. A. Niehaus, [Implementation and benchmark of a long-range corrected functional in the density functional based tight-binding method](#), *J. Chem. Phys.* **143**, 184107 (2015). pages 88, 95, 127, 171, 235
- [118] V. Q. Vuong et al., [Parameterization and benchmark of long-range corrected DFTB2 for organic molecules](#), *J. Chem. Theory Comput.* **14**, 115 (2018). pages 171, 235
- [119] D. Porezag, T. Frauenheim, T. Köhler, G. Seifert, and R. Kaschner, [Construction of tight-binding-like potentials on the basis of density-functional theory: Application to carbon](#), *Phys. Rev. B.* **51**, 12947 (1995). pages 94, 98, 167, 235
- [120] M. Elstner et al., [Self-consistent-charge density-functional tight-binding method for simulations of complex materials properties](#), *Phys. Rev. B* **58**, 7260 (1998). pages 96, 169, 236, 241
- [121] M. Gaus, Q. Cui, and M. Elstner, [DFTB3: Extension of the self-consistent-charge density-functional tight-binding method \(SCC-DFTB\)](#), *J. Chem. Theory Comput.* **7**, 931 (2011). pages 96, 98, 169, 236
- [122] R. S. Mulliken, [Report on Molecular Orbital Theory](#), *Journal de Chimie Physique et de Physico-Chimie Biologique* **497** (1949). pages 169, 237
- [123] T. Bredow and K. Jug, [Theory and range of modern semiempirical molecular orbital methods](#), *Theor. Chem. Acc.* **113**, 1 (2005). pages 94, 167, 239
- [124] R. Mitrić, U. Werner, M. Wohlgemuth, G. Seifert, and V. Bonačić-Koutecký, [Nonadiabatic Dynamics within Time-Dependent Density Functional Tight Binding Method.](#), *J. Phys. Chem. A.* **113**, 12700 (2009). pages 239

- [125] P. Löwdin, [Quantum Theory of Many-Particle Systems. I. Physical Interpretations by Means of Density Matrices, Natural Spin-Orbitals, and Convergence Problems in the Method of Configurational Interaction](#), Phys. Rev. **97**, 1474 (1955). pages 239
- [126] M. J. Frisch et al., [Gaussian 09](#), Gaussian Inc (2009). pages 240
- [127] [DFTB+ web page](#), <http://www.dftb-plus.info/>. pages 99, 240
- [128] [Crystallography Open Database](#), <http://www.crystallography.net/cod/>. pages 240
- [129] S. Schiefer, M. Huth, A. Dobrinevski, and B. Nickel, [Determination of the Crystal Structure of Substrate-Induced Pentacene Polymorphs in Fiber Structured Thin Films.](#), J. Am. Chem. Soc. **129**, 10316 (2007). pages 173, 196, 240
- [130] D. L. Dorset and M. P. McCourt, [Disorder and the molecular packing of C₆₀ buckminsterfullerene: A direct electron-crystallographic analysis](#), Acta Crystallogr. A **50**, 344 (1994). pages 173, 196, 240
- [131] C. Lee, W. Yang, and R. G. Parr, [Development of the Colle-Salvetti correlation-energy formula into a functional of the electron density.](#), Phys. Rev. B **37**, 785 (1988). pages 68, 161, 240
- [132] [Becke3LYP Method References and General Citation Guidelines](#), Gaussian NEWS, vol. 5, no. 2, summer 1994, p. 2. pages 162, 240
- [133] A. D. Becke, [A new mixing of Hartree-Fock and local density-functional theories](#), J. Chem. Phys. **98**, 1372 (1993). pages 240
- [134] W. J. Hehre, R. Ditchfield, and J. A. Pople, [Self-Consistent Molecular Orbital Methods. XII. Further Extensions of Gaussian-Type Basis Sets for Use in Molecular Orbital Studies of Organic Molecules](#), J. Chem. Phys. **56**, 2257 (1972). pages 100, 173, 240
- [135] P. C. Hariharan and J. A. Pople, [The influence of polarization functions on molecular orbital hydrogenation energies](#), Theoret. Chimica Acta **28**, 213 (1973). pages 100, 240
- [136] T. Yanai, D. P. Tew, and N. C. Handy, [A new hybrid exchange-correlation functional using the Coulomb-attenuating method \(CAM-B3LYP\)](#), Chem. Phys. Lett. **393**, 51 (2004). pages 162, 241
- [137] R. Bauernschmitt and R. Ahlrichs, [Treatment of electronic excitations within the adiabatic approximation of time dependent density functional theory.](#), Chem. Phys. Lett. **256**, 454 (1996). pages 241

- [138] C. Jamorski, M. E. Casida, and D. R. Salahub, [Dynamic Polarizabilities and Excitation Spectra from a Molecular Implementation of Time-Dependent Density-Functional Response Theory: N₂ as a Case Study](#), *J. Chem. Phys.* **104**, 5134 (1996). pages 241
- [139] M. Barbatti and K. Sen, [Effects of different initial condition samplings on photo-dynamics and spectrum of pyrrole](#), *Int. J. Quant. Chem.* **116**, 762 (2015). pages 241
- [140] L. Zhechkov, T. Heine, S. Patchkovskii, G. Seifert, and H. A. Duarte, [An efficient a posteriori treatment for dispersion interaction in density-functional-based tight binding](#), *J. Chem. Theory Comput.* **1**, 841 (2005). pages 241
- [141] M. Barbatti et al., [NEWTON-X: A Surface-Hopping Program for Nonadiabatic Molecular Dynamics](#), *WIREs: Comp. Mol. Sci.* **4**, 26 (2014). pages 242, 247
- [142] J. E. Subotnik et al., [Understanding the Surface Hopping View of Electronic Transitions and Decoherence](#), *Ann. Rev. Phys. Chem.* **67**, 387 (2016). pages 242
- [143] R. Crespo-Otero and M. Barbatti, [Specgtrum simulation and decomposition with nuclear ensemble: formal derivation and application to benzene, furan and 2-phenylfuran](#), *Theor. Chem. Acc.* **131**, 1237 (2012). pages 247
- [144] K. Sen, R. Crespo-Otero, O. Weingart, W. Thiel, and M. Barbatti, [Interfacial States in Donor-Acceptor Organic Heterojunctions: Computational Insights into Theophene-Oligomer/Fullerene Junctions](#), *J. Chem. Theory Comput.* **9**, 533 (2013). pages 247
- [145] D. Fazzi, M. Barbatti, and W. Thiel, [Hot and Cold Charge-Transfer Mechanisms in Organic Photovoltaics: Insights into the Excited States of Donor/Acceptor Interfaces](#), *J. Phys. Chem. Lett.* **8**, 4727 (2017). pages 247
- [146] L. Stojanović et al., [Nonadiabatic dynamics of cycloparaphenylenes with TD-DFTB surface hopping](#), *J. Chem. Theory Comput.* **13**, 5846 (2017). pages 247
- [147] T. Forster, [10th Spiers Memorial Lecture. Transfer Mechanisms of Electronic Excitation](#), *Faraday Discuss. Chem. Soc.* **27**, 7 (1959). pages 250
- [148] S. Joseph, M. K. Ravva, and J. Bredas, [Charge-transfer Dynamics in the Lowest Excited State of a Pentacene-Fullerene Complex: Implications for Organic Solar Cells](#), *J. Phys. Chem. Lett.* **8**, 5171 (2017). pages 266

Supplementary Information

How Long Do Energy and Charge Transfer Take? Tully-Type Mixed Time-Dependent Tight-Binding Density-Functional/Classical Trajectory Surface Hopping Study of a Model Buckminsterfullerene/Pentacene Heterojunction with and without Long-Range Correction

Ala Aldin M. H. M. Darghouth⁸, Mark E. Casida⁹,

Laboratoire de Chimie Inorganique Rédox (CIRE), Département de Chimie
Moléculaire (DCM),

Institut de Chimie Moléculaire de Grenoble (ICMG), Université Grenoble-Alpes,
301 rue de la Chimie, CS 40700, 38058 Grenoble Cedex 9, France

Xi Zhu (朱熹) [1]¹⁰, Bhaarithi Natarajan¹¹, Haibin Su (蘇海斌) [2]¹²

Division of Materials Science, Nanyang Technical University, 50 Nanyang 639789,
Singapore

Alexander Humeniuk¹³ and Roland Mitrić¹⁴

Institut für Physikalische und Theoretische Chemie,
Julius-Maximilians-Universität Würzburg,
Emil-Fischer-Straße 42, D-97074 Würzburg, Germany

- Short-time analysis for the 16 states initially localized on pentacene. Tables 7.3, 7.4, and 7.5. Figures 7.20 and 7.21.
- Short-time analysis for the 14 states initially delocalized over pentacene and buckminsterfullerene. Tables 7.6, 7.7, and 7.8. Figures 7.22 and 7.23.
- CT analysis of TD-DFTB FSSH calculations. Table 7.9. Figure 7.24.

8. ala.darghout@univ-grenoble-alpes.fr

9. mark.casida@univ-grenoble-alpes.fr

10. 0220ustc@gmail.com

11. phyever@gmail.com

12. hbsu@ntu.edu.sg

13. alexander.humeniuk@gmail.com

14. roland.mitric@uni-wuerzburg.de

Exciton Energy Transfer (EET)
Trajectory 2
Initial Excit.: $t = 0$ fs, $S = 1$, $E = 2.413$ eV, $f = 0.310$
97.0% $^1(\text{H,L}) + 3.0\%$ $^1(\text{H-8,L+8})$ on pentacene, $\Lambda = 0.99$
Before EET: $t = 35$ fs, $S = 1$, $E = 2.358$ eV, $f = 0.265$
98.2% $^1(\text{H,L}) + 1.8\%$ $^1(\text{H-6,L+8})$ on pentacene, $\Lambda = 0.986$
After EET: $t = 35.5$ fs, $S = 2$, $E = 2.339$ eV, $f = 0.0739$
52.3% $^1(\text{H-2,L+1}) + 47.7\%$ $^1(\text{H,L})$ on C_{60} , $\Lambda = 0.850$
Trajectory 4
Initial Excit.: $t = 0$ fs, $S = 3$, $E = 2.461$ eV, $f = 0.298$
95.4% $^1(\text{H,L+1}) + 4.6\%$ $^1(\text{H-7,L+9})$ on pentacene, $\Lambda = 0.97$
Before EET: $t = 21.5$ fs, $S = 5$, $E = 2.183$ eV, $f = 0.223$
86.9% $^1(\text{H,L+2}) + 13.1\%$ $^1(\text{H-1,L+1})$ delocalized, $\Lambda = 0.8934$
After EET: $t = 24$ fs, $S = 10$, $E = 2.405$ eV, $f = 0.0007$
57.8% $^1(\text{H-2,L+2}) + 42.2\%$ $^1(\text{H-5,L+1})$ on C_{60} , $\Lambda = 0.708$
Trajectory 6
Initial Excit.: $t = 0$ fs, $S = 4$, $E = 2.402$ eV, $f = 0.288$
96.5% $^1(\text{H,L+1}) + 3.5\%$ $^1(\text{H-7,L+8})$ on pentacene, $\Lambda = 0.97$
Before EET: $t = 17$ fs, $S = 2$, $E = 2.105$ eV, $f = 0.312$
99.0% $^1(\text{H,L+1}) + 1.0\%$ $^1(\text{H-11,L+12})$ on pentacene, $\Lambda = 0.984$
After EET: $t = 17.5$ fs, $S = 8$, $E = 2.359$ eV, $f = 0.0018$
88.7% $^1(\text{H-1,L+2}) + 11.3\%$ $^1(\text{H-2,L+3})$ on C_{60} , $\Lambda = 0.0.703$
Trajectory 7
Initial Excit.: $t = 0$ fs, $S = 2$, $E = 2.431$ eV, $f = 0.248$
94.9% $^1(\text{H,L}) + 5.1\%$ $^1(\text{H-3,L+1})$ on pentacene, $\Lambda = 0.95$
Before EET: $t = 0.5$ fs, $S = 3$, $E = 2.431$ eV, $f = 0.293$
97.6% $^1(\text{H,L+1}) + 2.4\%$ $^1(\text{H-6,L+7})$ on pentacene, $\Lambda = 0.966$
After EET: $t = 1$ fs, $S = 1$, $E = 2.126$ eV, $f = 0.0006$
93.5% $^1(\text{H-1,L}) + 6.5\%$ $^1(\text{H-2,L+2})$ on C_{60} , $\Lambda = 0.840$
Trajectory 9
Initial Excit.: $t = 0$ fs, $S = 1$, $E = 2.350$ eV, $f = 0.307$
96.6% $^1(\text{H,L}) + 3.4\%$ $^1(\text{H-7,L+9})$ on pentacene, $\Lambda = 0.99$
Before EET: $t = 4$ fs, $S = 4$, $E = 2.396$ eV, $f = 0.275$
83.3% $^1(\text{H,L+3}) + 16.7\%$ $^1(\text{H,L+2})$ on pentacene, $\Lambda = 0.791$
After EET: $t = 4.5$ fs, $S = 5$, $E = 2.397$ eV, $f = 0.0134$
63.8% $^1(\text{H-1,L+1}) + 36.2\%$ $^1(\text{H-2,L})$ on C_{60} , $\Lambda = 0.702$
Trajectory 11
Initial Excit.: $t = 0$ fs, $S = 1$, $E = 2.422$ eV, $f = 0.296$
97.3% $^1(\text{H,L}) + 2.7\%$ $^1(\text{H-7,L+8})$ on pentacene, $\Lambda = 0.98$
Before EET: $t = 13.5$ fs, $S = 2$, $E = 2.401$ eV, $f = 0.272$
81.6% $^1(\text{H,L}) + 18.4\%$ $^1(\text{H,L+1})$ on pentacene, $\Lambda = 0.747$
After EET: $t = 14$ fs, $S = 1$, $E = 2.396$ eV, $f = 0.0116$
69.2% $^1(\text{H-1,L+1}) + 30.8\%$ $^1(\text{H-2,L+2})$ on C_{60} , $\Lambda = 0.841$

Table 7.3 – Short-time analysis of the 16 states initially localized on pentacene. The time (t) to get exciton energy transfer from each trajectory (Traj.), the active states (S), the energies (E), the oscillator strengths (f), the molecular orbitals involved, the percentages of each transition involved in each excited state, and the degree of spatial overlap between occupied and virtual orbitals of the active state (Λ). Parts (a), (b), and (c) are continuations of the upper part of a single table.

Exciton Energy Transfer (EET)
Trajectory 13
Initial Excit.: $t = 0$ fs, $S = 1$, $E = 2.437$ eV, $f = 0.282$
96.5% $^1(\text{H,L}) + 3.5\%$ $^1(\text{H-7,L+8})$ on pentacene, $\Lambda = 0.98$
Before EET: $t = 13$ fs, $S = 1$, $E = 2.112$ eV, $f = 0.297$
99.2% $^1(\text{H,L}) + 0.8\%$ $^1(\text{H-11,L+8})$ on pentacene, $\Lambda = 0.985$
After EET: $t = 13.5$ fs, $S = 1$, $E = 2.091$ eV, $f = 0.0045$
86.1% $^1(\text{H-1,L+1}) + 13.9\%$ $^1(\text{H-2,L+2})$ on C_{60} , $\Lambda = 0.897$
Trajectory 15
Initial Excit.: $t = 0$ fs, $S = 1$, $E = 2.341$ eV, $f = 0.278$
97.4% $^1(\text{H,L}) + 2.6\%$ $^1(\text{H-6,L+7})$ on pentacene, $\Lambda = 0.97$
Before EET: $t = 16.5$ fs, $S = 1$, $E = 2.046$ eV, $f = 0.293$
99.1% $^1(\text{H,L}) + 0.9\%$ $^1(\text{H-10,L+8})$ on pentacene, $\Lambda = 0.979$
After EET: $t = 17.0$ fs, $S = 8$, $E = 2.380$ eV, $f = 0.0006$
99.1% $^1(\text{H-5,L+1}) + 0.9\%$ $^1(\text{H-4,L+3})$ on C_{60} , $\Lambda = 0.767$
Trajectory 17
Initial Excit.: $t = 0$ fs, $S = 1$, $E = 2.374$ eV, $f = 0.288$
95.6% $^1(\text{H,L}) + 4.4\%$ $^1(\text{H-7,L+8})$ on pentacene, $\Lambda = 0.98$
Before EET: $t = 19$ fs, $S = 2$, $E = 2.042$ eV, $f = 0.282$
78.3% $^1(\text{H,L+1}) + 21.7\%$ $^1(\text{H,L+2})$ on pentacene, $\Lambda = 0.848$
After EET: $t = 19.5$ fs, $S = 10$, $E = 2.451$ eV, $f = 0.0009$
71.9% $^1(\text{H-3,L+3}) + 28.1\%$ $^1(\text{H-5,L+1})$ on C_{60} , $\Lambda = 0.632$
Trajectory 18
Initial Excit.: $t = 0$ fs, $S = 4$, $E = 2.284$ eV, $f = 0.286$
67.1% $^1(\text{H,L+2}) + 32.9\%$ $^1(\text{H,L})$ on pentacene, $\Lambda = 0.71$
Before EET: $t = 2$ fs, $S = 10$, $E = 2.319$ eV, $f = 0.248$
96.7% $^1(\text{H,L+3}) + 3.3\%$ $^1(\text{H-3,L+2})$ on pentacene, $\Lambda = 0.960$
After EET: $t = 2.5$ fs, $S = 10$, $E = 2.301$ eV, $f = 0.0117$
69.9% $^1(\text{H-5,L+2}) + 30.1\%$ $^1(\text{H-3,L+2})$ on C_{60} , $\Lambda = 0.814$
Trajectory 20
Initial Excit.: $t = 0$ fs, $S = 1$, $E = 2.392$ eV, $f = 0.297$
96.6% $^1(\text{H,L}) + 3.4\%$ $^1(\text{H-7,L+8})$ on pentacene, $\Lambda = 0.99$
Before EET: $t = 4.5$ fs, $S = 7$, $E = 2.418$ eV, $f = 0.250$
96.4% $^1(\text{H,L+3}) + 3.6\%$ $^1(\text{H-6,L+8})$ on pentacene, $\Lambda = 0.941$
After EET: $t = 5.0$ fs, $S = 1$, $E = 1.924$ eV, $f = 0.0006$
78.9% $^1(\text{H-1,L}) + 21.1\%$ $^1(\text{H-2,L+1})$ on C_{60} , $\Lambda = 0.814$
Trajectory 22
Initial Excit.: $t = 0$ fs, $S = 1$, $E = 2.390$ eV, $f = 0.287$
96.4% $^1(\text{H,L}) + 3.6\%$ $^1(\text{H-7,L+8})$ on pentacene, $\Lambda = 0.98$
Before EET: $t = 6.5$ fs, $S = 10$, $E = 2.5083$ eV, $f = 0.257$
96.5% $^1(\text{H,L+3}) + 3.5\%$ $^1(\text{H,L+1})$ on pentacene, $\Lambda = 0.942$
After EET: $t = 7.0$ fs, $S = 10$, $E = 2.520$ eV, $f = 0.0188$
51.6% $^1(\text{H-5,L+1}) + 48.4\%$ $^1(\text{H-1,L+5})$ on C_{60} , $\Lambda = 0.731$

Table 7.4 – Short-time analysis of the 16 states initially localized on pentacene. The time (t) to get exciton energy transfer from each trajectory (Traj.), the active states (S), the energies (E), the oscillator strengths (f), the molecular orbitals involved, the percentages of each transition involved in each excited state, and the degree of spatial overlap between occupied and virtual orbitals of the active state (Λ). Parts (a), (b), and (c) are continuations of the upper part of a single table.

Exciton Energy Transfer (EET)
Trajectory 24
Initial Excit.: $t = 0$ fs, $S = 1$, $E = 2.336$ eV, $f = 0.325$
97.0% $^1(\text{H,L}) + 3.0\%$ $^1(\text{H-7,L+8})$ on pentacene, $\Lambda = 0.99$
Before EET: $t = 38.5$ fs, $S = 4$, $E = 2.386$ eV, $f = 0.286$
98.9% $^1(\text{H,L+2}) + 1.1\%$ $^1(\text{H-7,L+8})$ on pentacene, $\Lambda = 0.977$
After EET: $t = 39.0$ fs, $S = 1$, $E = 2.204$ eV, $f = 0.0006$
68.8% $^1(\text{H-2,L}) + 31.2\%$ $^1(\text{H-1,L+2})$ on C_{60} , $\Lambda = 0.855$
Trajectory 26
Initial Excit.: $t = 0$ fs, $S = 1$, $E = 2.327$ eV, $f = 0.333$
96.2% $^1(\text{H,L}) + 3.8\%$ $^1(\text{H-7,L+8})$ on pentacene, $\Lambda = 0.99$
Before EET: $t = 21.5$ fs, $S = 3$, $E = 2.237$ eV, $f = 0.324$
97.6% $^1(\text{H,L}) + 2.4\%$ $^1(\text{H-6,L+7})$ on pentacene, $\Lambda = 0.985$
After EET: $t = 22$ fs, $S = 1$, $E = 2.242$ eV, $f = 0.0011$
59.8% $^1(\text{H-2,L+1}) + 40.2\%$ $^1(\text{H-3,L+1})$ on C_{60} , $\Lambda = 0.828$
Trajectory 28
Initial Excit.: $t = 0$ fs, $S = 1$, $E = 2.435$ eV, $f = 0.306$
96.9% $^1(\text{H,L}) + 3.1\%$ $^1(\text{H-7,L+10})$ on pentacene, $\Lambda = 0.98$
Before EET: $t = 23.5$ fs, $S = 6$, $E = 2.325$ eV, $f = 0.261$
96.1% $^1(\text{H,L+2}) + 3.9\%$ $^1(\text{H-4,L})$ on pentacene, $\Lambda = 0.938$
After EET: $t = 24$ fs, $S = 8$, $E = 2.394$ eV, $f = 0.0105$
57.4% $^1(\text{H-1,L+3}) + 42.6\%$ $^1(\text{H-4,L})$ on C_{60} , $\Lambda = 0.736$
Trajectory 30
Initial Excit.: $t = 0$ fs, $S = 2$, $E = 2.421$ eV, $f = 0.224$
94.1% $^1(\text{H,L}) + 5.9\%$ $^1(\text{H-2,L+1})$ on pentacene, $\Lambda = 0.91$
Before EET: $t = 19$ fs, $S = 4$, $E = 2.087$ eV, $f = 0.296$
94.7% $^1(\text{H,L+2}) + 5.3\%$ $^1(\text{H-2,L})$ on pentacene, $\Lambda = 0.959$
After EET: $t = 19.5$ fs, $S = 3$, $E = 1.925$ eV, $f = 0.0003$
50.9% $^1(\text{H-3,L+1}) + 49.1\%$ $^1(\text{H-4,L})$ on C_{60} , $\Lambda = 0.786$

Table 7.5 – Short-time analysis of the 16 states initially localized on pentacene. The time (t) to get exciton energy transfer from each trajectory (Traj.), the active states (S), the energies (E), the oscillator strengths (f), the molecular orbitals involved, the percentages of each transition involved in each excited state, and the degree of spatial overlap between occupied and virtual orbitals of the active state (Λ). Parts (a), (b), and (c) are continuations of the upper part of a single table.

Exciton Energy Transfer (EET)
Trajectory 1
Initial Excit.: $t = 0$ fs, $S = 14$, $E = 2.467$ eV, $f = 0.127$
86.6% $^1(\text{H,L}+3)$ +13.4% $^1(\text{H-5,L}+4)$ delocalized, $\Lambda = 0.88$
Before EET: $t = 5$ fs, $S = 1$, $E = 1.998$ eV, $f = 0.0002$
66.8% $^1(\text{H-1,L})$ +33.2% $^1(\text{H-2,L})$ on C_{60} , $\Lambda = 0.830$
After EET: $t = 10$ fs, $S = 1$, $E = 2.652$ eV, $f = 0.2847$
97.9% $^1(\text{H,L})$ +2.1% $^1(\text{H-8,L}+8)$ on pentacene, $\Lambda = 0.983$
Trajectory 3
Initial Excit.: $t = 0$ fs, $S = 10$, $E = 2.265$ eV, $f = 0.252$
97.1% $^1(\text{H,L}+3)$ +2.9% $^1(\text{H-5,L}+1)$ delocalized, $\Lambda = 0.96$
Before EET: $t = 0.5$ fs, $S = 10$, $E = 2.224$ eV, $f = 0.001$
60.9% $^1(\text{H-5,L}+1)$ +39.1% $^1(\text{H-4,L}+2)$ on C_{60} , $\Lambda = 0.736$
After EET: $t = 21.5$ fs, $S = 2$, $E = 2.543$ eV, $f = 0.2889$
95.8% $^1(\text{H,L})$ +4.2% $^1(\text{H-3,L}+1)$ on pentacene, $\Lambda = 0.966$
Trajectory 5
Initial Excit.: $t = 0$ fs, $S = 10$, $E = 2.306$ eV, $f = 0.281$
97.2% $^1(\text{H,L}+3)$ +2.8% $^1(\text{H-9,L}+8)$ delocalized, $\Lambda = 0.97$
Before EET: $t = 0.5$ fs, $S = 10$, $E = 2.271$ eV, $f = 0.001$
66.5% $^1(\text{H-5,L}+2)$ +33.5% $^1(\text{H-3,L}+2)$ on C_{60} , $\Lambda = 0.776$
After EET: $t = 21.5$ fs, $S = 3$, $E = 3.061$ eV, $f = 0.0008$
65.0% $^1(\text{H-5,L})$ +35.0% $^1(\text{H,L}+4)$ on pentacene, $\Lambda = 0.800$
Trajectory 8
Initial Excit.: $t = 0$ fs, $S = 12$, $E = 2.401$ eV, $f = 0.182$
93.4% $^1(\text{H,L}+3)$ +6.6% $^1(\text{H-2,L}+6)$ delocalized, $\Lambda = 0.91$
Before EET: $t = 4$ fs, $S = 1$, $E = 2.473$ eV, $f = 0.258$
94.8% $^1(\text{H,L})$ +5.2% $^1(\text{H-6,L}+8)$ on pentacene, $\Lambda = 0.981$
After EET: $t = 16$ fs, $S = 12$, $E = 2.846$ eV, $f = 0.0015$
54.3% $^1(\text{H-1,L}+4)$ +45.7% $^1(\text{H-2,L}+4)$ on C_{60} , $\Lambda = 0.780$
Trajectory 10
Initial Excit.: $t = 0$ fs, $S = 14$, $E = 2.339$ eV, $f = 0.183$
96.4% $^1(\text{H,L}+3)$ +3.6% $^1(\text{H,L})$ delocalized, $\Lambda = 0.88$
Before EET: $t = 3.5$ fs, $S = 3$, $E = 2.236$ eV, $f = 0.002$
53.9% $^1(\text{H-4,L}+2)$ +46.1% $^1(\text{H-2,L}+1)$ on C_{60} , $\Lambda = 0.754$
After EET: $t = 14.5$ fs, $S = 2$, $E = 3.032$ eV, $f = 0.2457$
92.5% $^1(\text{H,L})$ +7.5% $^1(\text{H,L}+1)$ on pentacene, $\Lambda = 0.898$

Table 7.6 – Short-time analysis of the 14 states initially delocalized over pentacene and buckminsterfullerene. The time (t) to get exciton energy transfer from each trajectory (Traj.), the active states (S), the energies (E), the oscillator strengths (f), the molecular orbitals involved, the percentages of each transition involved in each excited state, and the degree of spatial overlap between occupied and virtual orbitals of the active state (Λ). Parts (a), (b), and (c) are continuations of the upper part of a single table.

Exciton Energy Transfer (EET)
Trajectory 12
Initial Excit.: $t = 0$ fs, $S = 12$, $E = 2.289$ eV, $f = 0.279$
97.5% $^1(\text{H,L}+3)$ +2.5% $^1(\text{H-6,L}+7)$ delocalized, $\Lambda = 0.97$
Before EET: $t = 1$ fs, $S = 10$, $E = 2.182$ eV, $f = 0.0003$
78.6% $^1(\text{H-5,L}+2)$ +21.4% $^1(\text{H-3,L}+1)$ on C_{60} , $\Lambda = 0.676$
After EET: $t = 7$ fs, $S = 1$, $E = 2.642$ eV, $f = 0.2618$
95.2% $^1(\text{H,L})$ +4.8% $^1(\text{H-6,L}+8)$ on pentacene, $\Lambda = 0.977$
Trajectory 14
Initial Excit.: $t = 0$ fs, $S = 14$, $E = 2.390$ eV, $f = 0.132$
89.0% $^1(\text{H,L}+3)$ +11.0% $^1(\text{H-2,L}+4)$ delocalized, $\Lambda = 0.85$
Before EET: $t = 2$ fs, $S = 14$, $E = 2.312$ eV, $f = 0.004$
75.2% $^1(\text{H-3,L}+4)$ +24.8% $^1(\text{H-8,L}+1)$ on C_{60} , $\Lambda = 0.778$
After EET: $t = 13.5$ fs, $S = 1$, $E = 3.063$ eV, $f = 0.2504$
95.2% $^1(\text{H,L})$ +4.8% $^1(\text{H-7,L}+8)$ on pentacene, $\Lambda = 0.979$
Trajectory 16
Initial Excit.: $t = 0$ fs, $S = 15$, $E = 2.396$ eV, $f = 0.228$
97.9% $^1(\text{H,L}+3)$ +2.1% $^1(\text{H-6,L}+7)$ delocalized, $\Lambda = 0.93$
Before EET: $t = 0.5$ fs, $S = 15$, $E = 2.368$ eV, $f = 0.003$
50.3% $^1(\text{H-11,L})$ +49.7% $^1(\text{H-3,L}+5)$ on C_{60} , $\Lambda = 0.730$
After EET: $t = 14.0$ fs, $S = 4$, $E = 2.996$ eV, $f = 0.2507$
91.8% $^1(\text{H,L}+2)$ +8.2% $^1(\text{H,L}+1)$ on pentacene, $\Lambda = 0.893$
Trajectory 19
Initial Excit.: $t = 0$ fs, $S = 9$, $E = 2.373$ eV, $f = 0.255$
94.5% $^1(\text{H,L}+3)$ +5.5% $^1(\text{H-5,L}+2)$ delocalized, $\Lambda = 0.96$
Before EET: $t = 1$ fs, $S = 3$, $E = 2.244$ eV, $f = 0.002$
51.7% $^1(\text{H-4,L}+1)$ +48.3% $^1(\text{H-5,L}+3)$ on C_{60} , $\Lambda = 0.806$
After EET: $t = 3$ fs, $S = 1$, $E = 2.489$ eV, $f = 0.3057$
97.2% $^1(\text{H,L})$ +2.8% $^1(\text{H-6,L}+7)$ on pentacene, $\Lambda = 0.981$
Trajectory 21
Initial Excit.: $t = 0$ fs, $S = 16$, $E = 2.341$ eV, $f = 0.151$
93.8% $^1(\text{H,L}+3)$ +6.2% $^1(\text{H-3,L})$ delocalized, $\Lambda = 0.84$
Before EET: $t = 2.5$ fs, $S = 9$, $E = 2.341$ eV, $f = 0.001$
58.6% $^1(\text{H-3,L}+1)$ +41.4% $^1(\text{H-5,L})$ on C_{60} , $\Lambda = 0.729$
After EET: $t = 6.0$ fs, $S = 1$, $E = 2.571$ eV, $f = 0.2666$
93.9% $^1(\text{H,L})$ +6.1% $^1(\text{H-6,L}+8)$ on pentacene, $\Lambda = 0.970$

Table 7.7 – Short-time analysis of the 14 states initially delocalized over pentacene and buckminsterfullerene. The time (t) to get exciton energy transfer from each trajectory (Traj.), the active states (S), the energies (E), the oscillator strengths (f), the molecular orbitals involved, the percentages of each transition involved in each excited state, and the degree of spatial overlap between occupied and virtual orbitals of the active state (Λ). Parts (a), (b), and (c) are continuations of the upper part of a single table.

Exciton Energy Transfer (EET)
Trajectory 23
Initial Excit.: $t = 0$ fs, $S = 17$, $E = 2.440$ eV, $f = 0.117$
86.3% $^1(\text{H,L}+3)$ +13.7% $^1(\text{H-4,L})$ delocalized, $\Lambda = 0.87$
Before EET: $t = 6$ fs, $S = 3$, $E = 2.624$ eV, $f = 0.007$
52.4% $^1(\text{H-2,L}+2)$ +47.6% $^1(\text{H-2,L})$ on C_{60} , $\Lambda = 0.782$
After EET: $t = 9.5$ fs, $S = 3$, $E = 3.249$ eV, $f = 0.1266$
70.5% $^1(\text{H-6,L})$ +29.5% $^1(\text{H,L}+10)$ on pentacene, $\Lambda = 0.764$
Trajectory 25
Initial Excit.: $t = 0$ fs, $S = 12$, $E = 2.364$ eV, $f = 0.155$
91.2% $^1(\text{H,L}+3)$ +8.8% $^1(\text{H-4,L}+5)$ delocalized, $\Lambda = 0.89$
Before EET: $t = 1.0$ fs, $S = 12$, $E = 2.352$ eV, $f = 0.012$
55.0% $^1(\text{H-5,L}+4)$ +45.0% $^1(\text{H-11,L}+2)$ on C_{60} , $\Lambda = 0.781$
After EET: $t = 11.0$ fs, $S = 1$, $E = 3.057$ eV, $f = 0.2392$
87.8% $^1(\text{H,L})$ +12.2% $^1(\text{H-6,L}+8)$ on pentacene, $\Lambda = 0.983$
Trajectory 27
Initial Excit.: $t = 0$ fs, $S = 13$, $E = 2.322$ eV, $f = 0.254$
97.9% $^1(\text{H,L}+3)$ +2.1% $^1(\text{H-6,L}+7)$ delocalized, $\Lambda = 0.96$
Before EET: $t = 0.5$ fs, $S = 13$, $E = 2.303$ eV, $f = 0.006$
56.2% $^1(\text{H-4,L}+5)$ +43.8% $^1(\text{H-1,L}+6)$ on C_{60} , $\Lambda = 0.774$
After EET: $t = 16.0$ fs, $S = 1$, $E = 3.111$ eV, $f = 0.2390$
89.4% $^1(\text{H,L})$ +10.6% $^1(\text{H-1,L}+1)$ on pentacene, $\Lambda = 0.974$
Trajectory 29
Initial Excit.: $t = 0$ fs, $S = 11$, $E = 2.371$ eV, $f = 0.164$
92.8% $^1(\text{H,L}+3)$ +7.2% $^1(\text{H-7,L})$ delocalized, $\Lambda = 0.88$
Before EET: $t = 1$ fs, $S = 11$, $E = 2.266$ eV, $f = 0.004$
53.5% $^1(\text{H-2,L}+4)$ +46.5% $^1(\text{H-7,L})$ on C_{60} , $\Lambda = 0.766$
After EET: $t = 16$ fs, $S = 8$, $E = 3.620$ eV, $f = 0.0774$
56.0% $^1(\text{H,L}+10)$ +44.0% $^1(\text{H-1,L}+1)$ on pentacene, $\Lambda = 0.729$

Table 7.8 – Short-time analysis of the 14 states initially delocalized over pentacene and buckminsterfullerene. The time (t) to get exciton energy transfer from each trajectory (Traj.), the active states (S), the energies (E), the oscillator strengths (f), the molecular orbitals involved, the percentages of each transition involved in each excited state, and the degree of spatial overlap between occupied and virtual orbitals of the active state (Λ). Parts (a), (b), and (c) are continuations of the upper part of a single table.

Table 7.9 – CT analysis of TD-DFTB FSSH calculations

TRAJ.	Initial State 0 fs	$C_{60} \rightarrow$ Pent CT Time in fs	Pent $\rightarrow C_{60}$ CT Time in fs
TRAJ-0001	Pent	5	6.5
TRAJ-0002	Pent	11	23
TRAJ-0003	Pent		5
TRAJ-0004	Pent	1.5	25.5
TRAJ-0005	DL	2	5
TRAJ-0006	Pent	1	13
TRAJ-0007	C_{60}	8	16
TRAJ-0008	Pent	2	20.5
TRAJ-0009	Pent	0.5	33.5
TRAJ-0010	Pent	2	9
TRAJ-0011	Pent	2	
TRAJ-0012	Pent	2.5	4.5
TRAJ-0013	Pent	3	4.5
TRAJ-0014	Pent	9	25
TRAJ-0015	Pent	0.5	3.5
TRAJ-0016	Pent		1.5
TRAJ-0017	Pent	0.5	4
TRAJ-0018	Pent	0.5	21
TRAJ-0019	DL	1.5	8
TRAJ-0020	Pent	1	6.5
TRAJ-0021	Pent	3	12
TRAJ-0022	Pent	1.5	37
TRAJ-0023	Pent		2.5
TRAJ-0024	Pent	1	12
TRAJ-0025	Pent		0.5
TRAJ-0026	Pent	1	
TRAJ-0027	Pent	4.5	21.5
TRAJ-0028	Pent	9.5	37.5
TRAJ-0029	Pent	4	23.5
TRAJ-0030	Pent	1	23.5

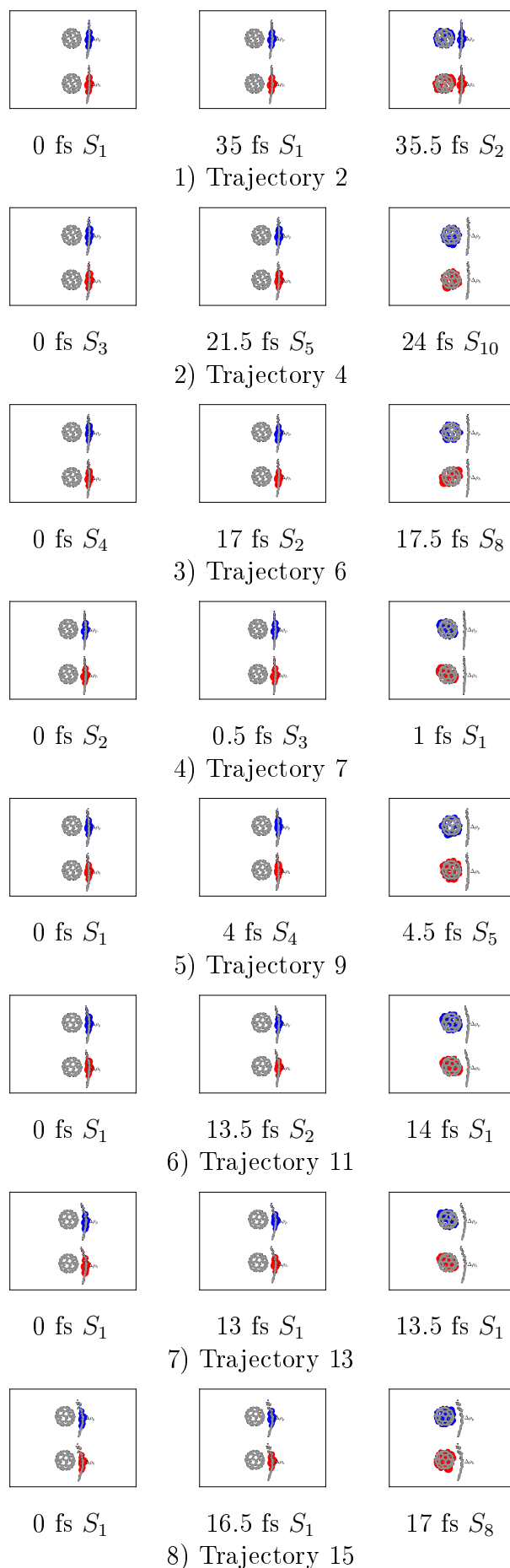


Figure 7.20 – Particle-hole charge analysis for 16 trajectories showing the $P \rightarrow P \rightarrow C_{60}$ nature of the temporal evolution of the active excited state.

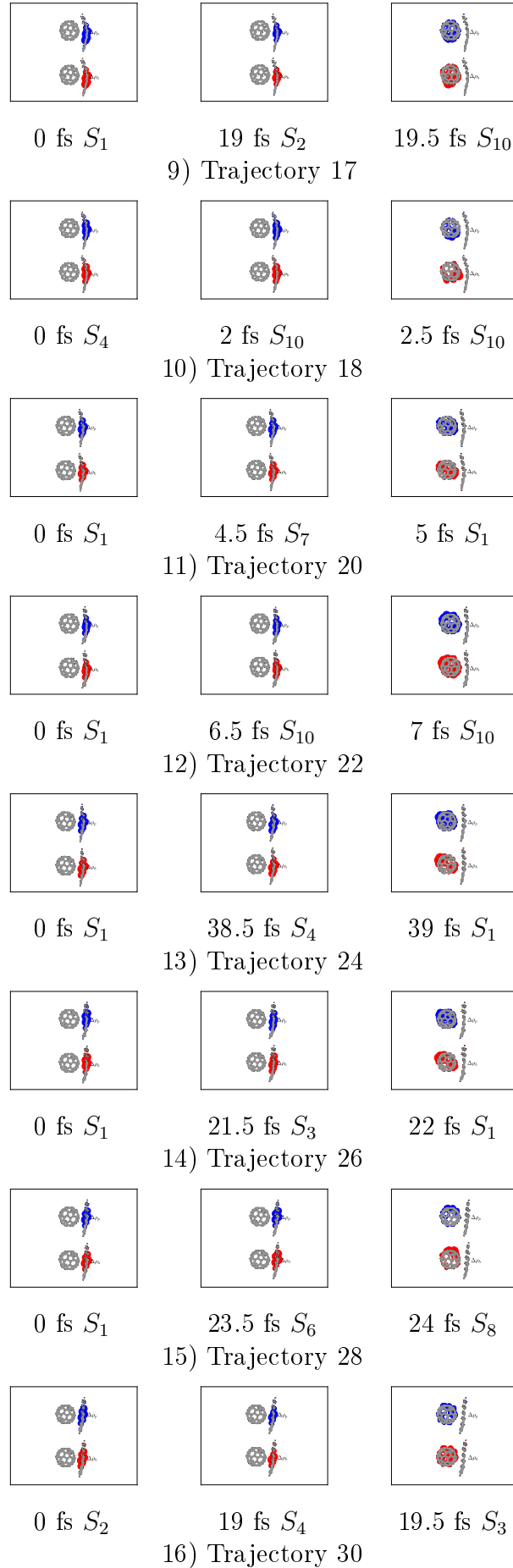


Figure 7.21 – Particle-hole charge analysis for 16 trajectories showing the $P \rightarrow P \rightarrow C_{60}$ nature of the temporal evolution of the active excited state.

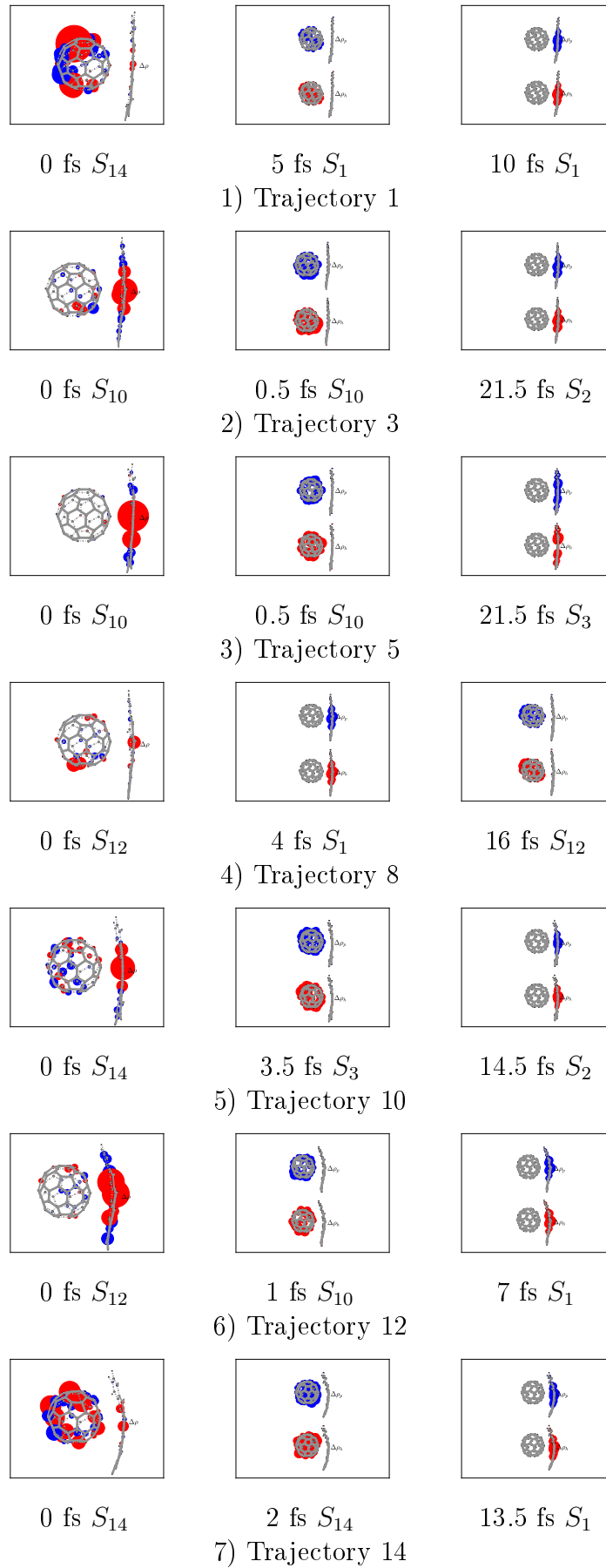


Figure 7.22 – Particle-hole charge analysis for 14 trajectories showing the DL \rightarrow C₆₀ \rightarrow P nature of the temporal evolution of the active excited state.

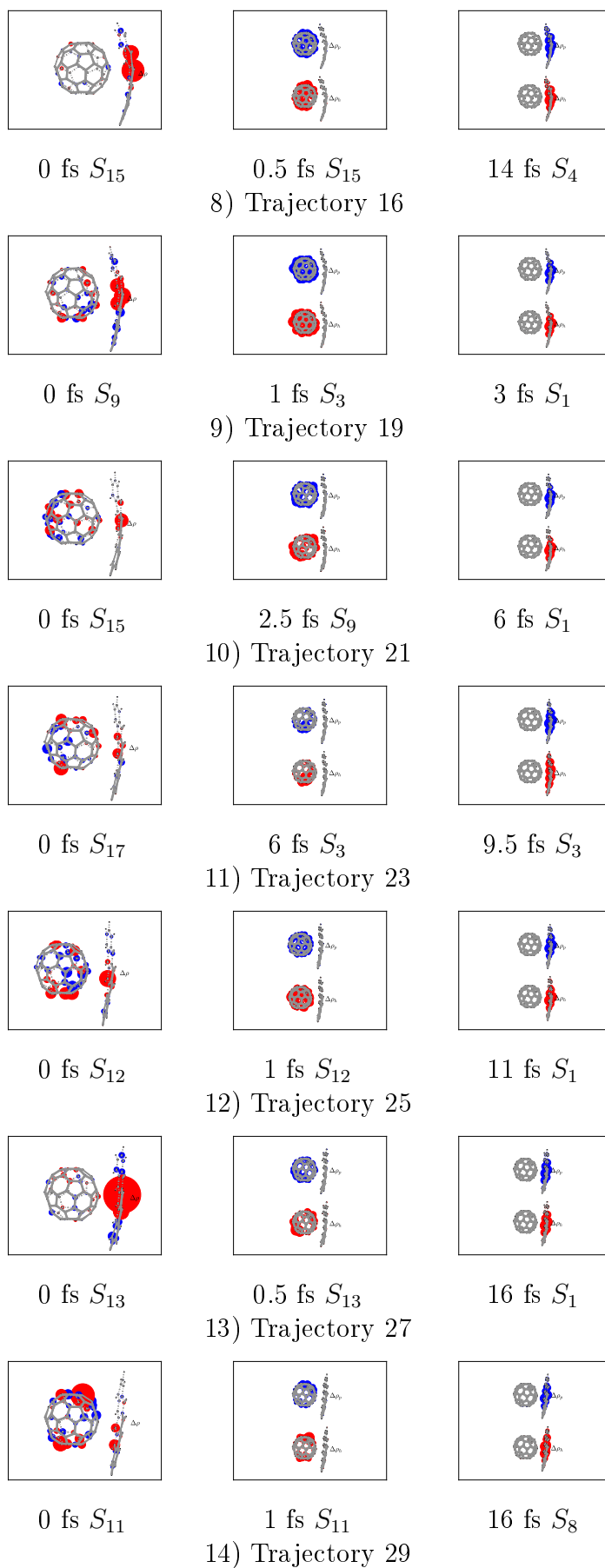


Figure 7.23 – Particle-hole charge analysis for 14 trajectories showing the DL \rightarrow C₆₀ \rightarrow P nature of the temporal evolution of the active excited state.

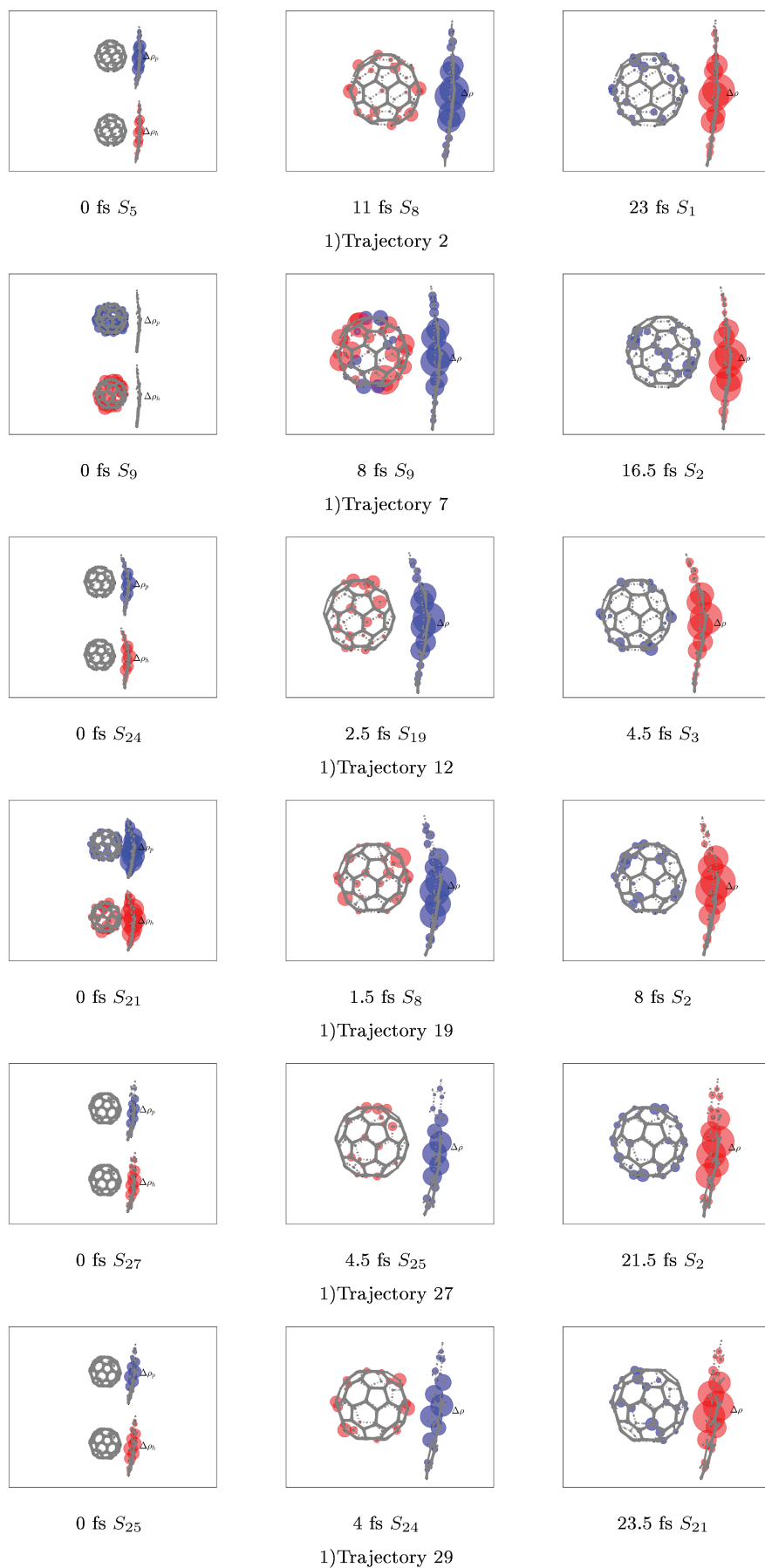


Figure 7.24 – Snapshots of the particle-hole charge density difference for the active state for 6 trajectories showing the time to get charge transfer of the active excited state by using DFTBABY without long-range correction.

Part III

Summary and Outlook

Chapter 8

Summary

The general ambiguity of the future of oil production, pollution associated with fossil fuel use, as well as the desire to diversify energy sources are all essential factors pushing mankind to develop alternative energy technologies including, notably, photovoltaic cells, the subject of this thesis. Among the various types of photovoltaic cells, organic photovoltaic cells fill a special niche defined by, among other things, their low production cost, permitting high-volume manufacture and lending themselves to large area applications, the fact that they can be made to flex and bend without breaking, their lightness compared with silicon-based solar cells, their ease of shaping and their printability, their high optical absorption coefficient, and the large degrees of freedom for molecular level design.

The first organic solar cells were primitive affairs with no donor/acceptor interface. However, following the seminal studies of Tang, it was realized how important such an interface was for improving the efficiency of the solar cells. As Tang had shown that exciton diffusion was limited to on the order of 10 nm, the idea emerged of creating solar cells by polymer phase separation, thus both greatly increasing the surface area of the interface and reducing the need for the exciton to diffuse very far before it reached an interface. This new generation of organic solar cells is referred to as bulk heterojunction (BHJ) solar cells. Some BHJ solar cells have already been commercialized though their photovoltaic efficiency is still low. Further progress in increasing organic solar cell efficiency is aided by a deeper understanding of the underlying mechanism of how these solar cells work.

Experimentally, the short-circuit current density (J_{sc}) and the open-circuit voltage (V_{oc}) are two of the most important measurable quantities. The solar cell will be efficient if the fill factor (FF), defined by the ratio of the maximum power density output by the solar cells divided by the product $J_{sc}V_{oc}$, is large. Many experimental efforts have focused on understanding the apparent relationship between solar cell

efficiency and energetic positions of the highest occupied molecular orbital (HOMO) of the donor with respect to the lowest unoccupied molecular orbital (LUMO) of the acceptor. In particular, approximate empirical relationships have been found between V_{oc} and the difference between the ionization potential (IP) of the donor and the electron affinity (EA) of the acceptor. Hence the emphasis found in the literature on IPs and EAs.

The first chapter of the original research part of this thesis reports our assessment of density-functional tight binding (DFTB) for the calculation and prediction of the IPs and EAs of medium-sized molecules of importance for molecular electronics. We chose to adopt the “semiempirical point of view” that it is more important to be able to predict trends for a series of molecules than to obtain accurate values for individual molecules. In fact, such accurate values may be obtained by interpolation of correlation curves. DFTB calculations were performed with and without self-consistent charge (SCC) and the results were compared against experiment and against results from other theoretical methods. IPs and EAs were determined in two different ways: (i) using a DFTB analogue of Koopmans’ theorem and (ii) using the Δ SCF method. The relative quality of least square fits to correlation plots was evaluated on the basis of the standard error (Δy). Perhaps surprisingly, both DFTB with and without SCC were found to have relatively small errors.

The second chapter of the original research part of this thesis reports our assessment of how well state-of-the-art DFTB can reproduce state-of-the-art DFT for describing excitonic effects in the spectra of aggregates. To this end, we have focused on an artificial model of parallel-stacked pentacenes and the realistic case of the known herringbone structure of solid pentacene. Part of the challenge here lies in the need to describe the van der Waals forces which bind the molecules together to form aggregates and the solid. A second part of the challenge lies in finding a balanced description of charge-transfer excitations. The first part is dealt with using Grimme’s semi-empirical D3 dispersion correction while the second part is dealt with by the use of either the global B3LYP hybrid or the range-separated CAM-B3LYP hybrid. The lc-DFTB method is parameterized to behave like CAM-B3LYP while DFTB from the same program (DFTBABY) is parameterized to behave like B3LYP. Taken together we hoped to find a good description of how best to model excitonic effects, such as H- and J-shifts as well as Davydov splittings, seen in aggregate spectra. Our results were analyzed in detail for parallel-stacked pentacenes based upon parallels with an analytic model for stacked ethylene molecules. Our analysis showed that the use of range-separated hybrids (RSHs) has a larger effect on charge-transfer intermolecular excitations than on energy-transfer intermolecular

excitations. Perhaps somewhat unexpectedly, TD-DFTB parameterized on the basis of B3LYP gave better results than TD-lc-DFTB parameterized on the basis of CAM-B3LYP for modelling excitonic effects on spectra. We attribute this failure of TD-lc-DFTB to the incorrect asymptotic behavior of the CAM-B3LYP functional.

The third and last chapter of the original research part of this thesis reports an application of DFTB to the investigation of the mechanism for energy transfer and charge separation at a model heterointerface. Our main goal was to answer the questions: (i) How much time does it take energy transfer to take place across the heterojunction? (ii) How much time does it take before the initial exciton separates into an electron on the acceptor and a hole on the donor? To answer these questions we applied Tully-type mixed time-dependent long-range corrected density-functional tight-binding (TD-lc-DFTB)/classical surface hopping photodynamics to a simple model interface. This simple model interface consisted of a van der Waals complex made up of one molecule of pentacene and one molecule of buckminsterfullerene (C_{60}). It should be emphasized that this is a 96 atom system for which we must carry out a large number of dynamics calculations in order to obtain interesting results, hence the need for a semi-empirical approach. Calculations were carried out for 500 fs for 30 trajectories prepared from a thermally-equilibrated ground-state distribution. The density of excited states was such that no single excited state dominated as the active state. Nevertheless interesting general conclusions could be obtained when the results were analyzed using not one, but several tools, for the active state as a function of time — namely the particle-hole charge density difference, explicit visualization of the molecular orbitals involved in the transitions, the degree of spatial overlap between hole and electron orbitals, oscillator strengths, and the transition dipole moment. This somewhat laborious procedure was necessary because the quantities are calculated for the supermolecule consisting of both molecules together, but we wanted to understand how energy and charge is transferred between the molecules within the supermolecule. Indeed minor changes in these quantities, which were initially misinterpreted as charge transfer, indicated merely that the excitation sloshes back and forth from one molecule to the other in an energy transfer process with the first step occurring within less than about 20 fs of the start of our dynamics run. However at a time between about 126.5 and 221 fs, depending upon the trajectory, a dramatic simultaneous change in all quantities and this was found to correlate with a true charge transfer between the two molecules. This is consistent with what is known experimentally with how long charge transfer takes at the bulk heterojunction in an organic solar cell.

Looking back to the original objective of the original thesis project, we can say

that the main objective of carrying out photochemical dynamics to obtain a detailed understanding of charge transfer at a donor/acceptor interface has been achieved. Of course, the final system is only a finite system which is much too small for either energy or charge to dissipate, even approximately. So, just as the excited state sloshes back and forth between the molecules so will the separated charges reunite and then reseparate in time.

Chapter 9

Future Outlook

The end of PhD studies should be a time for looking back and for looking forward. It is a time for looking back on what has been accomplished. This has been done to a great extent in the Summary section above. It has been a long road, involving a long period of tool accumulation needed in order to achieve the final goal of the project. Much was learned along the way which cannot be included in this thesis. New friends were made, many of whom are also collaborators, and a research network has been built. Perhaps the most important thing about the work reported here is that I was the pioneer whose job it was to break into the world of organic electronics at the nanointerface. The last two steps (exciton structure in aggregate spectra and photochemical dynamics) are undoubtedly the most significant and the most satisfying. They were also the most challenging. Some contradictions arise because they were carried out as overlapping, almost parallel projects. Thus the photochemical dynamics used the same long-range correction which was found to be problematic for studying exciton structure in aggregate spectra. It is not clear whether this is a problem or not. There was not enough time to clarify this point by, say, reparameterizing TD-lc-DFTB with a better RSH than the CAM-B3LYP functional.

Like the long-range correction, there is plenty of room to develop this project further. I am happy to say that the results point the way. Of course, one easy extension of the project is to vary the electron donor and acceptor. It is also clear that it is necessary to build and use better tools for analyzing exciton effects in supermolecule calculations on van der Waals aggregates. It is also necessary to go to larger systems where energy and charge have more chance to dissipate. Perhaps still more physics and chemistry will appear as the system grows? I do not know, but it is always wise to expect the unexpected. What is clear is that this work has taken a good step into the wilderness and gives a good idea of what can be done, what

can be done better, what to expect, and perhaps also what not to expect so that we can be surprised when something new happens. And this — AHA!, the “element of surprise” — is one of the most valuable and rewarding thing that we can expect in research.

Appendices

List of Tables

4.1	Some atomic units and their SI Values. This table is taken from Ref. [1].	52
5.1	Fitting data for outer valence IPs: $y = mx + b$, where x is the experimental IP and y is the calculated IP, both in eV. HF, Hartree-Fock; OEP, optimized effective potential; LDA, local density approximation; DFTB, density-functional tight binding (without self-consistent charge); SCC-DFTB, self-consistent charge DFTB.	107
5.2	Fitting data for first IPs [40]: $y = mx + b$, where x is the experimental IP and y is the theoretical IP, both in eV. HF, Hartree-Fock; OEP, optimized effective potential; LDA, local density approximation; DFTB, density-functional tight binding (without self-consistent charge); SCC-DFTB, self-consistent charge DFTB.	107
5.3	DFTB+ IPs (eV) for small molecules.	110
5.4	DFTB+ IPs (eV) for small molecules (continued).	111
5.5	Comparison values of the first ionization potential for the medium-sized molecules from experiment and from quantum chemistry calculations.	115
5.6	Comparison values of the first electron affinity for the medium-sized molecules from experiment and from quantum chemistry calculations.	116
5.7	Fitting data for first IPs of the medium-sized BDS molecules: $y = mx + b$, where x is the GW IP and y is another theoretical IP, both in eV. HF, Hartree-Fock; OVGF, outer valence Green's function; LDA, local density approximation; DFTB, density-functional tight binding (without self-consistent charge); SCC-DFTB, self-consistent charge DFTB.	119

5.8	Fitting data for first EAs of the medium-sized BDS molecules: $y = mx+b$, where x is the <i>GW</i> EA and y is another theoretical EA, both in eV. HF, Hartree-Fock; OVGF, outer valence Green's function; LDA, local density approximation; DFTB, density-functional tight binding (without self-consistent charge); SCC-DFTB, self-consistent charge DFTB.	122
6.1	Summary of different functionals used in this work. See Eq. (6.47). . .	162
6.2	Monomer lowest energy peak $^1(\text{H,L})$ calculated with various methods. . .	178
6.3	Intermolecular distances obtained for the tetramer of parallel stacked pentacene molecules.	181
6.4	Relative percentages of CT and ET excitonic transitions to the principle transition for two parallel stacked pentacenes as a function of method. See Eq. (6.5). DS is the Davydov splitting between the CT and ET excitonic transitions.	183
6.5	Relative percentages of CT and ET excitonic transitions to the principle transition for three parallel stacked pentacenes as a function of method. See Eq. (6.8). DS is the Davydov splitting between the lowest energy CT and the highest energy ET excitonic transitions.	185
6.6	Relative percentages of CT and ET excitonic transitions to the principle transition for three parallel stacked pentacenes as a function of method. See Eq. (6.8). DS is the Davydov splitting between the lowest energy CT and the highest energy ET excitonic transitions.	186
6.7	Relative percentages of CT and ET excitonic transitions to the principle transition for three parallel stacked pentacenes as a function of method. See Eq. (6.8). DS is the Davydov splitting between the lowest energy CT and the highest energy ET excitonic transitions.	187
6.8	Relative percentages of CT and ET excitonic transitions to the principle transition for three parallel stacked pentacenes as a function of method. See Eq. (6.8). DS is the Davydov splitting between the lowest energy CT and the highest energy ET excitonic transitions.	188
6.9	Relative percentages of CT and ET excitonic transitions to the principle transition for three parallel stacked pentacenes as a function of method. See Eq. (6.8). DS is the Davydov splitting between the lowest energy CT and the highest energy ET excitonic transitions.	189
7.1	The generally accepted model for organic heterojunction solar cells [3]. . .	223

7.2	Comparison of the excitation energies of the present work with those of Model 1 in given in Table 3 of Ref. [36].	246
7.3	Short-time analysis of the 16 states initially localized on pentacene. The time (t) to get exciton energy transfer from each trajectory (Traj.), the active states (S), the energies (E), the oscillator strengths (f), the molecular orbitals involved, the percentages of each transition involved in each excited state, and the degree of spatial overlap between occupied and virtual orbitals of the active state (Λ). Parts (a), (b), and (c) are continuations of the upper part of a single table.	283
7.4	Short-time analysis of the 16 states initially localized on pentacene. The time (t) to get exciton energy transfer from each trajectory (Traj.), the active states (S), the energies (E), the oscillator strengths (f), the molecular orbitals involved, the percentages of each transition involved in each excited state, and the degree of spatial overlap between occupied and virtual orbitals of the active state (Λ). Parts (a), (b), and (c) are continuations of the upper part of a single table.	284
7.5	Short-time analysis of the 16 states initially localized on pentacene. The time (t) to get exciton energy transfer from each trajectory (Traj.), the active states (S), the energies (E), the oscillator strengths (f), the molecular orbitals involved, the percentages of each transition involved in each excited state, and the degree of spatial overlap between occupied and virtual orbitals of the active state (Λ). Parts (a), (b), and (c) are continuations of the upper part of a single table.	285
7.6	Short-time analysis of the 14 states initially delocalized over pentacene and buckminsterfullerene. The time (t) to get exciton energy transfer from each trajectory (Traj.), the active states (S), the energies (E), the oscillator strengths (f), the molecular orbitals involved, the percentages of each transition involved in each excited state, and the degree of spatial overlap between occupied and virtual orbitals of the active state (Λ). Parts (a), (b), and (c) are continuations of the upper part of a single table.	286

7.7	Short-time analysis of the 14 states initially delocalized over pentacene and buckminsterfullerene. The time (t) to get exciton energy transfer from each trajectory (Traj.), the active states (S), the energies (E), the oscillator strengths (f), the molecular orbitals involved, the percentages of each transition involved in each excited state, and the degree of spatial overlap between occupied and virtual orbitals of the active state (Λ). Parts (a), (b), and (c) are continuations of the upper part of a single table.	287
7.8	Short-time analysis of the 14 states initially delocalized over pentacene and buckminsterfullerene. The time (t) to get exciton energy transfer from each trajectory (Traj.), the active states (S), the energies (E), the oscillator strengths (f), the molecular orbitals involved, the percentages of each transition involved in each excited state, and the degree of spatial overlap between occupied and virtual orbitals of the active state (Λ). Parts (a), (b), and (c) are continuations of the upper part of a single table.	288
7.9	CT analysis of TD-DFTB FSSH calculations	289

List of Figures

2.1	Chart showing the evolution of the efficiency of different types of cells. From the American National Renewable Energy Laboratory 2017. Organic solar cells are represented by filled red circles (lower right hand side of the graphic.)	12
2.2	Some organic electronics materials.	13
2.3	Solar Spectrum reference taken from reference [8]	14
2.4	Scheme illustrates how the difference in the work function of the electrodes leads to separate the hole and the particle.	15
2.5	Types of organic solar cell. Redrawn based on a figure from ref. [13] .	16
2.6	The fundamental steps involved in the mechanism of power conversion at N/D interface in an organic solar cell.	18
2.7	The Shockley-Queisser limit for the efficiency of a solar cell. Redrawn based on a figure from ref. [17]	19
2.8	Current-voltage curves for dark and light currents in solar cells with J_{sc} , V_{oc} , FF , J_{mpp} and V_{mpp} . Redrawn based on a figure from ref. [6].	20
3.1	The absorption spectrum of molecular system	29
3.2	The photophysical deactivation processes of electronically-excited states. 31	
3.3	Jablonski diagrams	31
3.4	The photophysical and photochemical processes. Taken from Ref. [11]	33
3.5	The quantum picture of the probability of electronic transitions from Franck-Condon principle. Taken from Ref. [5]	33
3.6	The energy difference between the absorbed and emitted radiation. Redrawn based on a figure from ref. [14]	34
3.7	The horizontal crossing between the energy levels in the intramolecular radiationless transitions.	36

3.8	The potential energy surfaces of the excimer formation in addition to the monomer emission and the excimer emission. Redrawn based on a figure from ref.[7]	39
3.9	The electron exchange mechanism of the electronic energy transfer.	41
3.10	The coulombic mechanism of the electronic energy transfer.	42
3.11	Illustration of Förster resonance energy transfer (FRET). Redrawn based on a figure from ref. [5]	42
3.12	The electron transfer mechanism.	44
3.13	The schematic explains the reactions pathway of the excited state after excitation which includes the potential energy surfaces of the ground state and the excited state.	46
4.1	Flow diagram for solving the HF equations.	61
4.2	Plots for $f(r) = 1 - \text{erf}(\omega r)$ and $f(r) = 1 - [\alpha + \beta \text{erf}(\omega r)]$. Redrawn based on a figure from ref. [26] values of $\alpha=0.19$ and $\beta=0.46$.	69
4.3	Jacob's ladder of DFTB. DFTB 0 is the original noniterative version without self-consistent charges (SCC). DFTB 2 treats SCC to second order while DFTB 3 treats third order	72
5.1	Eight typical molecules that are often used as acceptors or donors in organic electronics.	89
5.2	Graphical solution in the QP method. Upper: the diagonal line corresponds to ω while the horizontal curves correspond to $\langle \psi_s \hat{h}_H \psi_s \rangle + \Re \langle \psi_s \Sigma_{xc}^{G_0W_0}(\omega) \psi_s \rangle$ for different states, HOMO being red, LUMO blue, and higher states are jagged magenta. The QP solutions for HOMO and LUMO are marked with circles. Lower: the corresponding DOS . Pole strengths (the magnitude of the peaks in the DOS) are obtained from the slope where the diagonal line crosses the horizontal curves.	102
5.3	The 15 small molecules treated here.	104
5.4	a) Correlation plot for LDA "Koopmans' theorem IPs" versus experimental IPs [40]. b) Inversion plot for the same data constructed using Eq. (5.40) to show the "predictive ability" of the LDA least squares fit. The units for both axes in these plots are in eV.	105
5.5	Correlation plot for DFTB "Koopmans' theorem IPs" versus experimental IPs. a) Correlation plot for DFTB "Koopmans' theorem IPs" versus experimental IPs. b) Inversion plot for the same data constructed using Eq. (5.40) to show the "predictive ability" of the DFTB least squares fit. The units for both axes in these plots are in eV.	109

5.6	Correlation plot for DFTB versus LDA “Koopmans’ theorem IPs.” The units for both axes are eV.	112
5.7	Correlation graph of data from Table 5.5 showing how experimental and Green’s function IPs compare. The label “ <i>GW</i> ” [as opposed to <i>GW</i> DOS and <i>GW</i> QP] are calculated values taken from the litera- ture. (See Table 5.5.) Units are in eV. The <i>x</i> -axis corresponds to our <i>GW</i> QP calculations.	114
5.8	Correlation graph of data from Table 5.6 showing how experimental and Green’s function EAs compare. The label “ <i>GW</i> ” [as opposed to <i>GW</i> DOS and <i>GW</i> QP] are calculated values taken from the litera- ture. (See Table 5.6.)	117
5.9	Correlation graph of data from Table 5.5 showing how the DFTB, SCC-DFTB, and other methods compare with <i>GW</i> QP IPs.	118
5.10	Inversion plot showing how fitting parameters obtained for the SCC- DFTB KT IPs and medium-sized molecules predict the <i>GW</i> QP IPs of medium-sized molecules and the experimental IPs of small molecules.	120
5.11	Correlation graph of data from Table 5.5 showing how the DFTB, SCC-DFTB, and other methods (<i>y</i> -axis, eV) compare with <i>GW</i> QP (<i>x</i> -axis, eV) EAs.	121
5.12	Schematic of an organic solar cell as a Shockley diode.	124
6.1	Two vertically-stacked ethylene molecules.	143
6.2	Ethylene highest occupied molecular orbital (H) and lowest unoccu- pied molecular orbital (L).	144
6.3	Two-orbital two-electron model (TOTEM).	145
6.4	MO diagram for two stacked ethylene molecules. White indicates the positive phase parts of the <i>p</i> functions while grey indicates the neg- ative phase parts. Overlap between the MOs on different molecules have been neglected in normalizing the supermolecule MOs.	146
6.5	The four transitions in (TOTEM) ² and their associated transition dipole moments.	147
6.6	Exciton model classification of transitions in the (TOTEM) ² model. In each double box, the left hand side shows the orbital occupancy of the MOs in molecule 1 while the right hand side shows the orbital occupancy of the MOs in molecule 2.	148
6.7	Schematic of Kasha’s theory for two parallel stacked molecules.	149

6.8	MO diagram for three stacked ethylene molecules. White indicates the positive phase parts of the p functions while grey indicates the negative phase parts. Overlap between the MOs on different molecules have been neglected in normalizing the supermolecule MOs.	150
6.9	The nine single excitations for three stacked ethylene molecules along with their symmetry assignments.	151
6.10	The transition densities for the five symmetry allowed B_{1u} singlet excitations.	151
6.11	Periodic model labeling and hopping parameters used for our stacked ethylene tight-binding calculation.	153
6.12	Bands for the stacked ethylene tight-binding model with $\alpha = 0$, $\beta = -1$, and $\gamma = 0.1$. The paired arrows ($\uparrow\downarrow$) are meant to indicate filled bands below the fermi level.	155
6.13	The CMOs for the optically-allowed transitions of (TOTEM) ^N at the Γ -point.	157
6.14	Pentacene carbon numbering.	173
6.15	The configurations of the five models of parallel stacked pentacene (P_n stands for n parallel stacked pentacenes).	174
6.16	Simple Hückel molecular orbital theory results for the pentacene monomer. 175	
6.17	Pentacene monomer B3LYP/6-31G(d,p) MOs.	176
6.18	Pentacene monomer absorption spectra: (a) TD-LDA, TD-DFTB, and experiment; (b) TD-B3LYP, TD-DFTB, and experiment; (c) TD-CAM-B3LYP, TD-lc-DFTB, and experiment. The experimental curve is a spectrum measured in tetrahydrofuran. Intensities are in arbitrary units.	177
6.19	Monomer NTOs and renormalized coefficient: TD-B3LYP/6-31G(d,p)//B3LYP/6-31G(d,p) 633 nm.	179
6.20	Pentacene tetramer potential energy surfaces without dispersion correction: (a) LDA and DFTB; (b) B3LYP and DFTB; (c) CAM-B3LYP, lc-DFTB.	180
6.21	Pentacene tetramer potential energy surfaces without dispersion correction: (a) B3LYP+D3 and DFTB+D3; (b) CAM-B3LYP+D3, lc-DFTB+D3.	181
6.22	Dimer NTOs and renormalized coefficients: (a) TD-B3LYP/6-31G(d,p)//D3-B3LYP/6-31G(d,p) 621 nm, (b) TD-B3LYP/6-31G(d,p)//D3-B3LYP/6-31G(d,p) 735 nm.	182

6.23	Comparison of exciton diagrams for different functionals using the data from Tables 6.2 and 6.4.	184
6.24	Graph comparing the Davydov splittings, $E(\text{ET})-E(\text{CT})$, of the trimer and dimer. The 45° line indicates perfect agreement between dimer and trimer Davydov splittings.	190
6.25	Convergence of spectra as a function of number of pentacene molecules in the stack: (a) TD-LDA/6-31G(d,p), (b) TD-B3LYP/6-31G(d,p), (c) TD-CAM-B3LYP/6-31G(d,p), and (d) TD-HF/6-31G(d,p). . . .	192
6.26	TD-DFTB spectra of stacked pentacene: (a) with a fixed active space, (b) with a size-extensive active space.	193
6.27	TD-lc-DFTB spectra of stacked pentacene: (a) with a fixed active space, (b) with a size-consistent active space.	193
6.28	Comparison of pentacene spectra: (a) TD-DFTB and TD-B3LYP/6-31G(d,p) and (b) TD-lc-DFTB and TD-CAM-B3LYP/6-31G(d,p). .	195
6.29	Excitonic effects on the absorption spectrum of pentacene: curves, pentacene in tetrahydrofuran (THF) and as a thin film (from Ref. [121]); stick spectra, lower are the position of unshifted monomer and crystal peaks calculated using the Bethe-Salpeter equation (BSE) while the upper stick spectra have been shifted to match the experiment (from Ref. [20].) See also Ref. [125].	195
6.30	Herringbone cluster models used in this work. All are portions of the x-ray crystal structure: (a) pentamer, (b) “vertical” decamer, and (c) “horizontal” decamer.	196
6.31	Comparisons of calculations using various methods with the thin film absorption spectrum from Ref. [121]. The CT and ET excitation energies were calculated from Kasha’s exciton model using Eq. (6.97). .	197
6.32	Comparison of theoretical and experimental exciton shifts: (a) TD-B3LYP/6-31G(d,p), (b) TD-DFTB, (c) TD-CAM-B3LYP/6-31G(d,p), and (d) TD-lc-DFTB.	199
6.33	Ideal Kasha figures for co-planar inclined transition dipole moments: (a) laterally shifted parallel stacked pentacene dimer, (b) Kasha plot of excitation energies as a function of the angle θ , (c) 3D plot of Kasha’s model for oscillator strengths and excitation energies. . . .	201
6.34	TD-B3LYP/6-31G(d,p)//B3LYP+D3/6-31G(d,p) Kasha figures for co-planar inclined transition dipole moments: (a) excitation energies as a function of the angle θ , (b) 2D plot of oscillator strengths, (c) 3D plot of oscillator strengths and excitation energies,	202

6.35	TD-CAM-B3LYP/6-31G(d,p)//CAM-B3LYP+D3/6-31G(d,p) Kasha figures for co-planar inclined transition dipole moments: (a) excitation energies as a function of the angle θ , (b) 2D plot of oscillator strengths, (c) 3D plot of oscillator strengths and excitation energies,	204
7.1	The initial orientations of pentacene and buckminsterfullerene in the model of organic solar cells studied in this work.	226
7.2	Convergence of temperature with time during the DFTB+ equilibration.	242
7.3	Calculated absorption spectra using lc methods.	244
7.4	Dominant particle \rightarrow hole contributions and excitation energies showing the correspondence between the most intense TD-CAM-B3LYP/6-31G(d,p) absorption peak and the corresponding TD-lc-DFTB absorption peak.	245
7.5	Assignment of the physical character of the initial excitation of several trajectories based upon the two most important MO contributions to the singlet excitation: Traj 1, DL-type; Traj 2, P-type; Traj 18, P-type; Traj 6, P-type.	248
7.6	Variation of state populations during the first 50 fs of the simulation.	249
7.7	Temporal variation of properties for the active state of five initially P-type trajectories (trajectory numbers 4, 6, 17, 28, and 30): (a) Λ , (b) oscillator strength, and (c) transition dipole moment.	251
7.8	Temporal variation of properties for the active state of five initially DL-type trajectories (trajectory numbers 10, 14, 23, 25, and 27): (a) Λ , (b) oscillator strength, and (c) transition dipole moment.	252
7.9	Traj 6: Ground and excited state energies as a function of time: (a) first 500 fs, (b) zoom to 150-250 fs. The active state is marked by red bullets.	254
7.10	Traj. 6: Surface hopping during the first 250 fs of the trajectory. . . .	255
7.11	Traj. 6: Snapshots of the principle particle and hole MOs characterizing the active state.	256
7.12	Traj. 6: Snapshots of the particle-hole charge density difference for the active state.	257
7.13	Evolution of some properties of the Traj. 6 active state: (a) Λ , (b) oscillator strength, and (c) transition dipole moment.	258
7.14	Traj 27: Ground and excited state energies as a function of time: (a) first 500 fs, (b) zoom to 85-135 fs. The active state is marked by red bullets.	260

7.15	Traj. 27: Surface hopping during the first 250 fs of the trajectory. . .	261
7.16	Traj. 27: Snapshots of the principle particle and hole MOs character- izing the active state.	261
7.17	Traj 27: Snapshots of the particle-hole charge density difference for the active state.	262
7.18	Evolution of some properties of the Traj 27 active state: (a) Λ , (b) oscillator strength, and (c) transition dipole moment.	263
7.19	Charge density difference maps and CT times for the six trajectories where CT was observed.	264
7.20	Particle-hole charge analysis for 16 trajectories showing the $P \rightarrow P$ $\rightarrow C_{60}$ nature of the temporal evolution of the active excited state. .	290
7.21	Particle-hole charge analysis for 16 trajectories showing the $P \rightarrow P$ $\rightarrow C_{60}$ nature of the temporal evolution of the active excited state. .	291
7.22	Particle-hole charge analysis for 14 trajectories showing the $DL \rightarrow$ $C_{60} \rightarrow P$ nature of the temporal evolution of the active excited state.	292
7.23	Particle-hole charge analysis for 14 trajectories showing the $DL \rightarrow$ $C_{60} \rightarrow P$ nature of the temporal evolution of the active excited state.	293
7.24	Snapshots of the particle-hole charge density difference for the ac- tive state for 6 trajectories showing the time to get charge transfer of the active excited state by using DFTBABY without long-range correction.	294